High-power acid Biophotovoltaic cells for the generation of green electricity

Eva Maria Lain Rodriguez

Department of Chemical Engineering and Biotechnology
University of Cambridge

This dissertation is submitted for the degree of
Doctor of Philosophy in Biotechnology

Darwin College June 2018

Abstract

High-power acid Biophotovoltaic cells for the generation of green electricity

Eva Maria Lain Rodriguez

This thesis reports the development of acid-operating microbial fuel cells (MFCs) for the investigation of elevated electrical conductivity and resulting enhanced bioelectricity generation. This project describes the use of extremophile microorganisms as the biological material in MFCs, for the investigation of low internal resistance biological fuel cells. In particular, this thesis focuses on BPV (biological photovoltaic) cells, a type of MFC that utilises autotrophic biological material, which relies on oxygenic photosynthesis and hence simply requires water as the electron donor (unlike traditional MFCs, which are dependent of an organic substrate feed). Novel reactor designs based on acidophilic and metallotolerant microorganisms, studied using electrochemical techniques, are reported for the first time. The novel strategy consists in the adoption of very low pH and elevated heavy metal concentration levels for biological fuel cell operation, which is possible due to the choice of suitable extremophile microorganisms that are able to thrive under such severe physicochemical conditions. In order to support the analysis of the subject MFCs, a series of electrochemical and fluorescence techniques were employed. Chapter 3 reports the study of standard BPV cells, focusing on classic cell configuration and choice of biological material. BPV cells based on the standard prokaryotic and eukaryotic strains *Synechococcus elongatus* and *Chlorella vulgaris*, respectively, were built and electrochemically characterised by means of polarisation curves and continuous power output monitorisation. Subsequently, a study on the potential conditioning of BPV cells was conducted using Pulse Amplitude Modulation (PAM) Fluorimetry; it is the first documented observation of short-term electrolytic potential conditioning effects on photosynthetic efficiency and associated parameters. The work in chapters 4 and 5 explores the extent to which acidophiles may be used as the biological material in MFCs. A search to find a set of naturally-occurring, metallotolerant acidophiles is undertaken throughout the Rio Tinto ecosystem, selected for its unique extreme physicochemical nature and reported extremophile presence. Chapter 4 informs about the physicochemical characterisation of the chosen sampling points, describing the evolution of pH, electrical conductivity, heavy metal concentration, ferric/ferrous ion balance and dissolved oxygen throughout a natural year, in order to identify the sites with the hardest physicochemical conditions. Finally, chapter 5 investigates the presence of living microorganisms in the sampled sites, enabling the identification of the best location for the purpose of this study. A tailored sediment cell was built and tested in situ (for the first time in an extremophilic environment), and compared to the electrical performance of a novel BPV cell based on commercially-available photosynthetic acidophile *Dunaliella acidophila*.

Declaration

This dissertation is the result of my own work and includes nothing which is the outcome of work done in collaboration except as declared in the Preface and specified in the text.

It is not substantially the same as any that I have submitted, or, is being concurrently submitted for a degree or diploma or other qualification at the University of Cambridge or any other University or similar institution except as declared in the Preface and specified in the text. I further state that no substantial part of my dissertation has already been submitted, or, is being concurrently submitted for any such degree, diploma or other qualification at the University of Cambridge or any other University or similar institution except as declared in the Preface and specified in the text.

Eva Maria Lain Rodriguez

June 2018

Table of Contents

1 Chapter 1: Introduction

The transition towards renewable energy sources is one of the biggest challenges of the 21st century. Due to environmental and energy security reasons, the need to replace fossil fuels with green energy sources has become of paramount importance (Hook et al. 2013).

Undoubtedly, there is a pressing need to reduce the carbon footprint associated with energy sources, in order to minimise global warming. It is widely accepted that the anthropogenic release of greenhouse gases, particularly CO_2 emissions resulting from fossil fuel combustion, are a crucial cause for climate change (Doherty et al. 2009). In fact, the levels of this greenhouse effect gas have risen by over a third since the beginning of the Industrial Revolution (Mosleh Arany et al. 2018). On the other hand, energy security issues such as the depletion of fossil fuels or uncompetitive prices underlie the need to develop viable alternative energy sources (Fantazzini et al. 2011).

This need for a shift towards green energy sources is reflected by the growing legislation favouring renewable technologies in detriment of traditional fossil fuels. For instance, the European Commission has set a target of 20% final energy consumption from renewable sources in the European Union, to be met by 2020.

Solar energy appears to be the most appealing option out of the various renewable energy sources. The rationale underlying this assertion is that just one hour of solar energy reaching the Earth's surface (4.3×10^{20} J) is enough to meet the annual global energy demand (circa 4×10^{20} J), which makes solar energy tremendously attractive (Lewis and Nocera, 2006 and Thirugnanasambandam et al. 2010).

A number of issues are preventing a wide adoption of conventional solar energy technology, the primary of which seems to be that manufacturing costs are relatively elevated (Leong et al. 2009). Therefore, a meritorious alternative to synthetic solar panels could be to base panels on biological material or organisms that are capable of self-assembly as well as self-repair, due to their fabrication and maintenance cost-effectiveness.

1.1. Generation of electrical power in biological fuel cells

A large amount of work has been undertaken on the topic of biological-based solar panels, from pigment (Tang et al. 1975) and protein-based technology (Gross et al. 1978) to whole organism-based cells (Bombelli et al. 2011a). Although their power output is considerably low, whole organism-based technologies are particularly interesting because of their self-repair capacity, which both pigment and protein-based cells lack. This facet is crucial in order to ensure a long solar panel lifetime under otherwise incredibly damaging sunlight. Hence, whole organism-based cells, i.e. so-called biological photovoltaic cells (BPVs), are here considered to be the most promising option to develop and build onto a "green" solar-panel-powered future.

Biological photovoltaic cells are a type of Microbial Fuel Cell (MFC). Microbial fuel cells are power-generating devices that make use of biological exoelectrogenic as

well as catalytic redox processes, usually in combination with conventional abiotic electrochemical reactions (Logan et al. 2006). MFCs harness chemical energy from the metabolism of microorganisms, converting it directly into electrical power.

Fundamentals of MFCs

Microbial Fuel Cells are bioelectrochemical systems, wherein microorganisms, which in one form or another are able to generate an electric current, are used to produce power. Typically, MFCs utilise microorganisms to catalyse the oxidation of organic or inorganic matter, breaking down sugars and other nutrients provided by the medium in order to ensuingly release part of that energy as electrical current, by transferring electrodes from these substrates onto the anode electrode. When an appropriate cathode reaction is possible (i.e. the reduction of oxygen), electrical current flows from the cathode to the anode, due to the difference in half-cell potential between the two electrodes, entailing the generation of electrical power; the electrodes should be connected to each other via a resistor or load (Berk and Canfield, 1964). The electrons may be transferred from the microorganisms to the electrode in either a direct or an indirect manner. When the electrons are transferred directly from the microorganism to the electrode, either by direct membrane-associated transfer (Bond and Lovley, 2003) or by means of nanowires (Gorby et al. 2006), the device is classed as a "mediatorless" MFC. On the other hand, should electron transfer require shuttling from the microorganisms to the electrode by exogenous redox mediators, the device is known as a "mediated" MFC.

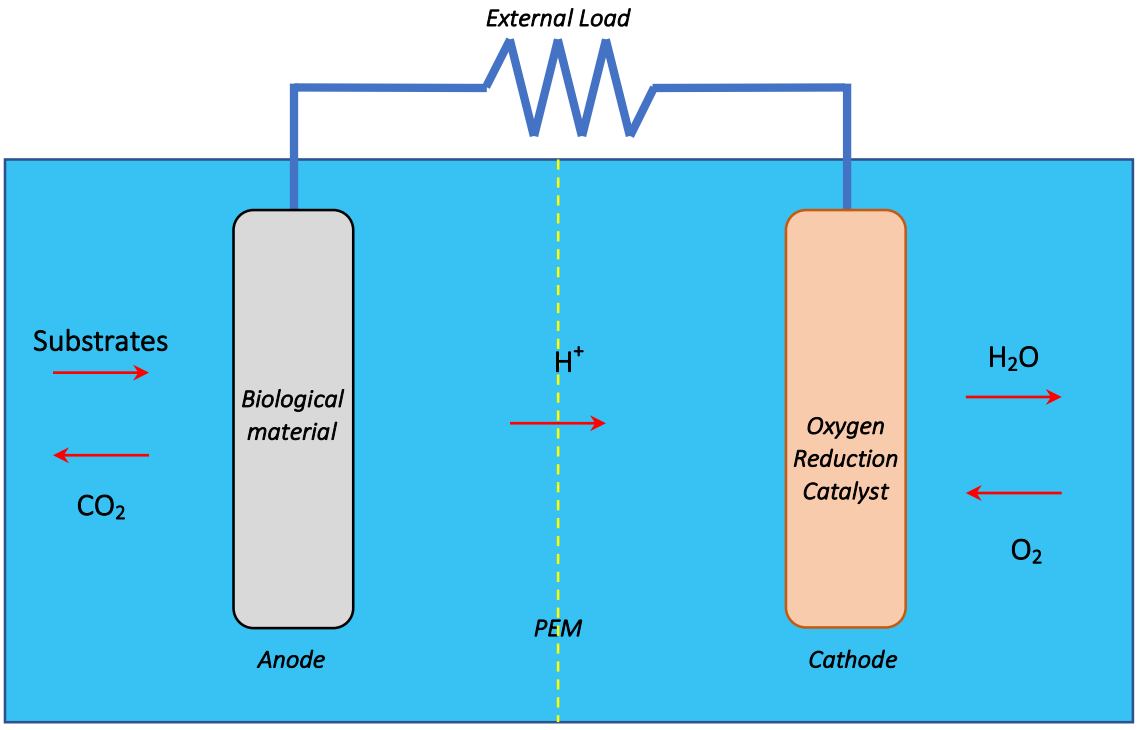

Figure 1: A typical MFC cell, illustrating the anode and cathode electrodes (connected via an external load) and respective hosting chambers, separated by a proton-exchange membrane (PEM).

A conventional MFC counts with two chambers, corresponding to the anode and the cathode compartments, which are usually physically separated from one another by an ion-exchange membrane, most commonly a proton-exchange membrane (PEM), i.e. Nafion (Ghasemi et al. 2012). In the anode compartment, microorganisms generate electrons and protons resulting from the oxidation of substrates (typically organic matter). Thereon, the electrons are injected into the anode electrode, being conducted through the external circuit unto the cathode electrode, where these react with dissolved molecular oxygen and protons that have migrated down a concentration gradient from the anode chamber (where they are generated), through the PEM, to the cathode chamber. In the subject electrochemical reaction, protons, molecular oxygen and electrons combine in order to reduce oxygen, leading to the formation of water (Sharma and Li, 2010).

The biological material in MFCs may take a number of forms, from pure culture biofilms (composed of a single strain), to mixed culture biofilms (composed of a consortia of microorganisms). Abundant research has led to the repeated observation that MFCs based on mixed cultures exhibit higher power outputs than their counterpart pure culture MFCs (Jothinathan and Wilson, 2017). It has been proposed that mixed cultures benefit from symbiotic interactions between the various component strains, which enhance energy conversion associated with electron transfer to the electrode, thereby exhibiting superior electrical performances (Erable et al., 2009).

Applications of MFCs

MFCs were initially developed at the beginning of the 20th century (Potter, 1911). However, they remained a scientific curiosity until relatively recently, when the scientific understanding behind the mechanisms underlying their working principle was improved, propitiating an improvement of electrical performance that opened a window for implementation at an industrial level, building up an interest to its associated commercial potential (Logan, 2008). Since the start of the 21st century, microbial fuel cells have found use in a growing number of applications, in which, in addition to undertaking the original process of interest, an added value may be obtained from the generated electrical power. The main practical applications for MFCs are outlined thus:

- Wastewater treatment

A promising application for MFCs lies in the generation of electrical power from wastewater treatment, by coupling water sanitation to electricity generation. Requiring about 0.5-2 kWh/m^3, the energy consumption for wastewater treatment accounts approximately for 1% of the average daily electricity consumption in England and Wales, corresponding to 6.34 GWh (DTI, 2005).

Wastewater treatment with MFCs represents a sustainable technology that is able to generate energy from the oxidation of a variety of compounds present in the wastewater, resulting in the simultaneous carbon removal from the water to be treated (>90% purge) as well as electricity generation (Pant et al. 2010). The added value accompanying the required sanitation process is particularly useful; despite

the considerable energy input required for treatment with classic methods, wastewater contains three to five times as much energy (Gude, 2015). The energy locked in wastewater is present majorly as thermal energy (~7 kWh/m^3) and in a smaller yet substantial proportion as chemical energy, i.e. organic matter (~1.8 kWh/m^3) and as other nutritional elements (~0.7 kWh/m^3), e.g. phosphorous (Gude et al. 2013). While the thermal energy may not be harvested, chemical energy (~26%) may be efficiently unlocked with microorganisms, yielding enough electrical power to at least make the process energy-independent (if not energy-generating). Therefore, this technology is doubly useful, as MFCs are able to perform the dual task of breaking down the subject effluents while unlocking energy from these, unlike standard water sanitation systems, which are energy-consuming. Hence, MFCs pose an interesting option for the treatment of industrial, agricultural or municipal effluents, for example.

A well-established technique for the generation of electrical energy from wastewater treatment is anaerobic digestion, in which microorganisms convert the organic content from the sludge into methane. From stoichiometric estimations, microorganisms are able to generate 1 Kg of methane from 4 Kg of carbon, measured as chemical oxygen demand, COD (Khandan et al. 2014). The utilization of biogas from anaerobic digestion has been reported to produce 350 kWh of power for each million gallons of wastewater (Burton, 1996). Another option for energy recovery from wastewater are phototrophic (algae-based) wastewater treatment processes, which generate energy-rich algal biomass that can subsequently be used as feedstock (Shoener et al. 2014).

MFCs also pose a sustainable method for organic removal from waste sludges, by means of the direct conversion of organic waste into useful energy, making it possible to obtain electrical power simultaneously to the digestion of a variety of biodegradable organic compounds, such as those present in the sludge resulting from industrial and agricultural activities (Pant et al. 2010).

- Biohydrogen production

The production of hydrogen gas via microbial fermentation is well-established. However, yields are considerably low; 2-3 moles of hydrogen are recovered per mole of glucose fermented (Logan, 2004). While certain microorganisms are able to readily hydrolyse glucose and cellulose, these are limited to sugars, as they are unable to process other organic metabolites such as organic acids (e.g. acetic acid), unless an additional energy input is provided.

With the aid of supplementary voltage, MFCs operating under anaerobic conditions (at least at the cathode level) are able to generate molecular hydrogen through the reduction of protons at the cathode with a higher efficiency than typical fermentation (Lieu et al. 2005). In MFCs, microorganisms generate electrical energy from the chemical energy stored in cellulose as well as other organic matter, shuttling electrons resulting from the oxidation of these substrates to the anode, thereby releasing protons. Together with molecular oxygen, the generated electrons and protons react at the cathode, generating water. The bacteria used generate a cell potential of around 0.3 V, to which an additional input of 0.2 V is added in order to

promote the hydrogen evolution process at the cathode. This process is significantly more efficient than typical biohydrogen production, as it makes more accessible the endothermic barrier of hydrogen production via sugar fermentation, allowing the processing of a set of otherwise unused substrates such as acetic acid (Rozendal et al. 2006). This type of MFC, supplemented with additional voltage, is known as a microbial electrolysis cell (MEC), which constitutes a hydrogen production bioreactor that combines an MFC with electrolysis (Sun et al. 2008).

Recently, self-powered biohydrogen-generating MFCs have been developed, which no longer rely on an external voltage supply. A self-powered system constituted by a single-chamber MFC coupled to a two-chamber MEC was proven to successfully produce biohydrogen, without an external voltage input (Sun et al. 2008). Subsequently, researchers merged the two processes (hydrogen production and electricity generation) into a single device, by utilizing one anode while dividing the cathode into two chambers, each corresponding to one of the subject processes (Zhang and Angelidaki, 2012). This kind of system represents a very attractive option for the doubly useful production of biohydrogen and processing of organic waste.

- Powering remote sensors

Remote or wireless sensors have an ample variety of applications, such as meteorological monitoring and environmental stewardship systems, as well as naval control and intelligence technology. While these are relatively widespread, they are still limited by the lack of a power source that is able to operate long-term, as the replacement of standard batteries may not be operational due to neither being possible, practical nor economically viable. For instance, the batteries in a deep-sea sensor typically have a lifetime below three years, and the labour required to replace these can cost about $ 500k (Guzman et al. 2010). Moreover, network security (e.g. in defense and national security communication systems) could be compromised.

Microbial fuel cells pose an attractive alternative to classic batteries for powering remote sensors and telemetry systems. Due to their self-renewable quality, MFCs can solve the problem of replacing the batteries, offering maintenance-free and consistent power, extending hardware lifetime a considerable length beyond their current duration (Shantaram et al. 2005). In practice, microbial fuel cells have been used in marine sediment sensors. These cells are known as benthic MFCs (Tender et al. 2002), and have been successfully deployed in undersea sensor and communication technology (Tender et al. 2008). This technology therefore constitutes a very attractive alternative to the classic batteries employed in remote hardware, by overcoming the issue of limited lifetime, hence enhancing the practicality of these systems.

As outlined above, MFCs have use in a range of very interesting applications, showing a promising potential for future technological developments in bioremediation, bioelectrosynthesis of compounds of interest, self-renewable fuel cells and biosensors, for instance.

Although the need to utilise organic substrates makes MFCs useful for certain bioremediation applications (i.e. wastewater treatment), such reliance can be regarded as a limitation for the generation of energy alone. When power generation is not coupled to any other function, an ideal biological fuel cell should be autonomous, that is, it does not require any organic input. This is possible when the biological material used is able to fix carbon (i.e. autotrophic), such as photosynthetic algae. This type of fuel cell, known as Biological Photovoltaic (BPV) cell, is a type of Microbial Fuel Cell, which is based on microorganisms that undergo oxygenic photosynthesis. Unlike conventional MFCs, where the electron donors are organic compounds, e.g. glucose or acetate (Chang et al. 2006), BPV cells are able to use water as the electron donor. Hence, as no organic substrates are necessary for the functioning and longevity of these devices, they stand as an autonomous source of electrical power.

Fundamentals of BPV cells

Biological Photovoltaic (BPV) cells are a type of biological fuel cell, in which the biological material used is autotropic and undergoes oxygenic photosynthesis. BPVs are based on photosynthetic microorganisms that use water as the electron donor (instead of organic compounds like heterotrophs), and are able to fix inorganic carbon from atmospheric carbon dioxide into more complex organic molecules; they do not require the input of organic substrates as do MFCs.

The main advantage of BPV cells over classic MFCs is that they represent an autonomous source of energy, as their constituent microorganisms are autotrophic and hence do not rely on the input of organic substrates. Therefore, the possibilities of BPV cells stand well beyond those of standard MFCs, which are constrained by their need of an organic feed.

Akin to MFCs, a standard BPV counts with an anode electrode, which is the site for oxidation, and a cathode electrode, where reduction takes place. A power output is consequently achievable as a result of the potential difference between the two electrodes (Franks and Nevin, 2010). The anode compartment hosts the biological material, i.e. oxygenic photosynthetic microorganisms or subcellular fractions of these, while the cathode compartment is typically abiotic and counts with an electrode that is typically coated with an oxygen reduction catalyst (ORC). At the anode, microorganisms convert light energy into electrical energy and, directly or indirectly, feed the electrons resulting from the photolysis of water (the electron donor) onto the anode electrode. Thus, the electrons resulting from the photolysis of water are transferred to the cathode by means of the external circuit, while the generated protons migrate to the cathode compartment by diffusion down the concentration gradient, usually across a PEM (Yuan et al. 2016). Finally, the protons and electrons combine together with molecular oxygen (the electron acceptor), thereby reducing it to water in a reaction catalysed by the cathode electrode, which is usually coated with a platinum catalyst (Hug et al. 2014).

The subject biological material exhibits a net consumption of carbon dioxide, yielding molecular oxygen as a result of the photolysis of water in the light-dependent reactions of photosynthesis. Therefore, BPV cells display a negative

carbon footprint, and hence this "green" technology is particularly attractive from the environmental point of view of carbon emissions reduction.

There are a number of possible configurations for BPV cells. Accordingly, the fuel cell may count with a single chamber that hosts the two electrodes, or it may be divided into an anode and a cathode compartment that are physically separated, i.e. by an ion-exchange membrane, most commonly a proton-exchange membrane such as Nafion (Bombelli et al. 2011a). The latter, more complex configuration allows the compartmentalisation of the anode and cathode electrode surroundings, which is advantageous from a species crossover prevention point of view.

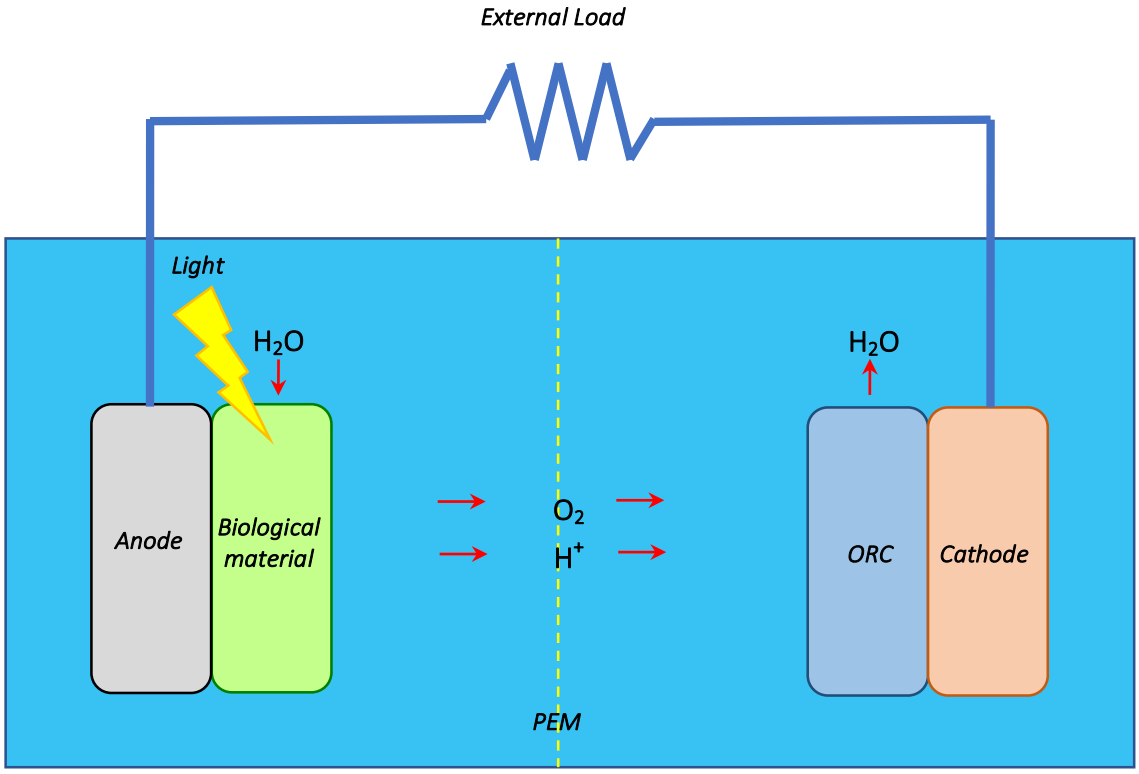

Figure 2: Simplified diagram of a BPV cell, illustrating its constituent components: The anode and cathode electrodes, the biological material associated with the anode, the oxygen reduction catalyst (ORC) attached to the cathode and the proton-exchange membrane (PEM). In addition, the diagram depicts the input of water into the anode compartment, which results in the formation of molecular oxygen and protons, which migrate through the PEM to the cathode compartment, where they react to form water again in a reaction catalysed by the ORC.

The nature of the biological material attached to the anode electrode can take up a wide range of forms. For instance, it may be constituted by whole living cells, or by fractions thereof.

There are three types of sub-cellular fractions used as the photoactive material in BPVs. The smallest morphological units capable of performing a charge separation event upon light absorption are photosynthetic pigments, e.g. chlorophyll and

xanthophyll, which have been used as the anodic catalyst in pigment-based BPVs (Lieu et al. 2006). The simplest morphological unit after single molecules is the use of isolated photosynthetic reaction centers, such as Photosystem II (Yehezkeli et al. 2012). Finally, the largest sub-cellular fraction utilised in BPVs consists of whole isolated chloroplasts or thylakoid membranes (Kayano et al. 1981). The main problem associated with sub-cellular based fuel cells lies in the limited lifetime of the devices as a result of the rapid deterioration suffered by its constituent biological material. All three types of sub-cellular fractions decay extremely quickly; for instance, cyanobacterial Photosystem II has an average half-lifetime of under one hour (Yao et al. 2012), which jeopardizes any possibility of operational feasibility.

On the contrary, BPV cells based on whole living cells are considerably more attractive due to their long durability as a result of their capability to self-repair the damage caused by light-induced decay of photosynthetically active components. In addition, its self-assembly quality reduces production costs (versus sub-cellular based BPV cells or traditional synthetic solar panels). The microorganisms used in whole-cell BPV devices are solely oxygenic photosynthetic microorganisms, which are able to convert light energy into electrical energy via the photolysis of water during light exposure, in light-dependent photosynthesis reactions, and the catabolism of organic compounds, both under light and in the dark (McCormick et al. 2011).

Both prokaryotic and eukaryotic cells may be used as the photoactive morphological units in BPV cells. Typical prokaryotic cells are usually cyanobacteria such as *Synechococcus elongatus* or *Synechocystis,* while the eukaryotic cells of choice tend to be green algae such as *Chlorella vulgaris*. The former perform considerably better, due to their more exposed membrane electron transport machinery as a result of the simpler cellular structure, which enhances electric current generation, and hence prokaryotes display higher power outputs (Schultze et al. 2009).

Prior work on BPV cells

BPV cells were originally developed in the 1980s. A range of cyanobacteria were shown to generate electrical current at the anode upon light irradiation, such as *Phormidium* (Ochiai et al. 1983), firstly, followed by *Synechococcus* (Yagishita et al. 1993) and *Synechocystis* (Yagishita et al. 1997).

Subsequent work was centred around the addition of both lipid-soluble (Martens and Hall, 1994) as well as lipid-insoluble (Thorne et al. 2011) exogenous electrochemical mediators, in order to facilitate the interception and shuttling of electrons between the cells and the electrode, with the aim of enhancing power output. However, the elevated cost and toxicity of suitable electrochemical mediators represents a considerable drawback (Gil et al. 2003), therefore research soon shifted back to mediator-free BPV cells (Logan, 2009).

A growing amount of research on mediator-less BPV cells has been performed lately, employing a variety of prokaryotic (Gorby et al. 2006) as well as eukaryotic (Luimstra et al. 2014) bacteria. The studied devices are operated at moderate temperature and pH values, circa 22°C and neutral pH, respectively. Nonetheless,

while the concept of BPV cells is very attractive, power outputs remain too low as to being commercially viable merely beyond a scientific curiosity, requiring considerable further development and optimisation (Bombelli et al. 2011b).

1.2. Characterisation techniques for BPV cells

The study of BPV cells relies on a number of research techniques that make it possible to investigate such devices and the biofilms they host, both in situ and ex situ. The focus of this study lies on the methods that enable the characterisation of BPV devices in situ, from an electrical as well as from a biological point of view. These fall into two main categories: electrochemical techniques and fluorescence techniques.

Electrochemical techniques

The aim of the electrochemical techniques employed is to investigate the electrical properties and capability of a BPV device, by determining its power output as well as providing information about its electrochemical behaviour. This enables a deeper understanding of the underlying electrochemical processes behind the biological generation of electric current, making it possible to modulate various electrical parameters of a device, most notably to maximise its power output.

Four main electrochemical techniques are employed in this study, as outlined thus:

- Polarisation curves

Polarisation curves depict cell voltage as a function of current density, as well as the associated power output. These may be performed by connecting a BPV device to a number of different resistances and measuring the resulting cell potential. This makes it possible to calculate the electric current that corresponds to each voltage value, starting from OCP (open circuit potential, at infinite resistance) down to short-circuit (0 resistance) and, in turn, to calculate the corresponding power output values. In addition to providing an insight into both the maximum possible potential difference and current output of the device, polarisation curves allow the determination of electric power as a function of resistance, hence making it possible to identify the precise resistance at which the power output of a particular device is at its maximum, key for its optimisation.

Polarisation curves are a standard electrochemical technique used in the characterisation of BPV cells, as typically reported in BPV publications (e.g. De Caprariis et al. 2014).

- Power output as a function of time

Power output may be evaluated as a function of time, by connecting the BPV device (and the resistor of choice) to a data logger, which continuously measures and records the cell voltage signal. Current, and consequently power, are then calculated, using the value of the resistance employed (typically chosen to obtain

the maximum power output for a given device, as inferred from a preliminary polarisation curve).

Power output monitorisation is also a classic electrochemical technique, which is commonly employed in the study of BPV cell performance, as commonly published in BPV literature (e.g. McCormick et al. 2011).

- Cyclic voltammetry

Cyclic voltammetry tests are performed by connecting the BPV device to a potentiostat, in a three-electrode configuration (working electrode, counter electrode and reference electrode). In cyclic voltammetry studies, a working electrode (either the cell anode or cathode) is subjected to a series of potentials, relative to a reference electrode (e.g. an Ag/AgCl electrode), which increase and decrease linearly (vs. time) in anodic or cathodic sweeps, for a chosen number of cycles. By scanning the electric current signal corresponding to each applied voltage, information about the presence and nature (i.e. reversibility) of redox reactions and participating species may be obtained.

This technique is employed in the elucidation of the electron transport pathways as well as the mechanisms underlying the operating principle of BPV cells, and is therefore used in fundamental BPV cell studies (e.g. Li et al. 2015).

- Chronoamperometry

Chronoamperometry analyses are carried out with a potentiostat, by connecting the BPV in a three-electrode configuration (working electrode, counter electrode and reference electrode), as for the cyclic voltammetry studies. In chronoamperometry tests, the working electrode is subjected to a fixed potential (relative to the reference electrode) and the resulting current signal is recorded. As electric current drops with time, information about diffusion parameters of the redox-active species is inferred.

This technique is typically used to track changes induced by variations in light exposure and other external stimuli (e.g. Sawa et al. 2017).

Fluorescence techniques

The aim of the fluorescence techniques used is to obtain information about the efficiency and kinetics of the photosynthetic biofilm hosted within the BPV device, by taking advantage of the fluorescence properties exhibited by various pigments contained within the electron transport machinery that constitutes metabolic processes of interest such as photosynthesis.

These techniques shed light on the structure of the biofilm, as well as the underlying electron transfer mechanisms and kinetics. Used in conjunction with electrochemical techniques, fluorescence parameters may be correlated to electrochemical aspects, making it possible to explain, predict and, to a certain extent, modulate the exoelectrogenic behaviour of the biofilm within the BPV device.

Two main fluorescence techniques are employed in this study, summarised thus:

- Pulse Amplitude Modulation (PAM) Fluorimetry

The aim of PAM Fluorimetry is to obtain information about photosynthesis and the fate of the absorbed light energy, by analysing fluorescence yield. This technique works by inducing the saturation of the photosynthetic reaction centres within living cells, thereby subjecting the biofilm of interest to varying levels of light. The resulting fluorescence is then recorded, corresponding to the following three types of emitted light: "measuring light", which results in a minimum fluorescence signal, "actinic light", which results in an intermediate fluorescence signal, and a strong "saturating pulse", which leads to a maximum fluorescence signal. The analysis of these signals provides information about the fate of the absorbed energy as well as the kinetics of photosynthesis.

PAM Fluorimetry allows the determination of photosynthesis process parameters such as "Maximum quantum yield", corresponding to photosynthetic efficiency (after dark adaption), "Effective quantum yield", which is a light-adapted quantum yield value (particular for each actinic light level). It also allows the determination of photosynthesis kinetic parameters such as "Electron Transport Rate", which quantifies the flux of electrons between Photosystem I and Photosystem II, as well as quenching parameters (e.g. photosynthetic quenching, corresponding to the conversion of energy into chemical work, and non-photosynthetic quenching, which represents a measure of energy conversion into alternative forms such as heat).

Fluorescence techniques have proved very helpful in providing information about photosynthetic processes, as they are a non-invasive method that provides real-time information about the efficiency and kinetics of photosynthesis.

There are two types of fluorescence experimented by photosynthetic apparatus. Firstly, there is the so-called passive fluorescence, or epifluorescence, which is a continuous process consisting in the absorption of blue light and its ensuing re-emission as red light by chlorophyll molecules. However, this phenomenon is not visible to the naked eye due to the overpowering reflected green light. The second type of fluorescence is known as active, or stimulated, fluorescence. This phenomenon occurs when a new photon arrives while the photosynthetic apparatus is still processing a previous photon. In such case, antenna pigments absorb the energy from the new photon, but, as it cannot be passed onto the reaction centre, this energy is re-emitted as fluorescence. It is therefore logical that active fluorescence will be at a minimum in the dark while at a maximum in bright light.

The light energy absorbed by the photosynthetic apparatus has three main possible fates: chemical work (principally photosynthesis, as well as other processes), fluorescence or alternative means of dissipation (mainly heat, as well as vibration).

Fluorimetry techniques are used to induce and manipulate photosynthesis and fluorescence, in order to probe the various fates of the irradiated light, in order to draw information from various kinetic, efficiency and biological parameters of photosynthesis.

There are two main commercially available fluorescence techniques used to investigate photosynthetic processes. These are Pulse Amplitude Modulation (PAM) Fluorimetry and Fast Rate Repetition Fluorimetry (FRRF). Both work by inducing the saturation of reaction centres, the difference being that PAM works with relatively long pulses of light, thereby inducing multiple turnovers, while FRRF utilises extremely short flashes of light, with which single turnovers are achieved. Both techniques are useful in providing information about photosynthesis and the fate of the absorbed light. However, since the intensity of the signals is lower in FRRF, and is hence susceptible to larger errors, PAM was chosen for this project, given that it is a more precise method.

PAM is concerned with measuring fluorescence yield, which is beyond fluorescence intensity. A PAM fluorometer induces fluorescence by emitting a pattern of 5 μs long light pulses, at variable frequencies (up to 20 kHz), with its set of light-emitting diodes. As the resulting induced fluorescence signal follows the pattern of the irradiated modulated light, all other light signals received by the photodetector can be discarded via an electronic transformation, outputting the signal of interest that corresponds exclusively to the pattern of 5 μs long light pulses.

There are three different types of light emitted by a PAM fluorometer. Firstly, the lowest light level used, known as "weak measuring light", employs very soft light with an intensity of 0.15 μmol photons m^{-2} s^{-1}. The resulting fluorescence is at its minimum value, called minimum fluorescence or F_0; this irradiated light is strong enough to induce fluorescence but not photosynthesis, i.e. to "close" the reaction centres, and is therefore a proportional measure of biomass, and hence of the available open reaction centres. A second type of light is used, with an intermediate intensity of up to 2,000 μmol photons m^{-2} s^{-1}. This light is strong enough to induce photosynthesis and therefore to close a proportion of the available reaction centres, which can be manipulated as a function of the intensity of the light employed. Finally, a very high intensity light is used, with more than 10,000 μmol photons m^{-2} s^{-1}, which is known as the "saturating pulse". This very bright light causes all reaction centres to "close", which corresponds to fluorescence at its maximum value, called maximum fluorescence or F_m.

In order to start each experiment with all reaction centres "open", a period of dark adaption is ensured, typically 15 minutes long. After dark adaption, all reaction centres are ready to receive and process photons, and hence quantum yield is at its maximum, known as the "Maximum quantum yield", a function of maximum fluorescence (F_m) and minimum fluorescence (F_0).

Conversely, under the irradiation of actinic light, i.e. strong enough to induce photosynthesis, some of the reaction centres will be closed and therefore the observed minimum (F') and maximum (F_m') values of fluorescence will be elevated and reduced, respectively. This light-adapted value of quantum yield, which is particular for each level of actinic light, is known as the "Effective quantum yield", a function of light-adapted maximum fluorescence (F_m) and light-adapted minimum fluorescence (F_0).

Quantum yield is a measure of photosynthetic stress, reflecting various factors such as light-caused strain, limitation of iron and other nutrients as well as oxygen effects, amongst others. In summary, quantum yield is inversely related to stress, e.g. there is an inverse relationship between effective quantum yield and light irradiance (McMinn and Hegseth, 2003).

The two main types of curves extracted from PAM data are Rapid Light Curves (RLCs) and Induction Curves (ICs). Both curves shed light on photosynthesis, the former concerning its kinetics and the latter its efficiency.

Rapid Light Curves plot relative Electron Transport Rate (rETR) as a function of irradiance (E), which is similar to the traditional Photosynthesis vs. Irradiance function. The Electron Transport Rate (ETR) quantifies the flux of electrons between Photosystem II (PSII) and Photosystem I (PSI). It is a function of light-adapted values of maximum and minimum fluorescence, as well as irradiance or photon flux density (PPFD) and the coefficient of light absorption (a*). As it depends on light adapted variables, its value will vary according to light intensity.

RLCs consist of eight 10-second-long steps of increasing light intensity, at each of which rETR is measured. This allows the elucidation of several photosynthetic kinetic parameters. Firstly, the initial steps of the curve, corresponding to low light levels, display a quasi-linear increase in rETR as a function of irradiance. The slope of this light-limited section of the curve is photosynthetic efficiency (α). This parameter indicates the ETR contribution per photon. Secondly, a maximum value of rETR ($rETR_{max}$) may be observed as a maximum light-saturated rate is achieved. As rETR is proportional to photosynthetic rate (P), $rETR_{max}$ is therefore an indicator of maximum photosynthetic capacity (P_{max}). The final kinetics parameter that can be obtained from the previous two values is the light saturation coefficient, otherwise known as photoadaptive index, E_k. This parameter indicates whether cells are correctly adapted to their light environment, i.e. ambient light and the photoadaptive index should be similar in order for cells to be healthy.

The second type of curve that can be generated with PAM data is an Induction Curve (IC). ICs plot fluorescence as a function of time, illustrating the response of the photosynthetic apparatus to varying levels of light. ICs consist of several steps of increasing light intensity, at each of which the cells are subjected to a saturating pulse of light. Initially, maximum quantum yield is assayed by subjecting the biofilm to a saturating light pulse within weak measuring light background conditions, i.e. under dark adaption and hence minimum fluorescence. Subsequently, a series of increasing actinic light intensity steps are undertaken, at each of which a saturating light pulse investigates the effective quantum yield for each light level, i.e. under light adaption. This curve allows the investigation of quenching parameters, which are indicators of photoprotection mechanisms and are classed into photosynthetic quenching (qP), when the reduction in fluorescence is due to the conversion of energy into chemical work, i.e. photosynthesis, and non-photosynthetic quenching (qN), which corresponds to the conversion of energy into other forms, mainly dissipation as heat.

Both qP and qN range from 0 to 1. However, there is a third quenching parameter that is used in reference to non-photosynthetic quenching, NPQ, the value of which ranges from 0 up to 10 and is a function of maximum fluorescence (F_m) and light-adapted maximum fluorescence (F'_m).

The advantage of assessing NPQ over doing so for qN and qP lies in that it eliminates the error derived from the assumption that minimum fluorescence suffers no quenching. This assumption is not entirely true, as some "dark" quenching does indeed take place, mainly as a result of chlororespiration, reverse electron flow and state 2 transitions.

The investigation of these fluorimetric parameters in biofilms of interest enables the characterisation of their photosynthetic activity, often in response to environmental changes such as the effect of light intensity and temperature on the dynamics of photosynthesis (e.g. Jodlowska and Sliwinska, 2014).

Fluorimetry studies were conducted on the BPV biofilms in order to compliment the electrochemical information obtained previously. This was performed through the use of PAM, which enabled obtaining RLCs and ICs that shed light onto the photosynthetic processes and alternative fates of the irradiated photons.

- Confocal Microscopy

The aim of confocal microscopy is to image planes of cells in a biofilm by inducing the fluorescence of particular pigments, e.g. Chlorophyll a. This provides information about the structure of a biofilm, allowing the determination of important parameters such as cell density and biofilm thickness, which are indicators of cell viability and proliferation.

<u>Potential conditioning of biofilms</u>

There are previous reports on the short-term potential conditioning of biofilms, using galvanic curves. For instance, a recent study by Ciniciato et al. (2016) looks at the relationship between PAM-derived parameters and cell potential of a BPV device, by investigating the fluorescence aspects corresponding to each external load applied during a polarisation curve.

1.3. Extremophiles: Fundamentals and applications

From the Latin "extremus" and the Greek "philia", Extremophilic (or extreme-loving) organisms are able to thrive under physicochemically extreme conditions, which are inhospitable for most known forms of life in the planet. Unlike conventional organisms that live in moderate conditions (i.e. mesophiles or neutrophiles), extremophiles are genetically adapted to tolerate limit conditions of temperature, pH, pressure, salinity, radiation and dryness, for instance.

The notion of the fact that a set of organisms is able to withstand a broader range of physicochemical conditions than had been traditionally thought entails a number of implications. Firstly, it sheds light on the origin of life, as extremophiles are

compatible with the early, harsh environmental conditions on Earth. Secondly, it is remarkably significant from an astrobiology perspective, as it points the direction towards the discovery of new forms of life, somewhat relaxing the constraints on its physical possibilities, widening the scope at which extra-terrestrial life may be searched for. In addition, the discovery of microorganisms that are able to thrive in the harsh conditions that are ordinarily given in industry opens new possibilities for the application of biotechnology processes beyond the traditional limited range of pH and temperature.

Types of extremophiles

Evidence of such organisms has been found under a wide range of extreme conditions, listed thus:

- High temperatures:

Organisms able to grow at temperatures above 41°C are known as thermophiles. Evidence of these has been observed in extremely high temperatures, up to 122°C (Madigan and Martino, 2006).

They are found in geothermally heated sites, such as hot springs, e.g. *Thermus aquaticus* at the Grand Prismatic Spring in Yellowstone National Park (Seckbach et al. 2013) and deep-sea hydrothermal vents, e.g. *Methanopyrus kandleri* at a black smoker from the Kairei hydrothermal field, located in the Central Indian Ridge, in the Indian Ocean (Takai et al. 2008), which is able to grow at 122°C.

Most thermophiles belong to the Archaea domain, although there are also a variety of thermophile bacteria, considered to be among the earliest on Earth (Horiike et al. 2009). Examples of thermophile archaea include *Strain 121(Geogemma barossii)*, which lives at 121°C in the Pacific Ocean (Kashefi and Lovley, 2003) and *Pyrolobus fumarrii*, which lives at 113°C in the Atlantic Ocean (Blöchl et al. 1997). Conversely, examples of thermophile bacteria include the gram-negative bacterium *Geothermobacterium ferrireducens,* which thrives in temperatures up to 100°C in the Osbidian Pool at Yellowstone National Park (Kashefi et al. 2002) and the gram-negative *Aquifex aeolics,* which grows in temperatures up to 95°C in many underwater volcanoes (Huber et al. 1998).

- Low temperatures:

Extremophiles that survive and are able to grow and reproduce at temperatures below 10°C are termed cryophiles (or psycrophiles). Evidence of these organisms has been found in environments as cold as -39°C (Panikov et al. 2006).

They are located in sites that are permanently cold, such as polar ice, permafrost, glaciers and deep ocean waters (Neufeld et al. 2013).

Most psychrophiles belong to the Bacteria domain, such as *Psychrobacter*, which is able to grow in temperatures down to -10°C in Antarctic soil (Kim et al. 2012) and *Chryseobacterium greenlandensis*, which survived more than 120,000 years inside a

three Km deep ice block in Greenland (Loveland-Curtze et al. 2009). However, there are also some eukaryotic psychrophiles, such as the lichen *Umbilicaria Antarctica*, which is able to photosynthesise at temperatures as low as -24°C (Frey and McKenzie Lamb, 1939) and the fungus *Penicillium*, which in addition to the classic penicillin-producing mesophile strains, counts with cold-tolerant counterparts (Gupta et al. 2014).

- High pH:

When organisms are able to tolerate pH levels above 8.5, these are known as alkaliphiles. They have been found to survive under considerably alkaline conditions, up to pH 11.

They are found in sites where the pH is continually elevated, usually in soda lakes, e.g*. Natronococcus amylolyticus,* isolated from Lake Magadi, a Kenyan soda lake (Kanal et al. 1995).

Known alkalophiles belong to the Archaea domain, such as the halobacterium *Natromonas,* which grows optimally in 3.5 M sodium chloride (Natarajan et al. 2014).

- Low pH:

Acidophiles are organisms that are able to thrive in acidic conditions, which range from mildly acidic to extremely low pH conditions (even down to negative pH values).

They can be found in locations where pH is continuously low, such as acid mine drainage effluents, e.g. *Dunaliella acidophila* (Pick, 1998), volcanic streams, e.g. *Acidianus infernus* (Segerer et al. 1986), certain edible liquids such as vinegar and fruit juices, e.g. *Alicyclobacillus* (Pettipher et al. 1997), and in the human stomach, e.g. *Helicobacter pylori* (Amieva and Peek, 2016).

Acidophiles are widely extended throughout the domains of life. Firstly, there are many archaeal acidophiles such as the order Sulfolobales from the Crenarchaeota branch (Dworkin and Falkow, 2006). Secondly, there is a wide variety of acidophilic prokaryotic bacteria, such as the order Acidithiobacillales, of Proteobacteria (Carbajosa et al. 2010). Finally, there is a series of eukaryotic acidophiles such as the photosynthetic alga *Dunaliella acidophila* (Pick, 1998).

Acidophiles are particularly interesting for the purposes of this study, as the aim is to replace the standard mesophile microorganisms used in classic MFCs with metallotolerant acidophiles, which are able to thrive in a growth medium that enhances electrical conductivity and consequently cell performance.

- High salinity:

Organisms that are able to thrive in high salt concentrations are known as halotolerant or halophiles; they are able to tolerate more than eight times the concentration of salt in ocean water, up to 5.1 M of salt content (Ollivier et al. 1994).

Halophiles are usually found in locations where salt concentration is continuously high, such as inland seas, e.g. *Halobacterium volcanii*, found in the Dead Sea (Mullakhanbhai and Larsen, 1975), evaporating ponds of seawater, e.g. *Salinvibrio costicola,* found in salterns at the Canary Islands (Garcia et al. 1987), and hypersaline lakes, e.g. the diatom *Nitzschia*, found in the Makgadikgadi Pans in Botswana (Aletsee and Jahnke, 1992).

Halophiles include archaeal strains such as the genus *Halobacterium* (Gontia-Mishra et al. 2017), bacterial strains like *Salinibacter ruber* (Mongodin, 2005) and eukaryotic species such as the alga *Dunaliella salina* (Borowitzka and Siva, 2007).

- High pressure:

The presence of living organisms has been found in environments where these are subjected to extreme pressures, such as the Mariana Trench. These organisms, known as piezophiles or barophiles, are able to withstand pressures of up to 1,100 bar, e.g. *Pyrococcus* sp. (Fiala et al. 1986).

- High levels of radiation:

High levels of radiation are usually detrimental to life, as they cause mutations to the genetic material. However, certain organisms, termed "radioresistant", are adapted to tolerate high levels of ionising radiation, such as *Deinococcus radiodurans,* capable of withstanding a dose of 15,000 Gy, and 5,000 J/m^2 of UV radiation from sunlight.

- Desiccation:

Certain organisms are able to grow in conditions of very low water availability, where relative humidity is extremely low. These organisms, such as *Chroococcidiopsis*, are known as "xerotolerant" (i.e. tolerant of dry conditions) and are found in very dry environments such as the Atacama Desert (Chile) and McMurdo Dry Valleys (Antarctica), where relative humidity is circa 60%.

Practical applications of extremophiles

Classic biotechnology processes are constrained by the physicochemical conditions under which the employed microorganisms are viable, which often limits these to narrow ranges of temperature, pH, metal content or pressure, amongst other requirements, compromising the optimisation and technical possibilities of the processes. Extremophiles are particularly useful in order to extend the physicochemical range at which biotechnological processes are possible, as they can be coupled to the more aggressive conditions that are realistically found in an

industrial setting. Most of the reactions that are commonly used at an industrial level, for example in the food, biofuel, textile and pharmaceutical sectors, are severely constrained by biological limits. In the context of such limitations, the use of extremophiles poses a promising potential. The interest in extremophiles lies in the fact that these physicochemical parameters are no longer constrained to the near-neutral pH and moderate temperatures and pressures that mesophiles and neutrophiles require to function, making it possible to operate the industrial processes of interest under more severe physicochemical conditions, which may be more favourable.

Extremophiles have found use in a number of biotechnology applications, in which mesophiles are not able to fulfil the process requirements due to the need to function at extreme physicochemical parameters for process operation and optimisation. These include both whole-cell uses as well as applications based on subcellular fractions (i.e. enzymes). The main industrial applications for extremophiles are outlined thus:

- Polymerase Chain Reaction (PCR):

Polymerase Chain Reaction (PCR) constitutes a molecular biotechnology procedure whereby a small amount of DNA (even a single copy) is amplified exponentially, producing a very high number of copies (billions if so chosen) of the original genetic material, or selected sections thereof (Mullis et al. 1987).

PCR is based on thermal cycling, i.e. the application of alternating heating and cooling cycles, corresponding to the following steps: DNA melting (denaturation), at ~95°C, annealing, at ~68°C, and replication (elongation), at ~72°C, whereby the target DNA is replicated, the resulting double strand is melted and each ensuing DNA single strand is subsequently used as template for DNA replication again. This cyclic sequence of steps constitutes a chain reaction through which it is possible to amplify an original (minute) quantity of DNA by several orders of magnitude.

PCR relies on thermostable enzymes that will withstand its thermal cycling principle, in particular the elevated temperature of the DNA melting step. In order to denature the DNA double helix, separating its two constituent DNA strands, temperatures above 90°C are required, and hence the process needs a thermophilic DNA polymerase that is able to withstand these (Chien et al. 1976). Suitable thermostable enzymes are those isolated from thermophiles, such as the classic *Thermus aquaticus,* Taq (Tindall and Kunkel, 1988) and *Pyrococcus furiosus*, Pfu (Lundberg et al. 1991).

In addition to being incredibly useful, PCR is remarkably cheap, fast and reliable. It is therefore key for a number of genetically-based clinical and research techniques, such as DNA sequencing, gene cloning, disease diagnosis, and DNA profiling, of paramount importance in a variety of fields.

PCR applications include forensic science, e.g. genetic fingerprinting and forensic DNA typing (Ninfa et al. 2009), parentage testing (Marjanovic et al. 2006), medical applications, e.g. genetic testing (Saiki et al. 1985), tissue typing (Quill, 2008) and

genetic therapy (Garibyan, 2013), infectious disease applications, e.g. viral infection detection and "viral load" quantification (Cai et al. 2014), monitorisation of disease spreading through animal populations (Suarez et al. 2003) and HIV early detection and monitorisation (Kwok et al. 1987), research applications, e.g. production of hybridization probes for Southern or Northern blotting, DNA cloning and sequencing (Patten et al. 2009), gene mapping with sequence-tagged sites (Boehnke et al. 1989), phylogenetic analysis of DNA from ancient sources such as frozen mammoth tissue (Hagelberg, 1994) or recovered Neanderthal bones, quantification of gene expression levels and genetic mapping.

- Biofuel synthesis:

The set of chemical products obtained from organic substrates that are able to be used as fuel is known as biofuels. Currently, this market mainly revolves around bioethanol, biodiesel, biobutanol and biogas, typically generated from the microbial-catalysed conversion of biomass proceeding from corn, sugar cane, agricultural waste or lignocellulosic biomass into biofuel (Barnard et al. 2010).

The generation of fuels from biomass typically involves high temperatures and extreme pH levels, at which mesophiles are of little use. However, extremophiles pose an interesting option for the generation of these fuels, as they are tremendously robust and count with highly stable enzymes, and are thus able to undertake or at least take part in the aggressive hydrolysis processes or in the synthesis of valuable compounds.

Most of the extremophiles used in biofuel production are of a thermophilic nature, combined with a tolerance for extremes of pH. Thermophiles are able to readily ferment simple sugars such as pentose and hexose, optionally processing more complex carbohydrates as well (Zaldivar et al. 2001). High-temperature fermentations are advantageous for a number of reasons. Firstly, it is more favourable for the chemical process. In addition, it requires a lower energy input due to the minimised cooling requirements and facilitates the removal of volatile products that may otherwise cause product inhibition. Finally, such processes are less likely to suffer from microbial contamination. Examples of thermophilic biofuel production include the generation of ethanol, e.g. by *Thermoanaerobacterium saccharolyticum* (Demain et al. 2005) and *Clostridium thermocellum* (Lamed and Zeikus, 1980) and the generation of biodiesel, e.g. by *Cyanidium caldarium* (De Luca et al. 1981) and *Galdieria sulphuraria* (Pulz and Gross, 2004).

In addition to thermophiles, other types of extremophiles are used in the production of biofuels. These include methanogens, which produce biogas (hydrogen) by anaerobic fermentation, such as *Caldicellulosiruptor saccharolyticus* (Kadar et al. 2004) and *Clostridium thermocellum* (Levin et al. 2006). Another example of extremophiles employed in the production of biofuels are psychrophiles, which are leveraged for their cold-active lipases, relevant within the biodiesel production process. Examples of these include *Rhizopus delmar* and *Candida rugosa* (Al-Zuhair, 2007).

- Medical applications:

Extremophiles are able to synthetize a variety of medically-valuable compounds, including several antibiotics, antifungals and antitumor molecules (Littlechild, 2015). In addition to the compounds produced by mesophiles, extremophiles are capable of generating antimicrobial peptides, e.g. by Halobacteriaceae and thermophile *Sulfobolus,* which act on an ample range of microorganisms, including archaeal cells. Extremophiles are also capable of producing diketopiperazines, e.g. by halophile *Naloterrigena hispanica* and *Natronococcus occultus* (Martins and Carvalho, 2007), which act on blood clotting and have antimicrobial, antiviral and antitumor functions.

As well as antiseptic molecules, extremophiles are able to synthetize bioplastics, i.e. plastics that are biocompatible and optionally biodegradable, and therefore advantageous versus traditional petroleum-based plastics. In particular, they are able to produce polyhydroxyalkanoates (PHAs), a group of polyesters, e.g. *Haloferax medeterrani*can (DasSarma et al. 2009).

Finally, extremophiles pose the option of an alternative vaccine delivery system (Stuart et al. 2001). The internal gas vesicles of halophilic archaea can be engineered, e.g. in *Halobacterium* NRC-1, to express parts of a virus of interest, e.g. the simian immunodeficiency virus (Stuart et al. 2004). The advantage of recombinant methods for the generation of vaccines from extremophiles versus mesophiles is that they do not require the addition of adjuvants, unlike those derived from mesophiles, e.g. requiring the addition of cholera toxin B (Coker et al. 2016).

Extremophiles in biomining

The mining industry is concerned with the development of metal sourcing and recovery processes, coupled with waste treatment, which minimise costs while maximising efficiency, with a tendency towards environmentally friendly operations. Both focuses of the industry may be approached from a biological perspective, by introducing microorganisms in the processes of interest for both mineral and waste treatment. These are necessarily extremophiles, as they must thrive in very extreme physicochemical environments, where extremes of pH, elevated concentrations of heavy metals, metalloids and other (toxic) solutes as well as high (positive) redox potentials are typical.

Firstly, microorganisms can be employed in the recovery of metals from their ores. For instance, they play a very important role in the extraction of metals from refractory primary mineral deposits or concentrates such as copper sulphide (chalcopyrite) and zinc sulphide (sphalerite) ores, which are otherwise incredibly difficult to leach (Schippers et al. 2014). In fact, as much as 15% of copper and 5% of gold are globally processed with microorganisms (Brierley and Brierley, 2013). In bioleaching processes, microorganisms are involved in the oxidative dissolution (or pretreatment for the subsequent chemical leaching) of the input minerals, resulting in the solubilisation, followed by the recovery, of the metals of interest. Typically, these require acidophilies such as *Acidithiobacillus,* for moderate

temperature processes, or *Sulfolobus,* for higher temperature applications (Vera et al. 2013). In addition, certain chemical substances utilised in the classic processes, such as cyanide, can be substituted by the use of microorganisms that catalyse such reactions. Moreover, microorganisms often make the recovery of low-grade ores or mine tailings economically viable. Typically, biomining processes require lower energy inputs and contaminate significantly less than their physicochemical counterparts; they are seen as environmentally benign processes, with smaller associated carbon footprints.

Secondly, microorganisms can be used for the treatment of mining waste, process waters and waste streams, by means of increasingly popular bioremediation methods. Bioremediation is a very effective and low-cost modern technique, which has recently gained considerable attention. It is very common for mine water to be contaminated with heavy metals and sulphates, due to the oxidation of sulphide minerals, which leads to the generation of sulfuric acid and the further oxidation and accommodation of metals in solution. This phenomenon is known as Acid Mine Drainage (AMD), which poses a risk to the environment and the subject water must therefore be appropriately treated. The aim of the remediation strategies is to remove contaminants from the water, mainly iron and sulphate, which certain microorganisms are able to metabolise and precipitate. For example, sulphate-reducing bacteria can be used to reduce sulphates to sulphides, thereby causing their precipitation together with a series of metals such as iron, zinc and copper (Hards and Higgins, 2004).

Finally, mining sites are an ideal location for the purpose of finding naturally-occurring extremophilic microorganisms. One of the oldest and most classic mining locations is Rio Tinto, which is an exceptional source of extremophiles due to its similarities with extra-terrestrial environments. In fact, it is considered to be the terrestrial analogue of Mars, due to the heavy presence of jarosites and associated sulphates (identified in Mars by NASA) as well as the very acid pH and high heavy metal content of its waters (Edwards et al. 2007).

<u>Biotechnological challenges and opportunities of extremophiles</u>

Classic biotechnology processes are severely limited by the physicochemical conditions that the conventionally employed microorganisms tolerate. This compromises the feasibility and optimisation of such processes, posing a promising opportunity for the implementation of extremophiles, which may tolerate the industrially common harsh conditions of temperature, pH, metal content or pressure, for example, which a certain process may require and that mesophiles are unable to fulfil. Extremophiles therefore offer the opportunity to push the physicochemical boundaries of traditional biotechnology into the more aggressive conditions that are often advantageous for industrial processes, opening a window for a new generation of biotechnological processes and applications.

A very interesting opportunity for the substitution of traditionally employed microorganisms with extremophiles is the field of Microbial Fuel Cells. Through tailoring the bioreactor to the requirements of the process, primarily by selecting the appropriate microorganism of choice, applications such as bioremediation could

be significantly improved. One such example would be the treatment of methanol at temperatures circa 55◦C (Dhamwichukorn et al. 2001). However, the current state of this field is rather premature, and there is very little work on the combination of extremophiles and biological fuel cells, entailing thence a vast untapped potential. A very appealing application in which the substitution of standard microorganisms with extremophiles would be of great interest is BPV cells. While these have proved to be a sustainable green source of electrical power, the low power outputs recorded thus far have prevented these platforms to compete commercially with conventional solar panels.

The challenge of BPV performance can be tackled form several angles, ranging from the biological (selecting microorganisms or undertaking genetic modifications for a better exoelectrogenic capacity) to the physical (electrode materials and configuration) and chemical (modulating the chemical conditions to favour electricity generation). A key parameter that had not been optimised before was pH, as BPV cells had been operated at the near-neutral pH that is optimum for the standard microorganisms employed as the biological material.

The present investigation aims to address the issue of pH. By operating the BPV cell at a lower pH, the hypothesis is that higher current densities and associated power outputs would be obtained. On the one hand, the higher resulting electrical conductivity would entail a lower internal resistance and hence exhibit an improved electrical performance. On the other hand, the higher concentration of protons would favour the oxygen reduction reaction taking place at the cathode due to their heightened availability. The focus of this work is to improve the power output obtained by prior BPV studies; it is of paramount importance to tackle this aspect, given that power output is currently too low for BPVs to achieve grid parity upon scale-up, which is probably the major obstacle stopping BPVs from becoming a real alternative renewable energy source.

The challenge of operating BPV cells at a lower pH lies primarily in the adequate choice of microorganisms that are able to survive and thrive under such exigent physicochemical conditions. In order to find naturally-occurring acidophilic microorganisms, the Rio Tinto mine and surrounding area was chosen, as it is known to host a wide range of extremophiles in its unique, diverse and extreme physicochemical environment.

Arguably the most longevous mines in the world, the Rio Tinto mines have been operating since the Tartessians Era, around the year 3,000 BC, and were continued to be exploited through the Phoenician and Roman Eras (Rickard, 1928). In modern times, the mines had been operating continuously since 1873, when they were bought by the Rio Tinto company, until 2001, when its then owner company Riotinto S.A.L. had to shut down the mines due to the falling price of copper.

The present investigation coincides with the period slightly prior and during the reopening of the Rio Tinto mines in July 2015, following 14 years of inactivity. Therefore, the physicochemical and microbial characterisation undertaken in this study is of great environmental interest, as it evaluates the impact (or lack thereof) that the return of activity at the mines has on the subject ecosystem. It is of

paramount importance to assess whether the harsh physicochemical conditions found throughout the ecosystem are a result of contamination from mining activity, or whether high acidity levels and toxicity indexes were already present prior to the reopening of the mine. In addition, it is essential to examine the effect of such industrial activity on the microbial diversity throughout the ecosystem, in particular as the range of extremophiles found in the Rio Tinto mines and surrounding environment is uniquely precious and has recently been the subject of numerous research studies, drawing international attention, for instance from NASA. Hence, it is crucial to verify that mining activities do not harm microbial diversity and that this marvellous ecosystem, unique in the whole planet, is preserved.

The aim of this project is to build onto the existing knowledge on whole-cell BPVs. Hence, before exploring the effect of pH, a study on standard BPV cells based on classic microorganisms and cell configuration was undertaken (Chapter 3). In this chapter, BPV cells based on both a classic prokaryotic strain (*Synechococcus elongatus*) and a classic eukaryotic strain (*Chlorella vulgaris*) are built, tested and characterised by means of electrochemical and fluorescence techniques. Subsequently, the realms of acidophilic microorganisms that could potentially be used as the biological material in BPV cells are explored. The aim of the investigation was to find a set of naturally-occurring acidophiles, for which the Rio Tinto ecosystem was selected, as it is a unique site in the planet known for the presence of microorganisms thriving in its extreme physicochemical conditions. Hence, the first approach of this study was to investigate a series of locations within the Rio Tinto environment, in order to determine the sites with the toughest conditions of pH, electrical conductivity and heavy metal content throughout the year (Chapter 4). Thorough monitoring of the chosen sampling sites was performed, assessing the environmental impact resulting from the reopening of the mine. In parallel, an investigation on the presence of living microorganisms at these sites allowed the choice of the best location for the purpose of this study. Subsequently, a tailored sediment cell was built and tested in situ, and compared to the performance of a BPV cell based on a commercially-available photosynthetic acidophile (Chapter 5). Finally, the methods and materials employed throughout the study are described extensively in Chapter 2.

2 Chapter 2: Materials and Methods

2.1. Cultures and growth conditions

- Bacterial strains

The strains and sources thereof used in this thesis are summarised in the following table:

Strain	**Source**
Synechococcus elongatus sp. WH 5701	Donated by Professor Howe (Department of Biochemistry, University of Cambridge)
Chlorella Vulgaris	
Dunaliella acidophila	CCAP (SAMS Research Services Ltd.)

Table 1: Table showing the various bacterial strains used and their respective sources.

- Growth conditions

The three strains were cultured and maintained at 22°C, under sterile conditions, in a 12 hour light: 12 hour dark cycle, using a light intensity of 15 Wm^{-2}.

Biofilm growth was initiated by centrifugation of 2 ml of exponential phase culture (4000 g, 10 min), resuspension in fresh medium and inoculation onto the pertinent electrode support.

S. elongatus was grown in BG11 medium, *C. vulgaris* was grown in BB medium and *D. acidophila* was grown in AJS medium.

Growth of suspension cultures was monitored by direct spectrophotometrical OD_{680} determination. On the other hand, biofilm growth was measured by spectrophotometrical OD_{680} determination after rinsing, scraping and resuspension in fresh medium.

- Growth media

The recipes for the different growth media used in this thesis are given as follows:

Blue-Green (BG11) medium

Per litre:		
1.5 g	$NaNO_3$	
75 mg	$MgSO_4.7H_2O$	
40 mg	K_2HPO_4	
36 mg	$CaCl_2.2H_2O$	
20 mg	Na_2CO_3	
6 mg	Citric acid	
6 mg	Ammonium ferric citrate green	
1 mg	$EDTANa_2$	
1.0 ml	Trace elements solution, consisting of (per litre):	
	2.86 g	H_3BO_3
	1.81 g	$MnCl_2.4H_2O$
	390 mg	$Na_2MoO_4.2H_2O$
	220 mg	$ZnSO_4.7H_2O$
	80 mg	$CuSO_4.5H_2O$
	50 mg	$Co(NO_3)_2.6H_2O$

Table 2: Table showing the chemical composition of Blue-Green (BG11) medium.

Make up to 1 litre with deionized water, adjust pH to 7.1 with 1 M NaOH or 1 M HCl and autoclave.

Bold's Basal (BB) medium

Per litre:		
250 mg	$NaNO_3$	
75 mg	$MgSO_4.7H_2O$	
25 mg	NaCl	
75 mg	K_2HPO_4	
175 mg	KH_2PO_4	
25 mg	$CaCl_2.2H_2O$	
1.0 ml	Trace elements solution, consisting of (per litre):	
	1.44 g	$MnCl_2.4H_2O$
	8.82 g	$ZnSO_4.7H_2O$
	1.57 g	$CuSO_4.5H_2O$
	490 mg	$Co(NO_3)_2.6H_2O$
	710 mg	MoO_3
1.0 ml	Stock solution 1, consisting of (per litre):	
	1.42 g	H_3BO_3
1.0 ml	Stock solution 2, consisting of (per litre):	
	50.0 g	EDTA
	31.0 g	KOH
1.0 ml	Stock solution 3, consisting of (per litre):	
	4.98 g	$FeSO_4.7H_2O$
	1.0 ml	H_2SO_4 (concentrated)

Table 3: Table showing the chemical composition of Bold's Basal (BB) medium.

Make up to 1 litre with deionized water and autoclave.

Acidified JM:SE (AJS) Medium

Acidified 97:3 mixture of JM Medium and SE2 Medium

- Jaworski's Medium (JM)

Per litre:		
	Stock solutions, consisting of (per 200 ml):	
1.0 ml	4.0 g	$Ca(NO_3)_2.4H_2O$
1.0 ml	2.48 g	KH_2PO_4
1.0 ml	10.0 g	$MgSO_4.7H_2O$
1.0 ml	3.18 g	$NaHCO_3$
1.0 ml	450 mg	EDTAFeNa
	450 mg	$EDTANa_2$
1.0 ml	496 mg	H_3BO_3
	278 mg	$MnCl_2.4H_2O$
	200 mg	$(NH_4)6Mo_7O_{24}.4H_2O$
1.0 ml	8 mg	Cyanocobalamin
	8 mg	Thiamine HCl
	8 mg	Biotin
1.0 ml	16 g	$NaNO_3$
	7.2 g	$Na_2HPO_4.12H_2O$

Table 4: Table showing the chemical composition of Jaworski's medium (JM).

Make up to 1 litre with deionized water and autoclave.

- Soil Extract 2 (SE2) Medium

105 g	Airdried sieved soil
660 ml	Deionized water

Table 5: Table showing the chemical composition of Soil Extract 2 (SE2) medium.

Place the soil and water in a 1 litre bottle and autoclave once immediately and again after 24 hours. Leave to settle for one week, decant the supernatant and filter.

For 1 litre of AJS Medium, mix 970 ml of JM and 30 ml of SE2. Adjust the pH to 1.5 with 10 ml of concentrated H_2SO_4 and autoclave.

2.2 Electrochemical measurements

- Construction of the BPV cells

Two BPV cell device designs were used, as described in chapter 3; the first configuration is designed to undergo electrochemical tests alone, while the second design is adequate for fluorescence tests in addition to electrochemical tests. For the in-situ BPV cell, a sediment fuel cell was designed, as described in chapter 5.

- BPV cell operation and electrochemical measurements

The following equations are necessary for the interpretation of the data obtained with electrochemical techniques:

- $E_{cell} = IR$

Equation 1: Cell voltage (E_{cell}) as a function of electrical current (I) and resistance (R).

- $W = E_{cell}I$

Equation 2: Electrical power (W) as a function of cell voltage (E_{cell}) and electrical current (I).

Polarisation curves were undertaken by measuring cell voltage as a function of varying external load, from 1 MΩ down to 220 Ω, allowing the determination of optimum resistance for maximum power output.

Power output was monitored by connecting the BPV devices to their corresponding maximum power output resistances, and continuously recording cell voltage with a data logger (ADC16 Pico Technology High Resolution Data Logger, monitored via

PicoLog software interface). For the sediment cell, cell voltage was recorded manually on a daily basis, with a voltmeter (Bytan Digital Multimeter).

For the chronoamperometries (short-term potential conditioning of biofilms), the BPV cells were connected to a potentiostat (PGSTAT128N, Autolab), and multi-step chronoamperometries were performed (controlled with Nova software interface). The bioanode was subjected to a series of potential values, at each of which fluorescence tests were undertaken.

2.3 Pulse Amplitude Modulation (PAM) Fluorimetry

PAM experiments were undertaken with a Dual-PAM-100 (Walz, Germany), according to the standard published method (Pankowski and McMinn, 2009).

Before each experiment, the biofilms were dark adapted for 15 minutes. For the rapid light curves, a series of programmed light levels were emitted by the red diode (33, 96, 186, 291, 425, 576, 835 and 1114 µmol photons/m^2s). Conversely, a 576 µmol photons/m^2s saturating pulse was applied, as recommended for these two strains in the literature (Ciniciato et al. 2016). The duration of the varying light levels was 10 seconds, while that of the saturating pulse was 800 ms. The software used to program the rapid light curves was Wincontrol (Walz).

The parameters obtained from the PAM measurements were maximum quantum yield, maximum relative electron transport rate, alpha and the light saturation coefficient, calculated as follows:

- Maximum quantum yield:

$$\text{Maximum quantum yield} = \frac{F_m - F_0}{F_m}$$

This value is interpreted as photosynthetic efficiency, given that it is a measure of the maximum light utilization efficiency, i.e. the efficiency with which the photosynthetic apparatus shift from the state where all reaction centres are open to the state where all reaction centres are closed.

- Effective quantum yield:

$$\text{Effective quantum yield} = \frac{F_m{}' - F'}{F_m{}'}$$

This value corresponds to the light-adapted value of quantum yield, which is particular for each level of actinic light.

- Electron transport rate:

$$\text{ETR} = \frac{F_m{}' - F'}{F_m{}'} \times \frac{\text{PPFD}}{2} \times a *$$

Electron Transport Rate (ETR) is a function of light-adapted maximum fluorescence (F_m), light-adapted minimum fluorescence (F'), Photosynthetic Photon Flux Density (PPFD and the coefficient of light absorption (a*).

Since it is very difficult to measure a*, relative Electron Transport Rate (rETR) is usually employed instead.

- Maximum relative electron transport rate:

$$\mathrm{rETR_m} = \frac{\mathrm{F_m}' - F'}{\mathrm{F_m}'} \times PAR$$

Relative Electron Transport Rate (ETR) is a function of light-adapted maximum fluorescence (F_m), light-adapted minimum fluorescence (F') and Photosynthetically Active Radiation (PAR).

- Alpha (α): The slope of the light-limited section of the Rapid Light Curve.

- Light saturation coefficient:

$$\mathrm{E_k} = \frac{r\mathrm{ETR_m}}{\alpha}$$

The light saturation coefficient or photoadaptive index (E_k) is a function of Maximum Relative Electron Transport Rate ($rETR_m$) and alpha (α).

2.4 Sample collection and in-situ measurements

- In situ measurement of physicochemical parameters:

Sixteen different points along the Tinto River and nearby acid mine drainage sites were studied, in order to find the microorganisms thriving in the toughest physicochemical conditions possible, hypothesised to exhibit an improved electrochemical performance when used in a fuel cell platform.

At each location, electrical conductivity, pH and dissolved Oxygen were measured in situ (with a calibrated Hanna Instruments portable meter).

- Sample collection:

Liquid samples were taken from each location, subsequently filtered through cellulose nitrate filter paper, and stored in 500 ml bottles to which 2 ml of 65% nitric acid was added.

In addition, epilithon samples were collected from each site every trimester, as described by Snoeijs and Snoeijs (1993).

2.5 Chemical analysis

Chemical analyses were performed on the samples taken from the various chosen sites, with the aim of identifying the presence and quantifying the concentration of metals in solution, as well as the ferric/ferrous ion balance and sulphate concentration. Finally, the levels of heavy metals in solution were analysed globally by means of the Toxicity Index. The following analysis methods were employed:

- ICP-MS

The presence and concentration of heavy metals in solution was detected by sample ionization, with ICP (inductively coupled plasma), followed by separation and quantification by MS (mass spectrometry).

- Quantification of ferric/ferrous ion balance

The determination of the ferric/ferrous ion balance was undertaken by quantification of total iron (by ICP-MS), determination of ferrous ion and subsequent deduction of ferric ion. Ferrous ion was determined by a redox titration, using potassium permanganate as the titrating agent.

- Quantification of sulphate

Sulphate content in the liquid samples was quantified by precipitation and subsequent gravimetric determination. The sulphate anions present were precipitated as barium sulphate, using barium chloride as the precipitation agent, filtered, washed with distilled water, calcined and finally weighed on a precision balance.

- Toxicity Index (TI)

Finally, a comparison across the various samples at the chemical level was evaluated by means the Toxicity Index (TI). This parameter is a cumulative measure of the levels of heavy metals in solution, indicating relative contamination. This index was calculated according to the following equation, proposed by Feris et al. (2004):

$$TI = \Sigma[(\log Me_n / \log Me_{n\ reference})$$

Where n = Fe, Cu, Zn, Ni, Cd, As, Cr, Pb and Hg, and the reference levels are the following, as established by the WHO:

As	**Cd**	**Cr**	**Cu**	**Fe**	**Hg**	**Ni**	**Pb**	**Zn**
0,01 mg/L	0,003 mg/L	0,05 mg/L	2 mg/L	2 mg/L	0,001 mg/L	0,02 mg/L	0,01 mg/L	3 mg/L

Table 6: Reference levels of arsenic, cadmium, chromium, copper, iron, mercury, nickel, lead and zinc as established by the WHO.

2.6 Microbial analysis

In parallel to the observation of physicochemical parameters, the presence of living microorganisms in the sixteen chosen locations was investigated, in order to determine at which sites it is possible to find the sought extremophiles. Various analyses were performed, as described thus:

- Identification of microorganisms

Identification of the eukaryotic microorganisms present in the samples (both from epilithon samples and electrode scrapings) was undertaken by direct microscopic observation (Leica microscope). Through phenotypic feature observation, the different algae and protozoa present in the samples were identified (as described by Amaral et al. 2002, Lopez-Archilla et al. 1999 and Lopez-Archilla et al. 2001). This identification then allowed the calculation of average relative abundance of the various species, by direct microscopic counts. Prokaryotic microorganisms were identified by 16S rRNA cloning (into E.Coli cells with a pGEMT vector) and subsequent BLAST analysis of the output sequences.

- Total biomass abundance

Total biomass abundance was estimated directly from microscopic counts.

- Biological diversity

Biological diversity was estimated through Simpson's Index (Simpson, 1949). This index is a measure of the variety of species within an environment. Simpson's Index (D) ranges from 0 (infinite diversity) to 1 (no diversity), and is calculated with the following formula:

$D = \Sigma (n / N)^2$ where n = total number of organisms of a particular species

N = total number of organisms of all species

- Correlation coefficient R

The relationship between the presence of the various microbial species and each physicochemical parameter studied was investigated statistically by looking at the correlation coefficient R. This parameter is a measure of the strength and direction of a possible linear relationship between two variables of choice, indicating the degree of correlation from a perfect positive relationship (+1) to a perfect inverse relationship (-1), where 0 means no correlation.

3. Chapter 3: Classic Biological Photovoltaic Cells

3.1. Field background

An introduction to BPV cells

Biological Photovoltaic (BPV) cells are a type of Microbial Fuel Cell, which is based on oxygenic photosynthesis. Unlike conventional MFCs, where the electron donors are organic compounds such as glucose, acetate, glutamate and lactate that are to be catabolised by the microorganisms or sub-cellular fractions thereof (Chang et al. 2006), BPV cells utilise water as the electron donor. As no organic substrates are required, due to the autotrophic nature of the microorganisms they are based on, this technology represents an autonomous source of energy. The implication of this is that the use of BPV cells is potentially unlimited, standing beyond the possibilities of standard MFCs, which, although useful for certain bioremediation applications such as wastewater treatment, are limited by their reliance on a substrate feed.

A standard BPV cell consists of an anode compartment, in which photosynthetic organisms or fractions thereof are present, and a cathode compartment, in which the electrode usually incorporates an attached oxygen reduction reaction catalyst.

BPV cells use water as the electron donor, by catalysing its photolysis into molecular oxygen, protons and electrons (in the form of reducing equivalents), which are harvested by the anode electrode (where oxidation takes place) as described by Bombelli et al. 2011a. That is, the anode half-cell hosts the conversion of light energy into chemical energy via the photolysis of water. In turn, as in MFCs, the electron acceptor is usually oxygen, which is reduced to water in a reaction catalysed by the cathode (where reduction takes place), whereby oxygen complexes with the electrons delivered by the cathode electrode and protons arising from biochemical reactions (i.e. water photolysis), which diffuse to the cathode, optionally (depending on the configuration of the device) migrating across a proton-exchange membrane (Yuan et al. 2016). It is the difference between the anode half-cell potential and the cathode half-cell potential that establishes a cell voltage, which may be exploited in order to obtain a power output and generate electrical power (Franks and Nevin, 2010).

The electrodes may be immersed in a single chamber or isolated in two different compartments by means of a physical separator, such as an ion exchange membrane (typically a proton-permeable membrane, e.g. Nafion membrane). The use of such separator enables the compartmentalisation of the anode and cathode environments, thereby preventing the crossover of electrochemically active species other than those involved in the reactions of interest. Where a gas-impermeable separator is employed, molecular oxygen is unable to cross the membrane directly and the cathode reaction would rely on the diffusion of oxygen from the surrounding gas phase into the liquid phase.

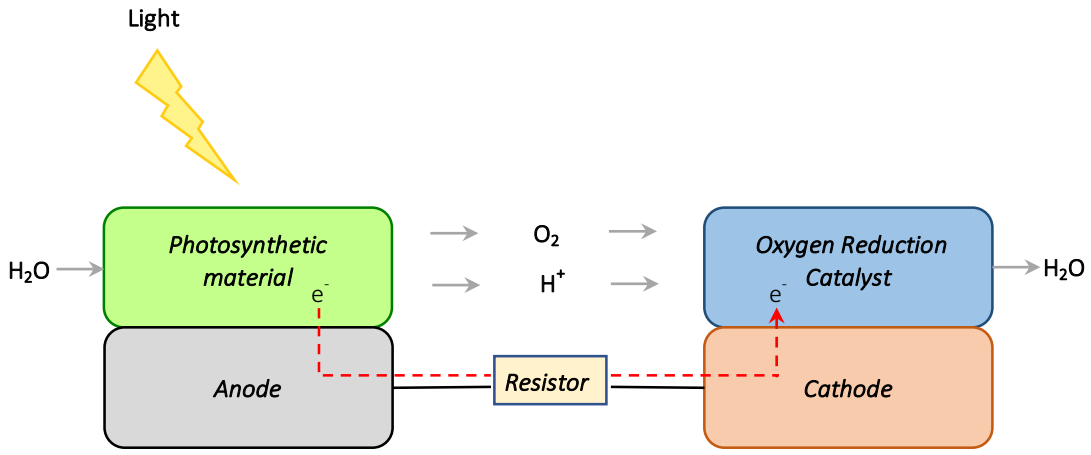

Figure 3: Simplified diagram of a BPV cell, illustrating its various components (anode with attached photosynthetic material, resistor and cathode with attached oxygen reduction catalyst) as well as the bioelectrochemical reactions taking place (photolysis of water at the anode and reduction of oxygen at the cathode) and the flow of electrons (from the anode to the cathode).

The photosynthetic material used as the anode morphological unit in BPV cells may vary significantly in size and complexity, ranging from the smallest element capable of undertaking a light-induced charge separation event, to whole-cell platforms. The various possibilities are outlined thus:

- Sub-cellular BPV cells

The smallest photosynthetic material upon which to base BPV cells would be pigments, such as chlorophyll and xanthophyll, which are able to catalyse a charge separation event upon radiation (Lieu et al. 2006).

The next level of complexity would be to use isolated photosynthetic reaction centres, i.e. Photosystem II, as the water-splitting catalysts in BPVs. For instance, Yehezkeli et al. (2012) synthesised cross-linked gold nanoparticles/photosystem II photoanodes that, upon illumination, yielded the electrolysis of water as well as the injection of electrons into the circuit via the anode electrode. As the useful lifetime of mesophilic cyanobacterial PSII is very limited, studies have used the (comparatively) highly stable Photosystem II complex from *Thermosynechococcus elongatus*, a thermophilic cyanobacterium that thrives at high temperatures (Badura et al. 2011).

The largest sub-cellular fractions used as photoactive material in BPVs are whole chloroplasts or thylakoid membranes. Kayano et al. (1981) immobilised isolated spinach chloroplasts in agar, which served as the photoanode in the fuel cell platform. In turn, Pinhassi et al. (2015) obtained photocurrents from thylakoid-graphite bioanodes, using *Synechocystis*-isolated thylakoid membranes. As endogenous redox mediators are lost during the thylakoid extraction and purification process, additional electrochemical mediators are typically employed in order to enhance current generation (Calkins et al. 2013). Other studies have managed to achieve power outputs from thylakoid membranes in vivo. For instance,

the insertion of nanoelectrodes into a chloroplast from a *C. reinhardtii* whole living cell made it possible to tap into its photosynthetic electron transport chain. This enabled the extraction of electrons directly from the thylakoid membrane, before these were used to fix carbon dioxide, thereby obtaining in vivo photocurrents (Ryu et al. 2010).

- Cellular BPV cells

The largest morphological unit used as photosynthetic material in BPV cells is whole microorganism cells. Cellular BPV cells use oxygenic photosynthetic microorganisms alone, without the presence of microorganisms with other types of metabolisms such as heterotrophic microorganisms (used alone in Microbial Fuel Cells or in conjunction with photosynthetic microorganisms in so-called Complex photosynthetic microbial fuel cells) or anoxygenic photosynthetic microorganisms (used in Photosynthetic Microbial Fuel Cells).

During the day (i.e. upon light irradiation), the photosynthetic microorganisms generate electrical current as a result of the photolysis of water. At night (i.e. in the dark), these microorganisms are still able to produce electrical current due to the catabolism of carbon compounds via respiration (McCormick et al. 2011).

Whole-cell BPVs may be based on prokaryotic cells (typically cyanobacteria), eukaryotic cells (e.g. green algae) or a mixture of these. The advantage of basing BPV cells on prokaryotic cells lies in their simpler cellular structure, which entails more accessible electron transport chain machinery. This is because, as opposed to eukaryotic cells, where the compartmentalisation into organelles isolates the electron chain machinery by multiple membrane layers, in prokaryotic cells these apparatuses are in contrast more exposed. Moreover, their simpler physiology also implies lower basal energy requirements. Hence, BPV cells based on prokaryotic fuel cells are more current-efficient (Schultze et al. 2009). In addition, their structural and physiological simplicity has led to a better understanding of the electron transfer mechanisms behind the generation of power in BPV cells. The prokaryotes of choice for use in BPV cells are typically cyanobacteria, usually *Synechococcus* or *Synechocystis.*

This whole-cell BPV modality is very attractive due to its self-assembly and self-repair qualities. On the one hand, the self-assembly aspect implies a cost-effective synthesis, both compared to existing synthetic solar panels, e.g. silicon-based, as well as to the sub-cellular based biological fuel cell configurations (Bombelli et al. 2011a). On the other hand, its self-repair quality guarantees a long device lifetime, which is a critical drawback of sub-cellular based fuel cells. This is because the lifetimes of photosynthetic reaction centres are typically very short, in relation to acceptable operational lifetimes of solar panels. For instance, the average half-lifetime of cyanobacterial Photosystem II is less than one hour. Evidently, such a rate of decay annihilates any operational feasibility potential of biological fuel cell platforms that lack effective repair or replacement mechanisms (Yao et al. 2012). Therefore, this study will focus on whole-cell BPV cells, as they appear to be the option with the most promising potential for industrial implementation.

Prior research on cellular BPV cells

The first studies on the obtention of photocurrent from microorganisms used cyanobacteria as the photosynthetic material on the anode half-cell. This capacity to transduce light energy into electrical power was proven for several different species, such as the filamentous strains *Phormidium* (Ochiai et al. 1983) and *Anabaena* (Tanaka et al. 1988) initially, and the unicellular strains *Synechococcus* (Yagishita et al. 1993) and *Synechocystis* (Yagishita et al. 1997) later on.

Early on, it was realised that the power output of cellular BPV cells may be limited by the availability of electron carriers to shuttle the electrons back and forth between the cells and the electrode. Therefore, subsequent studies focused on the use of additional electrochemical mediators in the enhancement of current generation by BPV cells. These mediators can be grouped into two main categories: lipid-soluble mediators and non-lipid-soluble mediators. The former have been shown to be most effective at improving the power output of a BPV cell, it would appear due to the ability of these mediators to intercept electrons directly from the electron transport chains located within the lipid bilayers that host photosynthetic and respiratory processes.

Studies have been conducted using a variety of different lipid-soluble mediators, such as diaminodurene (DAD) (Martens and Hall, 1994) and 2,6-dimethyl-1,4-benzoquinone (DMBQ) (Torimura et al. 2001). Unfortunately, the excellent power output results obtained by the use of lipid-soluble mediators are hindered by the fact that these are toxic in the longer term, having a severe negative impact on cell viability as a result of interfering with signaling processes (Xie et al. 2010). Therefore, a number of studies have focused on the alternative non-lipid-soluble mediators, which, despite having worse short-term power output results, are more attractive on overall as they allow long term cell viability. The classic non-lipid-soluble mediator used in BPV cell studies is ferricyanide, $[Fe(CN)_6]^{3-}$ (Thorne et al. 2011).

As explained above, microbial fuel cells can be mediated or mediator-free. Recently, the latter has become the preferred option, given that suitable electrochemical mediators are often expensive and toxic (Gil et al. 2003). The microorganisms used in mediator-free cells, which are able to donate electrons directly to the anode electrode, are termed “exoelectrogenic” (Logan, 2009).

Three mechanisms behind such direct exoelectrogenic activity have been elucidated. Firstly, electrons may exit the cell via outer membrane cytochromes that are in direct contact with the electrode (Myers and Myers, 1992). Secondly, so-called electron shuttles are excreted from the cells, in so acting as electrochemical mediators between the electron transport chains within the cells and the electrode (Rabaey et al. 2005). Lastly, certain bacteria may form structures resembling wires that emerge from the edges of the cell and are able to transfer electrical current. These conductive pili, termed “nanowires”, have been reported to appear in biofilms of different species. These were initially reported for (non-photosynthetic) dissimilatory metal reducing bacteria, such as *Geobacter sulfurreducens* (Reguera et al. 2005), and *Shewanella oneidensis* (Gorby et al. 2006). However, it was later found

that this capacity is not exclusive of dissimilatory metal reducing bacteria and is indeed also present in photosynthetic microorganisms. Initially, it was shown that the cyanobacterium *Synechocystis* sp. PCC 6803 is capable of developing these electrically conductive structures (Gorby et al. 2006). Subsequently, it was demonstrated that such exoelectrogenic activity is common for a variety of prokaryotic photosynthetic microorganisms (Pisciotta et al. 2010) as well as eukaryotic photosynthetic microorganisms (Luimstra et al. 2014).

The electrochemical mechanisms behind current generation in BPV cells

BPV cells obtain electrical current by tapping into the two main energy-producing biochemical processes in photosynthetic cells: photosynthesis and respiration. In cyanobacteria, the thylakoid membrane hosts both photosynthesis and respiration, while the cytoplasmic membrane bears the components of a simplified respiratory electron transport chain (Schultze et al. 2009).

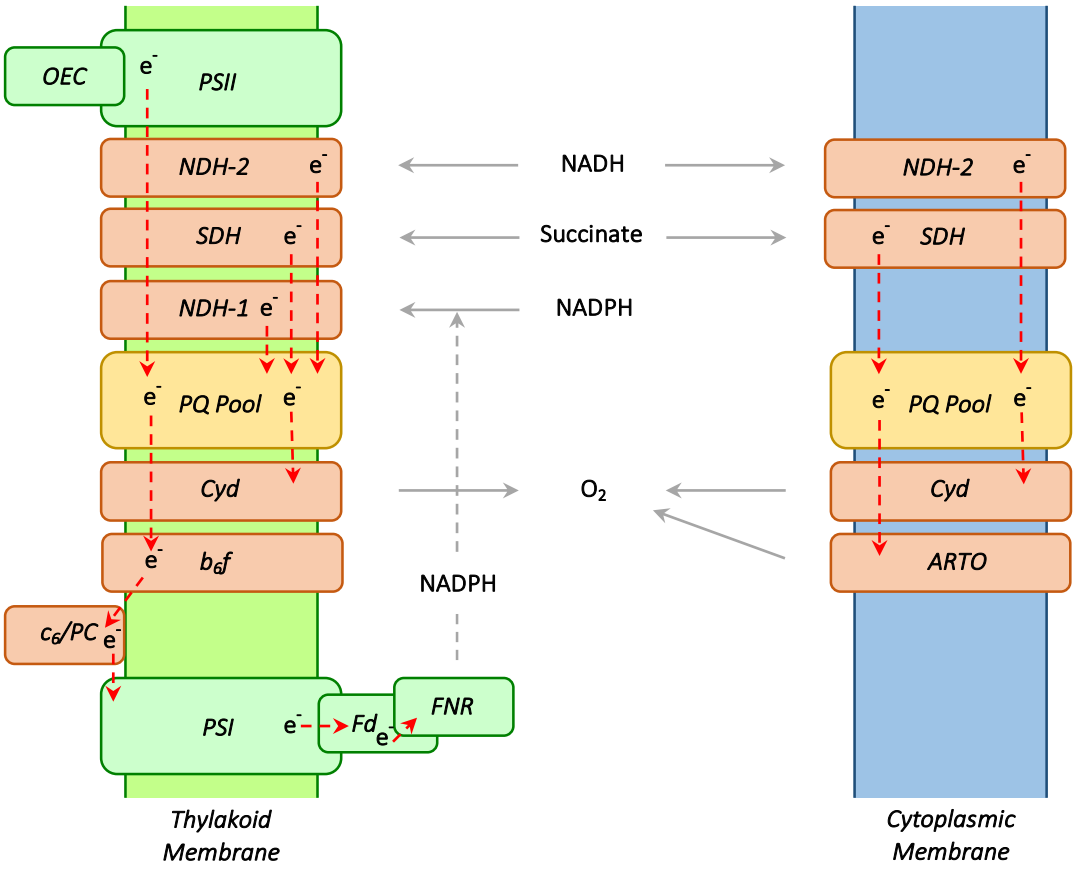

Figure 4: Typical electron transport chain mechanisms in cyanobacteria. The different components in the thylakoid membrane are PSII (Photosystem II), NDH-2 (NADH: plastoquinone oxidoreductase), SDH (succinate: plastoquinone oxidoreductase), NDH-1 (NADPH: plastoquinone oxidoreductase), the PQ Pool (plastoquinone pool), Cyd (cytochrome bd quinol oxidase), b6f (cytochrome b6f), c6/PC (cytochrome c6/plastocyanin), PSI (Photosystem I), Fd (ferredoxin), and FNR (ferredoxin:NADPH oxidoreductase). Conversely, the different components of the simplified respiratory chain in the cytoplasmic membrane are NDH-2 (NADH: plastoquinone oxidoreductase), SDH (succinate: plastoquinone oxidoreductase), the PQ Pool

(plastoquinone pool), Cyd (cytochrome bd quinol oxidase) and ARTO (alternative respiratory terminal oxidase). The diagram illustrates the flow of electrons between the various electrochemically active components, and their interaction with intermediate species (reducing equivalents NADPH and NADH, succinate and molecular oxygen).

The aim of BPV cells is to extract electrons from these energy-generating processes, by intercepting these from the electron transport chains and deriving them to the anode electrode. However, the electrically isolating quality of the lipid bilayers constituting the thylakoid and cytoplasmic membranes hosting the processes of interest makes it challenging to successfully tap into the electron path. This is why the addition of redox mediators such as ferricyanide enhances the generation of electrical current, as these are able to diffuse past the external cell barriers (the porous outer membrane and thin cell wall) and reception electrons on the outer side of the cytoplasmic membrane (putatively via transmembrane proteins).

In eukaryotic cells, the processes of photosynthesis and respiration are compartmentalised in specialised organelles (chloroplasts and mitochondria, respectively). This further isolation makes the deviation of electrons from the electron transport chains to an extracellular electrode even more challenging, which explains why typically higher current outputs are observed for prokaryotic-based BPV cells as opposed to their eukaryotic-based counterparts.

Characterisation techniques for BPV cells

There are a number of established methods for the characterisation of biofilms, both in situ and ex situ. This investigation is concerned with the study of biofilms in situ, on the one hand at the electrical performance level and at the photosynthesis level on the other. As explained in Chapter 1, the former is investigated with electrochemical techniques, while the latter is studied via fluorescence methods. Finally, the combination of both sets of methods provides a comprehensive approach towards the understanding of the interrelation between the kinetic parameters of photosynthesis and electrical performance.

In this chapter, the aim is to test classic BPV cells using standard methods, in order to establish a starting point to serve as reference for comparison with the novel developments carried out in this study.

3.2. Building and testing standard BPV cells

To begin this study, standard BPV devices as previously described in the literature (Bombelli et al. 2011a) were built and tested, in order to establish the starting point to serve as reference for the rest of the study. The performance of BPV devices is extremely sensitive to a number of factors such as design and configuration. Hence, it may be unadvisable to use published data as absolute references, but rather it is more accurate to replicate the previously published work in the lab and use it as the positive control for the rest of the study, employing the exact same device design and configuration, ensuring that comparisons between different experiments are reliable.

BPV devices were built and tested for both prokaryotic and eukaryotic cells, and were subsequently characterised using the previously outlined electrochemical and fluorescence techniques.

Materials and Methods

- Cultures and biofilm growth

The prokaryote of choice was the cyanobacterium *Synechococcus elongatus*, while the chosen eukaryote was *Chlorella vulgaris*. The strains were cultured as described in Chapter 2.

Prior to the introduction into the BPV devices, aliquots of the cultures were centrifuged, resuspended in fresh media and transferred onto the electrode surface.

- Construction of the BPV cells

Two BPV cell device designs were used; the first configuration is designed to undergo electrochemical tests alone, while the second design is adequate for fluorescence tests in addition to electrochemical tests (possible due to the use of transparent anode materials). The two types of BPV devices are outlined thus:

  - Carbon paper anode BPV cell

This design consisted of a single-chamber BPV, with a Toray paper anode electrode, with a 4 cm diameter circular shape, and a Platinum catalyst-coated carbon paper cathode, with a rectangular shape of 1 cm of width and 4 cm of length. The material for the connections was carbon yarn. For the BPV scaffold, circular Perspex pieces were used at the upper and bottom ends to sandwich the electrodes and a PDMS gasket separator, kept together with traversing screws, ensuring a liquid-proof seal.

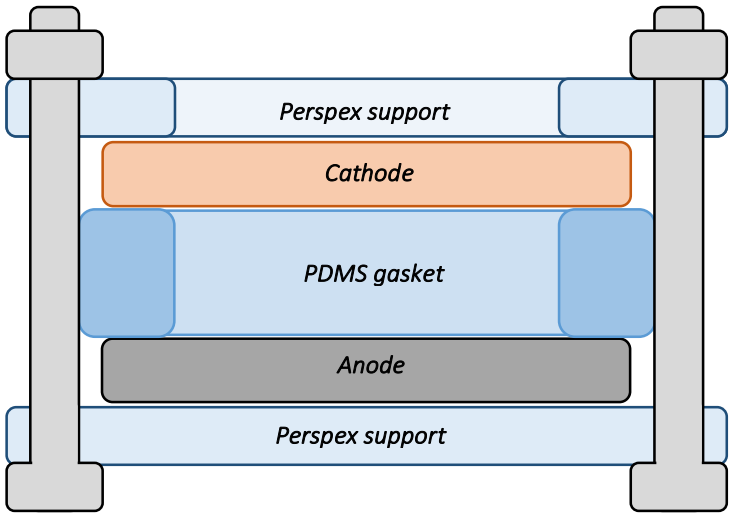

Figure 5: Diagram showing the structure of the carbon paper anode BPV device, illustrating the carbon paper anode electrode at the bottom and the carbon black cathode electrode at the top, separated by a PDMS gasket and sandwiched between a bottom Perspex plate and an upper Perspex disk with traversing screws.

- ITO-coated glass anode BPV cell

This design consisted of a single-chamber BPV, with an ITO-coated glass anode electrode (UQG Optics Cambridge) and a Platinum catalyst-coated carbon paper cathode. The anode had a circular shape, of 4 cm in diameter, and was divided into three wells (5 mm height, 10 mm diameter) by a perforated PDMS disk. On the other hand, the cathode had the same shape as the PDMS part (a 4 cm diameter disk, perforated with three 10 mm diameter circles). The material for the connections was again carbon yarn. For the BPV scaffold, circular Perspex pieces were used at the upper and bottom ends in order to sandwich a PDMS gasket and the perforated PDMS disk, and the various parts were kept together with traversing screws, ensuring a liquid-proof seal. Finally, the devices were sterilised prior to each experiment.

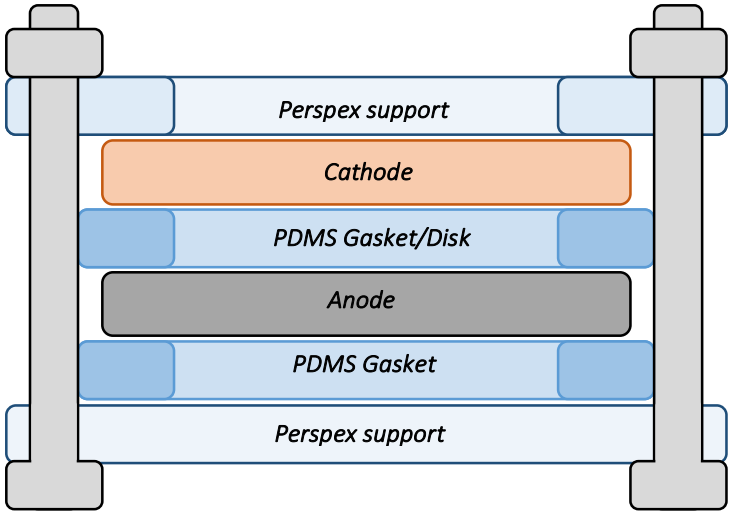

Figure 6: Diagram illustrating the structure of the ITO-coated glass anode BPV device, depicting the ITO-coated glass anode electrode at the bottom and the carbon black cathode electrode at the top, sandwiched between a bottom Perspex ring (designed to let the PAM LED lights through) and an upper Perspex disk with traversing screws and sealed by PDMS gaskets.

- BPV cell operation and electrochemical measurements

Firstly, polarization curves were undertaken by measuring cell voltage as a function of varying external load, from 1 MΩ down to 220 Ω. This allowed determining the optimum resistance for maximum power output.

Secondly, the BPV cells were connected to their corresponding maximum power output resistances, and cell voltage was continuously recorded with a data logger (ADC16 Pico Technology High Resolution Data Logger, monitored via PicoLog software interface).

Results

- Electrochemical tests
  - Polarisation curves

Firstly, polarisation curves were performed by measuring cell voltage as a function of external load.

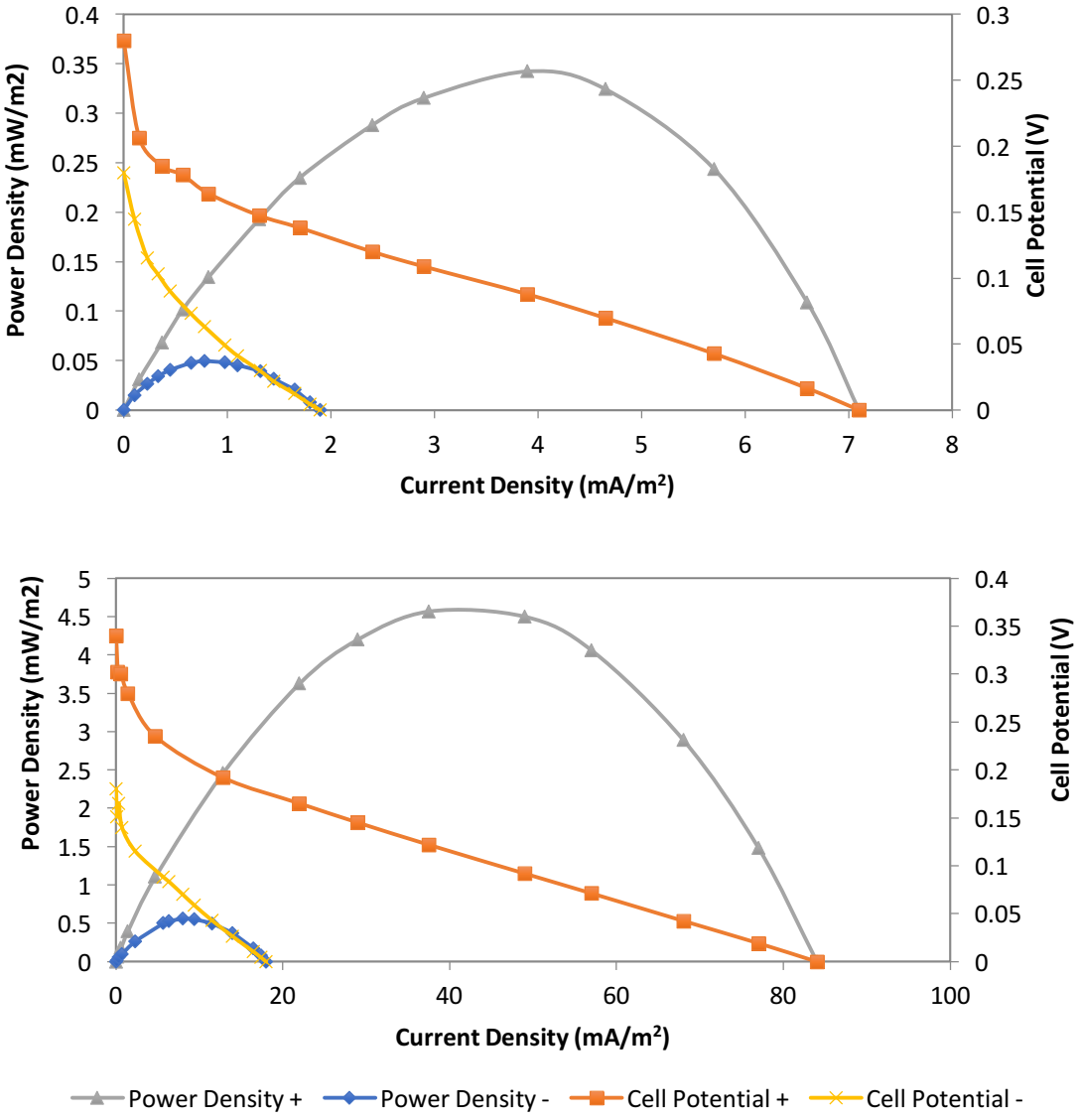

Figure 7: Top: BPV performance of Chlorella vulgaris, showing polarisation curves and power curves both for inoculated devices and negative control devices (containing BBM medium only). The external resistance applied at maximum power output was 18 kΩ. Bottom: BPV performance of Synechococcus elongatus, showing polarisation curves and power curves both for inoculated devices and negative control devices (containing BG11 medium only). The external resistance applied at maximum power output was 2.6 kΩ.

- Power output

Secondly, power output was measured continuously under a 12 hour light :12 hour dark cycle, during twenty days. The BPV cells were fitted with an external resistance corresponding to their maximum power output, as determined with the polarisation curves.

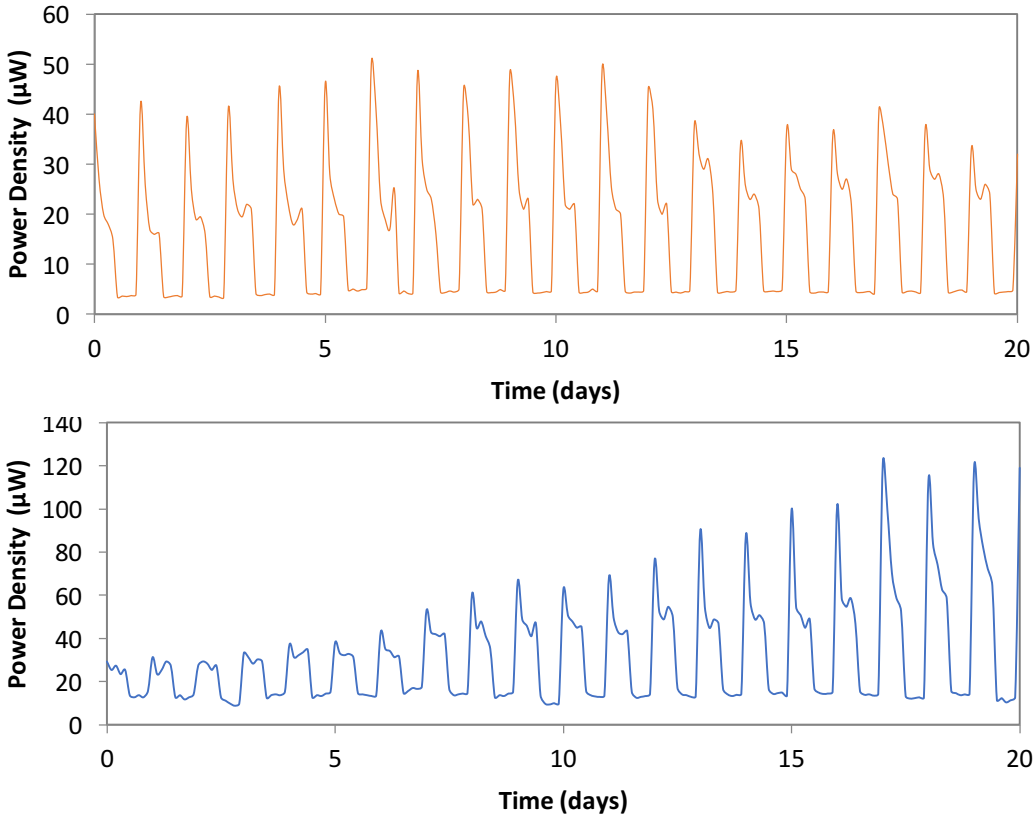

Figure 8: Top: Power output of Chlorella vulgaris BPV under a 12 hour light: 12 hour dark cycle during 20 days, with an external resistance of 18 kΩ. Bottom: Power output of Synechococcus elongatus BPV under a 12 hour light: 12 hour dark cycle during 20 days, with an external resistance of 2.6 kΩ.

Discussion

- Electrochemical tests

The results obtained reflect the exoelectrogenic capacity of pure cultures of microorganisms in a single-compartment BPV platform. Through the use of the same BPV device design, a direct comparison between different strains and conditions is possible. Comparatively, it can be observed that *Chlorella vulgaris* produces the lowest power output (with a peak power density of 0.34 mW/m^2 for the inoculated device and 0.05 mW/m^2 for the negative control). This is to be expected, for two main reasons. Firstly, its growth medium is not highly conductive, as reflected by the low power output of the negative control with BBM Medium. Moreover, *Chlorella vulgaris* is eukaryotic and its electron transfer machinery is

therefore better isolated from the outside of the cell, entailing a reduced capacity to leak electrons.

Conversely, *Synechococcus elongatus* showed the highest power output, displaying a considerably better performance (with a peak power density of 4.57 mW/m^2 for the inoculated device and 0.56 mW/m^2 for the negative control). On the one hand, this is explained by the enhanced exposure of the electron transport chain machinery in the prokaryotic strain, in comparison with the eukaryote where it is more protected from the exterior. Moreover, in comparison to BBM Medium, BG11 Medium has a higher electrical conductivity, as reflected in the power output of the negative control, which is so favourable that it even outperforms the BPV inoculated with *Chlorella vulgaris*.

Both strains displayed a very sensitive light-dependent exoelectrogenic response, as higher power outputs were exhibited under light conditions vs. dark conditions, under constant temperature. However, this is significantly more pronounced for *Synechococcus elongatus*, with average power densities of 0.993 mW/m^2 and 0.272 mW/m^2 in the light and dark, respectively, than for *Chlorella vulgaris*, with average power densities of 0.417 mW/m^2 and 0.242 mW/m^2 in the light and dark, respectively. The difference in light/dark power output ratios, which is considerably higher for *Synechococcus elongatus* (3.6) than for *Chlorella vulgaris* (1.7) may be a result of the more exposed electron transport apparatus of the prokaryote, which leads to a more sensitive response at the anode surface.

In addition, the long-term recording of power output made it possible to determine the longevity of the BPV devices. This revealed that a relatively stable power output was shown for about 20 days.

These findings are similar to previous reports on the performance and long-term power outputs of *S. elongatus* and *C. vulgaris* (McCormick et al. 2011).

3.3. PAM Study on potential conditioning of BPV cells : Field background

Pulse Amplitude Modulation Fluorimetry

Fluorescence techniques have proved very helpful in providing information about photosynthetic processes. In particular, they assist in the understanding of the transduction of light energy into other forms, shedding light on the various possible fates of the energy from the photons that reach the photosynthetic apparatus and hence on the efficiency and kinetics of photosynthesis and alternative decay pathways.

PAM makes use of the two types of fluorescence experimented by photosynthetic apparatus, passive fluorescence (epifluorescence) and active (stimulated) fluorescence. The induction and modulation of fluorescence is then used to distinguish between three main possible fates of the absorbed light energy: chemical work (mainly photosynthesis), fluorescence or alternative means of dissipation (principally heat).

Potential conditioning of biofilms

Potential conditioning techniques are useful in the investigation of the electrochemical processes underlying the generation of electrical power in BPVs. There are previous reports on the use of potential conditioning methods on biofilms, in combination with fluorescence techniques. For example, galvanic curves are combined with a PAM study of *Synechococcus elongatus* and *Chlorella vulgaris* biofilms in a recent study by Ciniciato et al. (2016), which investigates the fluorescence parameters corresponding to each external load applied during a polarisation curve.

The aim of this study is to build upon this previous work, by looking at short-term electrolytic potential conditioning of biofilms, and investigating the relationship between fluorescence parameters and half-cell potential of the working electrode.

3.4. PAM Study on short-term potential conditioning of BPV cells

Materials and Methods

- Cultures and biofilm growth

As for the experiments in Chapter 2, the chosen prokaryote and eukaryote strains were the commonly-used *Synechococcus elongatus* and *Chlorella vulgaris*. Strains were cultured as described in Chapter 2. Before being inoculated onto the working electrode surface within the BPV devices, aliquots of exponential-phase cultures were centrifuged, resuspended in fresh media and transferred into the BPV devices.

- BPV cell design

As described in chapter 2, PAM experiments were undertaken on a BPV cell that was specifically designed for such experiments. The device is therefore adapted for light to enter from below instead of from above, and uses a single-chamber configuration whereby the PAM LEDs are placed just below an ITO-coated glass working electrode (UQG Optics Cambridge).

The anode had a circular shape, of 4 cm in diameter, and was divided into three wells (5 mm height, 10 mm diameter) by a perforated PDMS disk. On the other hand, the cathode had the same shape as the PDMS part (a 4 cm diameter disk, perforated with three 10 mm diameter circles). The purpose of such perforations was to let through the light emitted by the PAM LEDs. For the connections and the BPV scaffold, carbon yarn again and circular Perspex pieces were used again, sandwiched with PDMS gaskets and pressed together with traversing screws. As usual, the devices were sterilised prior to each experiment.

- Electrochemical conditioning and monitoring of BPV cells

The BPV cells were connected to a potentiostat (Autolab), and multi-step chronoamperometries were performed, whereby the bioanode was subjected to a series of potential values for 15 minutes of dark adaption at a time, during which

electrical current was recorded, and after each of which fluorescence tests were undertaken.

The starting potential corresponded to the observed equilibrium potential values for each BPV device type (230 mV for *Chlorella vulgaris* and 270 mV for *Synechococcus elongatus*). Subsequently, a series of potential steps were applied in 100 mV increments, until reaching a maximum value of 600 mV above OCP (830 mV for *Chlorella vulgaris* and 870 mV for *Synechococcus elongatus*). After the point of inflection, potential steps were then applied in 100 mV decrements, crossing OCP and reaching a minimum value of 600 mV below it (-370 mV for *Chlorella vulgaris* and -330 mV for *Synechococcus elongatus*). Finally, a series of increasing 100 mV potential steps were applied following the minimum value, up until reaching the equilibrium potential again.

Hence, the multi-step chronoamperometries were performed in a cyclic voltammetry fashion, with a starting potential corresponding to equilibrium potential or OCP, and upper and lower vortex potentials of 600 mV above and 600 mV below the starting potential, respectively. Therefore, the results analyse the relationship between fluorescence and electrochemical parameters by analysing separately the anodic sweep and cathodic sweep sections of the tests.

- PAM Measurements

Before each experiment, the biofilms were dark-adapted for 15 minutes. For the rapid light curves, a series of programmed light levels were emitted by the red diode (33, 96, 186, 291, 425, 576, 835 and 1114 µmol photons/m^2s). Conversely, a 576 µmol photons/m^2s saturating pulse was applied, as recommended for these two strains in the literature (Ciniciato et al. 2016).

Results

- Maximum quantum yield (F_v/F_m)

Firstly, the relationship between maximum quantum yield and applied potential was investigated.

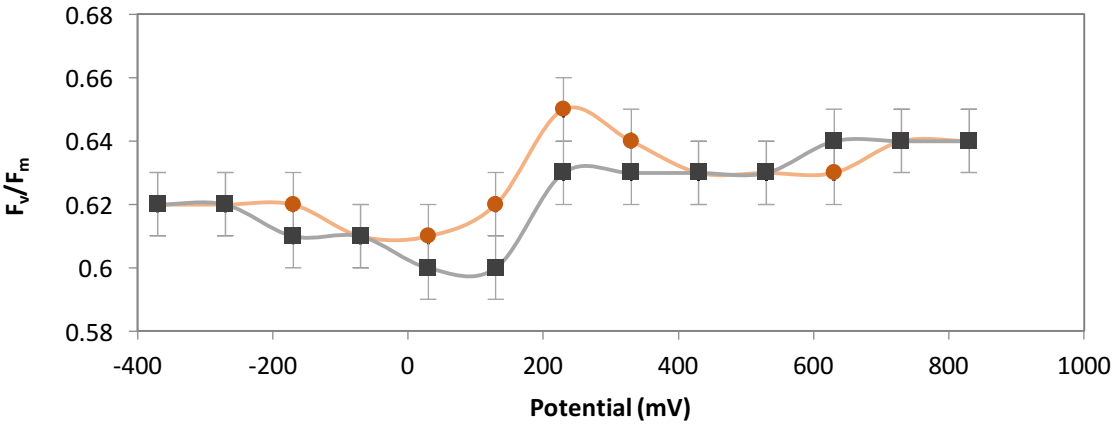

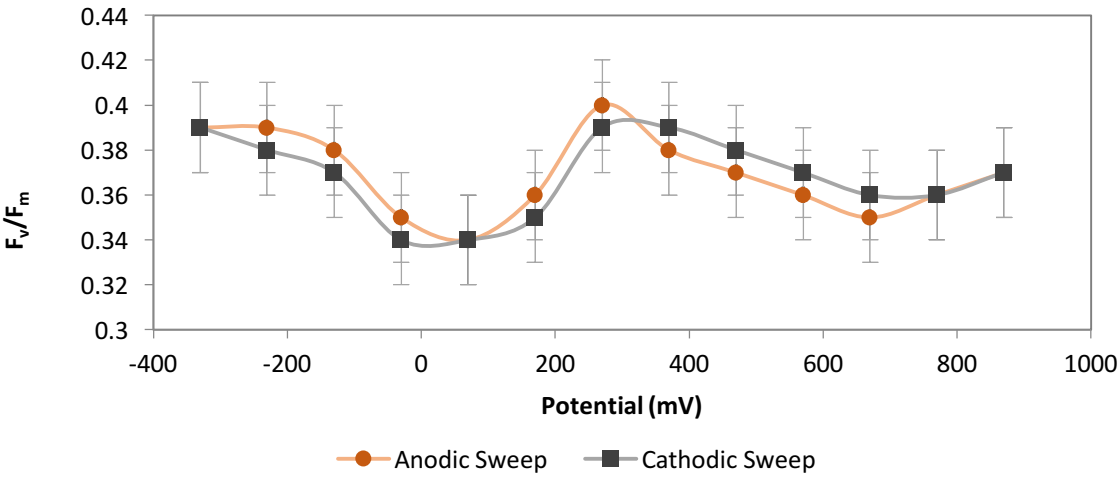

Figure 9: Relationship between applied potential and maximum quantum yield F_v/F_m for a BPV device inoculated with Chlorella vulgaris (top) and for a BPV device inoculated with Synechococcus elongatus (bottom).

As shown in figure 9, F_v/F_m is highest at the starting point of the test, corresponding to OCP (0.65 ±0.1 at 230 mV and 0.40 ±0.2 at 270 mV for *Chlorella vulgaris* and *Synechococcus elongatus*, respectively). These values correspond to OCP, where no current was recorded at the bioanode, and hence are considered to be properties of standard biofilms of the strains used (i.e. healthy biofilms growing on a particular support material, unharmed and unaffected by electrical current).

Once the flow of current in the BPV device is induced, by increasing the applied potential above OCP, F_v/F_m is seen to gradually decrease down to 0,63 ±0.1 at 430 mV and 0.35 ±0.2 at 670 mV for *Chlorella vulgaris* and *Synechococcus elongatus*, respectively. This is followed by a partial recovery of F_v/F_m up to 0.64 ±0.1 and 0.37 ±0.2 for *Chlorella vulgaris* and *Synechococcus elongatus*, respectively, as potential rises up to the upper vortex potential for each strain (830 mV for the former and 870 mV for the latter).

As the applied potential decreases below the maximum value, the same pattern as that seen for the anodic sweep is observed, whereby maximum quantum yield initially decreases and ensuingly rises back up towards OCP.

However, changes are less pronounced in the cathodic sweep in comparison with the anodic sweep. In fact, F_v/F_m simply plateaus off towards OCP in the case of *Chlorella vulgaris*. It should be pointed out that the quantum yield values observed at OCP for the anodic and cathodic sweeps are slightly different, with the latter being lower than the former.

As the applied potential decreases below OCP, a more prominent drop in F_v/F_m is observed, reaching minimum values of 0.60 ±0.1 and 0.34 ±0.2 for *Chlorella vulgaris* and *Synechococcus elongatus*, respectively. As the applied potential continues to decrease, maximum quantum yield gradually increases, recovering partially up to 0.62 ±0.1 and 0.39 ±0.2 for *Chlorella vulgaris* and *Synechococcus elongatus*, respectively.

Once the direction of the potential sweep is inversed and increasing potential steps are applied, a similar pattern as that observed for the cathodic sweep is seen, i.e. F_v/F_m follows a valley between the lower vortex potential and OCP. However, contrary to the region of potentials above OCP (corresponding to positive currents from the bianode), changes are less pronounced in the anodic sweep relative to the cathodic sweep.

While the behaviour of both strains is very similar, the response of *Synechococcus elongatus* appears to be more pronounced than that of Chlorella vulgaris, which has a flatter shape. This is reflected by the differences in maximum variation between both strains, where, within one direction of potential sweep (e.g. anodic sweep), it is considerably larger for *Synechococcus elongatus* (0,06 ±0.1, a 15% variation) in comparison to its counterpart (0,04 ±0.2, a 6% variation).

- Maximum relative electron transfer rate ($rETR_m$)

Secondly, the relationship between maximum relative electron transfer rate_and applied potential was investigated.

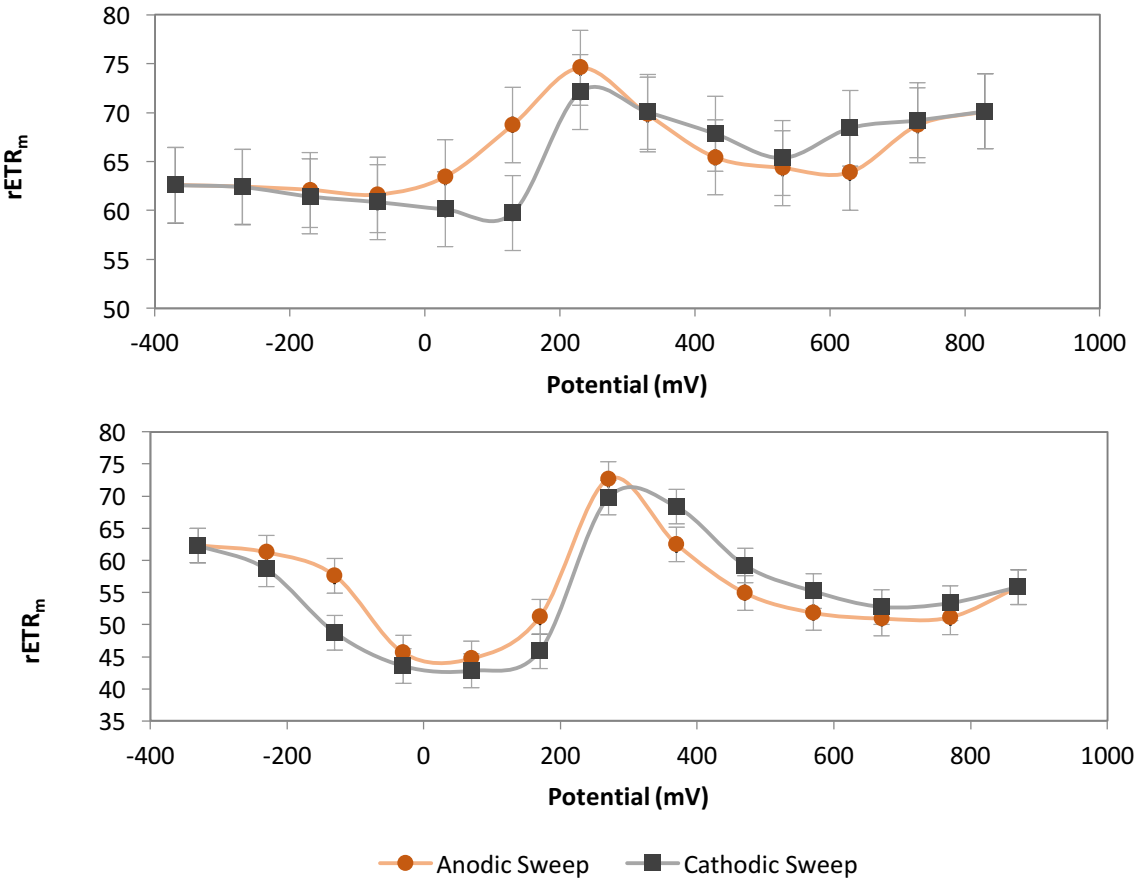

Figure 10: Relationship between applied potential and maximum relative electron transfer rate $rETR_m$ for a Chlorella vulgaris-based BPV device (top) and a Synechococcus elongatus-based BPV device (bottom).

As illustrated in figure 10, $rETR_m$ is at a maximum at the beginning of the test, i.e. at equilibrium potential (74.59 ±3.84 at 230 mV and 72.63 ±2.68 at 270 mV for

Chlorella vulgaris and *Synechococcus elongatus*, respectively). As for the rest of bioelectrochemical parameters corresponding to equilibrium potential, the initial $rETR_m$ values are regarded as intrinsic of the biofilms used, under unharmed conditions, where there is no stress caused by electrical current.

As observed for F_v/F_m, once electrical current starts to flow between the bioanode and the cathode, as potential is increased above OCP, $rETR_m$ is seen to decrease initially down to 63.87±3.84 at 630 mV and 50.94 ±2.68 at 670 mV for *Chlorella vulgaris* and *Synechococcus elongatus*, respectively. Subsequently, as potential is further increased, $rETR_m$ exhibits a partial recovery, rising up to 70.12 ±3.84 and 55.85 ±2.68 at the upper vortex potentials of *Chlorella vulgaris* and *Synechococcus elongatus*, respectively.

Below the upper vortex potentials, once the sweep direction is reversed, $rETR_m$ follows the same pattern as in the anodic sweep, yet in a less pronounced fashion down to the equilibrium potential, as was the case for F_v/F_m. Below OCP, maximum relative electron transfer rate is shown to decrease down to 59.74 ±3.84 and 42 .81 ±2.68 at the lower vortex potentials of -370 mV and -330 mV for *Chlorella vulgaris* and *Synechococcus elongatus*, respectively.

Finally, as potential increases from the lower vortex up to equilibrium, $rETR_m$ displays the same behaviour as the cathodic sweep, yet in a less prominent manner (inversely mirroring the pattern observed in the section of the test corresponding to positive electrical current values, again as was the case for F_v/F_m).

The behaviour displayed by both strains is very similar, responding to the application of potential in a similar fashion. However, as observed for maximum quantum yield, *Chlorella vulgaris* responds in a less accentuated fashion in comparison to *Synechococcus elongatus*. This can be seen in the distance between the maximum and minimum values of $rETR_m$ within the same potential sweeping direction, e.g. 13.74 ±3.84 (18% variation) for *Chlorella vulgaris* and 27.89 ±2.68 (a 38% variation) for *Synechococcus elongatus*, within the anodic sweep.

- Alpha (α)

Thirdly, the relationship between alpha and applied potential was investigated.

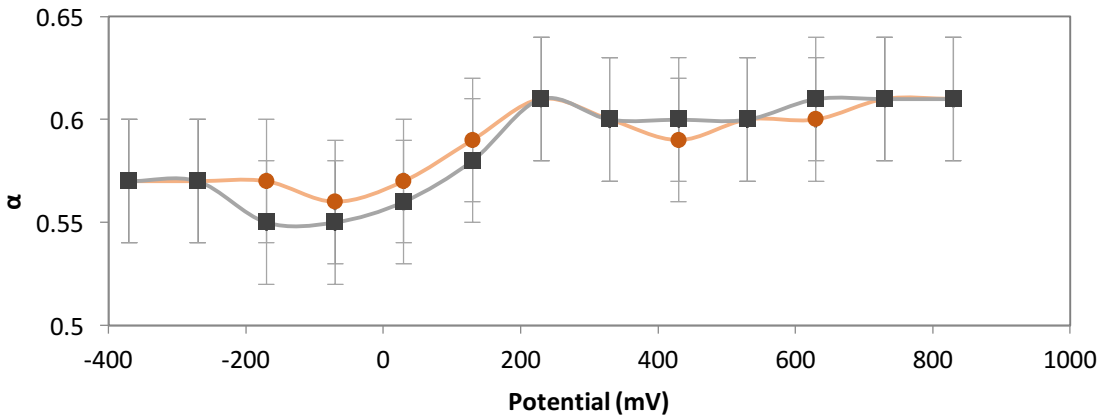

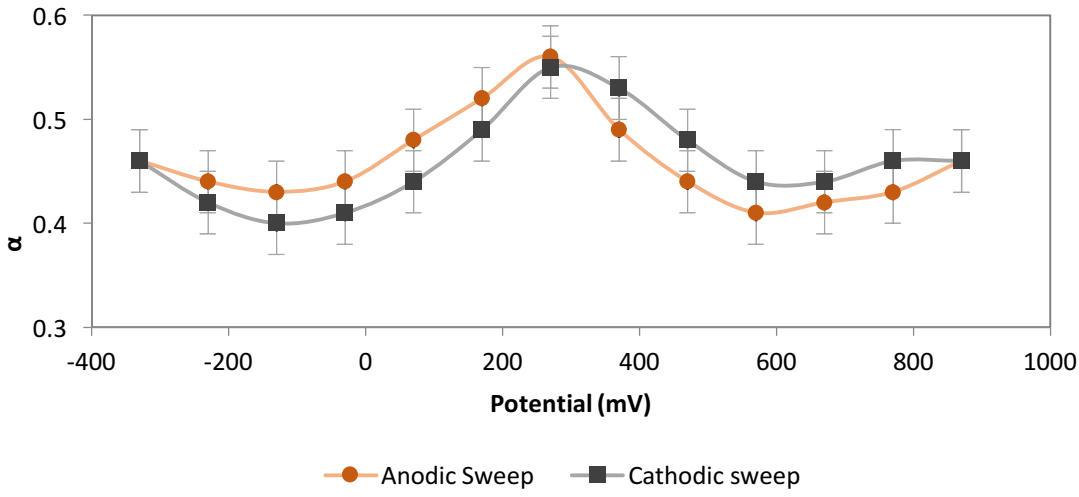

Figure 11: Relationship between applied potential and alpha (α) for BPV device inoculated with Chlorella vulgaris (top) and one inoculated with Synechococcus elongatus (bottom).

As shown in figure 11, the maximum value of α occurs at the starting equilibrium potential (0.61 ±0.03 at 230 mV and 0.56 ±0.03 at 270 mV for *Chlorella vulgaris* and *Synechococcus elongatus*, respectively). This point in the test is considered to reflect the conditions of minimum stress for the biofilm, given that at the time there is no electrical current flowing between the electrodes in the BPV device.

As observed for F_v/F_m and $rETR_m$, once the applied potential is increased above equilibrium and electrical current starts to flow between the bioanode and the cathode, α decreases initially down to 0.59 ±0.03 at 430 mV and 0.41 ±0.03 at 570 mV for *Chlorella vulgaris* and *Synechococcus elongatus*, respectively. Afterwards, as potential is increased between this point, alpha exhibits a recovery (full in the case of the eukaryote and partial in the case of the prokaryote), rising up to 0.61 ±0.03 and 0.46 ±0.03 at the upper vortex potentials of *Chlorella vulgaris* and *Synechococcus elongatus*, respectively.

As potential is reversed below the upper vortex potentials again, the pattern followed by α is the same as that displayed during the anodic sweep, although the magnitude of the changes is smaller in the region of positive electrical current of the cathodic sweep (as observed for F_v/F_m and $rETR_m$). However, after crossing equilibrium potential, the changes in alpha are again larger than those observed in the region of negative electrical current within the anodic sweep, with the values of alpha seen to decrease down to 0.55 ±0.03 and 0.40 ±0.03, to then partially recover up to 0.57 ±0.03 and 0.46 ±0.03 for *Chlorella vulgaris* and *Synechococcus elongatus*, respectively.

While the general response to applied potential is very similar for both strains, the eukaryote displays very mild changes in comparison to the prokaryote. The difference between the maximum and minimum values of alpha within the same potential sweeping direction, e.g. anodic sweep, is considerably larger for

Synechococcus elongatus (Δα = 0.14 ±0.03, a 25% variation) in comparison to *Chlorella vulgaris* (Δα is 0.06 ±0.03, a 10% variation).

- Light saturation coefficient (E_k)

Lastly, the relationship between the light saturation coefficient and applied potential was reviewed.

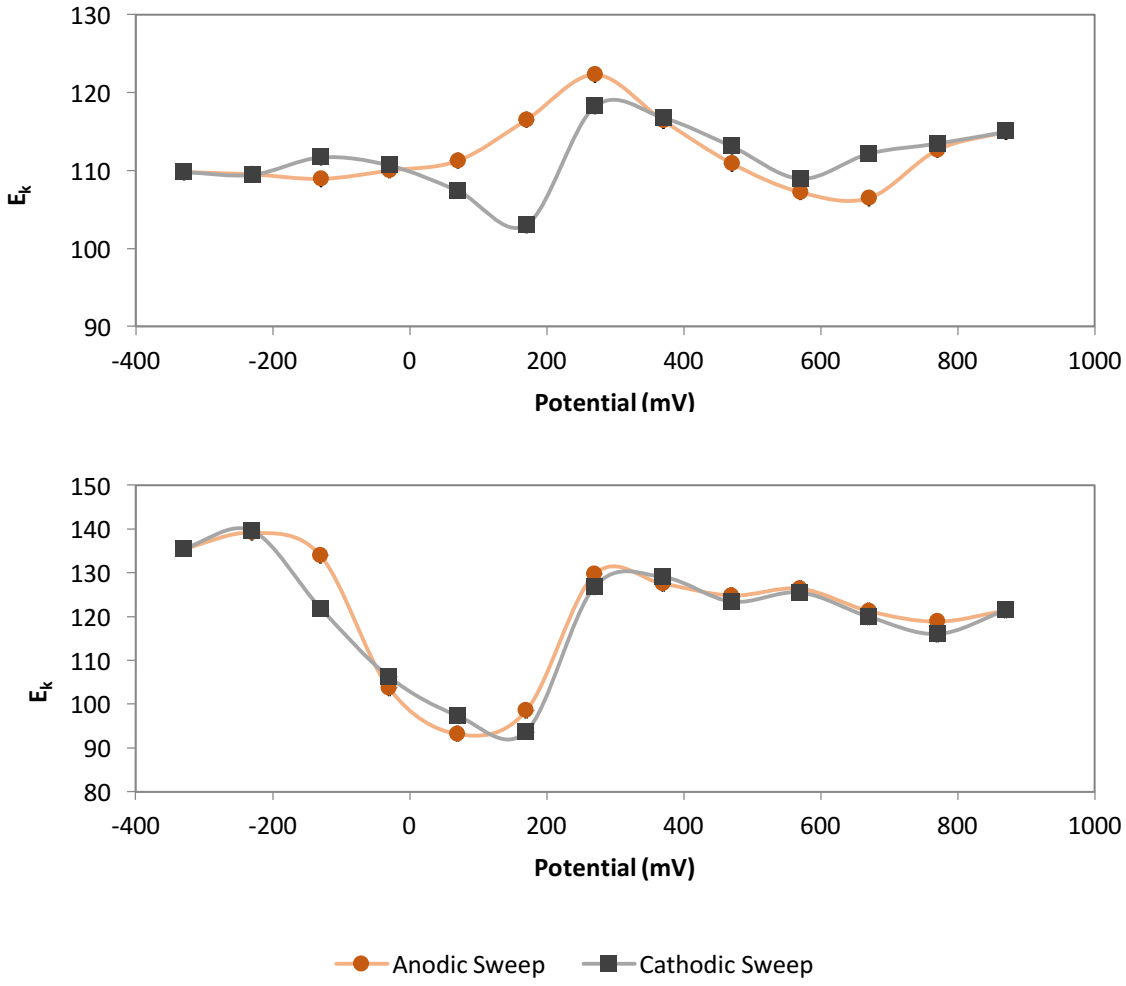

Figure 12: Relationship between applied potential and light saturation coefficient (E_k) for a BPV device inoculated with Chlorella vulgaris (top) and a device inoculated with Synechococcus elongatus (bottom).

As shown in figure 12, the maximum value of E_k occurs at the starting equilibrium potential for *Chlorella vulgaris* (122.28 ±10.16 at 230 mV) and at the second most negative potential for *Synechococcus elongatus* (139.55 ±10.16 at -230 mV). This is different to the observations for F_v/F_m, $rETR_m$ and α, in which the maximum levels recorded always corresponded the conditions of minimum stress for the biofilm i.e. zero current at equilibrium potential.

In contrast to the observations for F_v/F_m, $rETR_m$ and α, E_k does not seem to follow a particular tendency throughout most of the potentiostatic tests, in which the shape

of the potential versus E_k graph is rather flat. The only exception to this is the region with negative electrical currents of the potentiostatic test on *Synechococcus elongatus*, which shows a valley at potentials immediately below equilibrium, with values rising back up again as potential decreases further.

The behaviour of both strains is similar in that no apparent correlation between applied potential and E_k can be observed. Moreover, in contrast to the previously discussed parameters, changes in the light saturation coefficient do not seem to be related with the magnitude of electrical current, with the anodic and cathodic sweeps crossing over seemingly arbitrarily.

Discussion

The results show that potentiostatic conditioning exerts a significant effect over the biofilm formed on the electrode, significantly affecting the dynamics of bioelectrochemical processes such as photosynthesis.

- Maximum quantum yield

Maximum quantum yield is a measure of photosynthetic efficiency, quantifying the maximum light utilization efficiency (i.e. the shift between minimum fluorescence, where all reaction centres are ready to receive and process a photon, and maximum fluorescence, where all reaction centres are occupied and are hence unavailable to receive or process a photon).

Firstly, results show that potentiostatic conditioning does have a significant effect on the photosynthetic efficiency displayed by biofilms conforming the bioanode. This conditioning results in an initial reduction of F_v/F_m, as the potential is shifted away from equilibrium voltage (+230 and +270 mV for *Chlorella vulgaris* and *Synechococcus elongatus*, respectively), both in the anodic and cathodic directions. Ensuing the initial drop close to OCP, maximum quantum yield rises again, as the difference in voltage increases.

F_v/F_m was shown to be highest at the starting point of the test, corresponding to OCP or equilibrium potential. This is expected, as at this potential there is no electrical current flowing between the bioanode and the cathode, and hence the stress levels of the biofilm are at a minimum. Conversely, it is logical to expect that, as observed in figure 9, once the flow of electrical current is induced and the biofilm is hence subjected to more stress, maximum quantum yield (i.e. photosynthetic efficiency) decreases. However, it is interesting that following the initial drop in F_v/F_m at the potentials directly above and below OCP, maximum quantum yield recovers, partially at least, back to higher levels. It therefore appears that an increase in current magnitude is immediately linked to a drop in F_v/F_m, while photosynthetic electron flux is again enhanced at more extreme potentials vs. equilibrium (both forcing electrodes through at cathodic potentials as well as draining electrons away at anodic potentials).

Although the same pattern of a drop followed by a subsequent recovery in F_v/F_m is observed both at the region above equilibrium potential as well as at the region

below it, the latter displays a more accentuated decline in maximum quantum yield. Hence, it would appear that negative electrical currents at the bioanode are linked to lower photosynthetic efficiency. This is logical, as the biofilm naturally performs as a bioanode in the BPV device, and hence forcing electrons into the biofilm reverses its default roll, entailing heightened stress levels or even damage to the photosynthetic apparatus.

When comparing the anodic and cathodic sweeps, it is interesting to observe that, within the potential region above OCP, changes in F_v/F_m are more pronounced in the anodic sweep, in comparison with the cathodic sweep, while the opposite is observed within the potential region below OCP. Thus, larger changes in F_v/F_m seem to be related to larger magnitudes of electrical current, again pointing towards a considerable effect of electrical current on photosynthetic efficiency.

Finally, it is worth noting that the behaviour of both strains upon varying applied potentials is very similar. However, *Synechococcus elongatus* seems to be more sensitive to induced changes in electrical current than *Chlorella vulgaris*, as reflected by the smaller variations displayed by the latter. This is probably a consequence of the further isolation of the photosynthetic apparatus in the eukaryotic strain, in comparison with the more exposed photosynthetic machinery of the prokaryotic strain, which is hence more sensitive to changes in potential.

There is no reported previous work on the effect of electrolytic potential conditioning on the photosynthetic efficiency of biofilms in BPV devices using fluorescence techniques. However, there are reports on the relationship between cell potential and photosynthetic efficiency in a galvanic set-up. Ciniciato et al. (2016) showed that, during the galvanic polarisation curve of BPV devices, a decrease in the external load (i.e. a decrease in cell potential) was linked to a drop in photosynthetic efficiency. This is in accordance with the results obtained in the present study, as Ciniciato et al. proved that F_v/F_m diminishes as electrical current increases when cell potential drops down to 190 mV below OCP, which can be compared to the same potential window around the starting potential. However, the present study tests F_v/F_m for a wider range of potentials (and therefore electrical currents), revealing that the initial tendency is reversed when the biofilms are subjected to more extreme electrical conditions.

- Maximum relative electron transfer rate

The maximum relative electron transfer rate quantifies the flux of electrons between Photosystem II (PSII) and Photosystem I (PSI), and is a measure of the efficiency of open reaction centers as well as the fraction of open reaction centers that are ready to absorb and process photons.

In first place, the findings show that potential conditioning has a considerable impact on the maximum relative electron transfer rates exhibited by the studied biofilms. The behaviour of $rETR_m$ follows a very similar pattern to F_v/F_m; both in the anodic and cathodic potential sweep directions, maximum relative electron transfer rate initially drops as potential shifts away from equilibrium voltage (+230 and +270 mV for *Chlorella vulgaris* and *Synechococcus elongatus*, respectively).

Subsequently, as more extreme potentials are applied to the biofilms, $rETR_m$ rises again. Maximum relative electron transfer rate therefore seems to go hand in hand with maximum quantum yield, with both appearing to drop after an increase in current magnitude occurs immediately above and below equilibrium potential, while more extreme potentials bring about a subsequent recovery as electron flux is forced. In coherence with the observations from $F_v/F_{m,}$ it can be seen that the magnitude of changes in $rETR_m$ is related to electrical current; larger magnitudes of electrical current are linked with a larger impact on photosynthetic efficiency, entailing bigger changes in $rETR_m$.

Again, the section of the test with negative electrical current at the working electrode exhibits a larger drop in maximum relative electron transfer rate. The implication that the biofilm acting as the cathode is linked to lower photosynthetic efficiency is to be expected, as its natural roll as a bioanode is reversed, entailing higher stress and damage to the photosynthetic machinery.

Lastly, as for maximum quantum yield, the behaviour displayed by both strains is very similar regarding the pattern displayed, yet the response of *Synechococcus elongatus* exhibits more drastic changes than *Chlorella vulgaris*, probably as a result of the more exposed bioelectrochemical machinery of the prokaryotic strain, which interacts more directly with the electrode.

Ciniciato et al. (2016) looked at the relationship between cell potential and maximum relative electron transfer rate, showing that a decrease in the external load (i.e. a decrease in cell potential) during a galvanic polarisation curve was linked to a drop in maximum relative electron transfer rate. This is coherent with the findings of this study; Ciniciato et al. showed that $rETR_m$ drops with increasing electrical current, as cell potential goes down from OCP to 190 mV below it. This potential window can be compared to the region surrounding the starting potential in the present study. Beyond this window, as observed for F_v/F_m, the initial observation is reversed, with the values of $rETR_m$ increasing as more extreme potentials are applied.

- Alpha

Alpha is the slope of the light-limited section of the RLC. This parameter indicates the ETR contribution per photon and is therefore a measure of photosynthetic efficiency.

As for F_v/F_m and $rETR_m$, it is observed that applying potential on the assayed biofilms has an important impact on the values of alpha they exhibit. This behaviour is very similar to that observed for F_v/F_m and $rETR_m$, which is logical as the three parameters are an indication of photosynthetic efficiency.

Again, as for F_v/F_m and $rETR_m$, the maximum values of alpha are observed at the beginning of the test, when no electrical current between the electrodes is recorded. Therefore, this point corresponds to the conditions of minimum stress to the biofilms, which explains why photosynthetic efficiency is at its highest.

In the same fashion as for maximum quantum yield and maximum relative electron transfer rate, alpha exhibits a drop in the regions of potential immediately above and below equilibrium potential. However, as the applied potential moves further away from the starting point, the values of alpha are seen to rise again (recovering partially in the case of *Synechococcus elongatus* and fully in the positive potential region of *Chlorella vulgaris*). This is possibly due to an enhancement of the electron flux of bioelectrochemical processes at more extreme potentials, as electrons are forced into or away from the biofilm.

Although the same pattern of a drop followed by a subsequent recovery in F_v/F_m is observed both at the region above equilibrium potential as well as at the region below it, the latter displays a more accentuated decline of maximum quantum yield. Hence, it would appear that negative electrical currents at the bioanode are linked to lower photosynthetic efficiency. This is logical, as the biofilm naturally performs as a bioanode in the BPV device, and hence forcing electrons into the biofilm reverses its default roll, entailing heightened stress levels or even damage to the photosynthetic apparatus.

In line with the observations on maximum quantum yield and maximum relative electron transfer rate, changes in alpha are cushioned in the positive electrical current region of the cathodic sweep as well as the negative electrical current region of the anodic sweep, in comparison to their counterparts. As for the previously discussed parameters, larger changes in alpha seem to be linked to higher electrical currents (in magnitude), indicating that it is electrical current (rather than potential itself) that has a direct impact on photosynthetic efficiency.

This behaviour is true for both strains tested, yet, coherently with previous observations, *Synechococcus elongatus* displays a significantly more sensitive response to applied potential than *Chlorella vulgaris,* possibly due to the more robust isolation of the photosynthetic apparatus in the latter, as previously discussed.

These results are, again, coherent with the findings of Ciniciato et al. (2016), which showed that α drops as cell potential decreases from OCP down to 190 mV below it (i.e. with increasing electrical current). As this potential window is comparable to the region immediately above and below the starting potential of the tests undertaken in the present study, this set of results may be regarded as consistent with the prior research. Again, as for F_v/F_m and $rETR_m$, the values of alpha are seen to increase as the potential applied separates further from equilibrium potential.

- Light saturation coefficient

The light saturation coefficient (or photoadaptive index) E_k is the light intensity at which the RLC stops being linear (beyond which photosynthetic rate is no longer directly proportional to light intensity). This parameter indicates whether biofilms are correctly adapted to their light environment, as the photoadaptive index should be similar to the ambient light to which the biofilm is exposed.

Contrary to F_v/F_m, $rETR_m$ and α, E_k does not seem to follow a particular pattern in response to applied potential.

Differently to F_v/F_m, $rETR_m$ and α, for which maximum values were observed at the beginning of the test, this is only the case for *Chlorella vulgaris*, yet not for *Synechococcus elongatus*, for which the maximum E_k value occurs towards the most negative potential end of the test (at -230 mV). For the previously discussed parameters, maximum values were always observed at equilibrium potential, due to the lack of electrical current between the electrodes and the biofilm therefore being at conditions of minimum stress.

As opposed to the pattern exhibited by F_v/F_m, $rETR_m$ and α, there does not appear to be a consistent relation between E_k and applied potential or electrical current magnitude. The shape of the potential versus E_k graph is generally very flat. This is because E_k is directly proportional to $rETR_m$ whilst inversely proportional to α; since these two parameters follow the same pattern in response to applied potential, E_k does not display a distinctive shape with varying potential. The only exception to this is the region with negative electrical currents in the test with *Synechococcus elongatus*, in which the more pronounced shape followed by $rETR_m$ in this region, in comparison to the milder changes displayed by α, results in E_k being heavily influenced by the former parameter, and hence an initial drop in E_k is observed, followed by a subsequent recovery.

Previous work on the effect of electrical potential and magnitude of current shows no apparent relationship with E_k (Ciniciato et al. 2016), which is consistent with the present tests.

4. Chapter 4: Physicochemical characterisation of the Rio Tinto ecosystem

The Rio Tinto environment

The mine of Rio Tinto is located in the Iberian Pyrite Belt, one of the world's oldest and largest mining locations. This area is among the vastest acid mine drainage and mine waste accumulation sites, and it hosts an incredibly peculiar geobiological system where, wonderfully, a suite of microorganisms thrives in its extreme physicochemical conditions.

The Iberian Pyrite Belt is a geographical area where massive polymetallic sulphides are abundant. It is located in the Southwest of the Iberian Peninsula, it is about 40 Km wide and stretches 250 Km from Alcacer do Sal, in Portugal, to Seville, in Spain.

The minerals in this region, mainly sulphide minerals, are of volcanic-sedimentary origin, having been formed about 350 million years ago. The most abundant sulphide minerals in this area are pyrite, chalcopyrite, sphalerite and galena (Mellado et al. 2006).

The region was first exploited by Iberians and Tartessians, around the year 3,000 BC. Later on, during the Phoenician Era (1,500 BC to 300 BC), the Romans carried out a tremendous mining activity whereby they obtained copious amounts of metals such as gold, silver, copper and iron (Rickard, 1928).

Rio Tinto is one of the eight giant massive sulphide mineral deposits in the Iberian Pyrite Belt, and is probably the largest source of massive sulphides in the world (Mellado et al. 2006).

Since the end of the 19th century, with the arrival of the British-run Rio Tinto Company, it has been hosting large-scale mining operations continuously until its shutdown in 2001, when Riotinto S.A.L. (its then owner) was forced to shut the mine due to the profitless price of copper, which had fallen to ground levels.

After 14 years of inactivity, the Rio Tinto mines were reopened in July 2015, coinciding with the present study. Therefore, the physicochemical and microbial characterisation undertaken during the year of sampling, starting slightly before the reopening and stretching 10 months after it, is of great interest in order to evaluate the impact of the mine being active on its ecosystem.

On the one hand, the extensive monitoring undertaken in this study enables to assess whether the extreme physicochemical conditions that are observed in this environment result from or are accentuated by mining activity. On the other hand, this will allow to determine if the rich microbial diversity found throughout the ecosystem is harmed by this return of activity. Therefore, from an environmental point of view, it is of paramount importance to confirm that this unique and incredibly precious microbial ecosystem is preserved upon the reopening of the mine.

The mine receives its name from the Tinto River, which originates very close to the mine pits, in a hill known as Peña del Hierro. It passes through the mining complex, running for about 100 Km up to the Atlantic Ocean (by the coast of Huelva). Together with the acid mine drainage streams and reservoirs resulting from geobiological and mining activity, Rio Tinto is an incredibly unusual, extreme and mesmerising ecosystem.

This ecosystem is unique in the whole planet, due to the proliferation of microbial life in its extreme physicochemical conditions, in particular the very acidic pH (2.3 on average) and high concentration of heavy metals in solution, mainly iron, as well as copper, zinc and arsenic (Amils et al. 2004). These extreme conditions are thought to be the most similar to other planets that could potentially bear or have contained water, such as subterranean Mars or the hypothetical acidic water ocean underneath the ice surface of Jupiter moon Europa. For this reason, the Rio Tinto ecosystem has attracted great interest across astrobiologists all around the planet and is a main research site of NASA.

The prolonged mining activity in the area has, without doubt, historically shaped its physicochemical conditions, drastically changing its hydrochemistry. This process of contamination, commonly referred to as acid mine drainage (AMD), consists in the release or leakage of acidic water that is rich in heavy metals into natural freshwater and is particularly extreme in the Rio Tinto area.

Acid generation behind AMD arises from the leaching of metal sulphide minerals, upon exposure to water and oxygen. As sulphur is oxidised from its sulphide (charge -2) form to its sulphate (charge +6) form, the surrounding liquid medium is acidified. In turn, this enhances the solubility of metal cations, mainly ferric and ferrous iron, as well as cupric copper, zinc and a suite of other metal species, which gradually become more and more concentrated in solution. In addition, this process may be catalysed by certain microorganisms with chemolithotrophic metabolisms (these obtain energy from the oxidation of the metal sulphide minerals). Again, this generates acidity as well as a build-up of metals in solution. The microorganisms that tolerate such harsh physicochemical conditions are known as acidophiles, as they are able to thrive in low pH.

A very curious phenomenon is that the acid pH is constant throughout the riverbed, mainly due to the buffering activity of the ferric/ferrous iron couple as well as that of the microbial community (Fernandez-Remolar et al. 2003).

Considering quite how extreme the physicochemical conditions in the Rio Tinto environment are, it is truly fascinating that thriving within it are living microorganisms. There are numerous reports on the microbial ecology of this ecosystem, revealing the presence of a wide range of microorganisms, including both prokaryotes such as sulphur and iron oxidising bacteria (Lopez-Archilla et al. 2001), as well as eukaryotes such as acidophilic algae (Amaral et al. 2002).

The purpose of this study was to utilise naturally-occurring acidophilic biofilms from the Rio Tinto ecosystem as the biological material in a BPV cell platform. In search for biofilms thriving in the most extreme physicochemical conditions, i.e.

lowest pH and highest metal concentrations in solution (the hypothesis is that cell performance increases as a result of heightened electrical conductivity), a number of locations throughout the Rio Tinto area were investigated throughout a whole year and the biofilms thriving in the most extreme sites were selected for the subsequent BPV cell studies.

Materials and Methods

- Sample collection and in situ measurements

In order to achieve the goal of collecting the biofilm thriving in the most acidic pH possible and toughest physicochemical conditions, sixteen different points along the Tinto River and nearby acid mine drainage sites were studied. First, the evolution of the physicochemical conditions of the selected sites was investigated by regularly monitoring these throughout the course of one natural year.

Sixteen sampling points were selected, which are found within five broad areas that are labelled A to E for the purposes of this study. Areas A and D constitute slagheap drainages, Areas B and C are the drainages from old railway tunnels and Area E corresponds to the Tintillo River. These sampling sites, which were investigated throughout a whole year, are illustrated in the following maps:

Figure 13: Map showing the seven sampling areas, A-E, at the Mine of Rio Tinto, the Tinto River and associated acid mine drainage sites.

Figure 14: Map showing the sixteen sampling sites, 1-16, at the Mine of Rio Tinto, the Tinto River and associated acid mine drainage sites.

Electrical conductivity, pH and dissolved Oxygen were measured in situ with a calibrated Hanna Instruments portable meter.

Liquid samples were taken from each location, subsequently filtered through cellulose nitrate filter paper, in order to eliminate suspended solids, and finally stored in 500 ml bottles to which 2 ml of 65% nitric acid was added (in order to avoid precipitation).

- Chemical analysis

Chemical analyses were performed on the samples taken from the sixteen sites, with the purpose of determining the presence and concentration of metals in solution, the ferric/ferrous ion balance and sulphate concentration, as described in chapter 2. Finally, relative contamination was assessed by means of the Toxicity Index.

Results

Area A: Drainage of the North Slagheap

The North Slagheap of the Rio Tinto mine is a site where mineral waste is dumped. This is generally sterile material (with a low copper grade) that is rich in other sulphides, mainly pyrite. When it rains, water accumulates in two dams. Sampling

points were established at both of these reservoirs (points 1 and 3), as well as at the streams emerging next to each dam, as a result of liquid filtration through the mineral and soil (points 2 and 4). A final point in this area was chosen, corresponding to an abandoned copper cementation plant through which lateral filtration streams flow (point 5). In this area, living biofilms were detected at all five points.

Figure 15: Map showing the five sampling points at the North Slagheap drainage area.

- Point 1

Point one is located in the northernmost dam at the North Slagheap drainage area. This reservoir of water originates both from the filtration of rainwater through the slagheap piles of waste mineral and soil, as well as from the direct accumulation of rainwater. Its coordinates are the following:

  - Latitude: 37°43'1.45"N
  - Longitude: 6°34'9.03"O

Firstly, pH and electrical conductivity were measured every fortnight throughout a year:

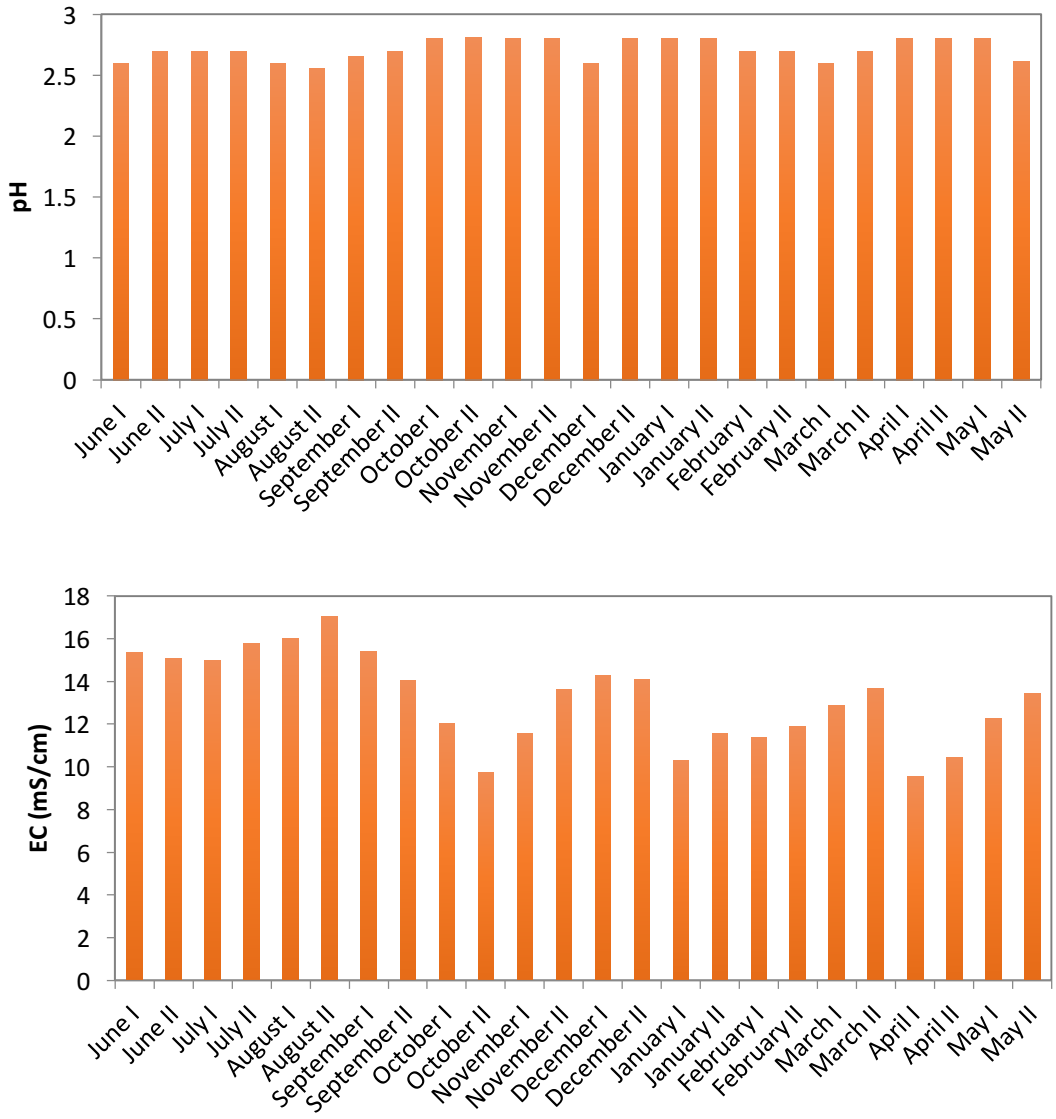

Figure 16: Graphs showing the bimonthly evolution of pH (top) and electrical conductivity (bottom) at sampling point 1, from June 2015 until May 2016.

The average pH is 2.7, with the lowest and highest values being 2.55 (in the second half of August 2015) and 2.8 (during most of the Autumn, Winter and Spring), respectively. Hence, a fairly constant pH is observed throughout the year, with very little variation.

In turn, the average value for electrical conductivity is 13.2 mS/cm. In this case, a larger variation is observed, with a highest value of 17.0 mS/cm in the second half of August 2015 and a lowest value of 9.5 mS/cm in the first half of April 2016.

Both of these results may be interpreted by looking at pluvial precipitations. The following table shows the monthly precipitations during the natural year of

sampling at the province of Huelva, as reported by AEMet (Asociación Estatal de Meteorología, the Spanish Statal Metereological Association):

June	July	August	September	October	November
0.0	2.4	0.2	1.6	103.4	60.6
December	January	February	March	April	May
65.2	50.4	35.2	12.0	58.4	95.4

Table 7: Table showing the monthly pluvial precipitation (mm/m^2) at the province of Huelva, from June 2015 until May 2016.

We can observe that both pH and electrical conductivity are correlated to pluvial precipitations. While pH is positively correlated to precipitations, electrical conductivity exhibits a negative correlation. The variation of both of these physicochemical parameters (while more pronounced in the case of electrical conductivity), is the result of the dissolution of ions in solution when it rains.

It may also be noted that pH and electrical conductivity are affected by temperatures; the warmer months are linked with higher EC and lower pH values, due to enhanced evaporation and resulting higher concentration of metal ions and protons in solution. Conversely, milder temperatures that entail lower levels of evaporation, together with more abundant pluvial precipitations, are linked with lower EC and higher pH values, as the ions in solution are more diluted.

The following table shows the average monthly temperatures during the natural year at the province of Huelva, as reported by AEMet:

June	July	August	September	October	November
23.9 °C	28.1 °C	26.1 °C	22.2 °C	20.0 °C	16.3 °C
December	January	February	March	April	May
14.4 °C	13.4 °C	12.8 °C	13.3 °C	16.3 °C	18.8 °C

Table 8: Table showing the average monthly temperatures at the province of Huelva, from June 2015 until May 2016.

Secondly, the chemical composition of the liquid at this point was monitored bimonthly, throughout a whole natural year. Samples were taken on a fortnightly basis and were subsequently tested for a series of heavy metals, by analysis with ICP-MS.

The average concentration of each metal throughout the year was calculated, as presented in the following graphs:

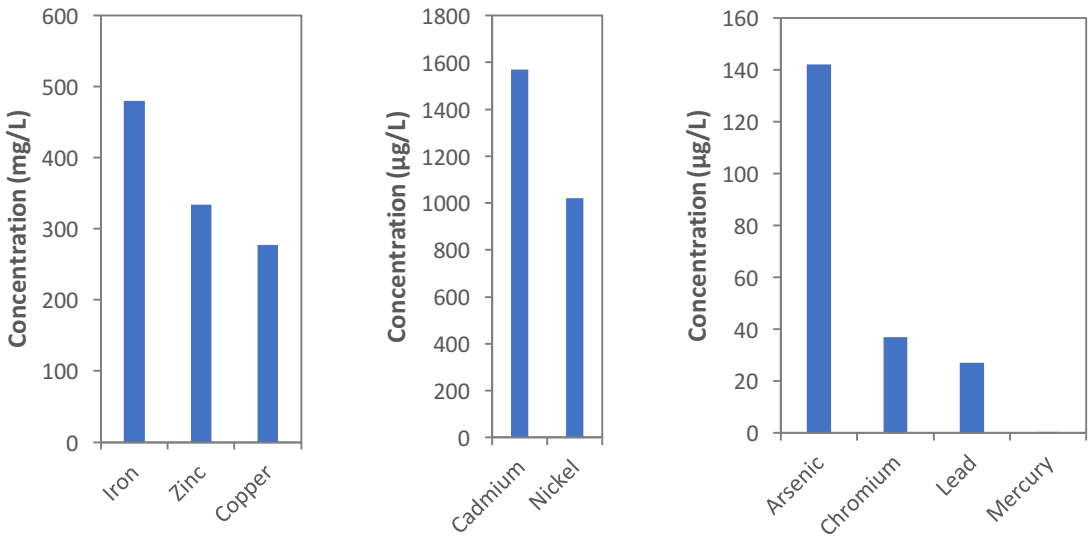

F*igure 17: Graphs showing the average concentrations of total iron, zinc, copper, cadmium, nickel, arsenic, chromium, lead and mercury in solution at point 1, from June 2015 until May 2016.*

The metals present in higher concentrations are iron, zinc and copper (average concentrations of 480 mg/L, 334 mg/L and 277 mg/L, respectively), followed by cadmium (1,569 µg/L) and nickel (1,021 µg/L). The minority elements, present in lower concentrations, are arsenic (142 µg/L), chromium (37 µg/L), lead (27 µg/L) and mercury (0.3 µg/L). The full results for the bimonthly evolution of total iron, copper, arsenic, lead and mercury, as well as the quarter-yearly evolution of cadmium, nickel and chromium in solution at point 1 from June 2015 until May 2016 can be found in figure A1 of the Appendix.

The levels of total copper, zinc, cadmium, nickel, arsenic and lead in solution are negatively correlated with pluvial precipitations, as can be seen by comparing these (table 7) to metal levels in solution (figure A1 of the Appendix), although it is slightly less obvious for nickel than for the rest of the metals. This observation is logical; with increased precipitations, the rainwater dilutes these metals in solution, causing a drop in their concentration. Hence, we can observe the highest levels of these metals in solution during the driest months (June-August 2015) and the lowest levels during the rainiest period (beginning in October 2015).

Moreover, the fact that the driest months coincide with the warmest period of the year, which may be seen by comparing pluvial precipitations in table 7 with average temperatures in table 8, accentuates this phenomenon, as is the case for EC and pH. On the other hand, the months with more abundant pluvial precipitations tend to be characterised by milder temperatures, which together contribute to further diluting ions in solution, hence the lower levels of heavy metals in solution during this period.

A highly relevant factor affecting microbial diversity and physiology is the oxidation state of the ferric/ferrous ion couple in solution. For this purpose, the proportion of the two ions was examined, as shown in the following graph:

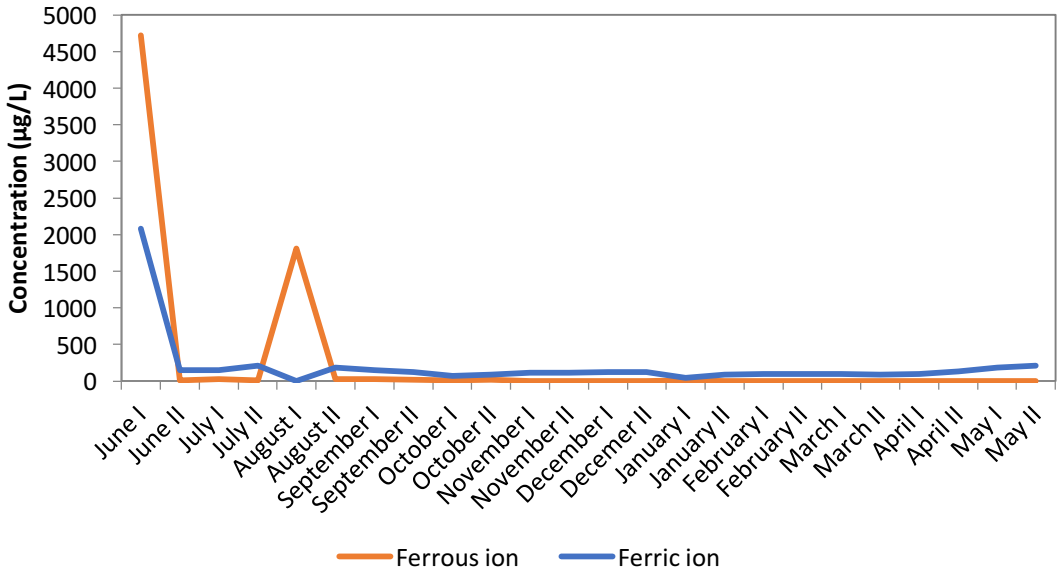

Figure 18: Graph showing the bimonthly evolution of ferric (blue) and ferrous (red) ion in solution at point 1, from June 2015 until May 2016.

The average balance of ferric ion with respect to total iron for the year is 0.87. Hence, the ferric/ferrous ion couple is at a very oxidised state at this point.

The toxicity index of this point at each trimester is shown below:

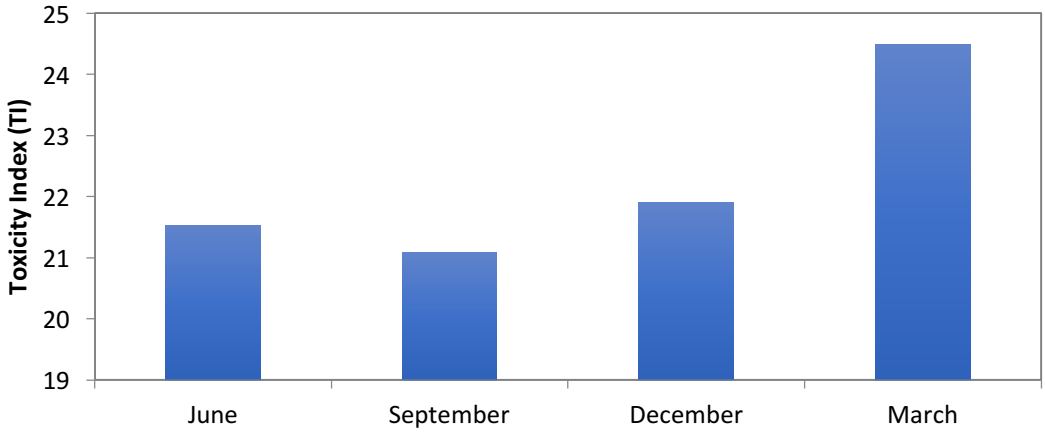

Figure 19: Graph showing the Toxicity Index of point 1 at June 2015, September 2015, December and March 2016.

The Toxicity Index is a measure of relative contamination, cumulatively assessing the concentration of the various heavy metals in solution, globally, as an individual factor.

With an average TI of 22.3, point 1 exhibits intermediate levels of contamination in comparison with the rest of the points. Moreover, the TI at this site remains considerably stable throughout most of the year, with values of 21.5, 21.1 and 21.9 in June, September and December, respectively (except for March, which has a higher TI of 24.5).

Dissolved oxygen was also measured at this point, as shown in the following graph:

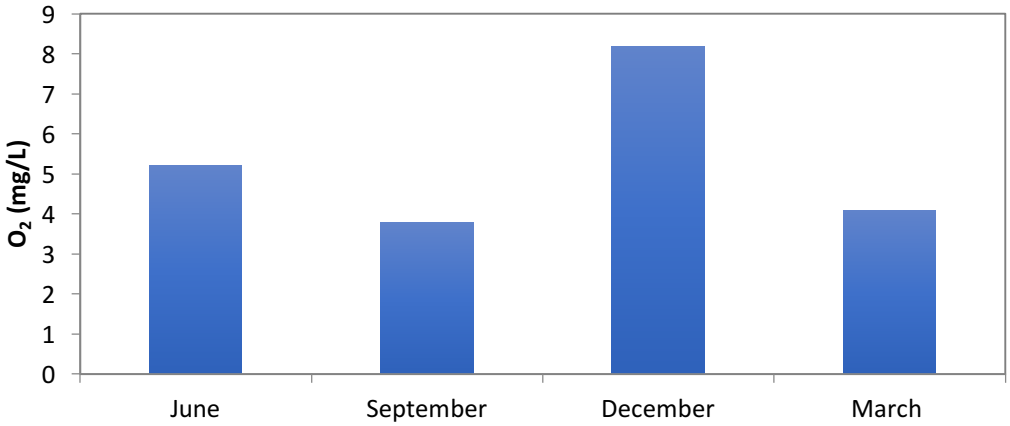

Figure 20: Graph showing dissolved oxygen (mg/L) at point 1 in June 2015, September 2015, December 2015 and March 2016.

The average dissolved oxygen throughout the year is 5.3 mg/L, with the highest value being recorded in December (8.2 mg/L) and the lowest value being noted in September (3.8 mg/L).

- Point 2

Point two is located downstream of point one; it corresponds to the filtrations through the northernmost dam at the North Slagheap drainage area. Its coordinates are the following:

  - Latitude: 37°42'57.76"N
  - Longitude: 6°34'8.66"O

Firstly, pH and electrical conductivity were measured each two weeks:

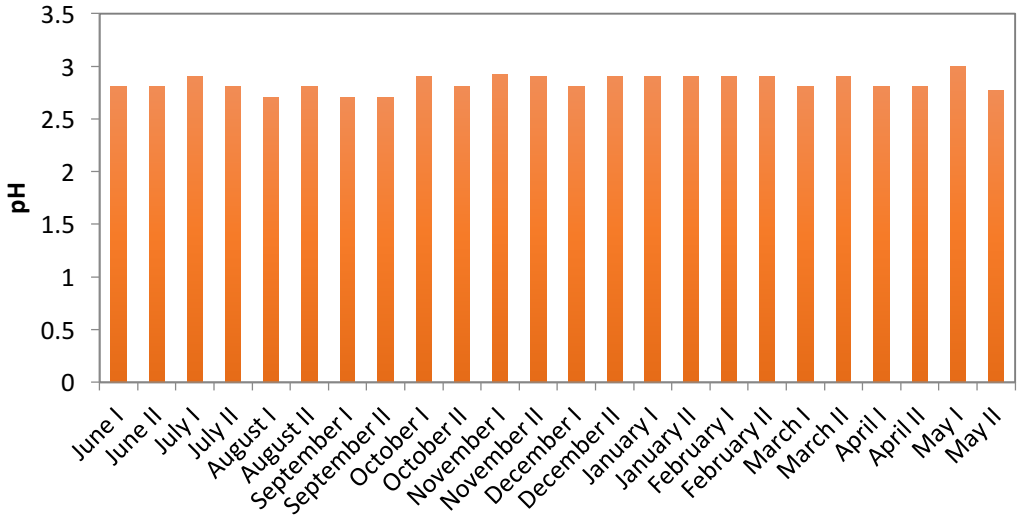

Figure 21: Graph showing the bimonthly evolution of pH at sampling point 2, from June 2015 until May 2016.

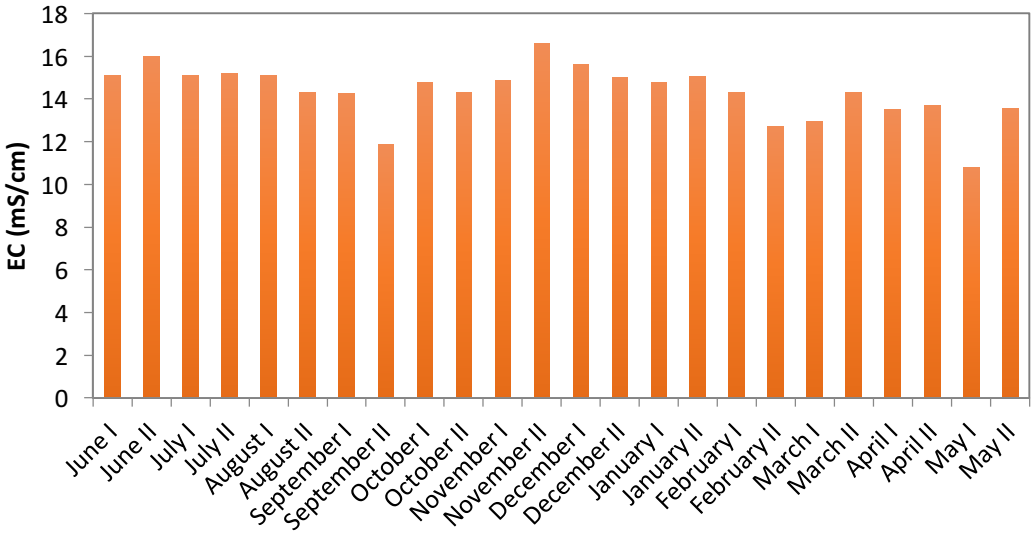

Figure 22: Graph showing the fortnightly evolution of electrical conductivity at sampling point 2, from June 2015 until May 2016.

The pH and EC values observed at site 2 are intermediate in comparison with the rest of the sampling sites.

The average pH is 2.8, with the lowest and highest values being 2.7 and 3.0, respectively. Hence, as for point 1, a fairly constant pH is observed throughout the year, with the slight difference that the pH at point 2 is consistently slightly higher than that of point 1, with values typically between 0.1 and 0.2 higher. This is probably due to the fact that the stream at point 2 partly results from a displacement of subterranean water by rainwater, which raises the pH.

In turn, the average value for electrical conductivity is 14.3 mS/cm. Again, a larger variation is observed in comparison with pH, with a highest value of 16.6 mS/cm in the second half of November 2015 and a lowest value of 10.8 mS/cm in the first half of May 2016.

Electrical conductivity is consistently higher at point 2 with respect to point 1. This is to be expected; as the water from the dam has run across additional mineral, it tends to bear higher quantities of leached metals in solution. Finally, an interesting observation is that the maxima and minima at point 2 correspond to rainy and dry times of the year, respectively (Table 2). This is the opposite pattern to that of point 1, denoting that higher precipitations entail a higher accumulation of metals in solution at point 2, possibly due to the need for displacement of subterranean water by rainwater.

Secondly, as for point 1, the chemical composition of the liquid at point 2 was monitored on a fortnightly basis, throughout a whole natural year. The samples were scanned for heavy metals, by analysis with ICP-MS, and the average concentrations for each metal throughout the year were calculated. These results are presented a:

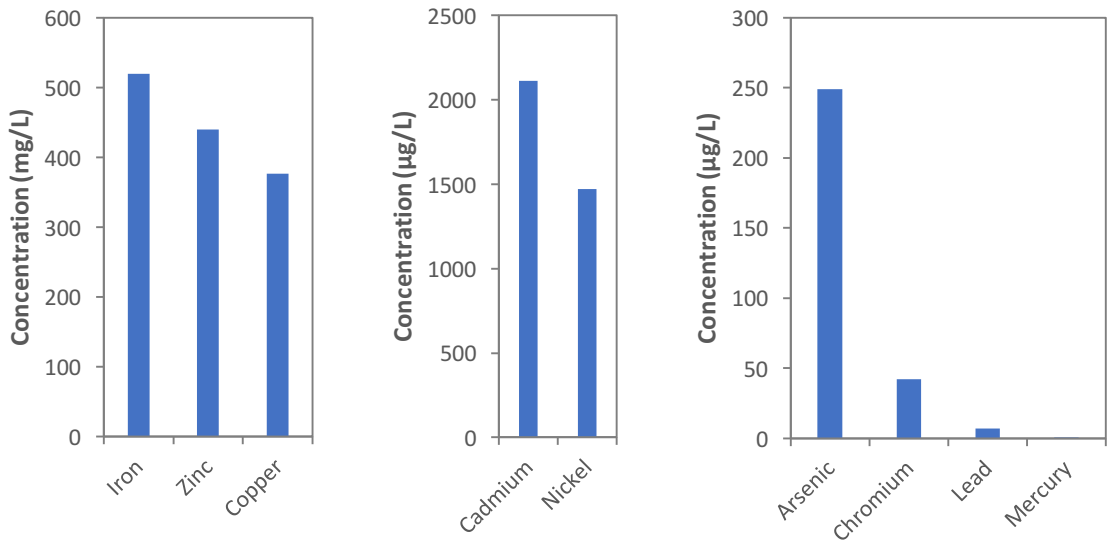

F*igure 23: Graphs showing the average concentrations of total iron, zinc, copper, cadmium, nickel, arsenic, chromium, lead and mercury in solution at point 2, from June 2015 until May 2016.*

The levels of metals in solution are considerably higher at point 2 than at point 1. This is logical; as the water from the dam has travelled through additional mineral, it is charged with extra quantities of subterranean leached metals.

The metals present in higher concentrations are iron, zinc and copper (average concentrations of 520 (vs 480) mg/L, 440 (vs 334) mg/L and 377 (vs 277 mg/L), respectively), followed by cadmium (2,113 vs 1,569 µg/L) and nickel (1,471 vs 1,021 µg/L). The minority elements, present in lower concentrations, are arsenic (249 vs 142 µg/L), chromium (42 vs 37 µg/L), lead (7 vs 27 µg/L) and mercury (0.3 vs 0.3 µg/L).

The complete heavy metal tests for the bimonthly evolution of total iron, copper, zinc, arsenic, lead and mercury and the quarter-yearly evolution of cadmium, nickel and chromium in solution at point 2, from June 2015 until May 2016, are presented in figure A2 of the Appendix.

As for point 1, although slightly delayed due to the lag time required to filter through the dam, the levels of these metals in solution are negatively correlated with pluvial precipitations, as can be seen by comparing both sets of values (figure A2 of the Appendix with Table 7). Again, this correlation extends to temperature; the warmer and drier months of the year are linked with higher concentrations of heavy metals in solution, while lower levels of these are associated with the rainier months that are accompanied with milder temperatures (as seen by further comparison with the average monthly temperatures, presented in Table 8).

The oxidation state of the ferric/ferrous ion couple was also monitored by analysing the levels of each ion in solution, as presented in the following graph:

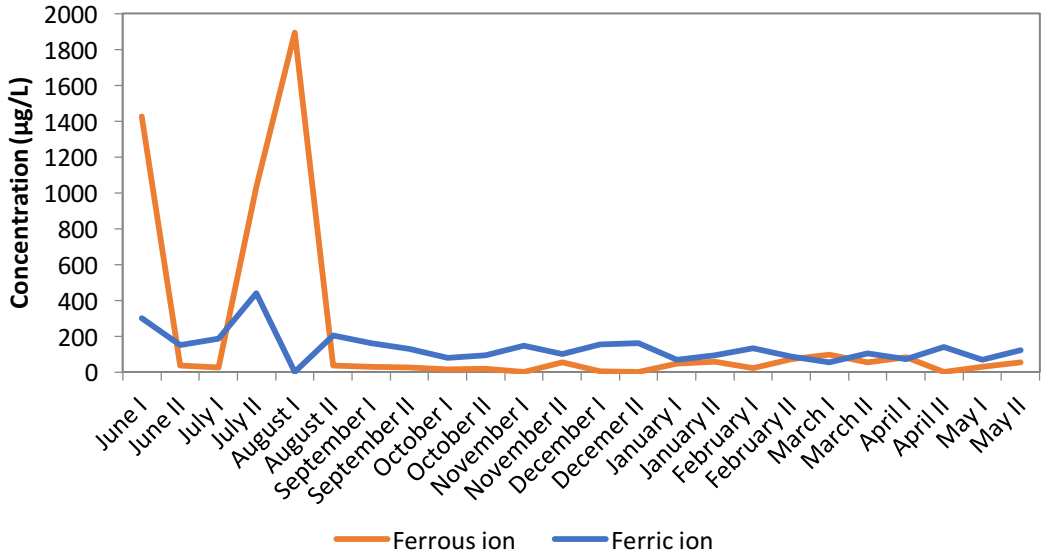

Figure 24: Graph showing the bimonthly evolution of ferric (blue) and ferrous (red) ion in solution at point 2, from June 2015 until May 2016.

The average balance of ferric ion with respect to total iron for the year is 0.69. While the ferric/ferrous ion couple is still at a rather oxidised state at this point, it is less so than at point 1. This is to be expected, as point 2 is located by a drainage stream that parts from point 1 and travels underground, where oxygen is unavailable.

It is worth noting that ferrous ion exhibits two pronounced peaks towards the beginning of the sampling period, possibly in response to the reactivation of the mine, which took place in July.

The toxicity index of this point at each trimester is shown below:

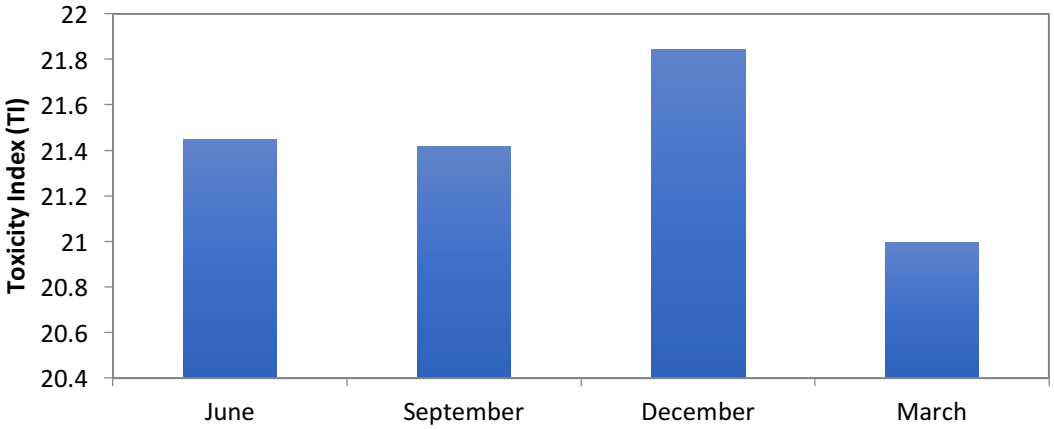

Figure 25: Graph showing the Toxicity Index of point 2 in June 2015, September 2015, December 2015 and March 2016.

Dissolved oxygen was again measured at this site, as shown in the following graph:

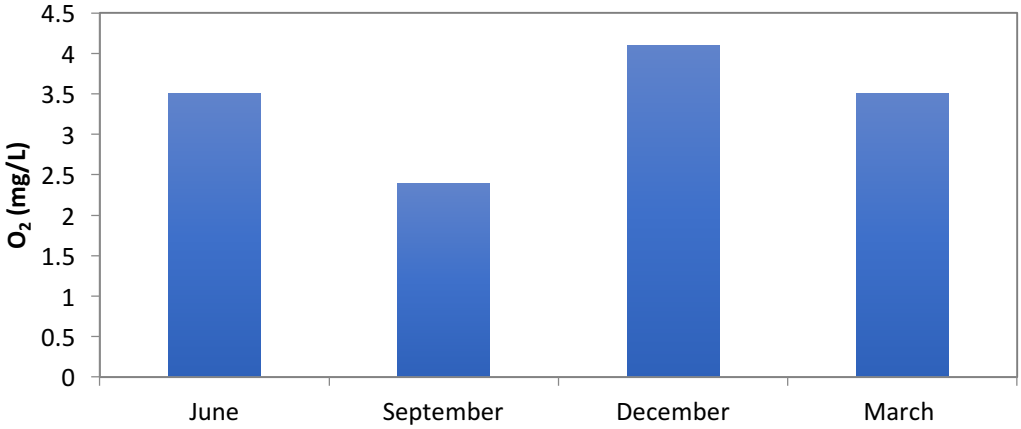

Figure 26: Graph showing dissolved oxygen (mg/L) at point 2 in June 2015, September 2015, December 2015 and March 2016.

The average dissolved oxygen throughout the year is 3.4 mg/L, with the highest value being recorded in December (4.1 mg/L) and the lowest value being noted in September (2.4 mg/L). This is consistently lower than point 1, reflecting the subterranean passage that the effluent takes to travel between both points.

- Point 3

Point three is located in the southernmost dam within the North Slagheap drainage area. Like point 1, this reservoir originates both from the filtration of rainwater through the slagheap piles of waste mineral and soil, as well as from the direct accumulation of rainwater.

Its coordinates are the following:

- Latitude: 37°42'51.73"N
- Longitude: 6°34'11.20"O

Physicochemical parameters were monitored at point 1. In first place, pH and electrical conductivity were measured every two weeks throughout a year:

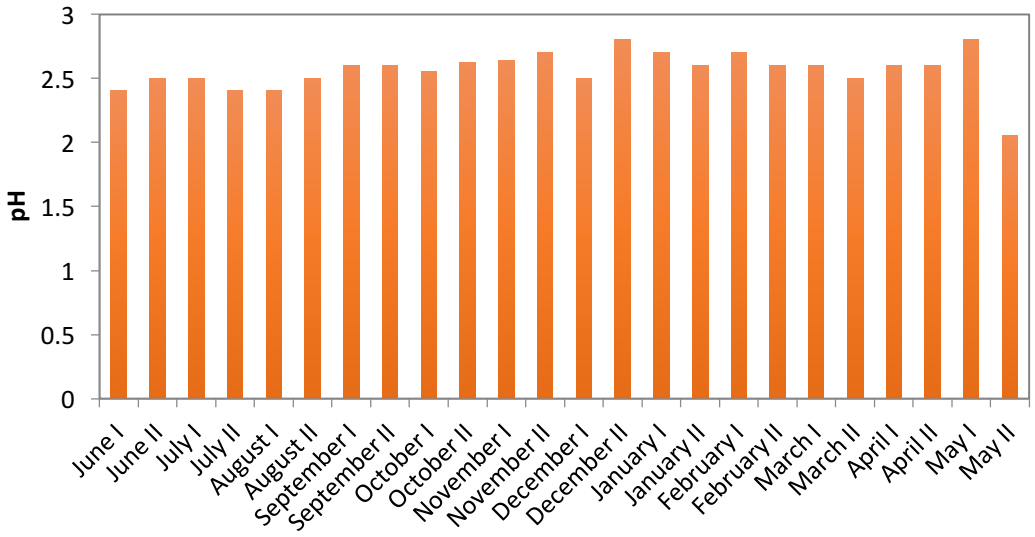

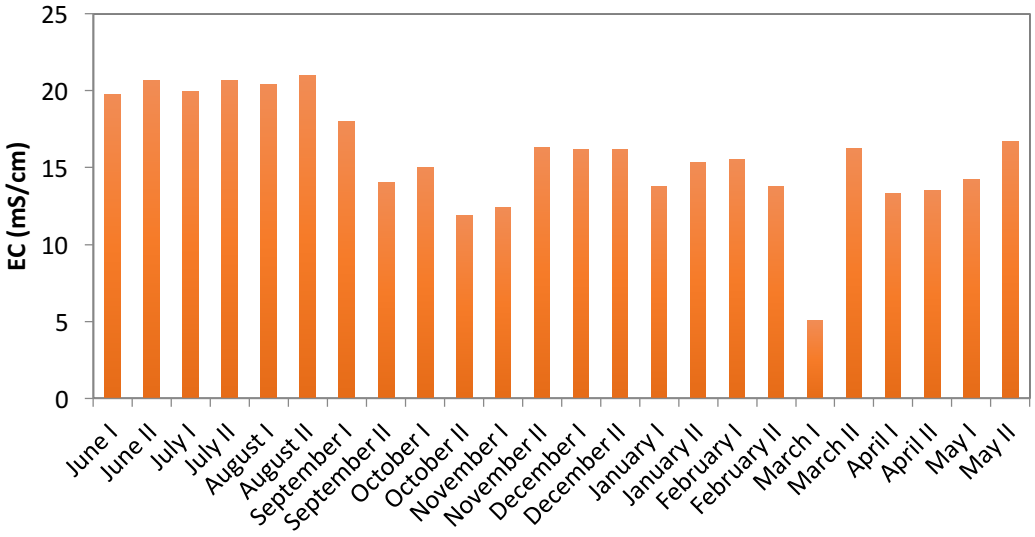

Figure 27: Graphs showing the bimonthly evolution of pH (page 69) and electrical conductivity (page 70) at sampling point 3, from June 2015 until May 2016.

The average pH is 2.6, with the lowest and highest values being 2.05 (in the second half of May 2016) and 2.8 (in the second half of December 2015), respectively. The pH observed throughout the year is rather constant, with very little variation.

In turn, the average value for electrical conductivity is 15.8 mS/cm. In this case, a larger variation is observed, with a highest value of 21.0 mS/cm in the second half of August 2015 and a lowest value of 5.0 mS/cm in the first half of March 2016.

It must be noted that the acid mine drainage phenomenon is more accentuated at the southernmost dam in comparison with the northernmost dam. On the one hand, the pH of point 3 is lower than that of pH 1, while electrical conductivity is higher at point 3, implying that the water is more acidic and charged with higher quantities of leached metals in solution.

As for the northernmost dam, the evolution of these two parameters can be understood by looking at monthly pluvial precipitations (Table 7) and average monthly temperatures (Table 8).

Secondly, as for the sampling sites described previously, the chemical composition of the liquid at point 3 was monitored bimonthly, throughout a whole natural year. Samples were taken on a fortnightly basis, and these were scanned for a series of heavy metals, by analysis with ICP-MS; the average concentration of each metal present in the samples was then calculated, as presented thus:

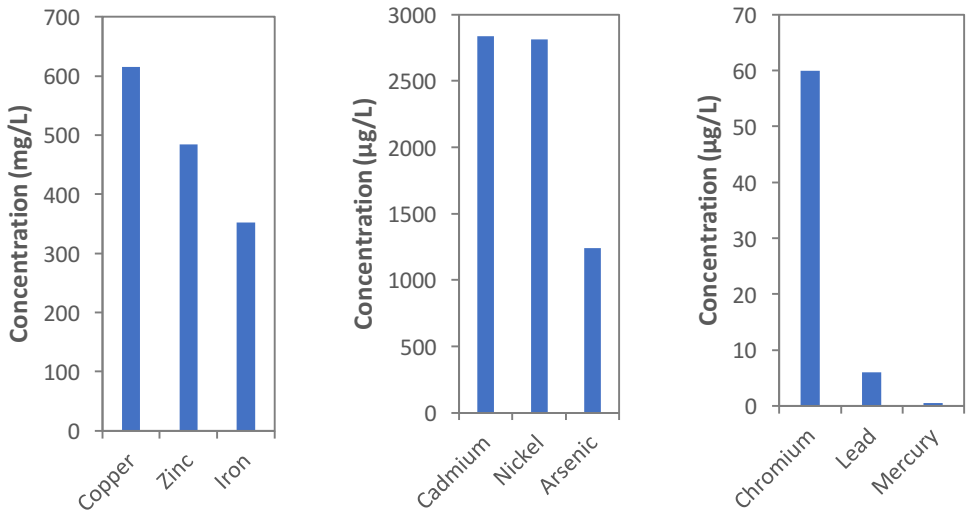

Figure 28: Graphs showing the average levels of total copper, zinc, iron, cadmium, nickel, arsenic, chromium, lead and mercury in solution at point 3, from June 2015 until May 2016.

The metals present in higher concentrations are copper, zinc and iron (average concentrations of 615 mg/L, 484 mg/L and 352 mg/L, respectively), followed by cadmium (2,838 µg/L), nickel (2,815 µg/L) and arsenic (1,241 µg/L). The minority elements, present in lower concentrations, are chromium (60 µg/L), lead (6 µg/L) and mercury (0.5 µg/L); the full sampling results for the evolution of heavy metals in solution at point 3 throughout the year are recorded in figure A3 of the Appendix. As noted earlier, the acid mine drainage phenomenon is more accentuated at the southernmost dam in comparison with the northernmost dam.

The oxidation state of the ferric/ferrous ion couple was also monitored by analysing the levels of each ion in solution, as presented below:

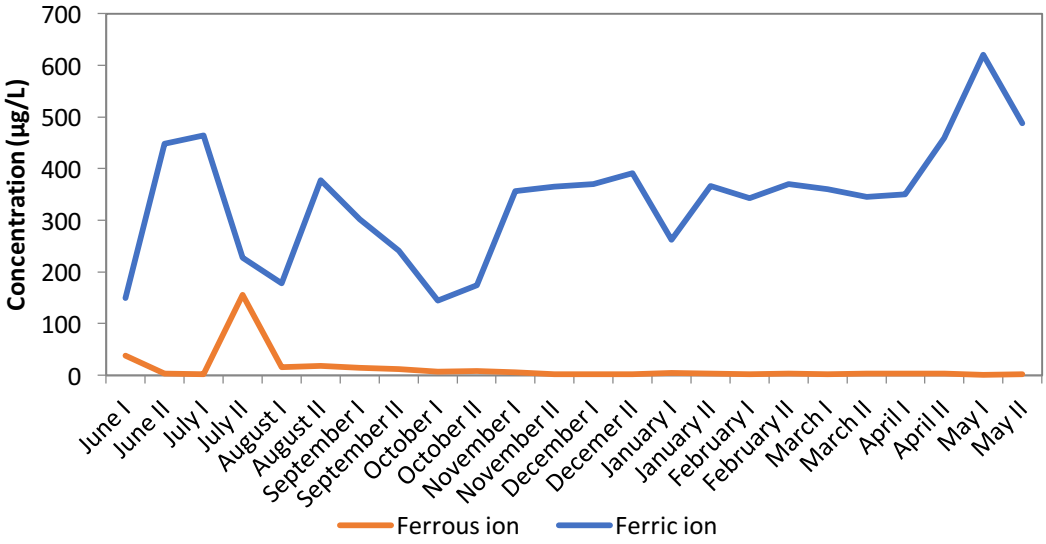

Figure 29: Graph showing the bimonthly evolution of ferric (blue) and ferrous (red) ion in solution at point 3, from June 2015 until May 2016.

The average balance of ferric ion with respect to total iron for the year is 0.96. At this point, iron is present almost uniquely as ferric ion; it is extremely oxidised.

It is worth noting that, at this point, the stream of water bears an orange/red tone, due to the presence of high levels of ferric iron. This acts as a filter for light, allowing through a limited range of frequencies that reduces the possibilities of pigment absorption spectra, which limits photosynthesis.

The toxicity index of this point at each trimester is shown below:

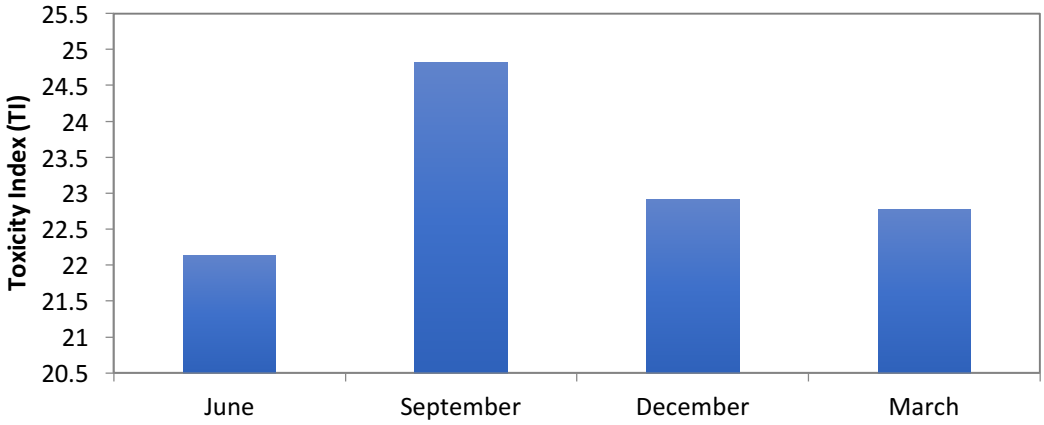

Figure 30: Graph showing the Toxicity Index of point 3 at June 2015, September 2015, December and March 2016.

Dissolved oxygen was also measured at this point, as shown in the following graph:

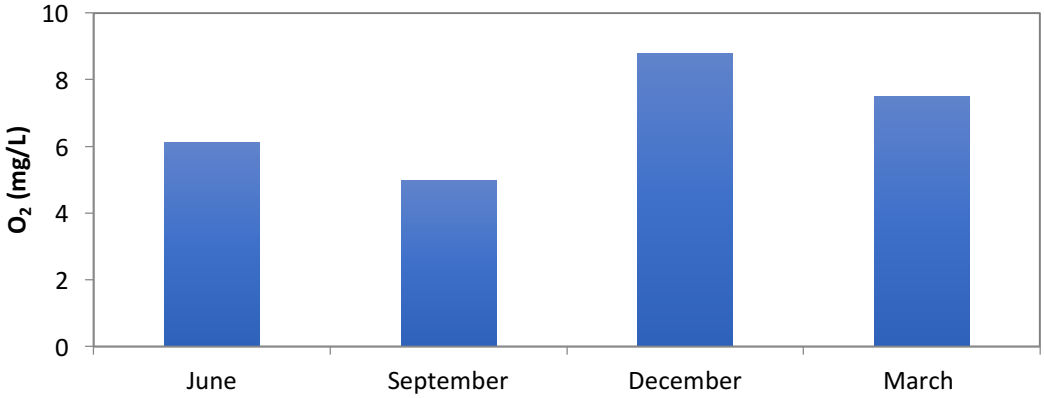

Figure 31: Graph illustrating dissolved oxygen (mg/L) at point 3 in June 2015, September 2015, December 2015 and March 2016.

The average dissolved oxygen throughout the year is 6.9 mg/L, with the highest value being recorded in December (8.8 mg/L) and the lowest value being noted in September (5.0 mg/L). This is similar to point 1, which is to be expected given the similar emplacement and physicochemical nature.

- Point 4

Point four is located downstream of point three; it corresponds to the filtrations through the southernmost dam at the North Slagheap drainage area. As the liquid at this point proceeds from the aforementioned dam, passing through additional subterranean mineral, we would expect it to carry higher quantities of leached metals in solution.

Its coordinates are the following:

- Latitude: 37°42'50.92"N
- Longitude: 6°34'7.49"O

Again, a series of physicochemical parameters were monitored at point 4. Firstly, pH and electrical conductivity were measured each two weeks throughout a year. These are illustrated in the following graphs:

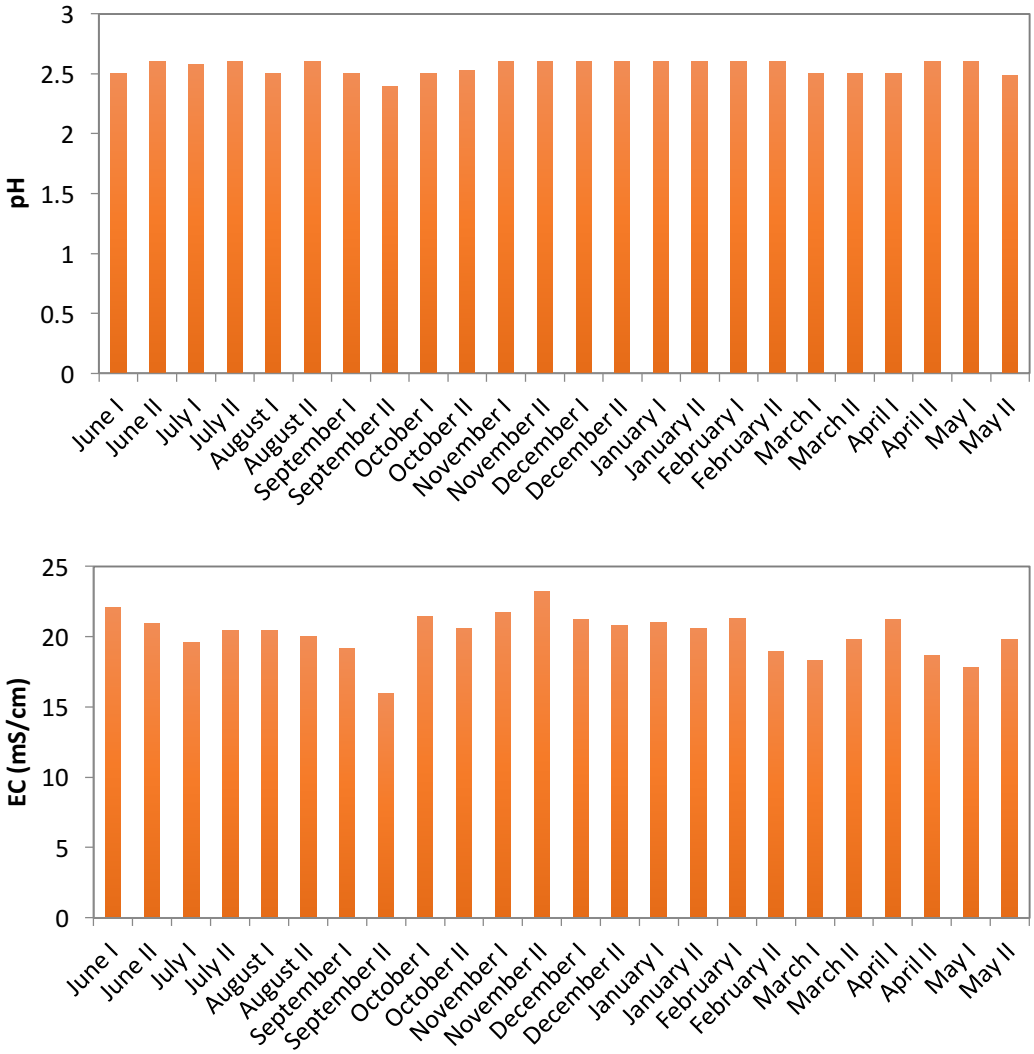

Figure 32: Graphs showing the bimonthly evolution of pH (top) and electrical conductivity (bottom) at sampling point 4, from June 2015 until May 2016.

The average pH is 2.6, with the lowest and highest values being 2.4 and 2.6, respectively. Therefore, in the same way as was the case for point 3, a rather constant pH is observed throughout the year.

In turn, the average value for electrical conductivity is 15.8 mS/cm. Again, a larger variation is observed in comparison with pH, with a highest value of 22.1 mS/cm in the first half of June 2015 and a lowest value of 15.9 mS/cm in the second half of September 2016. Therefore, electrical conductivity is consistently higher at point 4 with respect to point 3. This is to be expected, as it is the same case as the northernmost dam. As the water from the dam has travelled through additional subterranean mineral, it becomes charged even further with leached metals in solution.

Secondly, the chemical composition of the liquid at point 4 was monitored every two weeks, throughout a whole natural year. The samples were scanned for heavy metals, by analysis with ICP-MS, and the average levels were calculated. These values are presented thus:

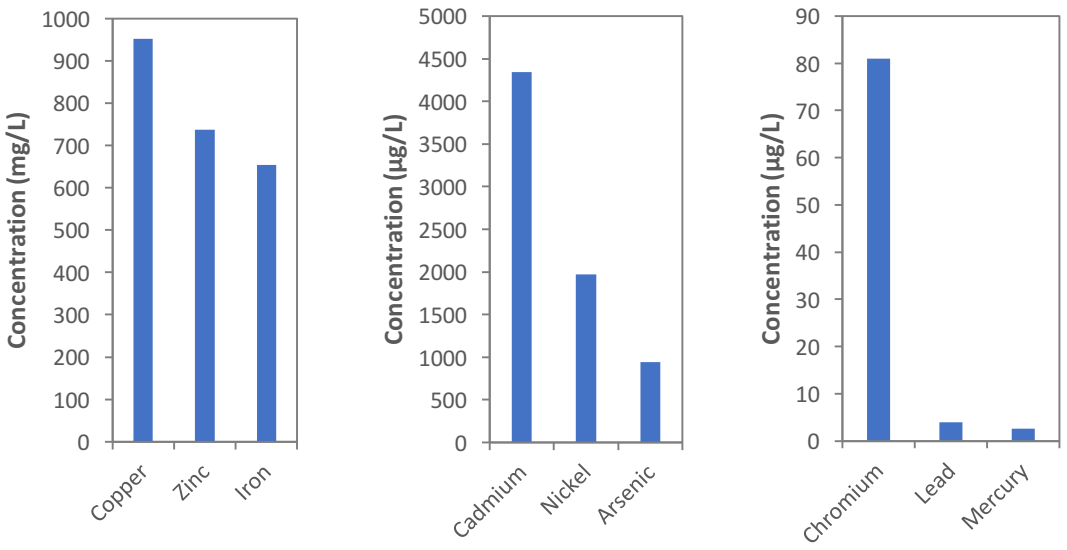

Figure 33: Graphs showing the average levels of copper, zinc, iron, cadmium, nickel, arsenic, chromium, lead and mercury in solution at point 4, from June 2015 until May 2016.

As was the case for the filtration from the northernmost dam, the levels of metals in solution at point 4 are considerably higher than those at point 3, with the exception of arsenic and lead. The rationale for this observation is, again, that the water from the dam has travelled through more mineral, thereby being charged with additional quantities of leached metals in solution.

The metals present in higher concentrations are copper, zinc and iron (average concentrations of 952 vs 614 mg/L, 737 vs 484 mg/L and 658 vs 352 mg/L, respectively), followed by cadmium (4,343 vs 2,838 µg/L) and nickel (3,970 vs 2,816 µg/L). The minority elements, present in lower concentrations, are arsenic

(944 vs 1,241 µg/L), chromium (81 vs 60 µg/L), lead (4 vs 5 µg/L) and mercury (2,6 vs 0.5 µg/L). The full sampling results for the bimonthly evolution of total copper, zinc, iron, arsenic, lead and mercury as well as the quarter-yearly evolution of cadmium, nickel and chromium in solution at point 4, from June 2015 until May 2016, are presented in figure A4 of the Appendix.

Despite being slightly delayed due to the lag time to filter through the dam, the levels of metals in solution are again negatively correlated with pluvial precipitations while positively correlated with temperatures (particularly during the warmer, drier months of the year), as can be seen by comparing the recorded evolution of metals in solution throughout the year (figure A4 of the Appendix) with the levels of rain (Table 7) and temperatures (Table 8).

It is also worth noting that the levels of metals in solution at the southernmost dam are considerably higher than those at the northernmost dam. This reflects the more acute acid mine drainage phenomenon that takes place at the southernmost dam, which is characterised by a lower pH as well as a higher electrical conductivity than its counterpart (probably as a result of different surrounding mineralogy).

The oxidation state of the ferric/ferrous ion couple was again monitored by analysing the levels of each ion in solution, as presented below:

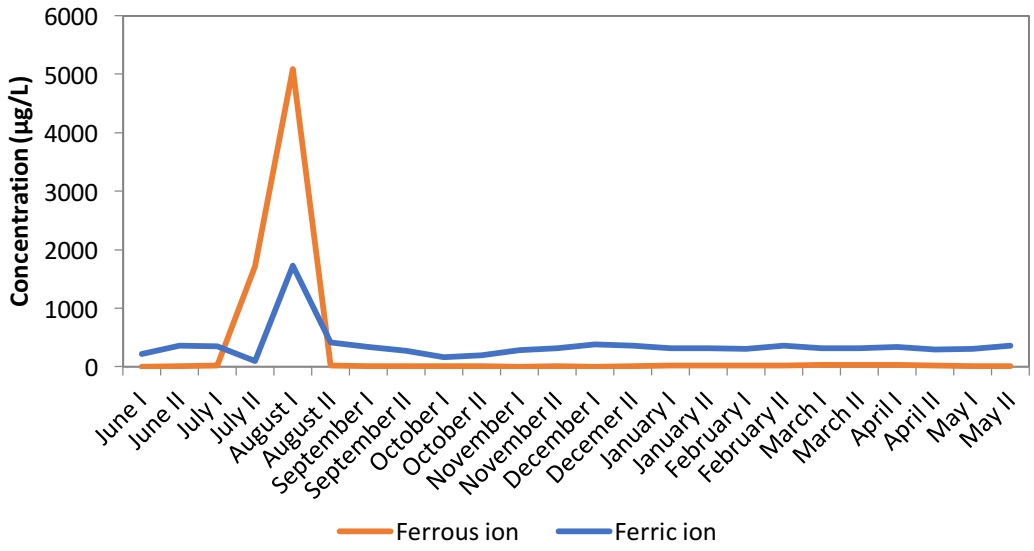

Figure 34: Graph showing the bimonthly evolution of ferric (blue) and ferrous (red) ion in solution at point 4, from June 2015 until May 2016.

The average balance of ferric ion with respect to total iron for the year is 0.89. As is the case for point 2 with respect to point 1, the ferric/ferrous ion couple is less oxidised at point 4 than at point 3, since the liquid has been travelling underground, where oxygen is virtually unavailable.

The toxicity index of this point at each trimester is shown below:

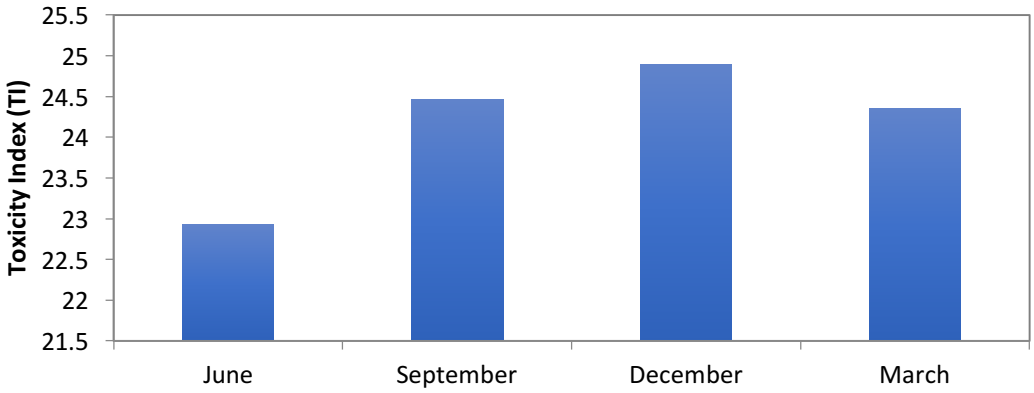

Figure 35: Graph showing the Toxicity Index of point 4 in June 2015, September 2015, December 2015 and March 2016.

Again, dissolved oxygen was measured at this point, as shown in the following graph:

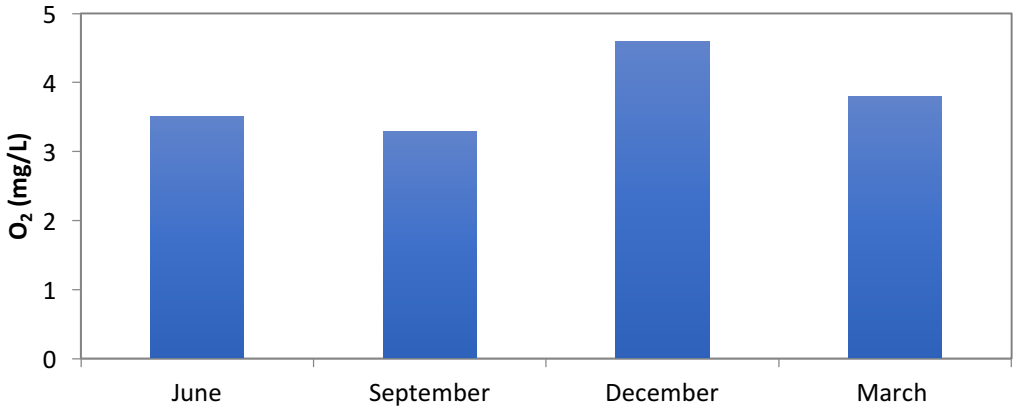

Figure 36: Graph representing dissolved oxygen (mg/L) at point 4 in June 2015, September 2015, December 2015 and March 2016.

The average dissolved oxygen throughout the year is 3.8 mg/L, with the highest value being recorded in December (4.6 mg/L) and the lowest value being noted in September (3.3 mg/L). Such levels are lower than those observed at point 3, it would appear that for the same reason as point 2 values being lower than point 1.

- Point 5

Point five is located at a filtration stream that proceeds from the southernmost dam, which passes through the old cementation plant. This facility was used to treat leached ore solutions containing high quantities of copper and iron in solution, the

remainders of which have precipitated as sulphate salts over the years. For this reason, the liquid at this point is charged with a high concentration of these metals.

Its coordinates are the following:

- Latitude: 37°42'50.65"N
- Longitude: 6°34'5.98"O

Again, a series of physicochemical parameters were monitored at point 5. In first place, pH and electrical conductivity were measured each two weeks throughout a year. These are illustrated in the following graphs:

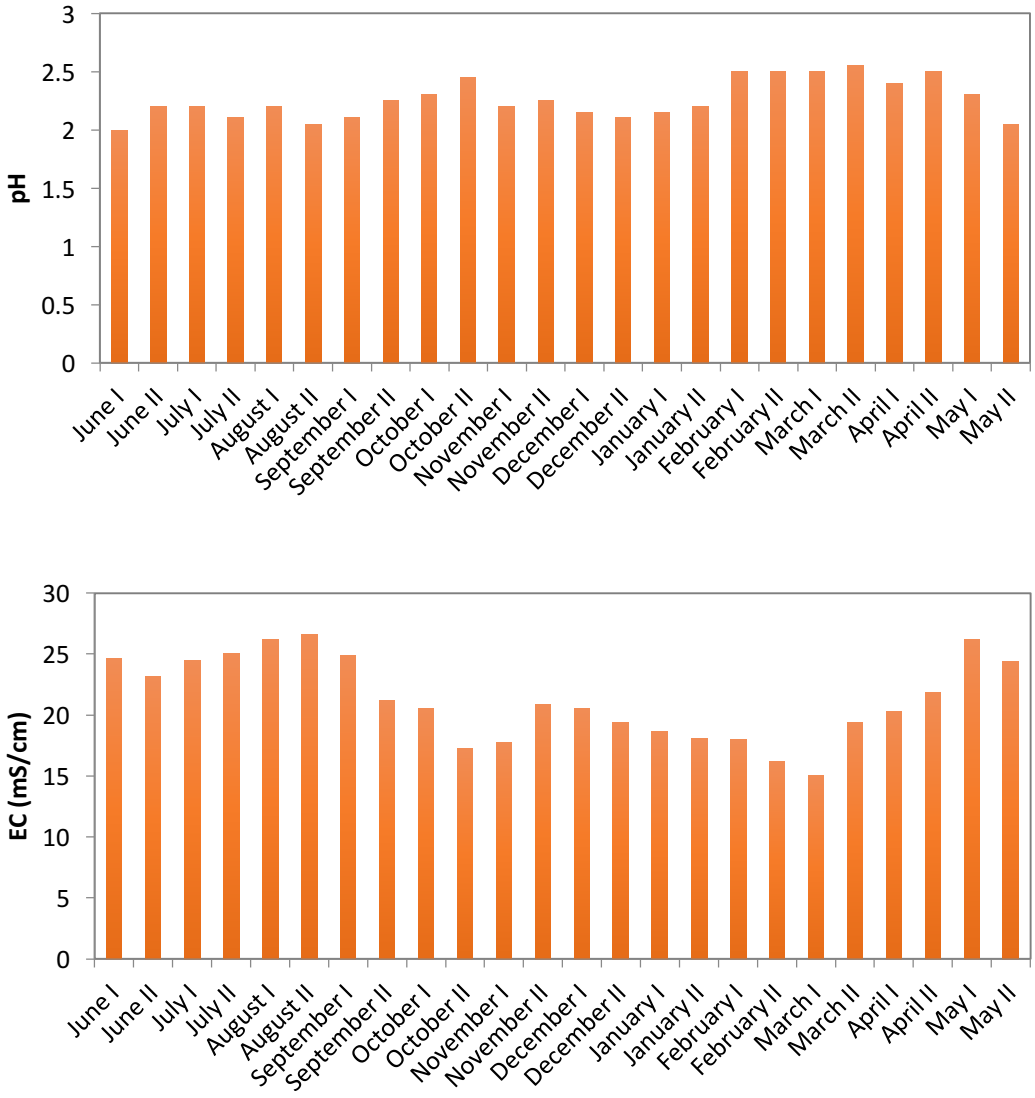

Figure 37: Graphs showing the bimonthly evolution of pH (top) and electrical conductivity (bottom) at sampling point 5, from June 2015 until May 2016.

The average pH at this site is 2.3, with the lowest and highest values being 2.0 and 2.6, respectively. The observed pH displays a larger variation than that of the previous points, possibly due to the larger impact of pluvial precipitations at this site. In turn, the average value for electrical conductivity is 21.3 mS/cm, with a maximum of 26.6 mS/cm and a minimum of 15.1 mS/cm. It is owrth noting that the physicochemical conditions at this point are the harshest of the North Slagheap drainage area; it exhibits the lowest pH values while displaying the highest electrical conductivity, linked with higher amounts of metals in solution, as presented below.

The chemical composition of point 5 was sampled every two weeks, as usual throughout a whole natural year. The liquid was scanned for heavy metals, by analysis with ICP-MS. The results of the average metal concentrations are presented thus:

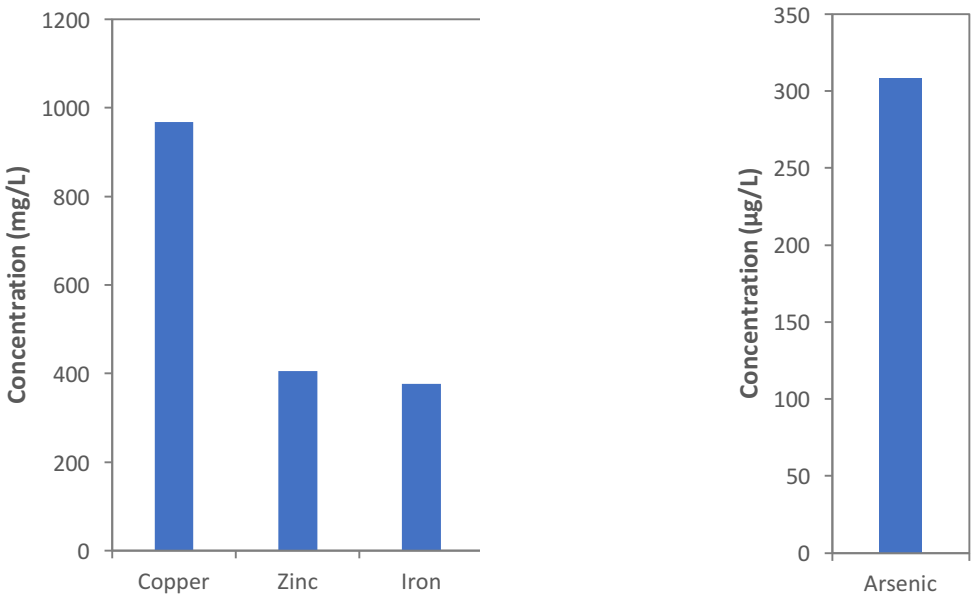

Figure 38: Graphs showing the average levels of total iron, copper, zinc and arsenic at point 5, from June 2015 until May 2016.

The metals present in higher concentrations are copper, zinc and iron (average concentrations of 968 mg/L, 405 mg/L and 377 mg/L, respectively). The minority element, present in lower concentrations, is arsenic (average of 308 µg/L). The other metals that usually appear in solution, i.e. chromium, lead and mercury, were detected at negligible concentrations (< 2 µg/L). This is due to the fact that the metals present in the old cementation plant are essentially those bared by the treated ore of interest, which contains copper and iron, and is often associated with zinc and arsenic. The complete graphs showing the bimonthly evolution of total iron, copper, zinc and arsenic at point 5, from June 2015 until May 2016, can be found in figure A5 of the Appendix.

The levels metals in solution are again negatively correlated with pluvial precipitations, as seen by comparing both sets of values (figure A5 from the Appendix with Table 7).

The oxidation state of the ferric/ferrous ion couple was again monitored by analysing the levels of each ion in solution, as presented below:

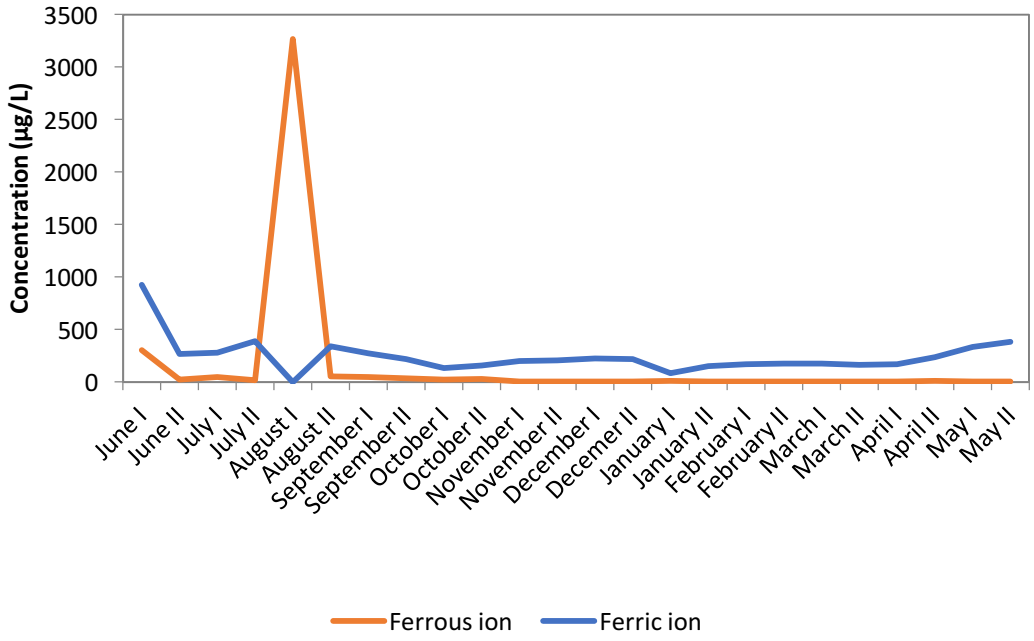

Figure 39: Graph showing the bimonthly evolution of ferric (blue) and ferrous (red) ion in solution at point 5, from June 2015 until May 2016.

The average balance of ferric ion with respect to total iron for the year is 0.88. Hence, the ferric/ferrous ion couple is notably oxidised at this site, with ferric ion constituting the predominant species.

The toxicity index of this point at each trimester is shown below:

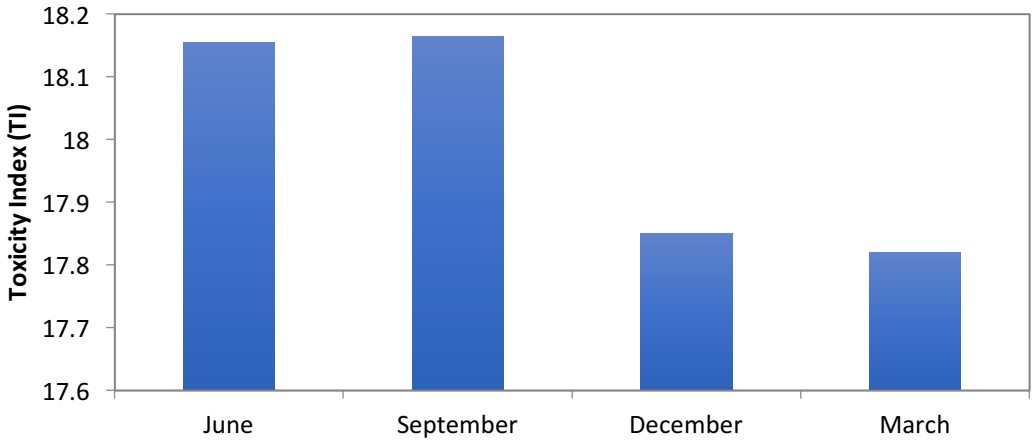

Figure 40: Graph illustrating the Toxicity Index of point 5 at June 2015, September 2015, December 2015 and March 2016.

Again, dissolved oxygen was measured at this point, as shown in the following graph:

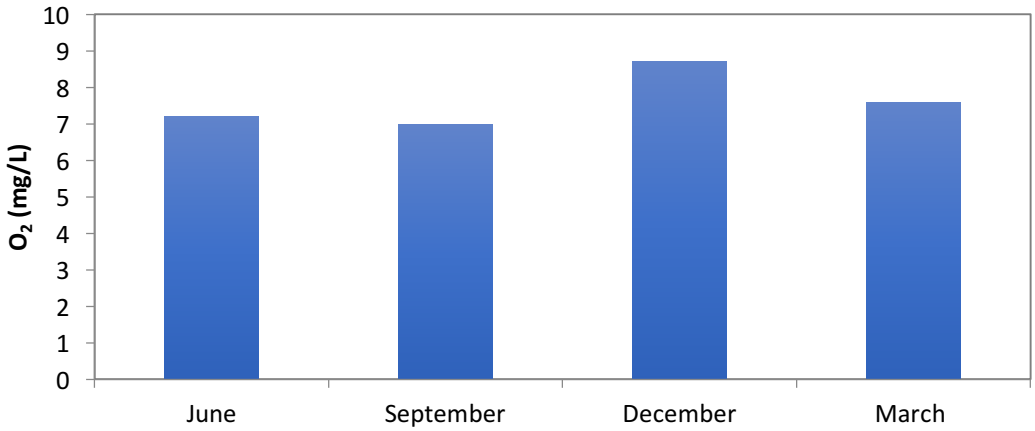

Figure 41: Graph representing dissolved oxygen (mg/L) at point 5 in June 2015, September 2015, December 2015 and March 2016.

The average dissolved oxygen throughout the year is 7.6 mg/L, with the maximum value being recorded in December (8.7 mg/L) and the lowest value being noted in September (7.0 mg/L).

The values of dissolved oxygen observed at this site are the highest recorded among all of the sampling stations, due to it being a shallow emplacement that is exposed to air.

Area B: Tunnel 5 and North Slagheap drainage

Tunnel 5 is an abandoned tunnel that was initially built by the Rio Tinto mining company at the end of the 19th century, and was used to transport mineral from the Lago open pit to a smelting facility in Huelva.

There is an acid mine drainage effluent that travels through tunnel 5, which is of great interest, as it is the most extreme point from a physicochemical perspective at which microorganisms are observed from the Rio Tinto ecosystem sampled so far. That is, it displays the lowest average and minimum pH values out of all the sampling sites where evidence of the presence of microorganisms is found (logically accompanied with very high heavy metal levels in solution as well as electrical conductivity). Therefore, this emplacement deserves particular attention, as the ultimate aim of this study consists in using the microorganisms found at this site as the biological material in a BPV cell.

The following three sampling points were established in this area: At the exit of Tunnel 5 (point 6), at a stream from North Slagheap filtrations that is to merge with the Tunnel 5 effluent (point 7) and a point downstream of the merging of the Tunnel 5 effluent and the North Slagheap filtration.

Figure 42: Map showing the three sampling points at the Tunnel 5 and North Slagheap drainage area.

In this area, living biofilms were detected at points 6 and 8. However, no biofilms were detected at point 7.

Information about the three sampling points is presented thus:

- Point 6

Point six is located at the exit of Tunnel 5. The effluent travelling across this tunnel originates from the Lago open pit, which is flooded.

Its coordinates are the following:

- Latitude: 37°42'23.71"N
- Longitude: 6°34'2.39"O

A series of physicochemical parameters were measured at this point. Firstly, pH and electrical conductivity were recorded on a fortnightly basis throughout the year of sampling. These are illustrated in the following graphs:

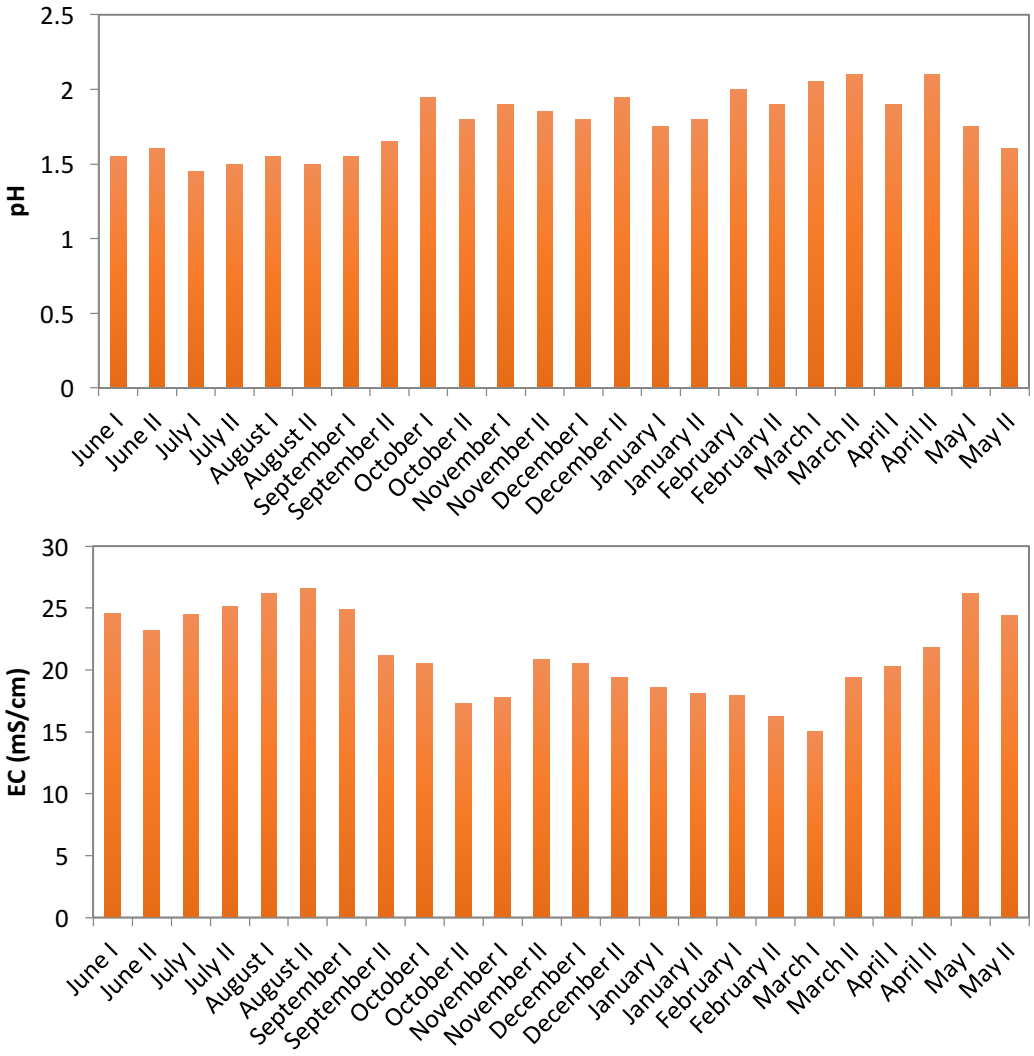

Figure 43: Graphs showing the bimonthly evolution of pH (top) and electrical conductivity (bottom) at sampling point 6, from June 2015 until May 2016.

The average pH is 1.8, with the lowest and highest values being 1.45 and 2.1, respectively. This location is of enormous interest; it is the most acidic out of all the sampled points. Moreover, the fact that it bears microbial life makes it a unique location in the whole planet.

In turn, the average value for electrical conductivity is 19.6 mS/cm, with a highest value of 26.2 mS/cm and a lowest value of 15.14 mS/cm.

As usual, both of these results may be interpreted by looking at pluvial precipitations as well as temperatures (pH is positively correlated to pluvial precipitations while electrical conductivity displays a negative correlation, and the opposite is true for temperatures).

Secondly, the chemical composition of the liquid at this point was monitored every two weeks, throughout the natural year of this study. The samples were analysed for heavy metals, by analysis with ICP-MS, and the average values were calculated. These are presented thus:

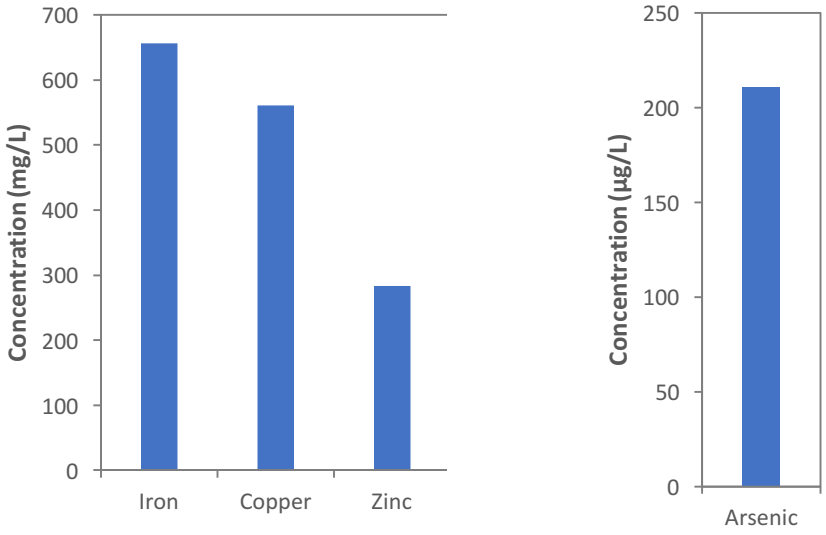

Figure 44: Graphs showing the average levels of total iron, copper, zinc and arsenic at point 6, from June 2015 until May 2016.

The metals present in higher concentrations are iron, copper and zinc (average concentrations of 656 mg/L, 561 mg/L and 283 mg/L, respectively). The minority element is arsenic, with 211 µg/L. The other elements that are often present (i.e. cadmium, nickel, chromium, lead and mercury) were detected in negligible quantities (<1 µg/L). The full results for the bimonthly evolution of total iron, copper, zinc and arsenic at point 6, from June 2015 until May 2016, can be found in figure A6 of the Appendix. Again, the levels of metals in solution are negatively correlated with pluvial precipitations (seen by comparing metal levels in solution in figure A6 of the Appendix and pluvial precipitations in Table 7).

The oxidation state of the ferric/ferrous ion couple was again monitored by analysing the levels of each ion in solution, as presented below:

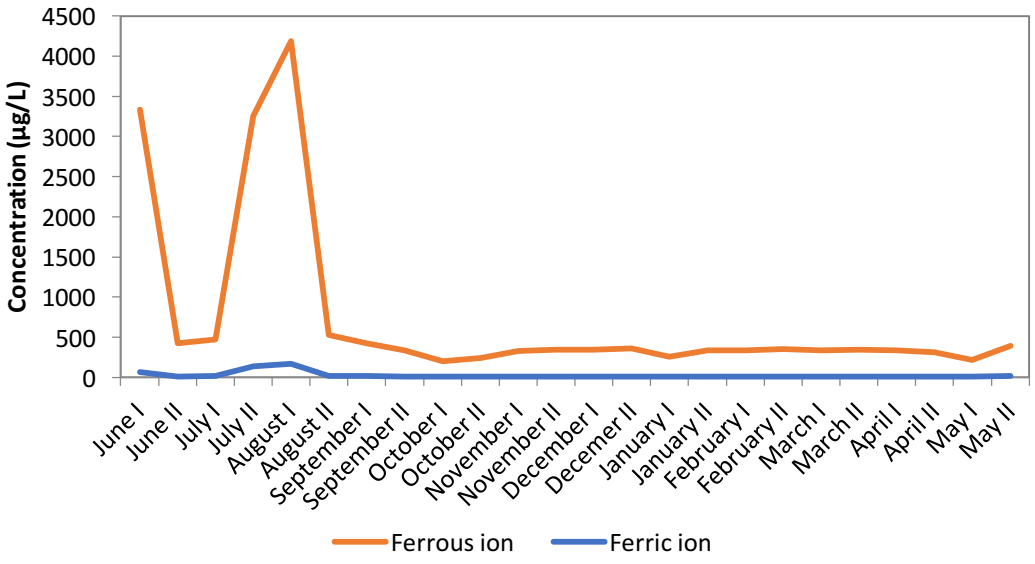

Figure 45: Graph showing the bimonthly evolution of ferric (blue) and ferrous (red) ion in solution at point 6, from June 2015 until May 2016.

The average balance of ferric ion with respect to total iron for the year is 0.03. This indicates that iron is almost totally present as ferrous ion, with ferric ion representing a minimal proportion of the total iron. This is the most reduced point out of all the sampling sites, which is coincides with the lowest pH.

The toxicity index of this point at each trimester is shown below:

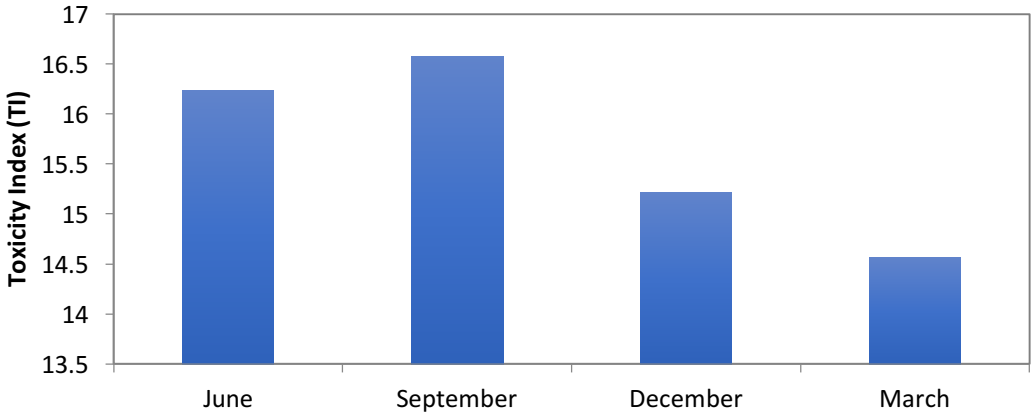

Figure 46: Graph showing the Toxicity Index of point 6 at June 2015, September 2015, December and March 2016.

Again, dissolved oxygen was measured at this point, as shown in the following graph:

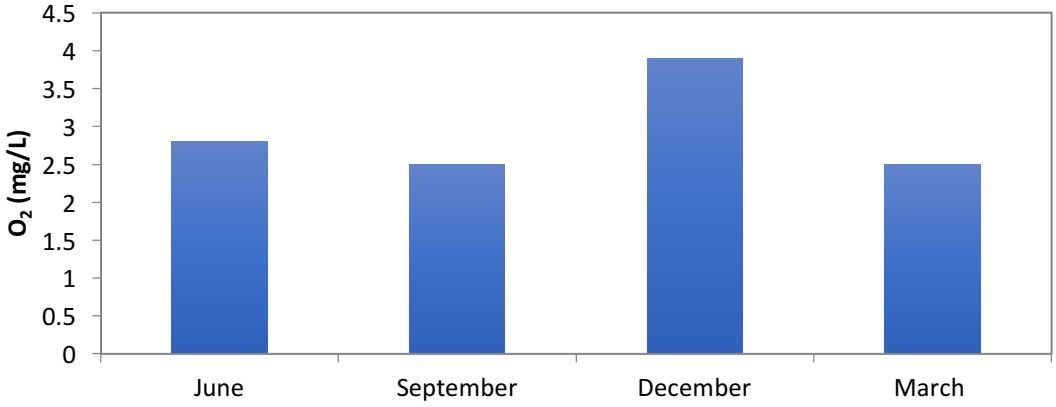

Figure 47: Graph showing dissolved oxygen (mg/L) at point 6 in June 2015, September 2015, December 2015 and March 2016.

The average dissolved oxygen throughout the year is 2.9 mg/L, with the highest value being recorded in December (3.9 mg/L) and the lowest value being noted in September (2.5 mg/L). These values are relatively low, reflecting the lack of air exposure of the stream upstream this point (tunnel 5).

- Point 7

Point seven is located at an effluent arising from North Slagheap drainage filtrations. It of interest because it merges with the stream exiting Tunnel 5, giving rise to a very peculiar microbial community.

Its coordinates are the following:

  - Latitude: 37°42'25.70"N
  - Longitude: 6°34'2.89"O

At this point, no evidence of microbial presence was found by confocal microscopy screening. Therefore, it was sampled with a reduced frequency (every three months).

First, pH and electrical conductivity were measured, as illustrated in the below graphs:

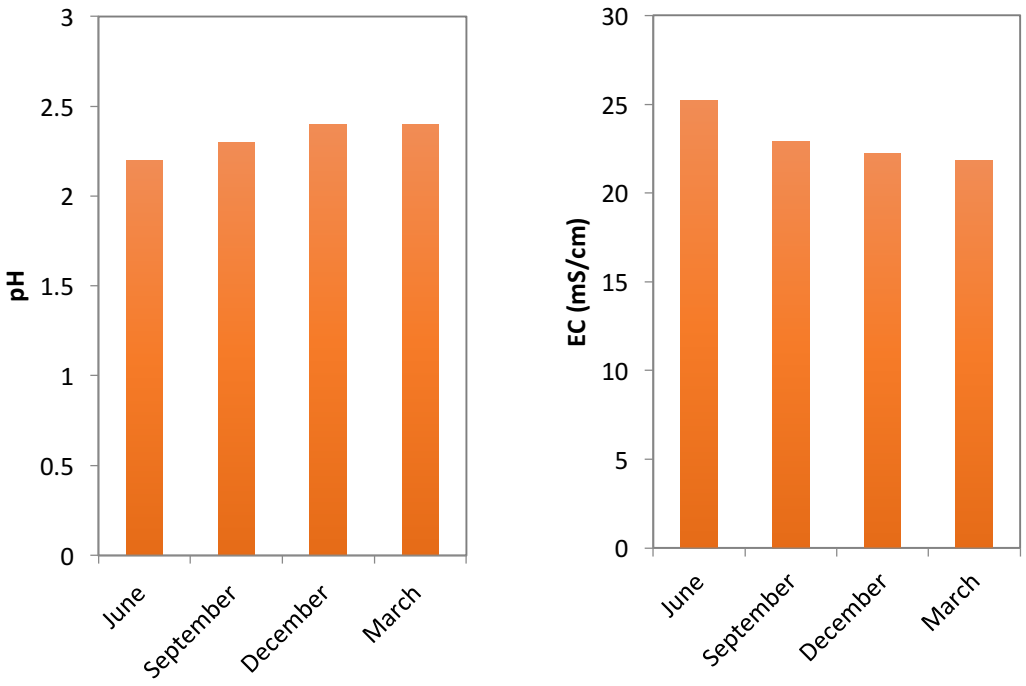

Figure 48: Graphs showing the trimestral evolution of pH (top) and electrical conductivity (bottom) at sampling point 7, displaying June 2015, September 2015, December 2015 and March 2016.

The average pH is 2.3; the lowest value is 2.2 in the summer season (June), while the winter (December) and spring (March) seasons are characterised by a higher pH of 2.4. This pattern is the same as that observed throughout the various sampling sites; drier spells are linked with higher concentration of protons in solution, while rainier times are associated with more dilute levels of protons in solution.

In turn, the average value for electrical conductivity is 23.0 mS/cm. It is not surprising that the highest levels of electrical conductivity occur in the summer (in June, with 25.2 mS/cm), when ions in solution are more concentrated. Conversely, the lowest levels occur in the spring season (21.8 mS/cm in March), when these are more diluted. This point displays the highest electrical conductivity out of all the sampled sites. Therefore, it is of enormous interest, as a key aim of this project consists in finding a biofilm that can withstand the highest possible electrical conductivity inside a Biophotovoltaic cell, in order to reduce its internal resistance as much as possible.

The pH and electrical conductivity measurements were accompanied by the analysis of the chemical composition of the liquid every three months. The samples were scanned for heavy metals by analysis with ICP-MS and the average levels calculated, as presented thus:

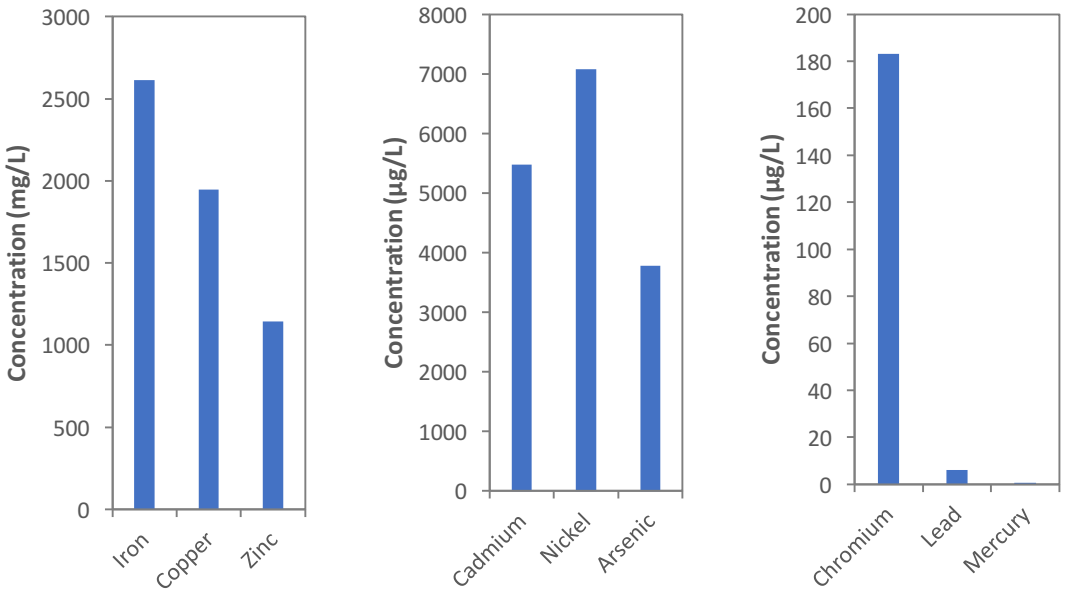

Figure 49: Graphs showing the average concentrations of total iron, copper, zinc, cadmium, nickel, arsenic, chromium, lead and mercury in solution at point 7, from June 2015 until March 2016.

The metals present in higher concentrations are iron, copper and zinc (average concentrations of 2,615 mg/L, 1,946 mg/L and 1,142 mg/L, respectively), followed by cadmium (5,475 µg/L) and nickel (7,075 µg/L). The minority elements, present in lower concentrations, are arsenic (3,775 µg/L), chromium (183 µg/L), lead (6 µg /L) and mercury (0.7 µg/L). The complete graphs showing the trimestral evolution of these metals in solution at point 7, showing June 2015, September 2015, December 2015 and March 2016, can be found in figure A7 of the Appendix.

As usual, the levels of metals in solution are negatively correlated with pluvial precipitations (figure A7 in the Appendix vs. Table 7), while the opposite trend is observed in comparison with temperatures (i.e. vs. Table 8).

Finally, the levels of metals at this point are considerably high, given the nature of the effluent origin.

As usual, the oxidation state of the ferric/ferrous ion couple was monitored, by analysing the levels of each ion in solution, shown below:

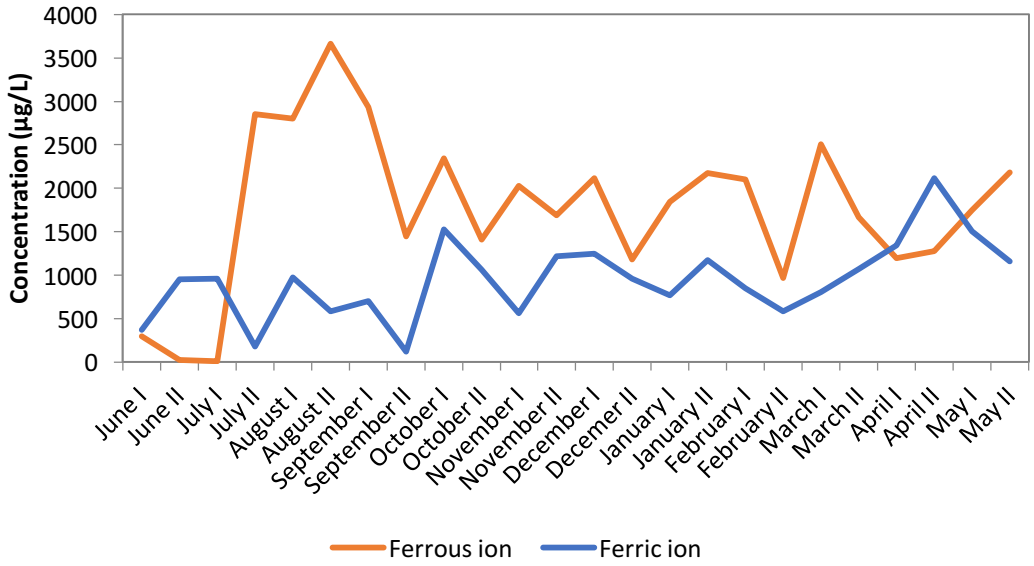

Figure 50: Graph illustrating the bimonthly evolution of ferric (blue) and ferrous (red) ion in solution at point 7, from June 2015 until May 2016.

The average balance of ferric ion with respect to total iron for the year is 0.41. This indicates that total iron is split almost equally between ferric and ferrous ion.

The toxicity index of this point at each trimester is shown thus:

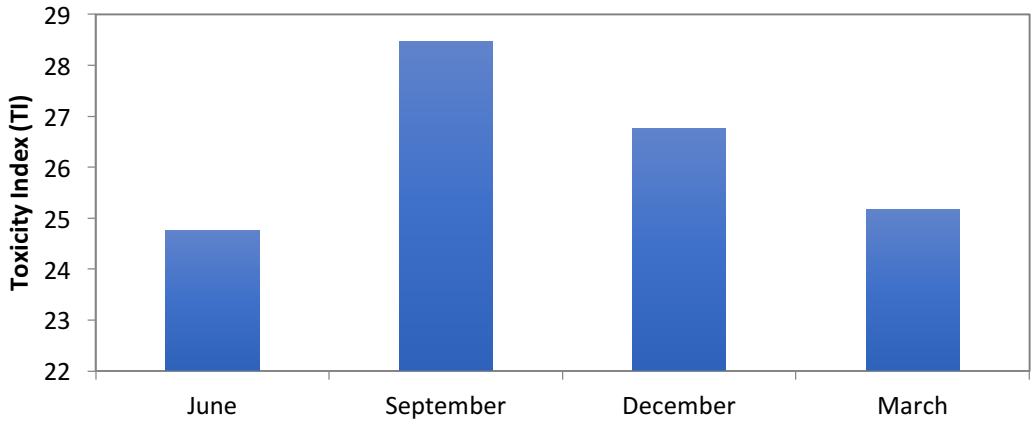

Figure 51: Graph showing the Toxicity Index of point 7 at June 2015, September 2015, December and March 2016.

Again, dissolved oxygen was measured at this point, as illustrated in the following graph:

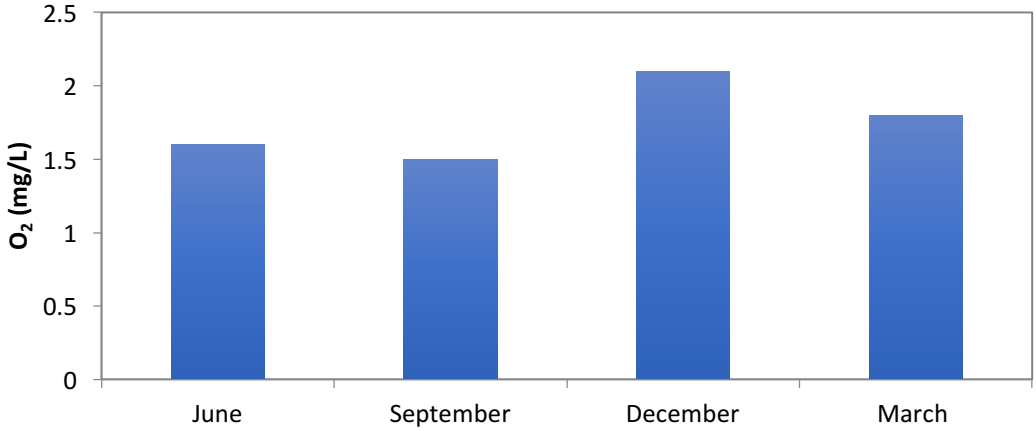

Figure 52: Graph showing dissolved oxygen (mg/L) at point 7 in June 2015, September 2015, December 2015 and March 2016.

The average dissolved oxygen throughout the year is 1.75 mg/L, with the highest value being recorded in December (2.1 mg/L) and the lowest value being noted in September (1.5 mg/L). These values are the lowest out of all the sampled points.

- Point 8

Point eight is located downstream of the confluence between the effluents coming from points 6 and 7. Its coordinates are the following:

  - Latitude: 37°42'25.19"N
  - Longitude: 6°33'54.70"O

In first place, pH and electrical conductivity were measured at this site on a fortnightly basis throughout a natural year, as presented in the following graphs:

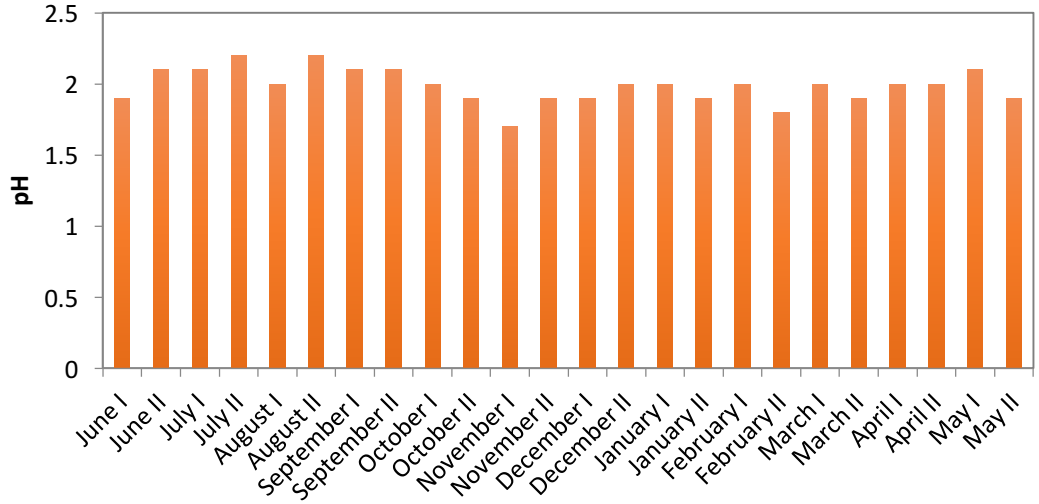

Figure 53: Graph showing the bimonthly evolution of pH at sampling point 8, from June 2015 until May 2016.

The average pH is 2.0, with the lowest and highest values being 1.70 and 2.20, respectively. This point displays the second lowest pH out of all the sampled sites. It is not as low as the effluent from tunnel 5, given that it is a mixture of it with the drainage filtrations that bear a slightly higher pH.

As is the case for the exit from tunnel 5, this site is rather unique in the entire planet, given its extreme acidity, in combination with the elevated electrical conductivity. It is particularly interesting due to the finding that the microbial diversity present at this site includes that found at the exit of tunnel 5, yet the mixture with the drainage effluent additionally gives rise to a whole new suite of microorganisms. All these coexist, forming incredibly peculiar biofilms within a truly exceptional ecosystem.

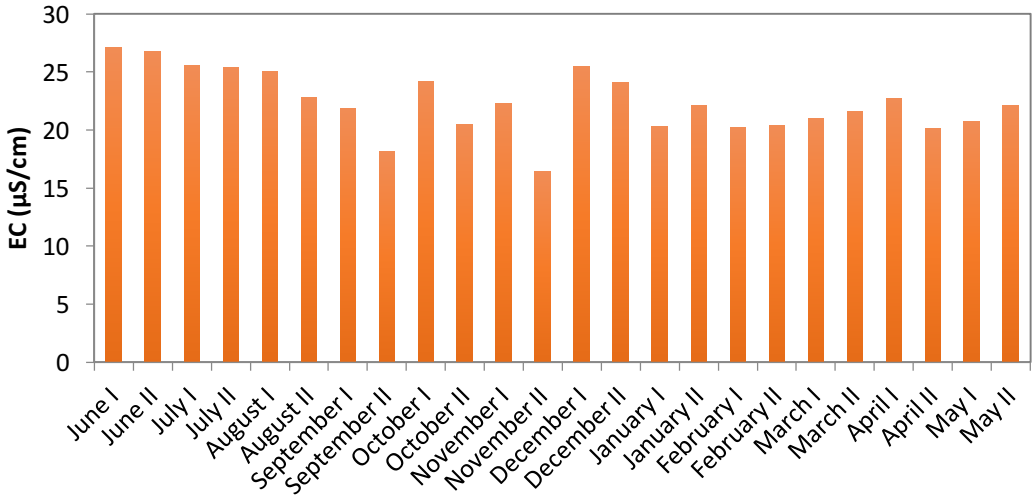

Figure 54: Graph illustrating the bimonthly evolution of electrical conductivity at sampling point 8, from June 2015 until May 2016.

In turn, the average value for electrical conductivity is 22.4 mS/cm. A larger variation is observed in comparison to pH, with a highest value of 27.10 mS/cm and a lowest value of 16.40 mS/cm. These figures are an indicator of the extremely high ionic content of the liquid, both due to metal content as well as acidity.

Therefore, this site has a great potential for harvesting biofilms of interest that could thrive in extreme physicochemical conditions within a Biophotovoltaic platform, as sought in this study.

As usual, the evolution of these two parameters can be understood by looking at pluvial precipitations (Table 7) as well as temperatures (Table 8). This is particularly important in order to identify the times of the year at which biofilms can be harvested when the physicochemical conditions are most extreme.

Secondly, the chemical composition of the liquid at this point was monitored every two weeks throughout the whole natural year of testing, and the samples were scanned for a series of heavy metals, by analysis with ICP-MS. The average levels of these metals are presented thus:

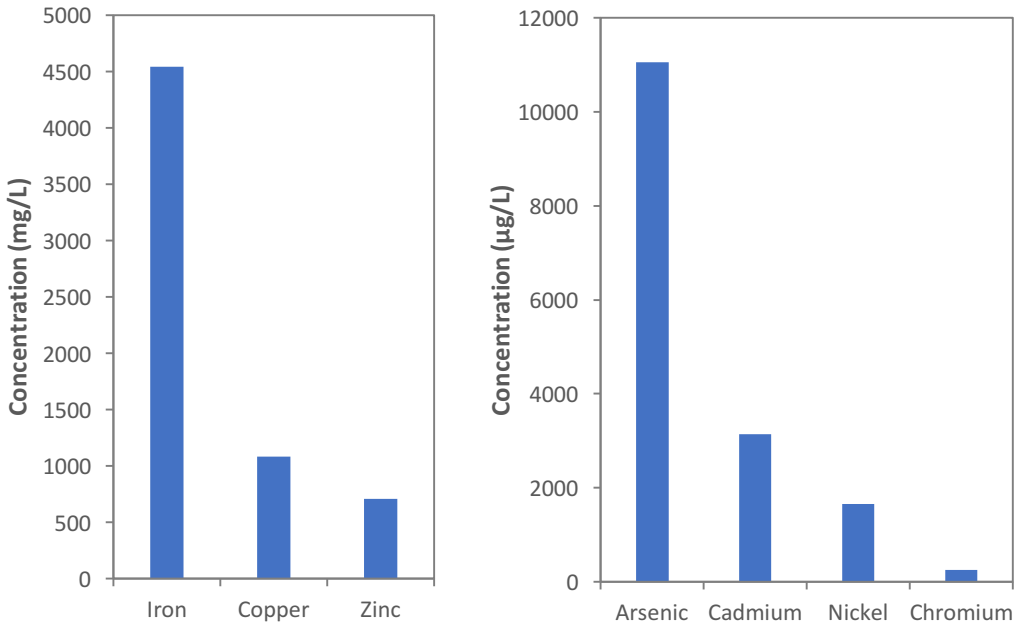

Figure 55: Graphs showing the average levels of total iron, copper, zinc, arsenic, cadmium, nickel and chromium in solution at point 8, from June 2015 until May 2016.

As the effluent from tunnel 5 merged and was mixed with the stream proceeding from the filtration drainage in this area, the levels of metals in solution at this site lie between those recorded for each of its components (i.e. points 6 and 7).

It is worth noting that this point bears the second highest overall levels of metals in solution and is therefore of great interest, given its extreme acidity as well.

The metals present in higher concentrations at this site are iron, copper and zinc (average concentrations of 4,538 mg/L, 1,080 mg/L and 709 mg/L, respectively). These are followed by arsenic (11,055 µg/L), cadmium (3,147 µg/L), nickel (1,654 µg/L) and chromium (253 µg/L).

The full results for the bimonthly evolution of total iron, copper, zinc and arsenic and the quarter-yearly evolution of cadmium, nickel and chromium in solution at point 8, from June 2015 until May 2016, are recorded in figure A8 of the Appendix.

Finally, the levels of metals in solution are as usual negatively correlated with pluvial precipitations and positively so with temperatures, as seen again by comparing both sets of values (i.e. figure A7 from the Appendix with Table 7 and Table 8). This is an essential factor in order to determine when best to harvest the biofilms for use in the Biophotovoltaic device.

In addition, the oxidation state of the ferric/ferrous ion couple was monitored, as usual, by analysing the levels of each ion in solution, as shown in the following graph:

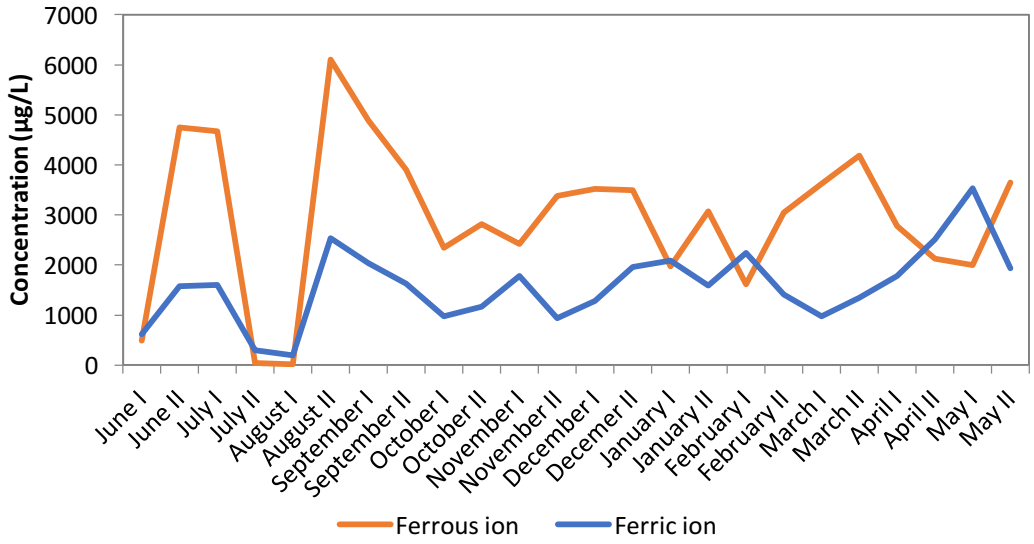

Figure 56: Graph showing the bimonthly evolution of ferric (blue) and ferrous (red) ion in solution at point 8, from June 2015 until May 2016.

The average balance of ferric ion with respect to total iron for the year is 0.35. This reflects the mixture between the effluent exiting tunnel 5, which is extremely reduced, and the more oxidised stream proceeding from the drainage of filtrations.

The toxicity index and dissolved oxygen of this point at each trimester are shown below:

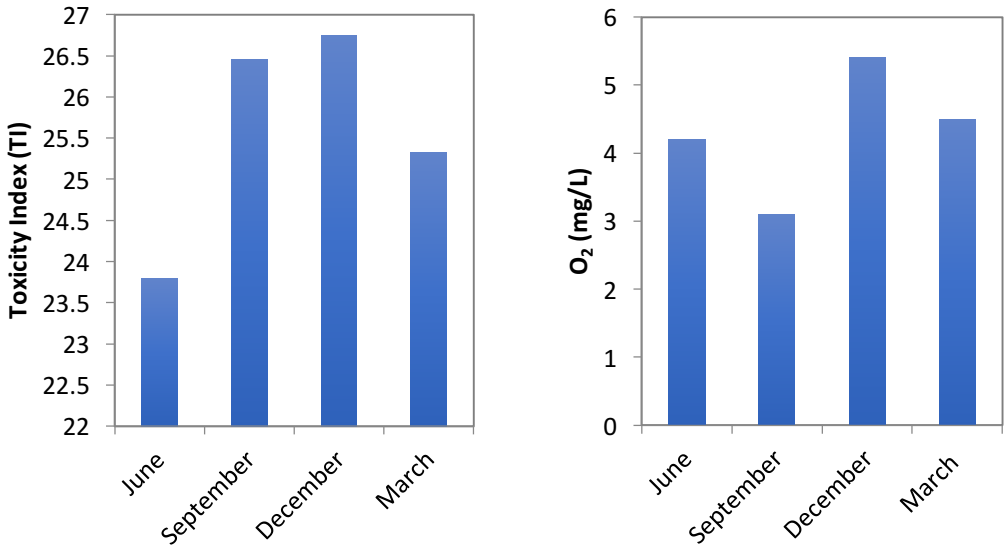

Figure 57: Graph showing the Toxicity Index (left) and dissolved oxygen (mg/L) of point 8 at June 2015, September 2015, December 2015 and March 2016.

The average dissolved oxygen throughout the year is 4.3 mg/L, with the highest value being recorded in December (5.4 mg/L) and the lowest value being noted in September (3.1 mg/L). These levels are higher than those observed at points 6 and 7, as a consequence of point 8 being downstream of a course exposed to air.

Area C: Tunnel 11, North Slagheap drainage and train area

Like tunnel 5, tunnel 11 is an old, abandoned tunnel that was initially built by the Rio Tinto mining company at the end of the 19th century, with the purpose of transporting mineral from the Cerro Colorado open pit to a smelting facility in Huelva. An acid mine drainage stream now that travels through tunnel 11, bearing highly acidic water that contains high levels of metals, despite which a very rich microbial ecosystem is observed.

Four sampling points were established in this area, at the effluent coming from Tunnel 11 by the old train station (point 9), downstream of point 9 after a stream of residual waters merges with the effluent with Tunnel 11 (point 10), downstream the effluent coming from Tunnel 11 after it has merged with North Slagheap filtration drainages (point 11) and downstream point 11, by the new train station (point 12).

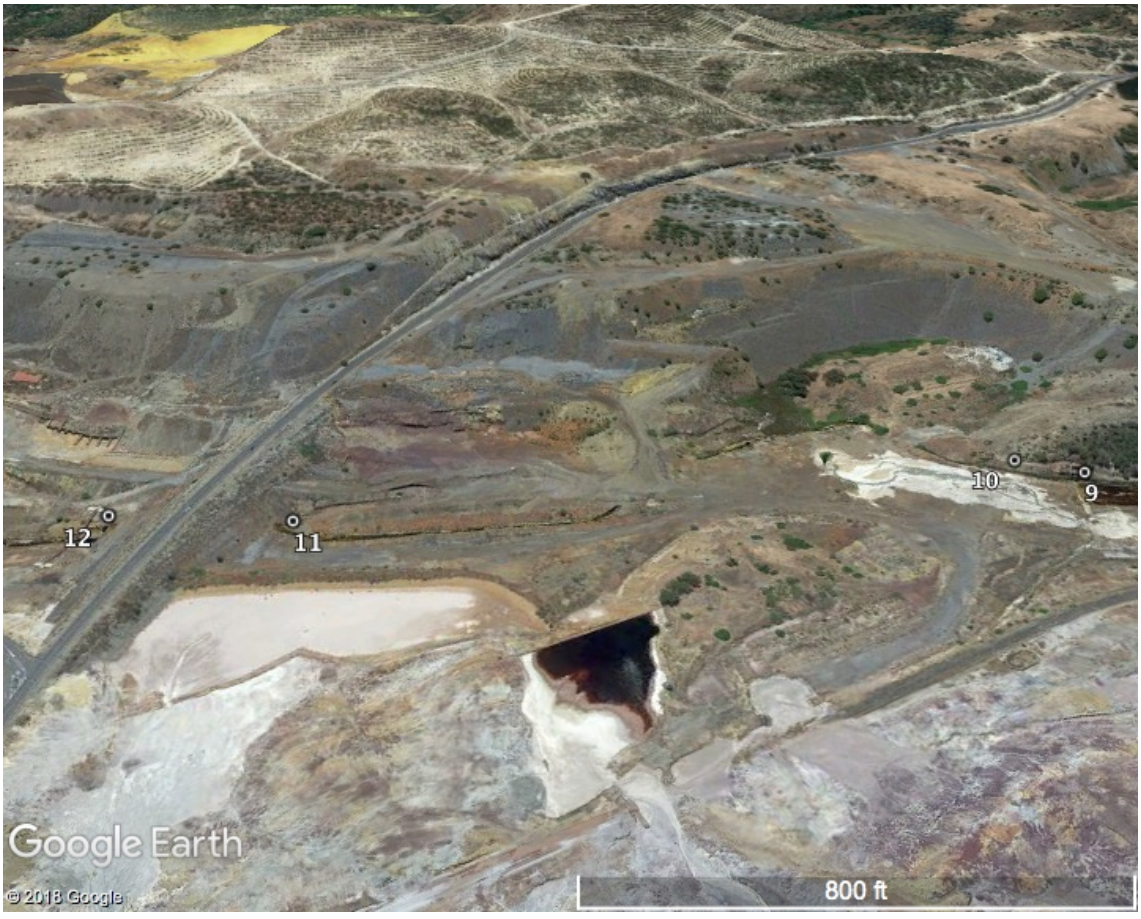

Figure 58: Map showing the four sampling points at the Tunnel 11 and North Slagheap drainage and train area.

In this area, living biofilms were detected at all points.

Information about the three sampling points is presented as follows:

- Point 9

Point nice is located at an effluent proceeding from Tunnel 11, by the old train station, where mineral used to be loaded onto trains back in the early 20th century.

Its coordinates are the following:

- Latitude: 37°41'33. 94"N
- Longitude: 6°34'17. 29"O

A series of physicochemical parameters were measured every two weeks throughout the whole year of sampling at this point. Firstly, pH and electrical conductivity were recorded, as illustrated in the following graphs:

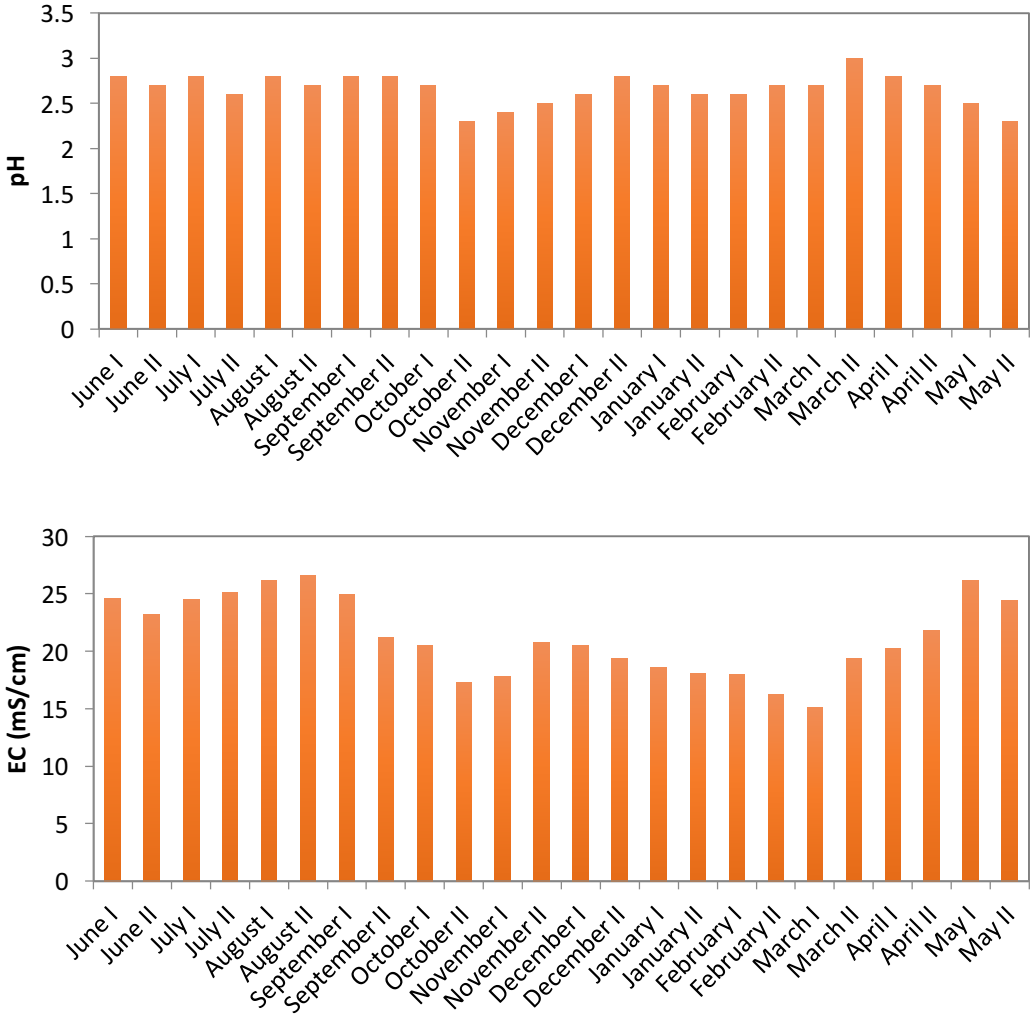

Figure 59: Graphs showing the bimonthly evolution of pH (top) and electrical conductivity (bottom) at sampling point 9, from June 2015 until May 2016.

The average pH is 2.7, with the lowest and highest values being 2.3 and 3.0, respectively.

In turn, the average value for electrical conductivity is 17.9 mS/cm, with maximum and minimum values of 11.0 mS/cm and 15.1 mS/cm, respectively.

Both of these results may be interpreted by looking at pluvial precipitations (Table 7) and temperatures (Table 8), given that they follow the same pattern as the rest of the sites. That is, both pH and electrical conductivity are correlated to pluvial precipitations and temperatures; pH displays a positive correlation to precipitations while electrical conductivity shows a negative correlation to these, and the opposite is observed with respect to temperatures.

Secondly, the chemical composition of the liquid at this point was monitored every two weeks, throughout the natural year of testing. The samples were scanned for a series of heavy metals, by analysis with ICP-MS, and the average levels throughout the year of sampling were subsequently calculated. These results are presented thus:

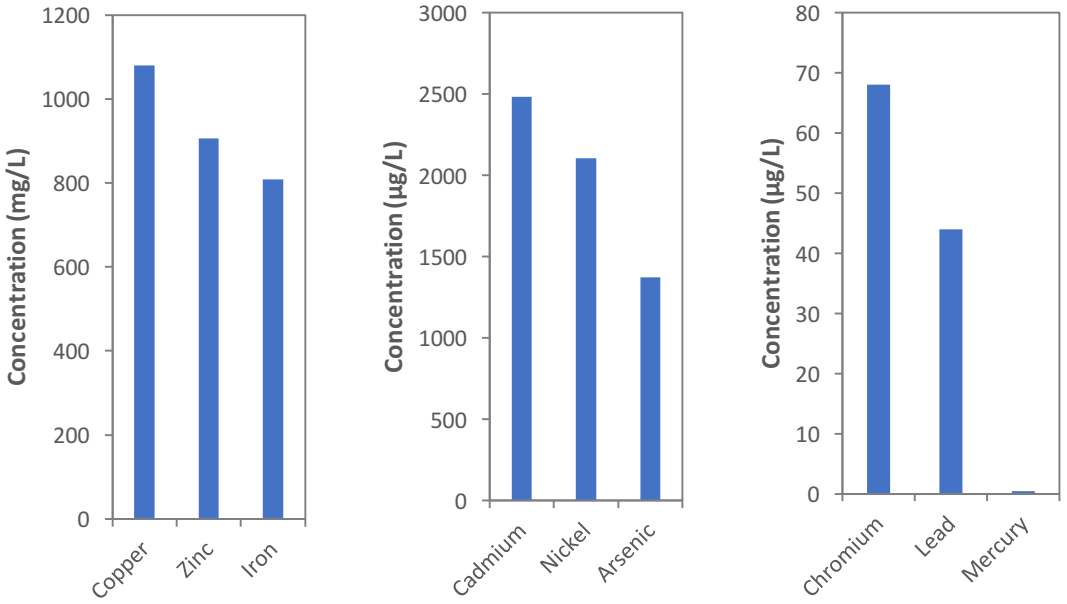

Figure 60: Graphs showing the average values of total copper, zinc, iron, cadmium, nickel, arsenic, chromium, lead and mercury at point 9, from June 2015 until May 2016.

The metals present in higher concentrations are copper, zinc and iron (average concentrations of 1,080 mg/L, 906 and 808 mg/L, respectively), followed by cadmium (2,484 µg/L), nickel (2,103 µg/L) and arsenic (1,373 µg/L). The minority elements, present in lower concentrations, are chromium (68 µg/L), lead (44 µg/L) and mercury (0.4 µg/L).

The full data for the bimonthly evolution of total iron, copper, zinc, arsenic, lead and mercury as well as the quarter-yearly evolution of cadmium, nickel and chromium in solution at point 9, from June 2015 until May 2016, is presented in figure A9 of the Appendix.

As usual, the levels of metals in solution are negatively correlated with pluvial precipitations and positively so with temperatures, as seen by comparing the concentrations of metals (figure A9 in the Appendix) with precipitations (Table 7) and temperatures (Table 8).

In addition, the oxidation state of the ferric/ferrous ion couple was monitored, as usual, by analysing the levels of each ion in solution, as shown below:

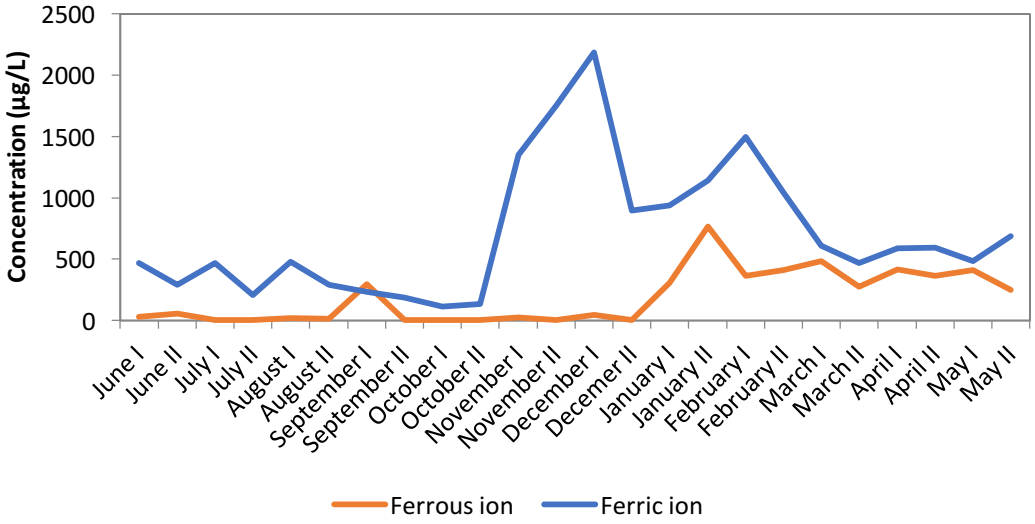

Figure 61: Graph showing the bimonthly evolution of ferric (blue) and ferrous (red) ion in solution at point 9, from June 2015 until May 2016.

The average proportion of ferric ion with respect to the total iron in solution is 0.83. This indicates a rather highly oxidised state of the ferric/ferrous ion couple, where ferric iron constitutes the predominant species.

The toxicity index and dissolved oxygen of this point at each trimester are shown below:

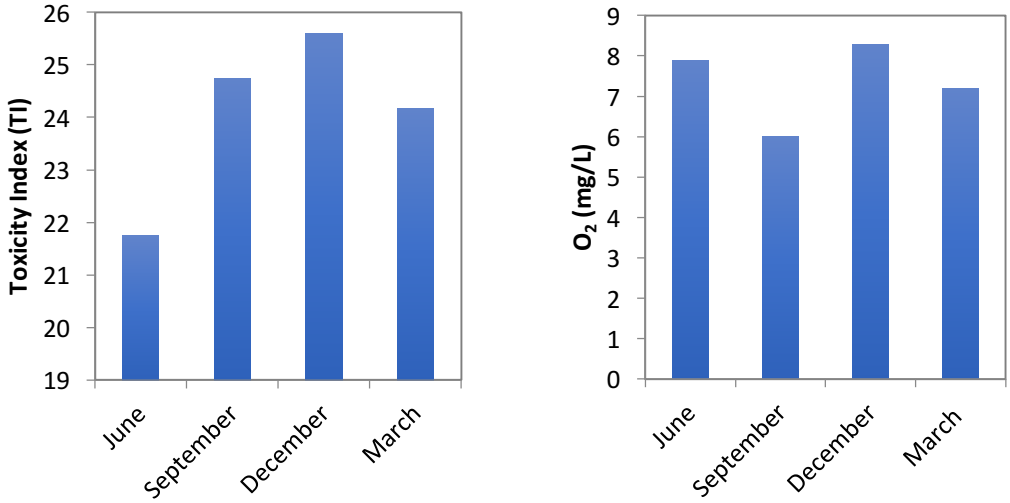

Figure 62: Graphs illustrating Toxicity Index (left) and dissolved oxygen (right) at point 9 in June 2015, September 2015, December and March 2016.

The average dissolved oxygen throughout the year is 7.4 mg/L, with the highest value being recorded in December (8.3 mg/L) and the lowest value being noted in September (6.0 mg/L).

- Point 10

Point ten is located by the effluent proceeding from Tunnel 11, after a stream with residual waters has merged with it.

Its coordinates are the following:

  - Latitude: 37°41'32.84"N
  - Longitude: 6°34'15.99"O

As usual, physicochemical parameters were monitored at this point. First, pH and electrical conductivity were measured, as illustrated in the below graphs:

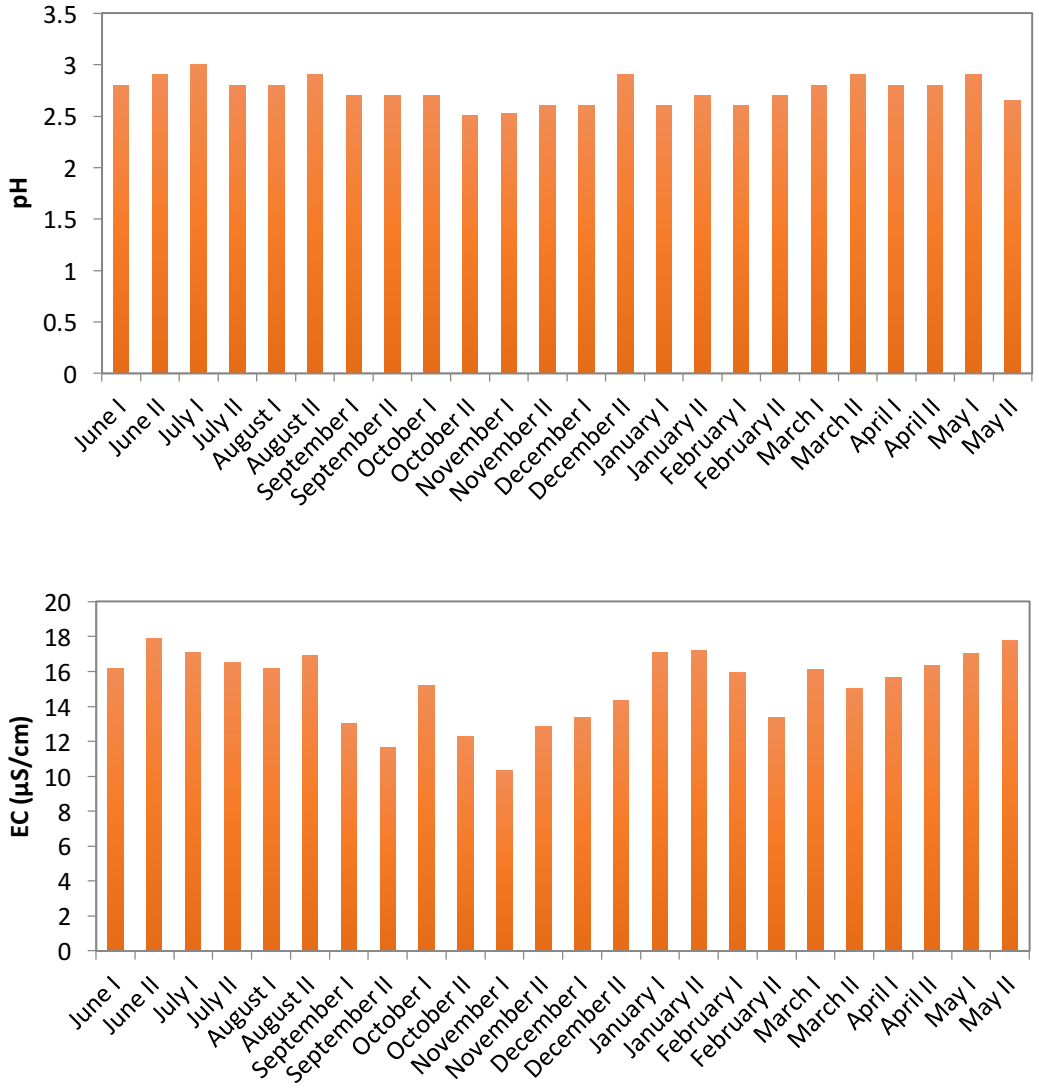

Figure 63: Graphs showing the bimonthly evolution of pH (top) and electrical conductivity (bottom) at sampling point 10, from June 2015 until May 2016.

The average pH is 2.8, with the lowest and highest values being 2.5 and 3.0, respectively. These values are higher than those for point 9, due to the influence of the residual water stream.

In turn, the average value for electrical conductivity is 17.2 mS/cm, with a highest value of 17.8 mS/cm and a lowest value of 10.3 mS/cm. As for pH, the electrical conductivity of Tunnel 11 is softened by the mixture with the residual water stream.

As usual, both of these results can be interpreted by looking at pluvial precipitations and temperatures (pH is positively correlated to pluvial precipitations while electrical conductivity displays a negative correlation, and the opposite can be said for temperatures).

Secondly, the chemical composition of the liquid at this point was monitored every two weeks, throughout the whole natural year of sampling. The site was assessed for the presence of heavy metals, by analysis with ICP-MS, and the average levels were calculated. These results are presented thus:

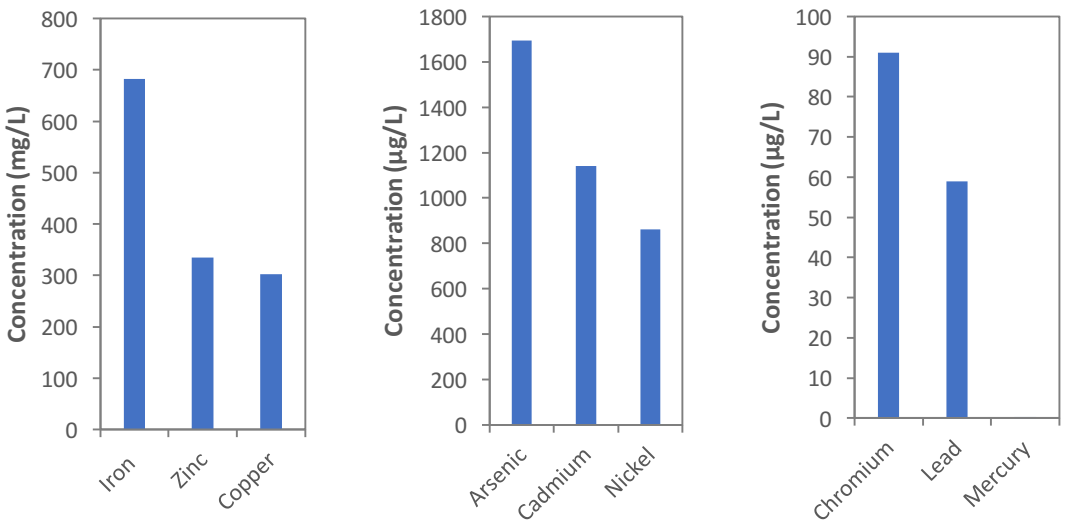

Figure 64: Graphs showing the average levels of total iron, zinc, copper, arsenic, cadmium, nickel, chromium, lead and mercury in solution at point 10, from June 2015 until May 2016.

The metals in solution at this point are considerably lower than those found at point 9; these are diluted with the stream of residual water. The metals present in higher concentrations are iron, zinc and copper (average concentrations of 683 mg/L, 335 mg/L and 303 mg/L, respectively), followed by arsenic (1,693 µg/L), cadmium (1,142 µg/L) and nickel (862 µg/L). Minority elements, present in lower concentrations, are chromium (91 µg/L), lead (59 µg/L) and mercury (0.3 µg/L).

The full graphs showing the bimonthly evolution of these metals in solution at point 10, from June 2015 until May 2016, are shown in figure A10 of the Appendix. As indicated by electrical conductivity, the levels of metals in solution are higher at this point than at the effluent prior to merging with the slagheap filtration drainage, as

usual negatively correlated to pluvial precipitations (Table 7 vs. figure A10 of the Appendix).

The oxidation state of the ferric/ferrous ion couple was also monitored, as shown below:

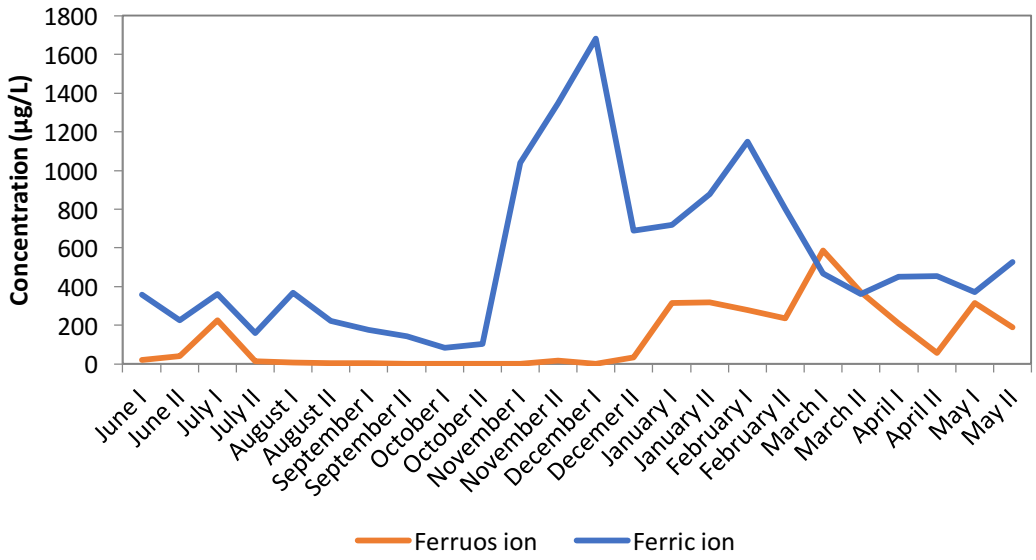

Figure 65: Graph showing the bimonthly evolution of ferric (blue) and ferrous (red) ion in solution at point 10, from June 2015 until May 2016.

The average proportion of ferric ion with respect to total iron in solution is 0.81. This is very similar to point 9, indicating as well quite a highly oxidised state of the ferric/ferrous ion couple.

The toxicity index of this point at each trimester is shown in the following graph:

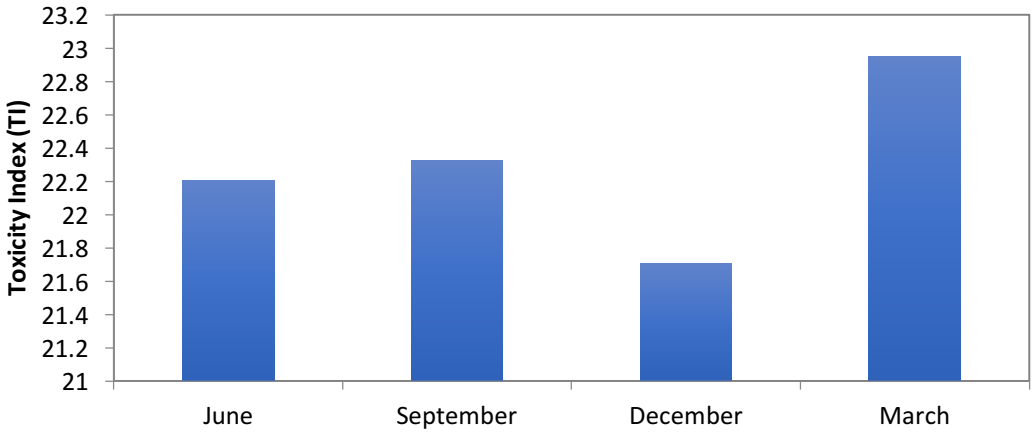

Figure 66: Graph showing the Toxicity Index of point 10 in June 2015, September 2015, December2015 and March 2016.

Dissolved oxygen was measured at this point, as usual, and is illustrated in the following graph:

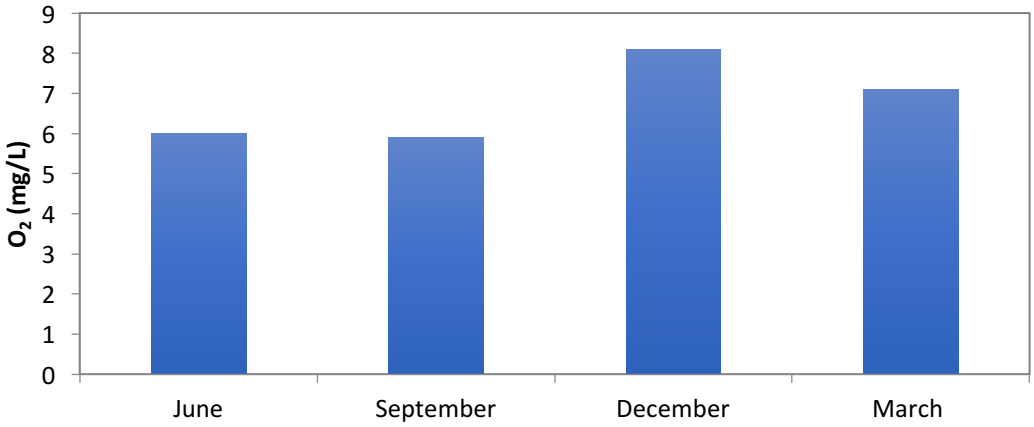

Figure 67: Graph showing dissolved oxygen (mg/L) at point 10 in June 2015, September 2015, December 2015 and March 2016.

The average dissolved oxygen throughout the year is 6.8 mg/L, with the highest value being recorded in December (8.1 mg/L) and the lowest value being noted in September (5.9 mg/L). These are similar to the values observed at point 9, due to the similarity in emplacement and physicochemical nature.

- Point 11

Point eleven is located at the effluent from Tunnel 11, downstream of point 9 and after a stream that proceeds from the North Slagheap filtration drainage has merged with the initial effluent. Its coordinates are the following:

  - Latitude: 37°41'26.88"N
  - Longitude: 6°33'56.30"O

First, pH and electrical conductivity were measured, as illustrated thus:

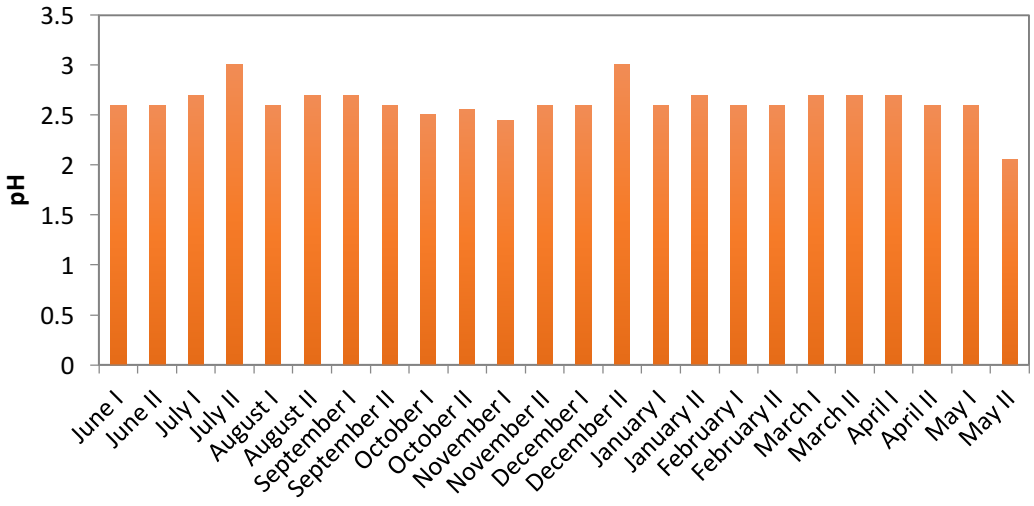

Figure 68: Graph showing the bimonthly evolution of pH at sampling point 11, from June 2015 until May 2016.

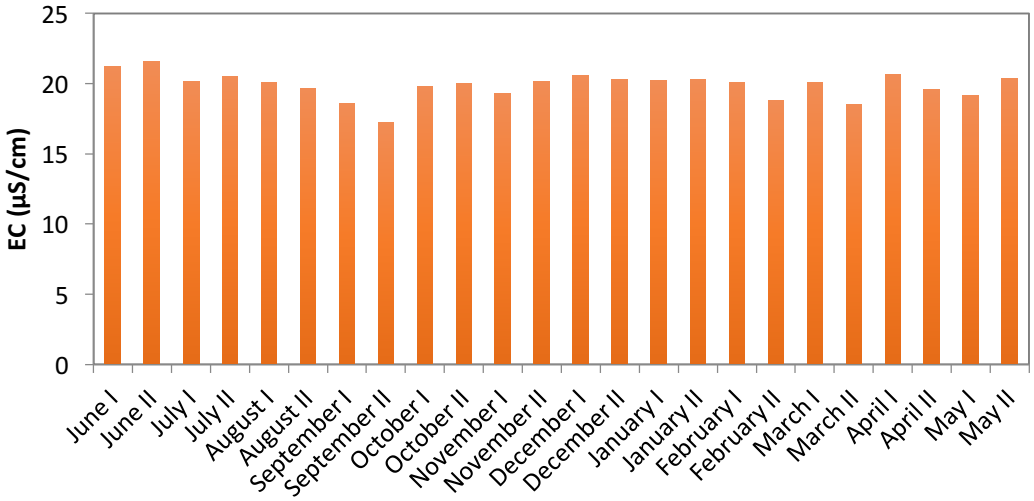

Figure 69: Graph showing the bimonthly evolution of electrical conductivity at sampling point 11, from June 2015 until May 2016.

The average pH is 2.6, with minimum and maximum values of 2.1 and 3.0, respectively. These are slightly lower than for point 9, due to the influence of the slagheap filtration drainage that merges with it.

In turn, the average value for electrical conductivity is 19.9 mS/cm, with a highest value of 21.6 mS/cm and a lowest value of 18.5 mS/cm. As for pH, the electrical conductivity of point 11 is slightly higher than that of point 9, due to the addition of metals from the slagheap filtration drainage stream.

Secondly, the chemical composition of the liquid at point 11 was monitored every two weeks, throughout a whole natural year. The samples were analysed for heavy metals, by analysis with ICP-MS. The average levels of metals found in solution throughout the sampling year are presented thus:

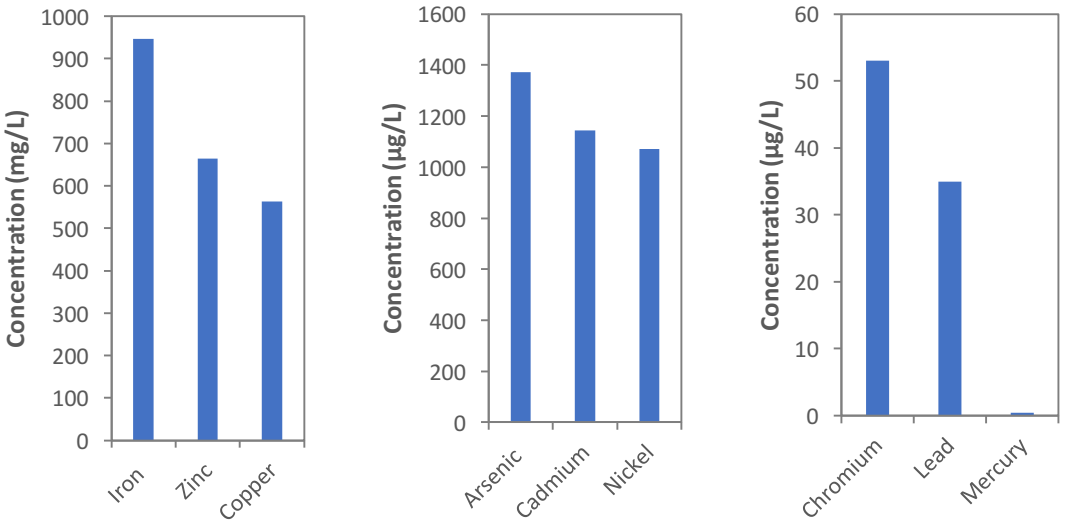

F*igure 70: Graphs showing average levels of total iron, zinc, copper, arsenic, cadmium, nickel, chromium, lead and mercury in solution at point 11, from June 2015 until May 2016.*

The metals present in higher concentrations are iron, zinc and copper (average concentrations of 946 mg/L, 665 mg/L and 563 mg/L, respectively), followed by arsenic (1,373 µg/L), cadmium (1,143 µg/L) and nickel (1,071 µg/L).

The minority elements, present in lower concentrations, are chromium (53 µg/L), lead (35 µg/L) and mercury (0.4 µg/L).

As for the rest of the elements examined, the full graphs showing the bimonthly evolution of total iron, copper, zinc, arsenic, lead and mercury and the quarter-yearly evolution of cadmium, nickel and chromium in solution at point 11, from June 2015 until May 2016, are presented in figure A11 of the Appendix.

As usual, the levels of metals in solution are negatively correlated with pluvial precipitations, as seen by comparing the concentrations of metals (figure A11 in the Appendix) with Table 7. In turn, these are positively correlated with temperatures, as elevated temperatures are linked with higher levels of metals in solution due to these becoming further concentrated as a result of enhanced evaporation (i.e. figure A11 in the Appendix vs. Table 8).

The oxidation state of the ferric/ferrous ion couple was monitored, as usual, by analysing the levels of each ion in solution, as shown below:

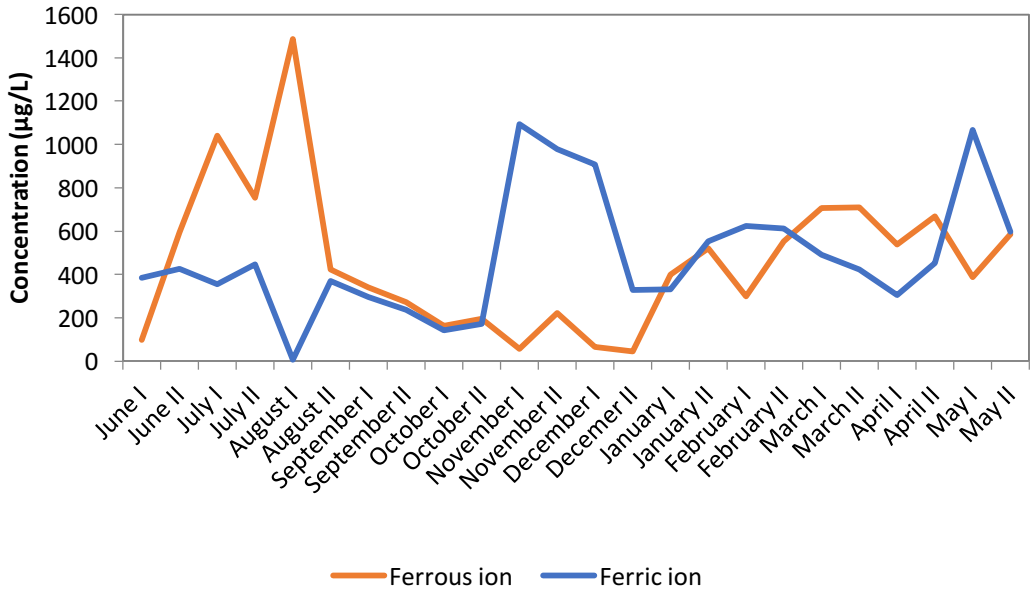

Figure 71: Graph showing the bimonthly evolution of ferric (blue) and ferrous (red) ion in solution at point 11, from June 2015 until May 2016.

The average proportion of ferric ion with respect to the total iron in solution is 0.53. This is considerably lower than that observed at points 9 and 10, which seems to be due to the fact that an underground drainage stream from slagheap filtrations merges with the Tunnel 11 drainage.

The toxicity index of this point at each trimester is shown below:

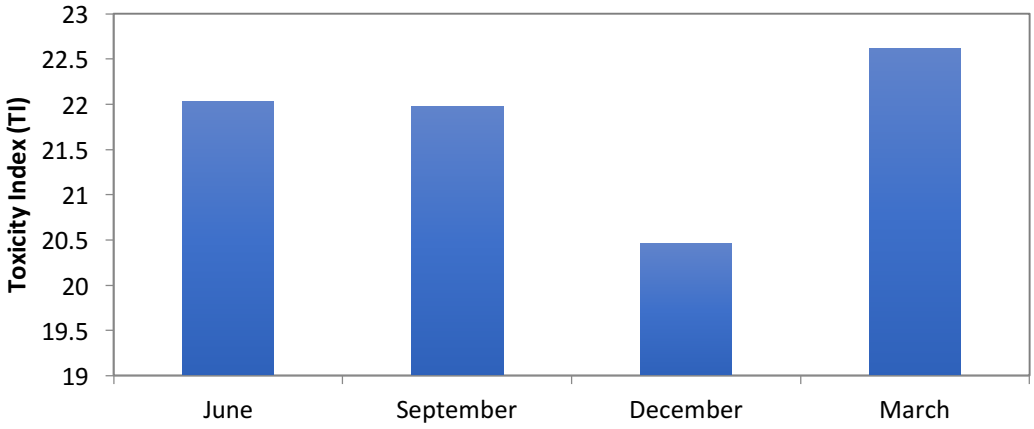

Figure 72: Graph showing the Toxicity Index of point 11 in June 2015, September 2015, December 2015 and March 2016.

Dissolved oxygen was also measured at this point, as shown in the following graph:

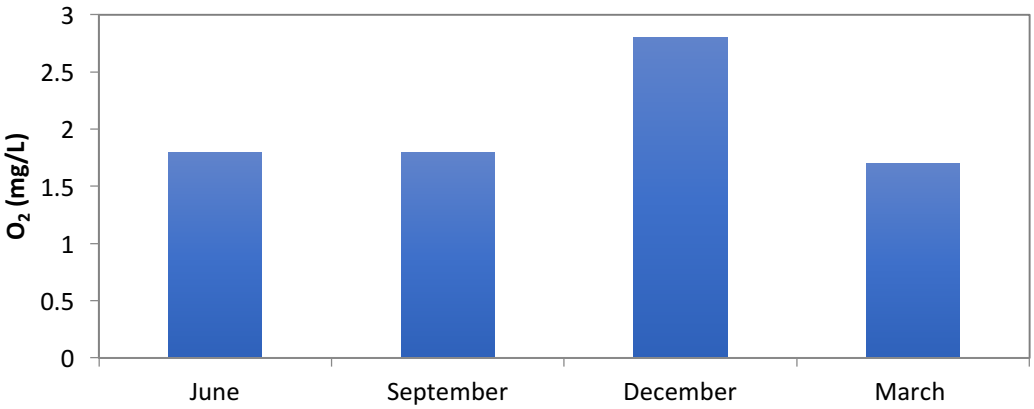

Figure 73: Graph showing dissolved oxygen (mg/L) at point 11 in June 2015, September 2015, December 2015 and March 2016.

The average level of dissolved oxygen throughout the year is 2.0 mg/L, with the highest value being recorded in December (2.8 mg/L) and the minimum level being noted in March (1.7 mg/L). These are lower than the previous two points within the same area, given the subterranean origin of point 11.

- Point 12

Point twelve is located on the effluent from Tunnel 11, downstream of points 9, 10 and 11, by the new train station. Its coordinates are the following:

  - Latitude: 37°41'24. 81"N
  - Longitude: 6°33'51. 70"O

As usual, physicochemical parameters were monitored at this site. First, pH and electrical conductivity were measured, as illustrated in the graphs below:

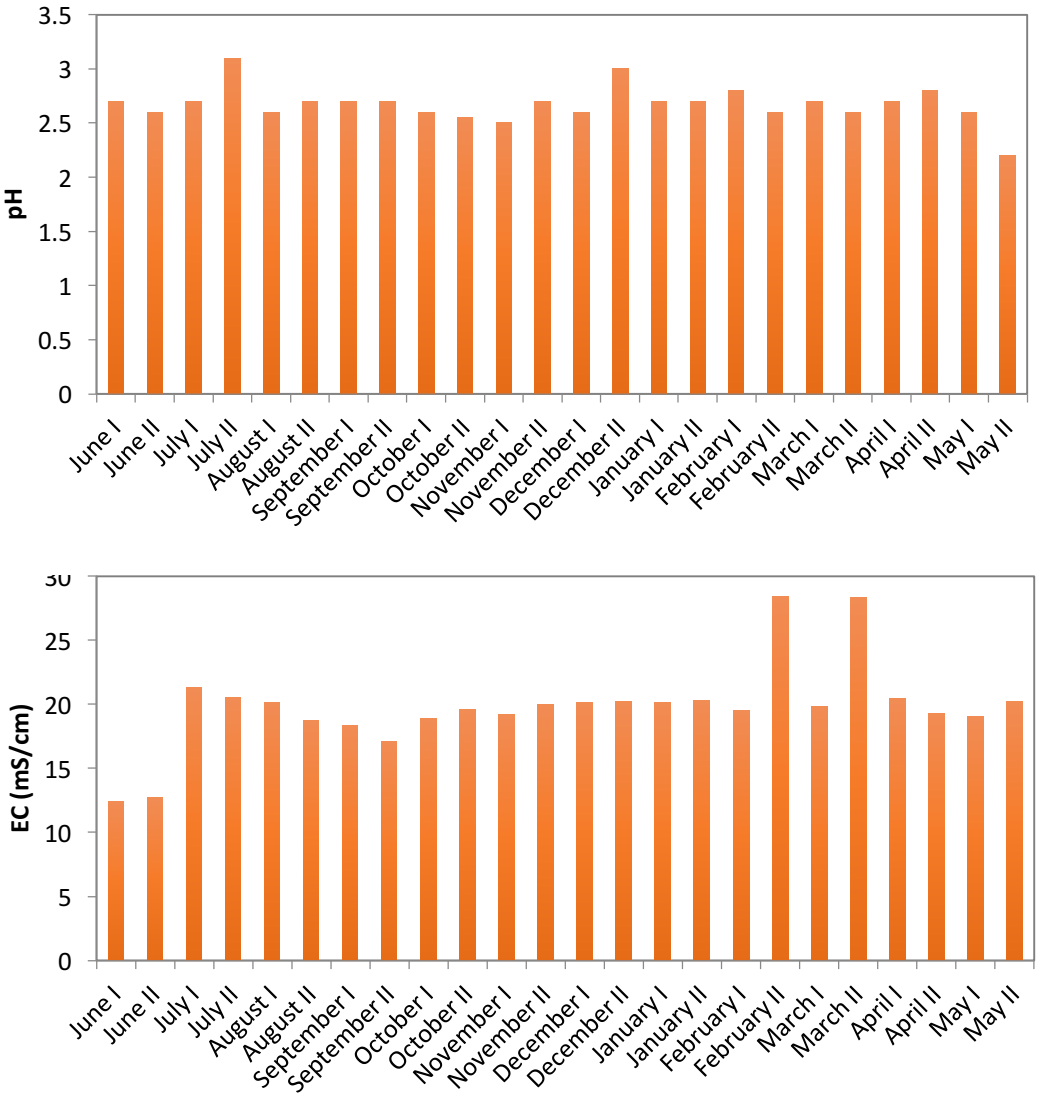

Figure 74: Graphs showing the bimonthly evolution of pH (top) and electrical conductivity (bottom) at sampling point 12, from June 2015 until May 2016.

The average pH is 2.7, with the lowest and highest values recorded being 2.2 and 3.1, respectively. These findings are very similar to those for point 11, which is to be expected, as point 12 lies downstream of it.

On the other hand, the average value for electrical conductivity is 18.9 mS/cm, with a highest value of 21.3 mS/cm and a lowest value of 17.1 mS/cm. As for pH, which is slightly higher at this site, the electrical conductivity of point 12 indicates a lower ionic content in comparison to point 11.

The evolution of the physicochemical parameters observed at this site is very similar to that at point 11, and hence can again be understood by looking at pluvial precipitations as well as temperatures (pH is positively correlated to pluvial precipitations while electrical conductivity displays a negative correlation; the

opposite is seen for temperatures, as may be noted by comparing Figure 74 with Table 7 and Table 8).

Secondly, the chemical composition of the liquid at this point was monitored every two weeks, throughout the whole natural year of the study. The samples were analysed for heavy metals, by analysis with ICP-MS, and the average levels were calculated. These results are presented thus:

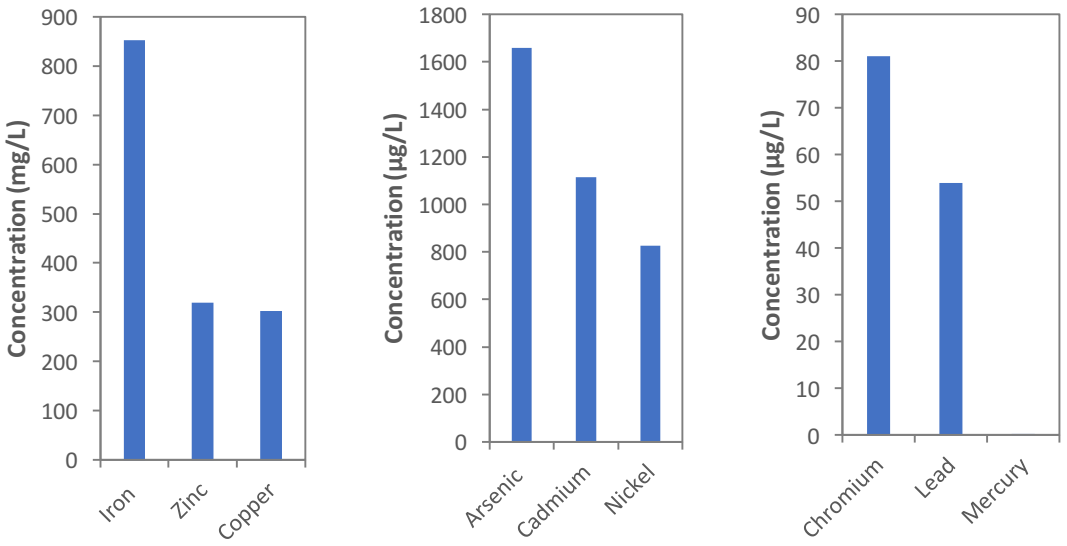

Figure 75: Graphs showing the average levels of total iron, zinc, copper, arsenic, cadmium, nickel, chromium, lead and mercury at point 12, from June 2015 until May 2016.

The metals present in higher concentrations are iron, zinc and copper (average concentrations of 852 mg/L, 320 mg/L and 303 mg/L, respectively), followed by arsenic (1,660 µg/L), cadmium (1,114 µg/L) and nickel (826 µg/L).

The minority elements, present in lower concentrations, are chromium (81 µg/L), lead (54 µg/L) and mercury (0.2 µg/L).

As expected, the levels of heavy metals in solution recorded at this site are very similar to those seen at point 11. The complete graphs showing the bimonthly evolution of total iron, copper, zinc, arsenic, lead and mercury, as well as the quarter-yearly evolution of cadmium, nickel and chromium in solution at point 12, from June 2015 until May 2016, are recorded in figure A12 of the Appendix.

Finally, the levels of metals in solution are, as usual, negatively correlated with pluvial precipitations and positively correlated with temperatures (figure A12 of the Appendix vs. Table 7 and Table 8).

The oxidation state of the ferric/ferrous ion couple was monitored, again, by analysing the levels of these ions in solution, as shown below:

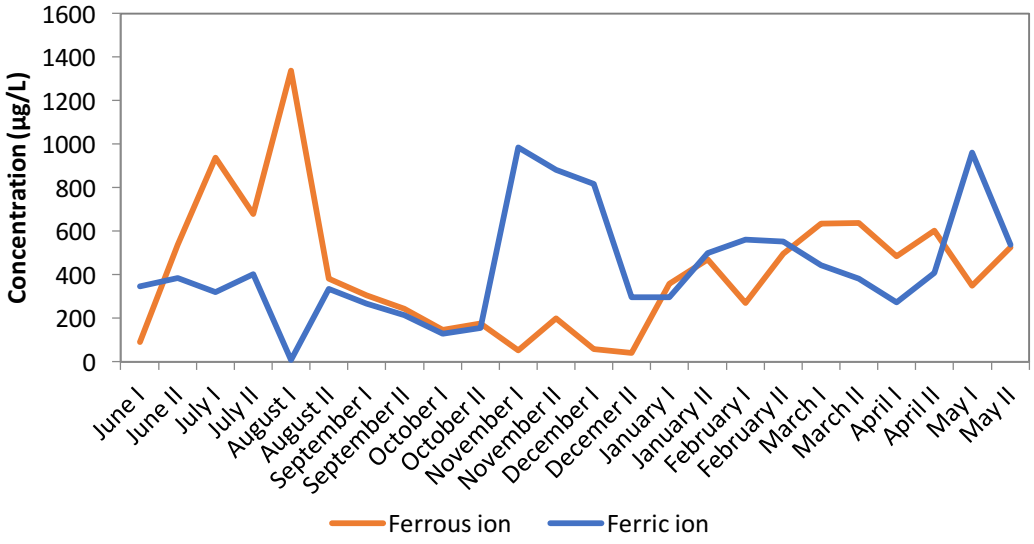

Figure 76: Graph showing the bimonthly evolution of ferric (blue) and ferrous (red) ion in solution at point 12, from June 2015 until May 2016.

The average proportion of ferric ion with respect to the total iron in solution is 0.56. This is very similar to point 11, which is to be expected given the proximity and similarity.

The toxicity index and dissolved oxygen of this point at each trimester is shown below:

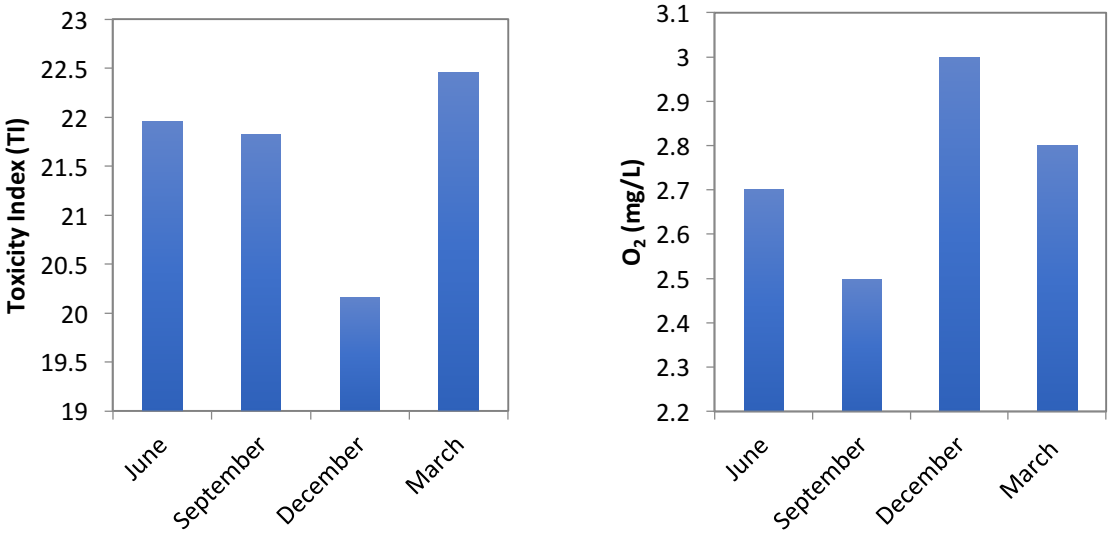

Figure 77: Graphs showing the Toxicity Index (left) and dissolved oxygen (mg/L) at point 12 in June 2015, September 2015, December 2015 and March 2016.

The average dissolved oxygen throughout the year is 2.75 mg/L, with the highest value being recorded in December (3.0 mg/L) and the lowest value being noted in September (2.5 mg/L).

Similarly to point 11, these values are lower than those observed within the same area at points 9 and 10, given their subterranean origin, although point 12 is slightly higher than point 11 due to it being downstream a creek exposed to air.

Area D: Atalaya Slagheap drainage, Gangosa stream and Tintillo River area

This area is located west of the Atalaya open pit. This pit is currently flooded, bearing high amounts of leached metals in a highly acidic solution.

Three sampling sites were chosen in this area. The first one, point 13, is located at an effluent from the Atalaya Slagheap filtration drainage, coinciding with the head of the Tintillo River. The second point is located right outside an old railway tunnel originating from the Atalaya open pit, through which an acid mine drainage flows (point 14). Finally, point 15 was chosen at a stream arising from the Atalaya Slagheap filtration drainage, called the Gangosa stream.

Figure 78: Map showing the four sampling points at the Atalaya Slagheap drainage, Gangosa stream and Tintillo River area.

In this area, living biofilms were detected at all three sampled points. Information about these sampling sites is presented thus:

- Point 13

Point 13 is located at an effluent originating from the Atalaya Slagheap filtration drainage, coinciding with the head of the Tintillo River.

Its coordinates are the following:

  - Latitude: 37°42'36. 07"N
  - Longitude: 6°37'21. 61"O

Physicochemical parameters were measured every fortnight throughout a natural year at this point. In first place, pH and electrical conductivity were recorded, as illustrated in the following graphs:

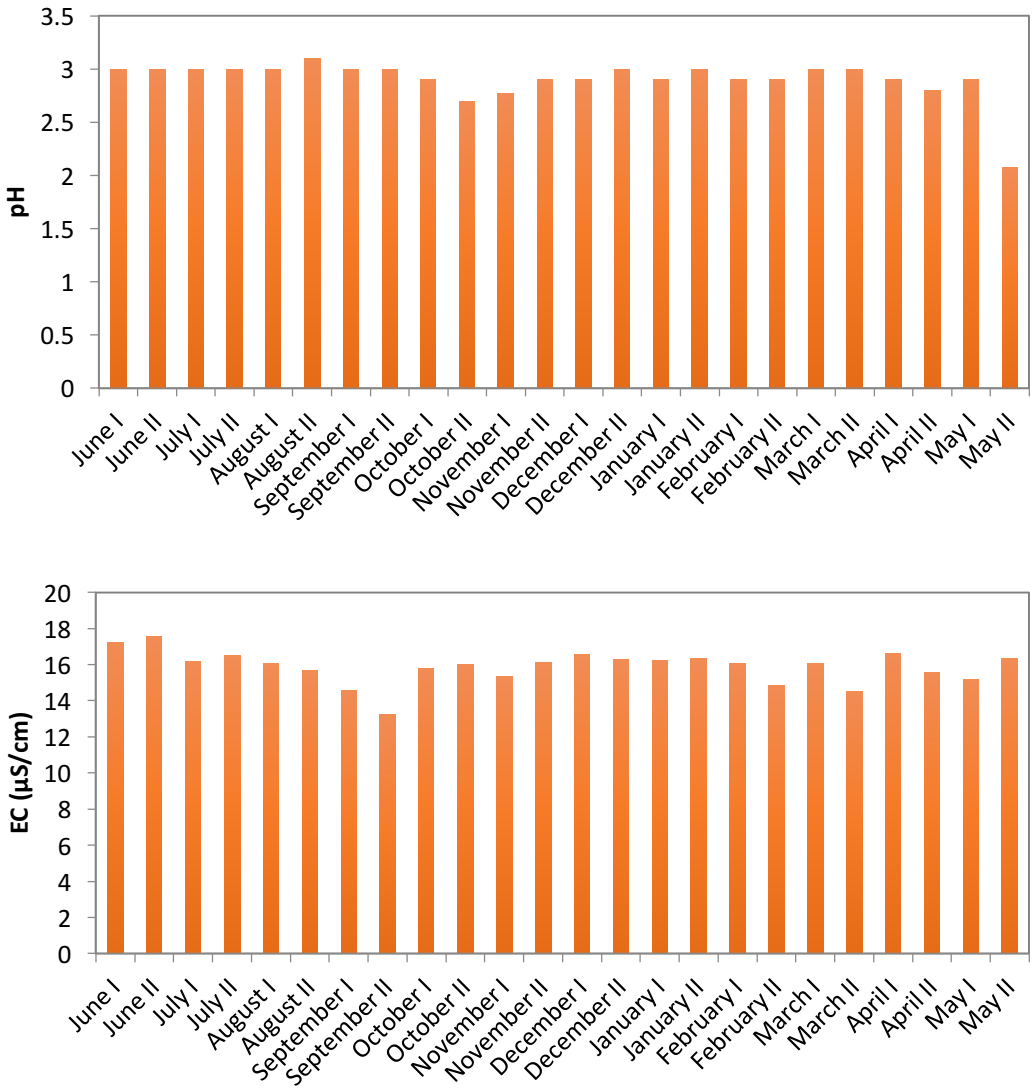

Figure 79: Graphs showing the bimonthly evolution of pH (top) and electrical conductivity (bottom) at sampling point 13, from June 2015 until May 2016.

The average pH is 2.9, with the lowest and highest values being 2.1 and 3.1, respectively. Although still extreme, these are less acidic than the values observed at the North Slagheap area.

On the other hand, the average level of electrical conductivity is 15.9 mS/cm, with a maximum observed value of 17.6 mS/cm and a minimum recorded value of 14.5 mS/cm. This indicates a similar ionic content than that found at the North Slagheap area.

Both pH and electrical conductivity follow the usual pattern with pluvial precipitations (pH is positively correlated to pluvial precipitations, while electrical conductivity displays a negative correlation), i.e. Figure 79 vs. Table 7.

In second place, the chemical composition of point 13 was monitored every fortnight, throughout a whole natural year. The samples were analysed for heavy metals, by analysis with ICP-MS.

The average metal levels in solution are presented thus:

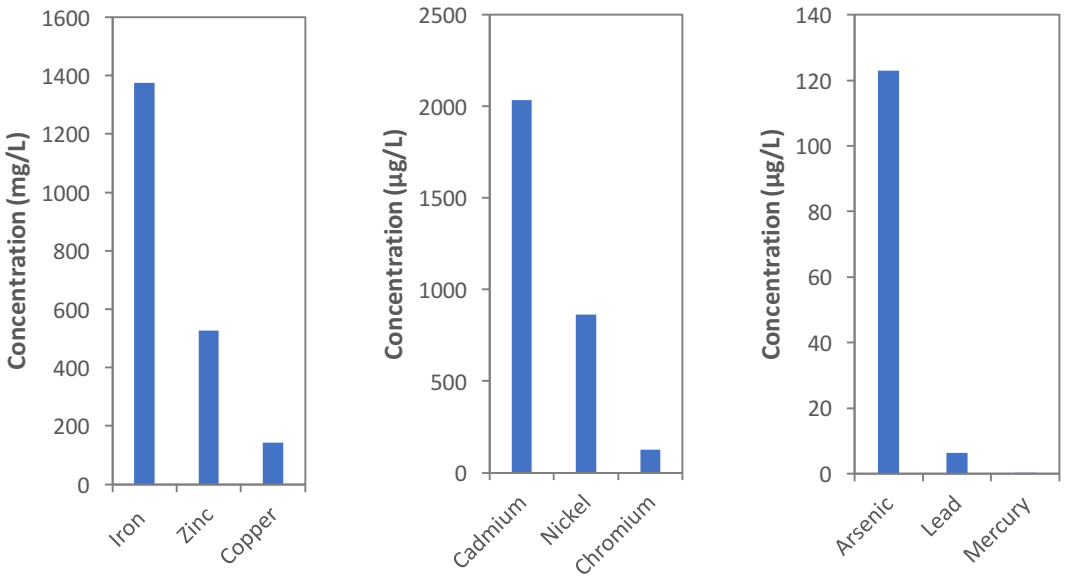

Figure 80: Graphs showing the average levels of iron, zinc, copper, cadmium, nickel, chromium, arsenic, lead and mercury in solution at point 13, from June 2015 until May 2016.

The metals present in higher concentrations are iron, zinc and copper (average concentrations of 1,376 mg/L, 526 mg/L and 143 mg/L, respectively), followed by cadmium (2,035 µg/L) and nickel (862 µg/L).

The minority elements, present in lower concentrations, are chromium (127 µg/L), arsenic (123 µg/L), lead (6,4 µg/L) and mercury (0.3 µg/L).

Except for lead and mercury, all other metals are present in lower quantities at this point than at the North Slagheap drainage area. The full results for the bimonthly

evolution of total iron, copper, zinc, arsenic, lead and mercury and the quarter-yearly evolution of cadmium, nickel and chromium in solution at point 13, from June 2015 until May 205, may be found in figure A13 of the Appendix.

(Again, the levels of metals in solution are negatively correlated with pluvial precipitations while positively so with temperatures, i.e. Table 7 and Table 8 vs. figure A13 in the Appendix.)

The oxidation state of the ferric/ferrous ion couple was monitored, again, by analysing the levels of these ions in solution, as shown below:

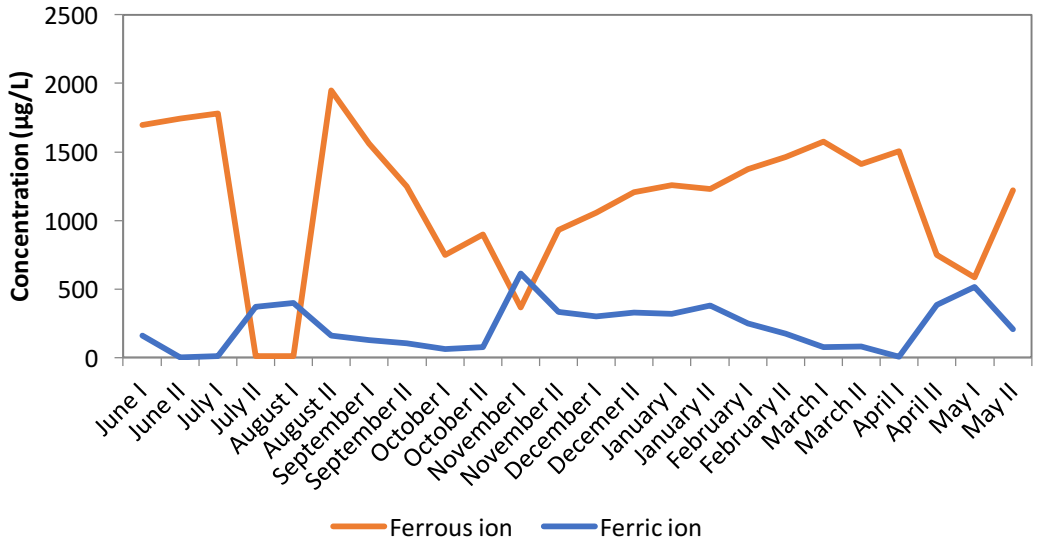

Figure 81: Graph showing the bimonthly evolution of ferric (blue) and ferrous (red) ion in solution at point 13, from June 2015 until May 2016.

The average proportion of ferric ion with respect to total iron in solution is 0.24. This indicates that the ferric/ferrous ion couple is present in a considerably reduced state, given the subterranean origin of the liquid at this point.

The toxicity index of this point at each trimester is shown below:

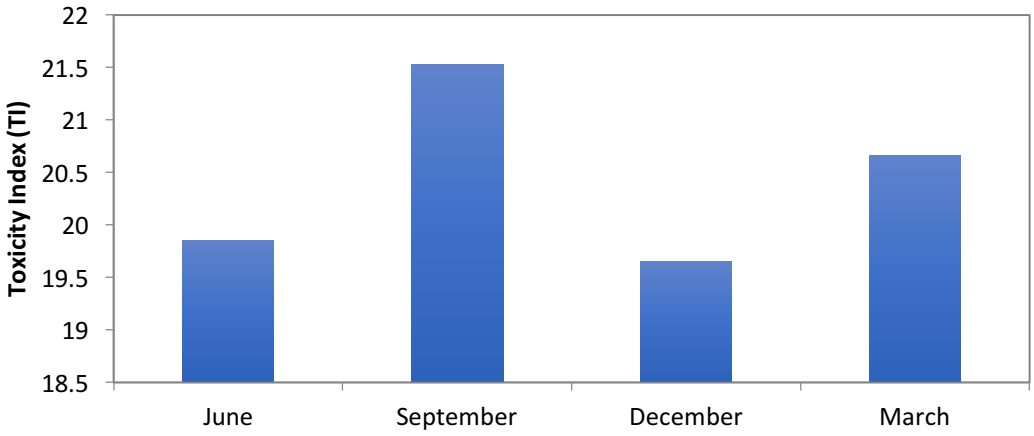

Figure 82: Graph showing the Toxicity Index of point 13 in June 2015, September 2015, December 2015 and March 2016.

Dissolved oxygen was also measured at this point, as shown in the following graph:

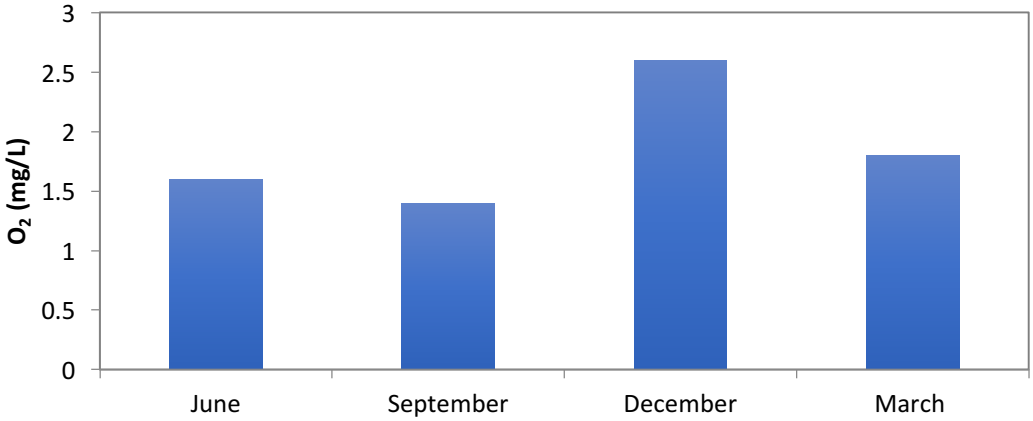

Figure 83: Graph showing dissolved oxygen (mg/L) at point 13 in June 2015, September 2015, December 2015 and March 2016.

The average dissolved oxygen throughout the year is 19 mg/L, with the highest value being recorded in December (2.6 mg/L) and the lowest value being noted in September (1.4 mg/L). These levels are rather low, which is explained by the subterranean origin.

- Point 14

Point 14 is located at the exit of an old railway tunnel, emerging from the Atalaya open pit. There is an acid mine drainage effluent flowing out of this tunnel, at the exit of which microbial biofilms are present. Its coordinates are the following:

  - Latitude: 37°42'37. 97"N
  - Longitude: 6°37'24. 88"O

In first place, pH and electrical conductivity were recorded on a fortnightly basis, as illustrated in the following graphs:

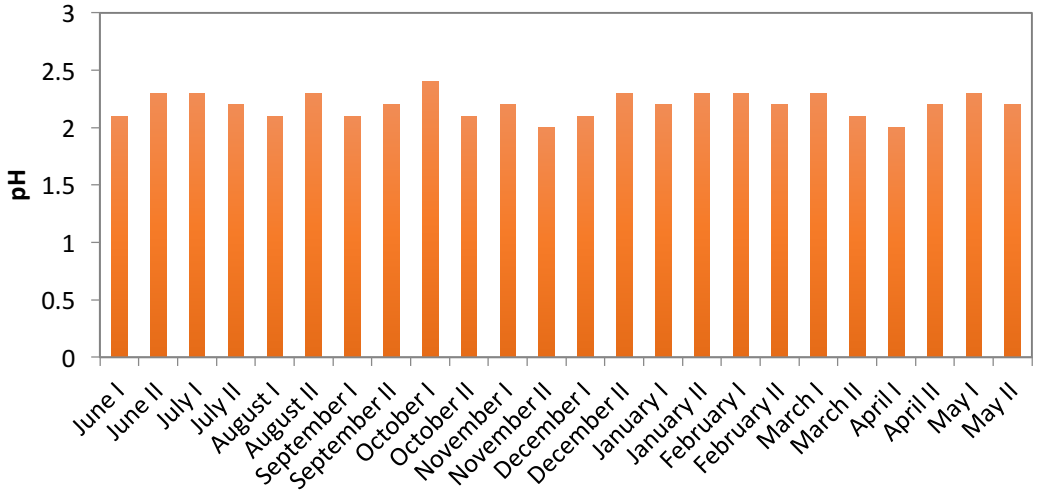

Figure 84: Graph showing the bimonthly evolution of pH at sampling point 14, from June 2015 until May 2016.

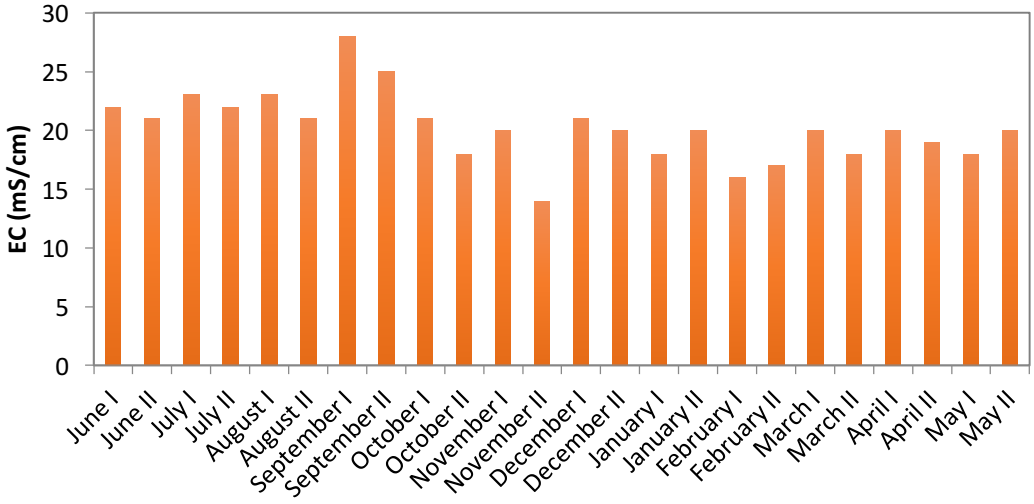

Figure 85: Graphs showing the bimonthly evolution of electrical conductivity at sampling point 14, from June 2015 until May 2016.

The average pH is 2.2, with the lowest and highest values being 2.0 and 2.4, respectively. Even though these are highly acidic, they are less so than the exit of Tunnel 5 from the Lago pit.

On the other hand, the average value for electrical conductivity is 20.2 mS/cm, with a maximum value of 25 mS/cm and a minimum value of 14 mS/cm. This indicates a similar ionic content than that found at the North Slagheap area and is just slightly higher than that at the exit of Tunnel 5 arising from the Lago pit.

Again, pH and electrical conductivity are in accordance with pluvial precipitations and temperatures.

In addition, the chemical composition of this point was monitored every two weeks. The samples were analysed for heavy metals, by analysis with ICP-MS, and the average values were calculated, as presented thus:

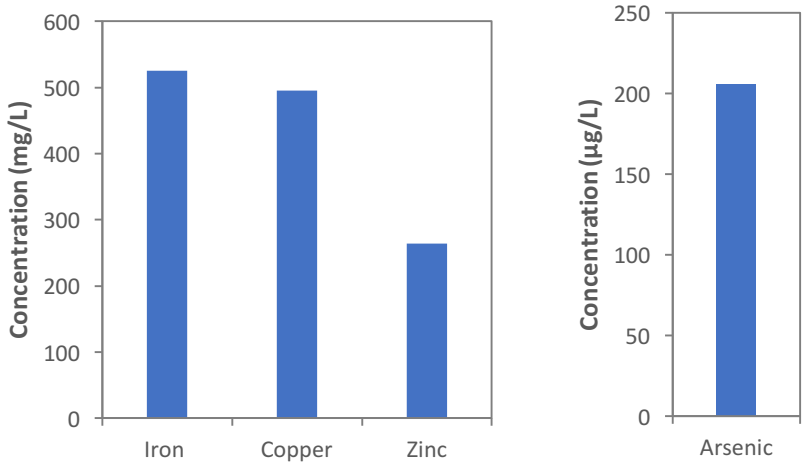

Figure 86: Graphs showing the average levels of total iron, copper, zinc and arsenic in solution at point 14, from June 2015 until May 2016.

The metals present in higher concentrations are iron, copper and zinc (average concentrations of 525 mg/L, 495 mg/L and 264 mg/L, respectively).

On the other hand, the minority element, present in lower concentrations, is arsenic (average of 206 µg/L). The rest of the metals that usually appear in solution, i.e. cadmium, nickel, chromium, lead and mercury, were present at negligible concentrations (< 2 µg/L). This is due to the fact that the metals present in the old cementation plant are those of the treated ore of interest, which bears copper and iron and is often associated to zinc and arsenic.

The full graphs showing the bimonthly evolution of total iron, copper, zinc and arsenic in solution at point 14, from June 2015 until May 2016, are found in figure A14 in the Appendix.

Again, the levels of metals in solution at this point are negatively correlated with pluvial precipitations, as seen by comparing both sets of values (Figure A14 in the Appendix with Table 7) while positively correlated with temperatures (i.e. Figure A14 in the Appendix vs. Table 8).

The toxicity index and dissolved oxygen levels of this point at each trimester is shown below:

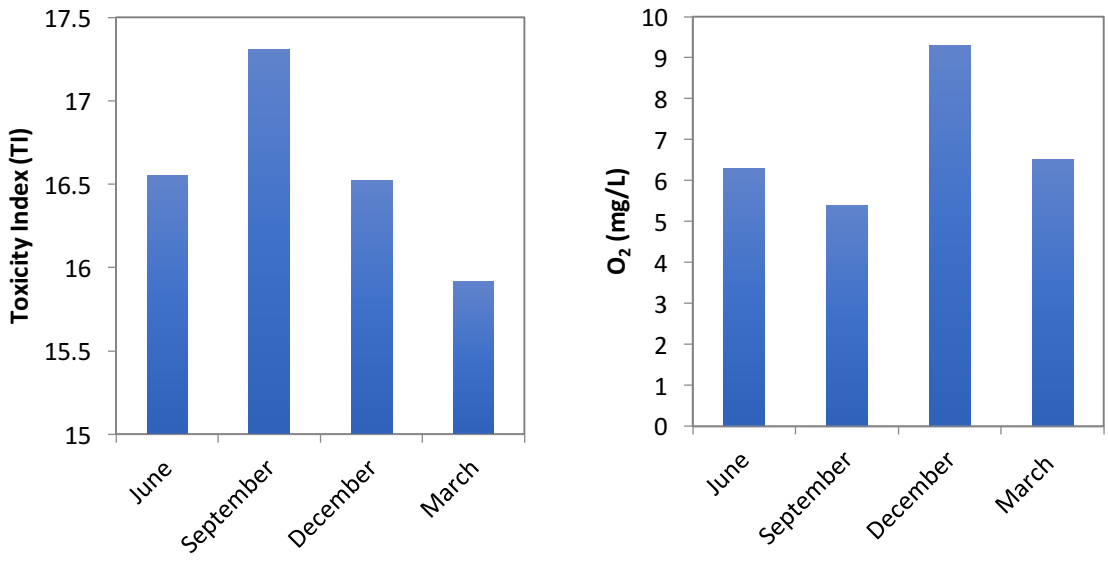

Figure 87: Graph showing the Toxicity Index and dissolved oxygen (mg/L) of point 14 in June 2015, September 2015, December 2015 and March 2016.

The average dissolved oxygen throughout the year is 6.9 mg/L, with the highest value being recorded in December (9.3 mg/L) and the lowest value being noted in September (5.4 mg/L).

It is worth noting that the average level of dissolved oxygen at this site is relatively high, while the concentration observed in December is the highest recorded value out of all the sampled stations throughout the year.

- Point 15

Point 15 is located at a stream called La Gangosa that arises from drainage of the Atalaya Slagheap filtrations. These are its coordinates:

  - Latitude: 37°42'40.95"N
  - Longitude: 6°37'38.24"O

Physicochemical parameters were measured at this point every two weeks throughout the whole year of sampling. Firstly, pH and electrical conductivity were recorded, as shown in the following graphs:

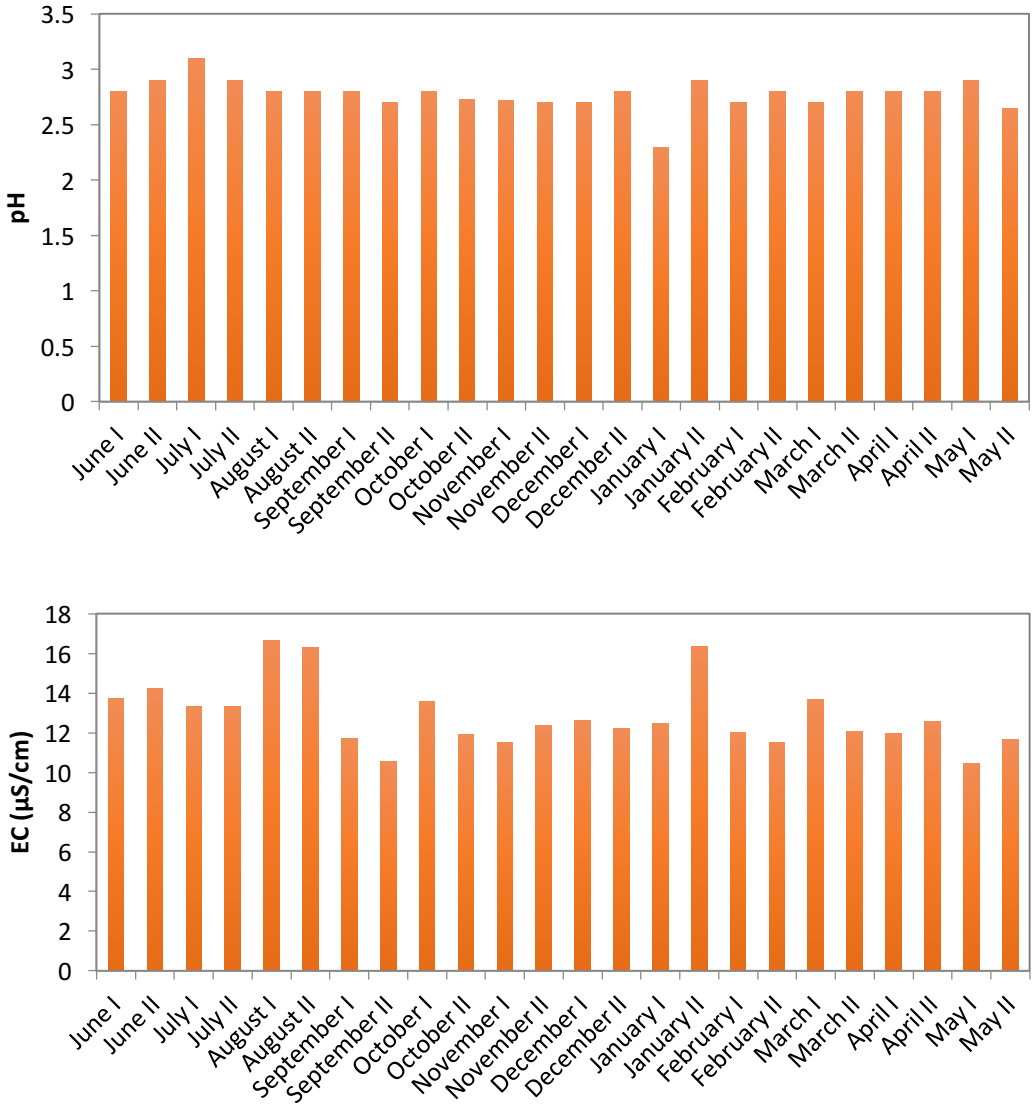

Figure 88: Graphs showing the bimonthly evolution of pH (top) and electrical conductivity (bottom) at sampling point 15, from June 2015 until May 2016.

The average pH is 2.8, with the lowest and highest values being 2.7 and 3.1, respectively. These values are very similar to those observed at point 13, which is logical, as both streams proceed from the same slagheap.

On the other hand, the average level of electrical conductivity throughout the year of sampling is 12.9 mS/cm, with a maximum recorded value of 16.7 mS/cm and a minimum observed value of 10.5 mS/cm. These levels are lower than those observed at point 13, despite both having the same source. The rationale behind this could lie in the fact that point 13 is also the head of the Tintillo River, which bears higher quantities of leached metals from the subsurface.

As usual, pH and electrical conductivity are in accordance with pluvial precipitations and temperatures (i.e. Figure 88 vs. Table 7 and Table 8).

The chemical composition of this point was also monitored every two weeks, throughout a whole year. The samples were analysed for heavy metals by analysis with ICP-MS, and the average values throughout the year were calculated, as illustrated thus:

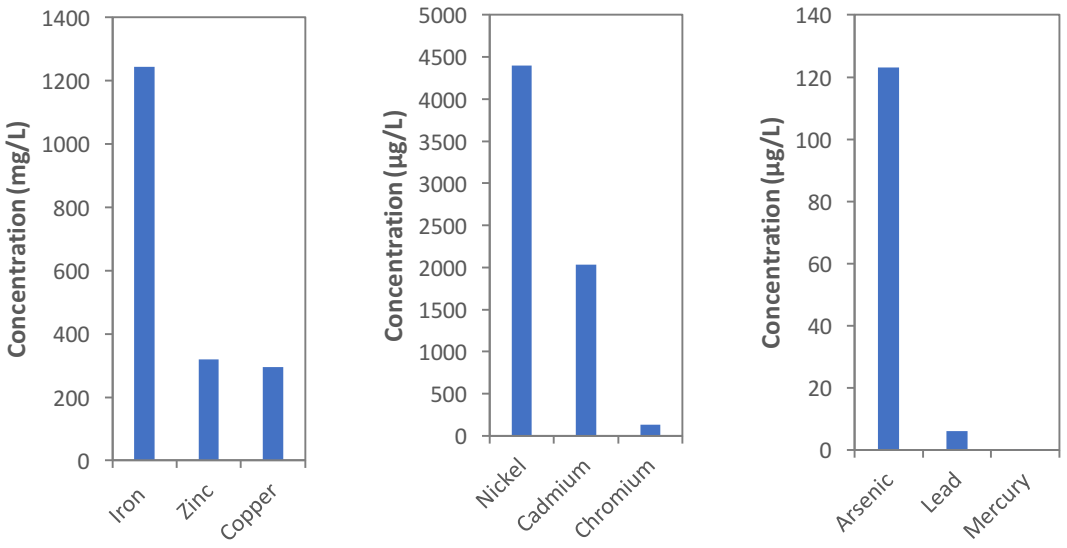

Figure 89: Graphs showing the average levels of total iron, zinc, copper, nickel, cadmium, chromium, arsenic, lead and mercury in solution at point 15, from June 2015 until May 2016.

The metals present in higher concentrations are iron, zinc and copper (average concentrations of 1,244 mg/L, 320 mg/L and 295 mg/L, respectively), followed by nickel (4,397 µg/L) and cadmium (2,035 µg/L).

The minoritary elements, present in lower concentrations, are chromium (127 µg/L), arsenic (123 µg/L), lead (6 µg/L) and mercury (0.3 µg/L).

Except for nickel, which is present in higher levels, the concentrations of all other metals are lower at this point than at point 13, for the same reason as electrical conductivity is lower.

The full graphs showing the bimonthly evolution of total iron, copper, zinc, arsenic, lead and mercury and the quarter-yearly evolution of cadmium, nickel and chromium in solution at point 15, from June 2015 until May 2016, are recorded in figure A15 of the Appendix. (The levels metals in solution are again negatively correlated with pluvial precipitations, i.e. Table 7 vs. figure A15 from the Appendix.)

The oxidation state of the ferric/ferrous ion couple was analysed by measuring the concentrations of these ions in solution, as presented below:

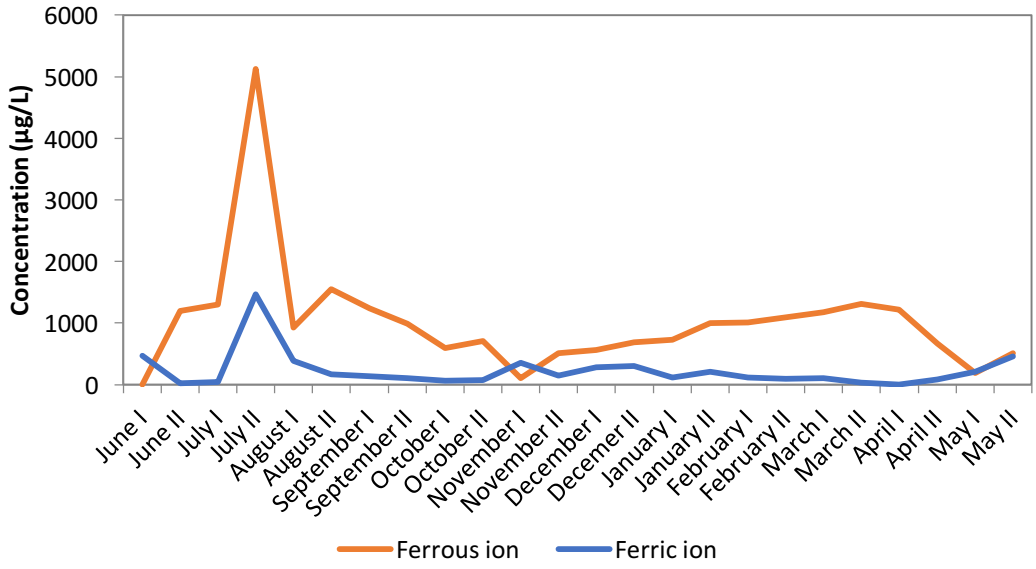

Figure 90: Graph showing the bimonthly evolution of ferric (blue) and ferrous (red) ion in solution at point 15, from June 2015 until May 2016.

The average proportion of ferric ion with respect to total iron in solution is 0.75. This indicates a relatively high oxidation state of the ferric/ferrous ion pair. The difference with the exit of tunnel 5 (point 6) is that the liquid at point 15 is mostly stagnant and is therefore much more exposed to oxygen.

The toxicity index and dissolved oxygen of this point at each trimester is shown in the following graphs:

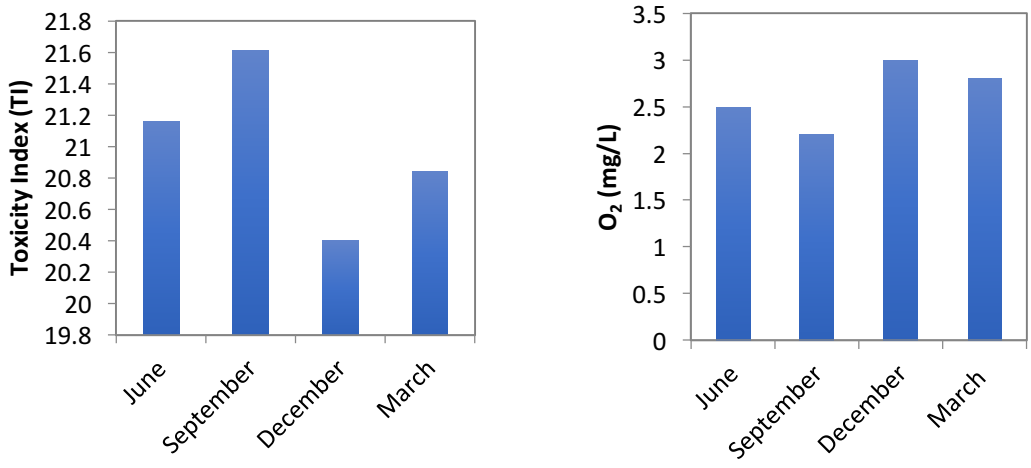

Figure 91: Graphs showing the Toxicity Index (left) and dissolved oxygen (right) of point 15 in June 2015, September 2015, December 2015 and March 2016.

The average dissolved oxygen throughout the year is 2.6 mg/L, with the highest value being recorded in December (3.0 mg/L) and the lowest value being noted in September (2.2 mg/L). These levels are notably low again, as is the case for point 13, due to the subterranean origin of the effluent at this site.

Area E: Tintillo River by the zone of confluence of drainages

This area is located downstream of Area D. Its emplacement is by the Tintillo River, after it has achieved considerable current from the confluence of various drainages originating from filtrations through the Atalaya Slagheap. There is one sampling site in this area, point 16, which was found to host microbial life.

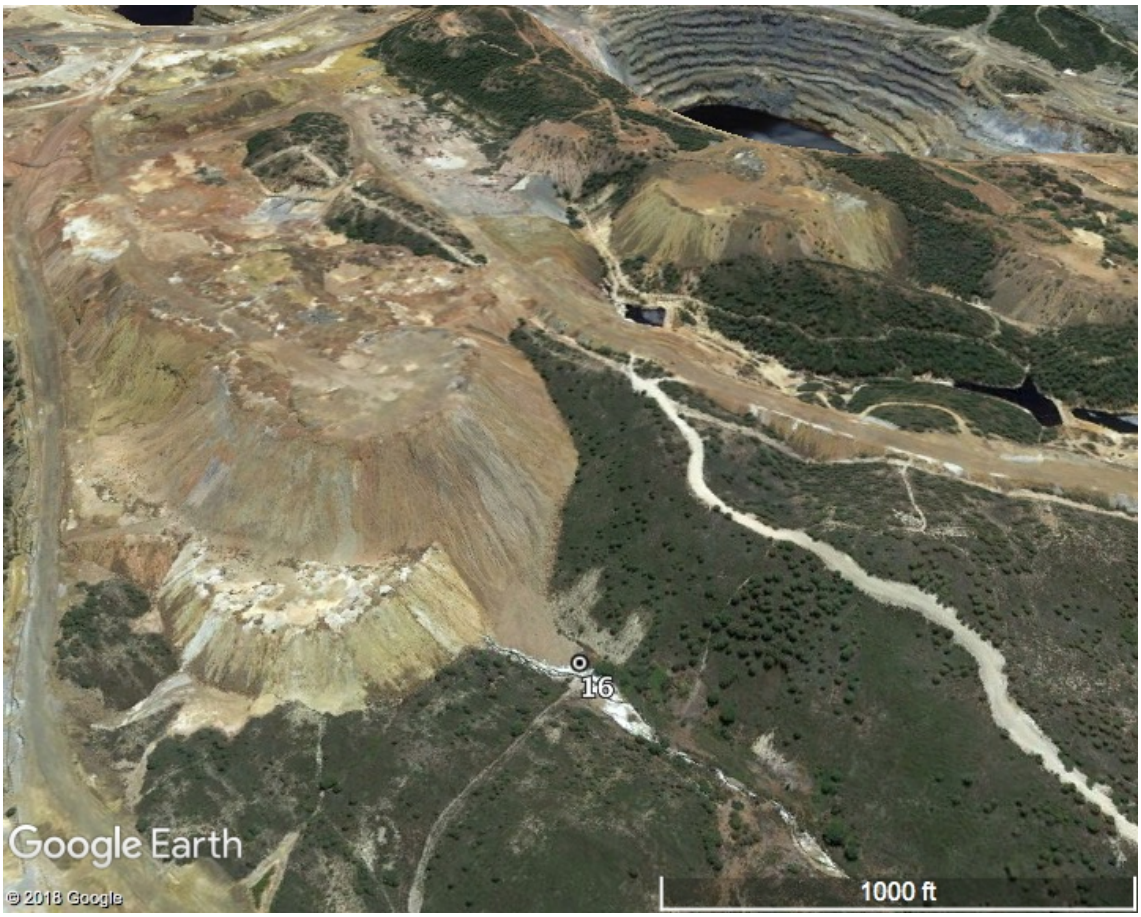

Figure 92: Map showing the sampling point at the Tintillo River, by the zone of confluence of drainages, as well as the foot of the Atalaya Slagheap hillside.

Information about this sampling site is presented thus:

- Point 16

The coordinates of sampling point 16 are the following:

  - Latitude: 37°42'53.14"N
  - Longitude: 6°36'30.34"O

Physicochemical parameters were measured every fortnight at point 16, throughout the year of interest. Firstly, pH and electrical conductivity were recorded, as illustrated in the following graphs:

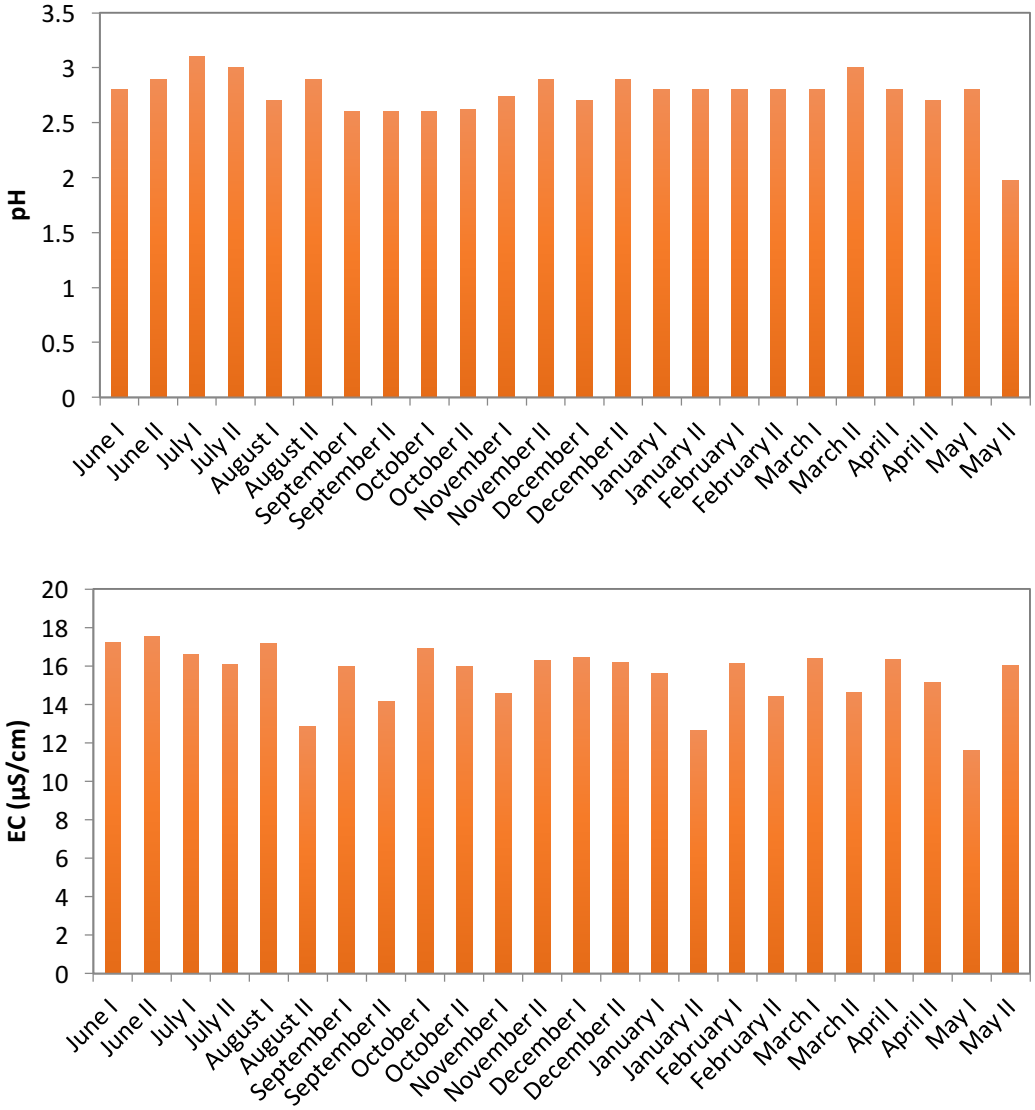

Figure 93: Graphs showing the bimonthly evolution of pH (top) and electrical conductivity (bottom) at sampling point 16, from June 2015 until May 2016.

The average pH is 2.8, with the lowest and highest values being 2.6 and 3.1, respectively. These values are very similar to those observed at point 15, which is to be expected, as both have the same source.

On the other hand, the average value for electrical conductivity is 15.5 mS/cm, with a highest value of 17.6 mS/cm and a lowest value of 12.7 mS/cm. These are more elevated than those recorded at point 15, despite the same source, which could simply mean that higher currents are linked with higher quantities of metals in solution.

As usual, pH and electrical conductivity are in accordance with pluvial precipitations, although very little variation was observed.

The chemical composition of this point was analysed every two weeks, throughout a whole year. The samples were scanned for heavy metals by analysis with ICP-MS, and the average levels of metals in solution were calculated, as illustrated thus:

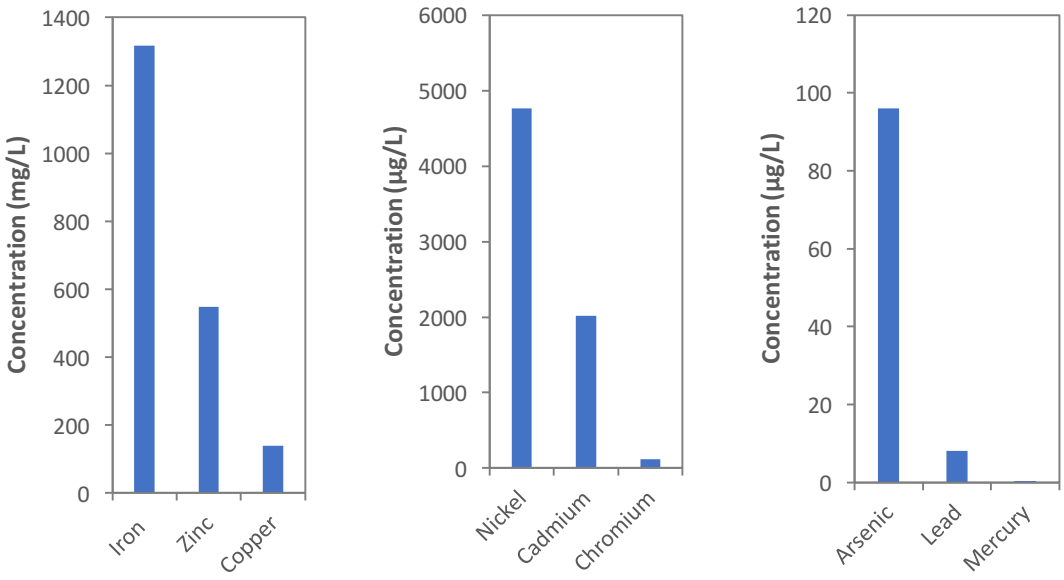

Figure 94: Graphs showing the average levels of total iron, zinc, copper, nickel, cadmium, chromium, arsenic, lead and mercury in solution at point 16, from June 2015 until May 2016.

The metals present in higher concentrations are iron, zinc and copper (average concentrations of 1,317 mg/L, 548 mg/L and 140 mg/L, respectively), followed by nickel (4,763 µg/L) and cadmium (2,017 µg/L).

The minority elements, present in lower concentrations, are chromium (119 µg/L), arsenic (96 µg/L), lead (8 µg/L) and mercury (0.4 µg/L).

The full results for the bimonthly evolution of total iron, copper, zinc, arsenic, lead and mercury, as well as the quarter-yearly evolution of cadmium, nickel and chromium in solution at point 16, from June 2015 until May 2016, are recorded in figure A16 of the Appendix.

As may be inferred from electrical conductivity, most metals are present in higher concentrations at this point than at point 15, and are again negatively correlated with pluvial precipitations and positively so with temperatures (figure A16 in the Appendix vs. Table 7 and Table 8).

In addition, the oxidation state of the ferric/ferrous ion couple was analysed as usual, by measuring the concentrations of the two ions in solution, as presented below:

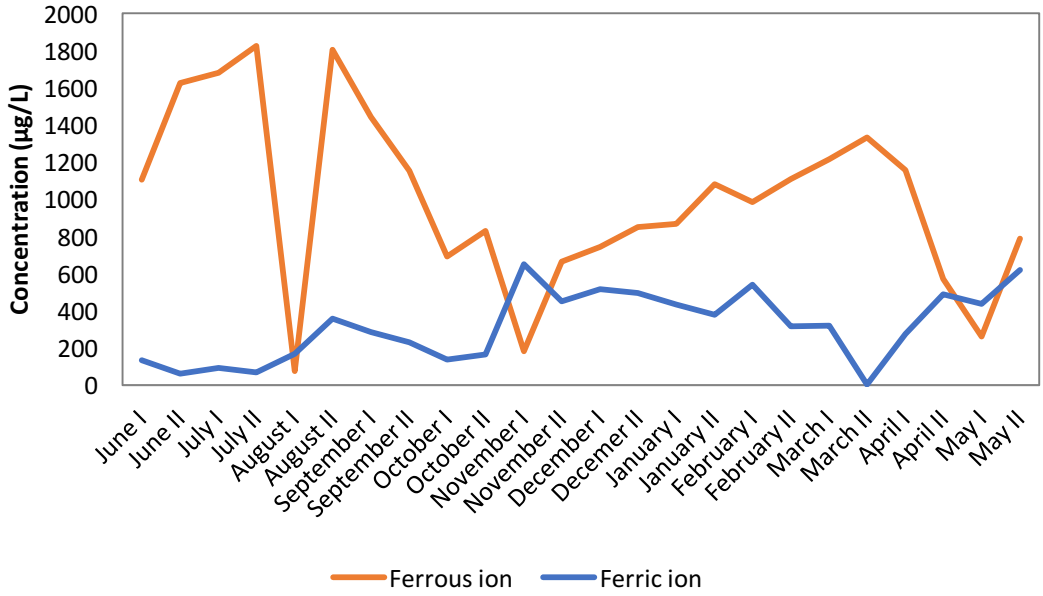

Figure 95: Graph showing the bimonthly evolution of ferric (blue) and ferrous (red) ion in solution at point 16, from June 2015 until May 2016.

The average proportion of ferric ion with respect to total iron in solution is 0.29. This reveals a rather reduced state of the ferric/ferrous ion pair, which is to be expected given the subterranean nature of the effluent at this point.

The toxicity index and dissolved oxygen of this point at each trimester is shown in the following graphs:

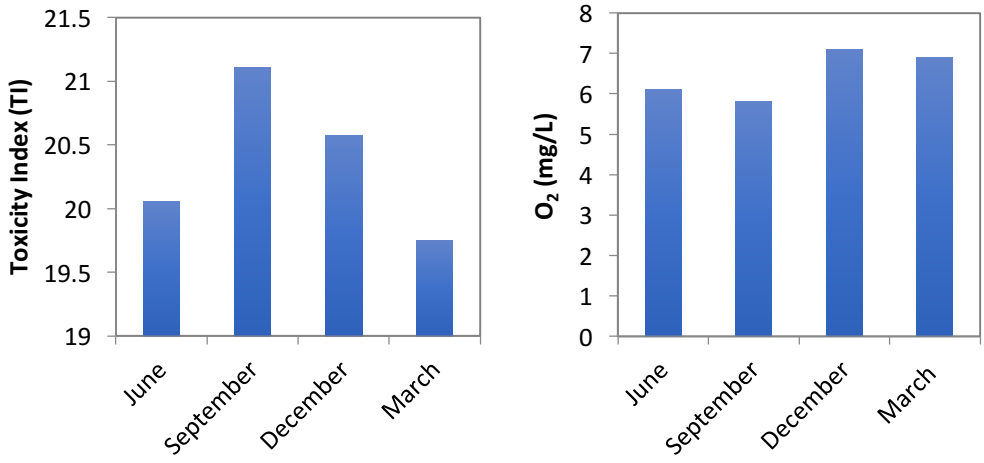

Figure 96: Graphs showing the Toxicity Index (left) and dissolved oxygen (right) at point 16 in June 2015, September 2015, December and March 2016.

The average dissolved oxygen throughout the year is 6.4 mg/L, with the highest value being recorded in December (7.1 mg/L) and the lowest value being noted in September (5.8 mg/L). These are notably higher than those at points 13 and 15, which are upstream, given the exposure to air of the creek spanning these sites.

Discussion

The most extreme sites, from a physicochemical perspective, were encountered in Area B. In this location, pH was found to be extremely low, impressively reaching a minimum of 1.45 at point 6 (during the first half of July 2015). In addition, point 8, located downstream of point 6, consistently displays a remarkably low pH as well, if slightly mitigated due to the slagheap drainage component.

Moreover, excluding the old cementation plant (point 5) where evidently elevated levels of metals in solution are found, Area B displays the highest electrical conductivity (average of 22.4 $mS\ cm^{-1}$ at point 8) as well as the highest Toxicity Index (26.3 and 25.6 at point 7 and 8, respectively).

As seen throughout the statistical analysis, it is not surprising that low pH levels are linked with high heavy metal concentrations. Firstly, the solubility of these increases with acidity; secondly, lower pH levels, in turn, trigger higher rates of mineral leaching, thereby contributing to a self-feeding vicious cycle whereby the concentration of heavy metals in solution increasingly escalates.

From a biological perspective, while no microbial presence was detected at point 7, there was indeed evidence of microorganisms at both other sampled sites in this area. Hence, point 6 is particularly interesting due to its remarkably extreme acidity, while point 8 is noteworthy for the maximum toxicity levels of heavy metals in solution that it bears.

On the other hand, Area D was found to have the mildest physicochemical conditions (relatively speaking, within the extremeness of the Rio Tinto environment). Except for point 14, which displayed a lower pH due to its location at the exit of an old tunnel, points 13 and 15 exhibited comparatively high pH values (average of 2.9 and 2.8, respectively). Accordingly, the toxicity Index at this point was not particularly high either, with average values of 20.4 and 21.0 at points 13 and 15, respectively. This is probably the case due to its proximity with the mouth of the Tintillo River; typically, there would be a downstream toxicity gradient due to the incorporation of leachates.

Regarding variations across the year, the study on the seasonal evolution of the physicochemical parameters revealed significant differences throughout the year. Firstly, the summer season was typically characterised by lower pH values, which were accompanied with higher heavy metal concentrations, especially towards the end of the summer. This may be explained by the negative balance of water during the summer months, both due to the minimal pluvial precipitations as well as the high evaporation levels as a result of the heat. Consequently, the effect of this is that ions in solution (both protons as well as dissolved heavy metals) become more concentrated, thereby making the physicochemical conditions even more extreme. Conversely, the rainier and colder seasons (i.e. late autumn, winter and early spring) are characterised by milder pH and toxicity levels, as the ions in solution are more diluted due to more abundant pluvial precipitations and lower levels of evaporation.

Finally, a crucial implication of the observations regarding the seasonal evolution of physicochemical parameters is that the restart of activity at the mine following 14 years of inactivity, in July 2015, was not detrimental for the environment. In first place, it was seen that the sampled sites already exhibited extremely harsh physicochemical conditions prior to the reopening of the mine, and hence are not the result of contamination from current mineral extraction and processing activities. Moreover, while the physicochemical conditions investigated did aggravate during the summer months, it was seen that this behaviour responded to the correlation observed between physicochemical parameters and pluvial precipitations/temperatures. Indeed, following the warmer, drier months of the year, the physicochemical parameters recorded during the autumn months proved to be less harsh than the levels of these observed prior to the reopening of the mine.

In conclusion, following an exhaustive investigation of physicochemical conditions throughout a series of sampling points within the Rio Tinto environment, the sites characterised with the harshest physicochemical conditions were determined (i.e. lowest pH and highest electrical conductivity and heavy metal content). The identification of these sites fulfils the first step required in the search for a set of naturally-occurring acidophiles that could be able to thrive in the most extreme physicochemical conditions possible within a BPV device. Moreover, the assessment of the evolution of the various parameters studied in this chapter confirmed that the reopening of the mine is not detrimental for the environment, from a physicochemical point of view.

5. Chapter 5: Biological Photovoltaic Cells based on naturally-occurring acidophilic biofilms from the Rio Tinto ecosystem

5.1. Sampling of acidophilic biofilms in the Rio Tinto ecosystem

The ultimate aim of the present study consists in the identification of naturally-occurring acidophilic biofilms that could putatively serve as the biological material in a BPV cell operating under the most extreme physicochemical conditions possible.

The purpose of this search is to find biofilms that are able to thrive under the unconventionally harsh conditions required in order to decrease the internal resistance of the BPV device as much as possible, i.e. elevated electrical conductivity, resulting from a highly acidic medium, rich in dissolved metals. Moreover, it is particularly important that the biological material is able to tolerate high levels of acidity, as in addition to increasing electrical conductivity, these enhance the activity of the cathode, by enabling it to utilise readily available protons in the reduction of oxygen that it catalyses, no longer limiting the electrical current of the BPV cell.

In order to find the extremophile microorganisms sought after in this study, an exhaustive physicochemical study of a variety of sites located throughout the Rio Tinto Environment was initially undertaken in order to lay the grounds of the search, as seen in Chapter 4. Subsequently, the physicochemical characterisation of the various sampling sites of choice was accompanied with a biological study of the evidence of microbial presence and diversity thereof, focusing on the site exhibiting the most extreme physicochemical conditions while bearing microbial presence, with the purpose of utilising it as the biological material in an in-situ BPV device, which is the subject of this chapter.

<u>Materials and Methods</u>

- Sample collection

In parallel to the observation of physicochemical parameters, the presence of living biofilms in the sixteen selected locations (along the Tinto River and nearby acid mine drainage sites) was investigated by means of optic microscopy. Epilithon samples were collected from each site every trimester, as described by Snoeijs and Snoeijs (1993).

- Identification of microorganisms

Identification of the eukaryotic microorganisms present in the samples was undertaken by direct microscopic observation. Both algae and protozoa were identified by looking at distinctive phenotypic features, which are described in previous studies of eukaryotic communities in the Tinto River (Amaral et al. 2002, Lopez-Archilla et al. 1999 and Lopez-Archilla et al. 2001). Based on this

identification, the average relative abundance of every species was calculated at each point.

- Total biomass abundance

Total biomass abundance was estimated directly from microscopic counts.

- Biological diversity

Biological diversity was estimated through Simpson's Index (Simpson, 1949), as described in Chapter 2.

Results

Area A: Drainage of the North Slagheap

- Point 1

Evidence of microbial presence was found at point one (located in the northernmost dam at the North Slagheap drainage area).

The total eukaryotic biomass abundance was estimated at this point, as shown in the following graph:

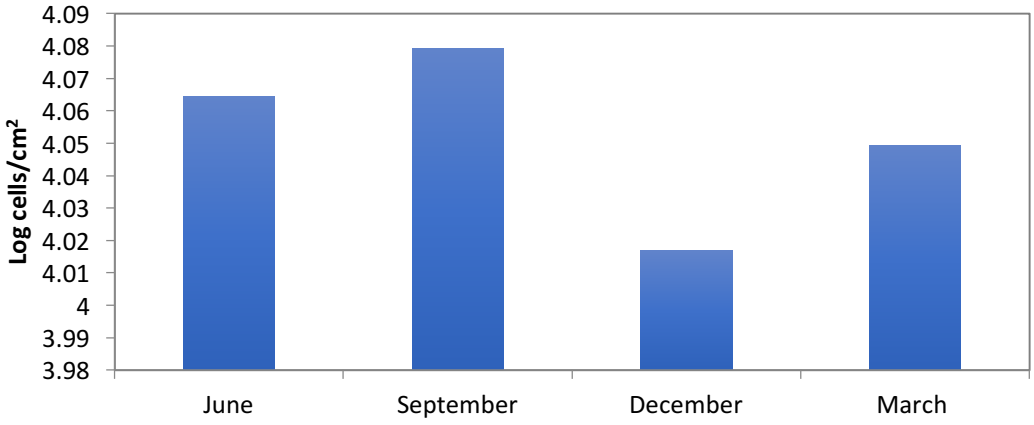

Figure 97: Graph showing total biomass abundance at point 1 during the months of June 2015, September 2015, December 2015 and March 2016.

Cell abundance was the highest in September (1.2×10^4), while it was lowest in December (1.0×10^4), probably due to temperature, primarily. However, it is worth noting that biomass abundance is fairly constant throughout the year.

At this point, the following eukaryotic species were identified: *Chlamydomonas* sp., *Euglena mutabilis*, *Cyanidium* sp., *Pinnularia* sp., *Zygnemopsis* sp., *Klebsordium* sp., *Chlorella* sp., *Dunaliella* sp., *Oxytrichia* sp., *Cercomonas* sp. and *Rotaria* sp.

The average relative abundance of the various identified eukaryotic species is shown in the following graph:

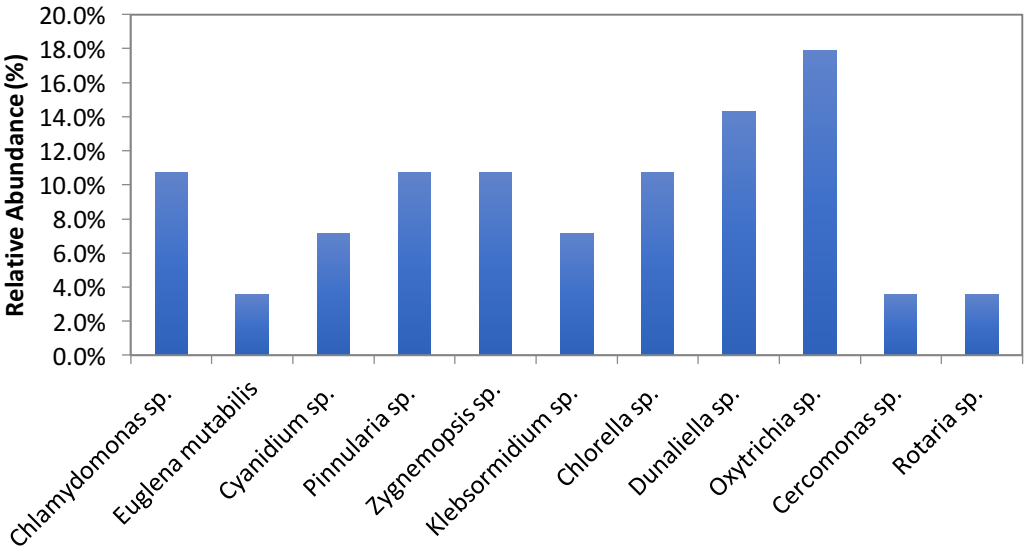

Figure 98: Graph showing the average relative abundance of the different species present at point 1.

At this point, the species found in the highest proportion was *Oxytrichia* sp., followed by *Dunaliella* sp. and *Chlamydomonas* sp., *Pinnularia* sp., *Zygnemopsis* sp., and *Chlorella* sp. In lower amounts, *Cyanidium* sp., *Klebsormidium* sp. , *Euglena mutabilis*, *Cercomonas* sp. and *Rotaria* sp. were found.

- Point 2

Again, microbial presence was identified at point two (located downstream of point one, by the filtrations through the northernmost dam at the North Slagheap drainage area).

In addition, the total biomass abundance was estimated at this point, as shown in the following graph:

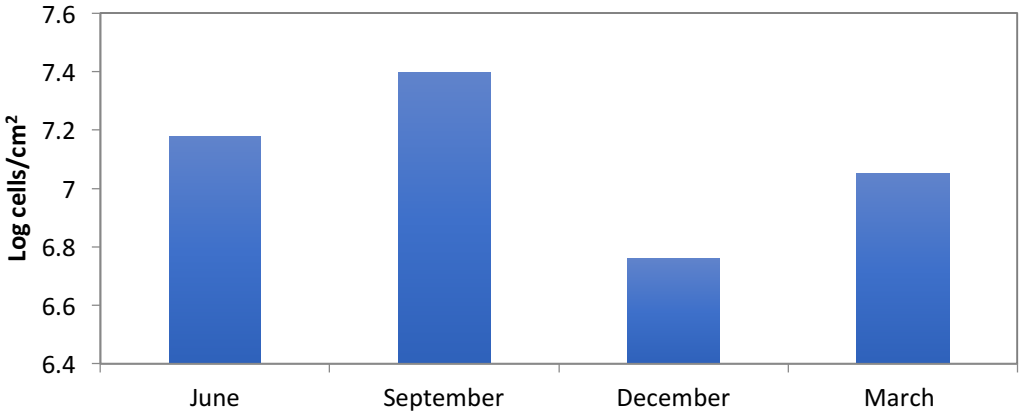

Figure 99: Graph showing total biomass abundance at point 2 during the months of June 2015, September 2015, December 2015 and March 2016.

Cell abundance was the highest in September (2.5×10^7), while it was lowest in December (5.8×10^6), probably due to temperature as well as pluvial precipitations (as the current at this point is rain-dependent).

At this site, biomass abundance varies significantly more than at point 1, possibly due to the higher physicochemical fluctuations.

At this point, the following eukaryotic species were identified: *Chlamydomonas* sp., *Euglena mutabilis*, *Cyanidium* sp., *Pinnularia* sp., *Zygnemopsis* sp., *Klebsordium* sp., *Chlorella* sp., *Dunaliella* sp., *Oxytrichia* sp. and *Labirynthula* sp.

The average relative abundance of the eukaryotic species observed at this site is shown in the following graph:

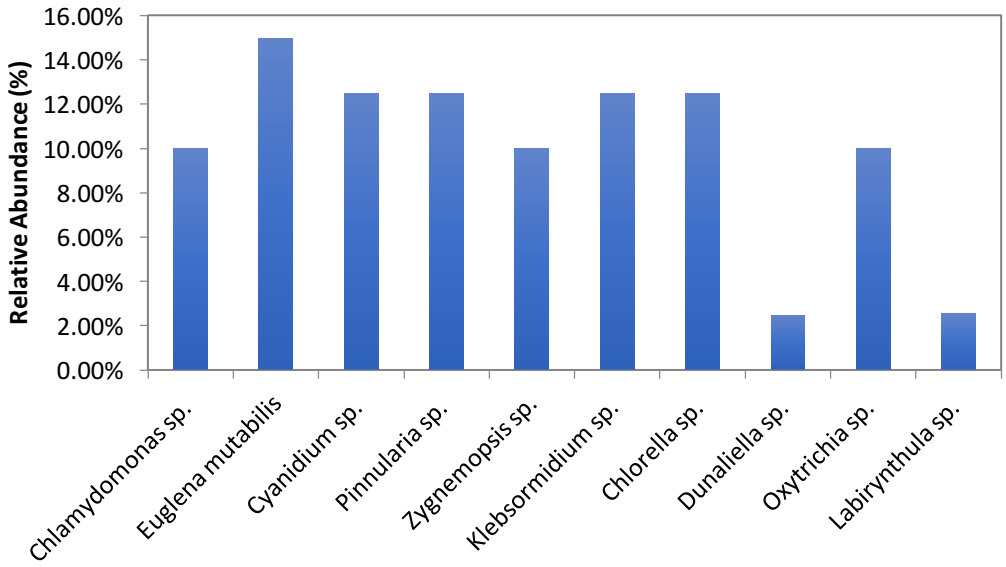

Figure 100: Graph showing the average relative abundance of the different species present at point 2.

At this point, the species found in the highest proportion was *Euglena mutabilis*, followed by *Cyanidium* sp., *Pi*nnularia sp., *Klebsormidium* sp. and *Chlorella* sp.

At slightly lower proportions, *Chlamydomonas* sp., *Zygnemopsis* sp. and *Oxytrichia* sp. were found. Finally, *Dunaliella* sp. and *Labirynthula* sp. were present in relatively very low numbers.

- Point 3

Sampling at point 3 (located in the southernmost dam at the North Slagheap drainage area) revealed the presence of microorganisms at this site.

Point 3 is analogous to point 1, as both emplacements are located in dams resulting from drainage of the North Slagheap. Hence, as is the case for physicochemical conditions, which are very similar at both sites, we would expect these to be similar on a microbiological level as well.

Biomass abundance was again estimated at this point, as depicted in the following graph:

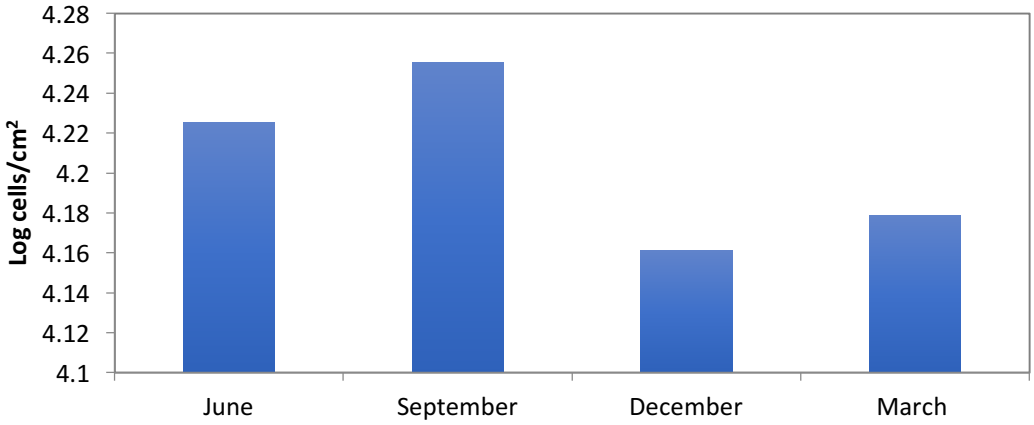

Figure 101: Graph showing total biomass abundance at point 3 during the months of June 2015, September 2015, December 2015 and March 2016.

Cell abundance was the highest in September (1.8×10^4), while it was lowest in December (1.5×10^4), again most likely as a consequence of temperature, primarily. As for point 1, biomass abundance is fairly constant throughout the year. In fact, both points present very similar microbiological patterns, which is to be expected from the highly similar physicochemical characteristics and emplacements.

At this point, the following eukaryotic species were identified: *Chlamydomonas* sp., Pinnularia sp., *Zygnemopsis* sp., *Klebsordium* sp., *Chlorella* sp., *Dunaliella* sp., *Oxytrichia* sp. and *Cercomonas* sp. Their average relative abundance is shown in the following graph:

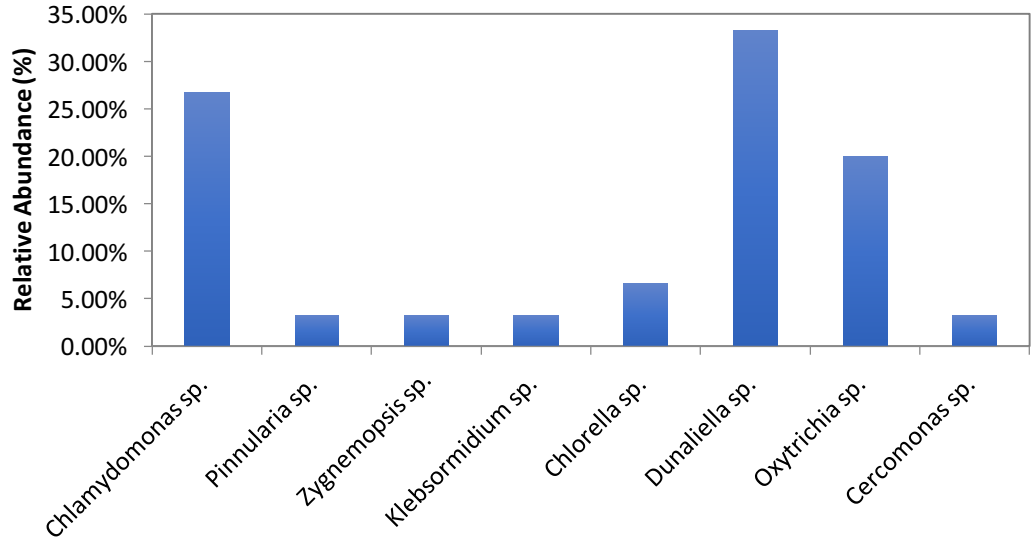

Figure 102: Graph showing the average relative abundance of the different species present at point 3.

At this point, the predominant species was *Dunaliella* sp, followed by *Chlamydomonas* sp. and *Oxytrichia* sp. In lower quantities, *Chlorella* sp. and *Cercomonas* sp. are found, followed by *Pinnularia* sp., *Zygnemopsis* sp., *Klebsormidium* sp. and *Cercomonas* sp. in even lower numbers.

- Point 4

Again, microbial presence was identified at point 4 (located downstream of point three, by the filtrations through the southernmost dam at the North Slagheap drainage area).

As was the case for point 3 and point 1, this site is analogous to point 2, given that both emplacements are located by the filtrations arising from the North Slagheap drainage dams. Therefore, in the same way as the physicochemical conditions of these two points are highly similar, it is to be expected for point 4 to resemble point 2 on a microbiological level too.

Total biomass abundance was estimated at this point, as shown in the following graph:

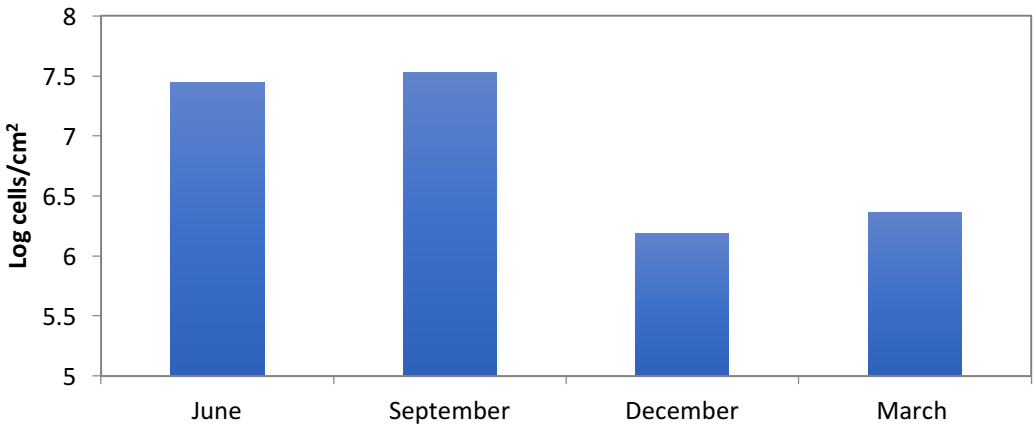

Figure 103: Graph showing total biomass abundance at point 4 during the months of June 2015, September 2015, December 2015 and March 2016.

Cell abundance was the highest in September (3.4×10^7), while it was lowest in December (1.5×10^6).

As expected, similarly to its behaviour at point 2 vs. point 1, biomass abundance varies significantly more at this site than at point 3, again possibly due to the larger physicochemical fluctuations.

At this point, the following eukaryotic species were identified: *Chlamydomonas* sp., *Zygnemopsis* sp., *Kleb*sordium sp., *Chlorella* sp., *Dunaliella* sp., *Oxytrichia* sp., *Cercomonas* sp, *Labirynthula* sp. and *Rotaria* sp.

The average relative abundance of the eukaryotic fauna is shown in the following graph:

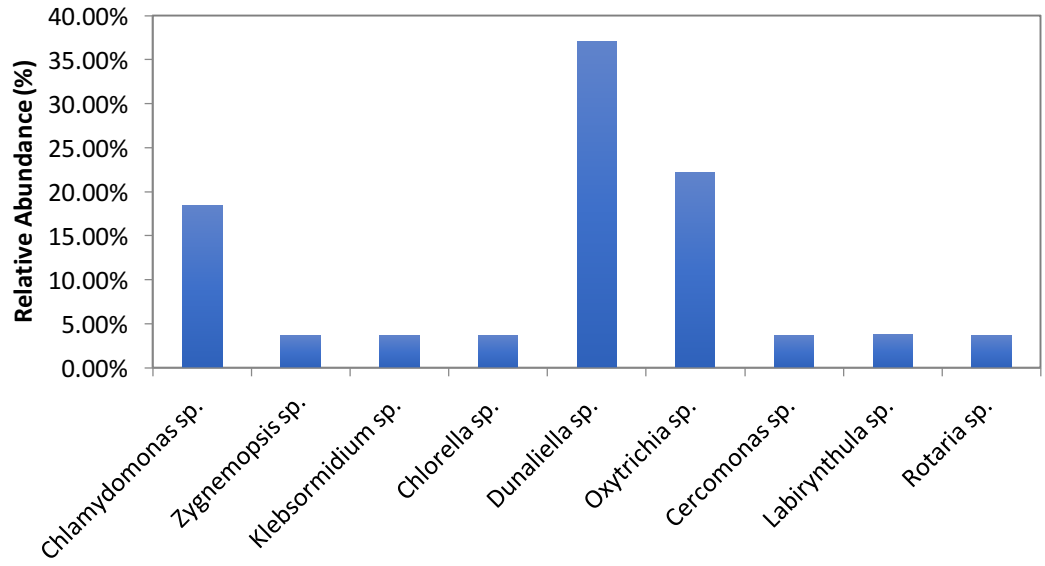

Figure 104: Graph showing the average relative abundance of the different species present at point 4.

At this site, the predominant species was *Dunaliella* sp, followed by *Oxytrichia* sp. and *Chlamydomonas* sp. Finally, *Zygnemopsis* sp., *Klebsormidium* sp., *Chlorella* sp., *Cercomonas* sp., *Labirynthula* sp. and *Rotaria* sp. were found in lower numbers.

- Point 5

As for points 1-4, microbial presence was identified at this site (a filtration stream coming from the southernmost dam, which passes through the old cementation plant).

Total biomass abundance was estimated at this point, as shown in the following graph:

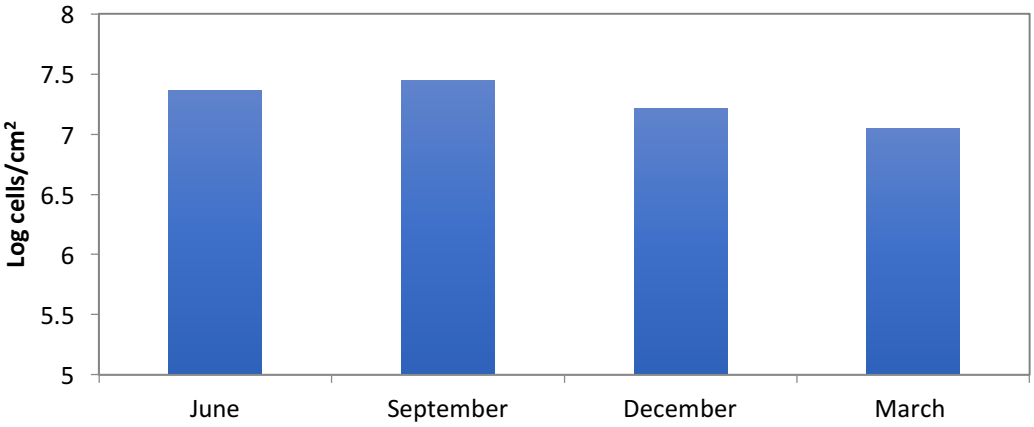

Figure 105: Graph displaying total biomass abundance at point 5 during the months of June 2015, September 2015, December 2015 and March 2016.

Cell abundance was the highest in September (2.8 x 10^7), while it was lowest in March (1.1 x 10^7). Alike at the filtration dams, biomass is fairly constant throughout the year, given the smaller fluctuations.

At this point, the following eukaryotic species were identified: *Chlamydomonas* sp., *Cyanidium* sp., *Pinnularia* sp., *Chlorella* sp., *Dunaliella* sp., *Oxytrichia* sp. and *Labirynthula*. Their average relative abundance is shown in the following graph:

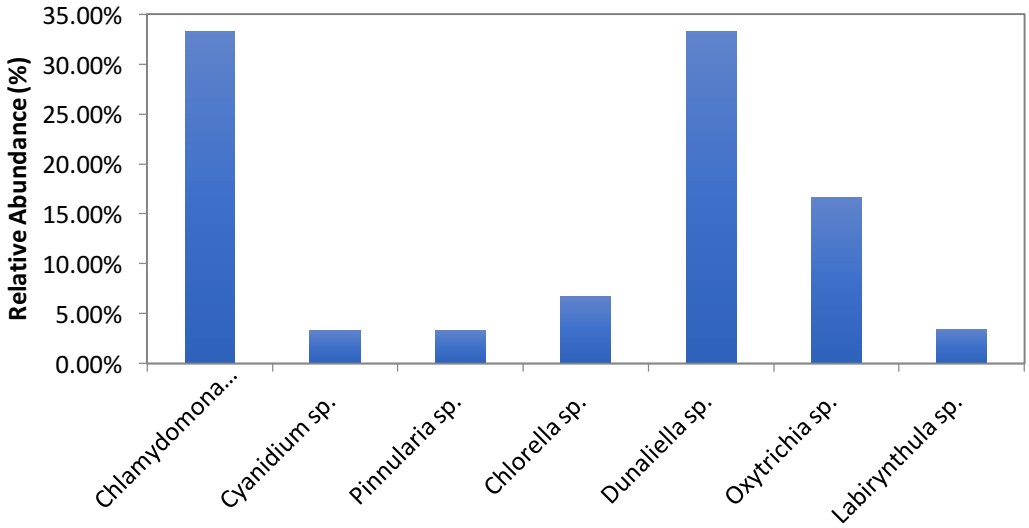

Figure 107: Graph showing the average relative abundance of the different species present at point 5.

At this point, the predominant species were *Chlamydomonas* sp. and *Dunaliella* sp. Secondly, *Oxytrichia* sp. was present in medium numbers, whilst *Chlorella* sp., *Cyanidium* sp., *Pinnularia* sp. and *Labirynthula* sp. were present in low numbers.

Area B: Tunnel 5 and North Slagheap drainage

Area B is of great interest, as the physicochemical study undertaken previously revealed that the locations exhibiting the most extreme conditions out of the chosen sampling sites are encountered in this area.

In particular, the lowest pH was recorded at point 6, while the highest electrical conductivity as well as the maximum Toxicity Index were observed at point 8.

Therefore, should evidence of microbial presence be found at these points, they would be ideal for the next step in order to fulfil the ultimate aim of this study, which consists in the implementation of an in-situ BPV cell at the most extreme site, from a physicochemical perspective, which hosts microbial life.

- Point 6

Evidence of microbial presence was found at point 6 (located at the exit of Tunnel 5; the effluent travelling across this tunnel originates from the flooded Lago open pit).

As usual, biomass abundance was estimated at this point, as shown in the following graph:

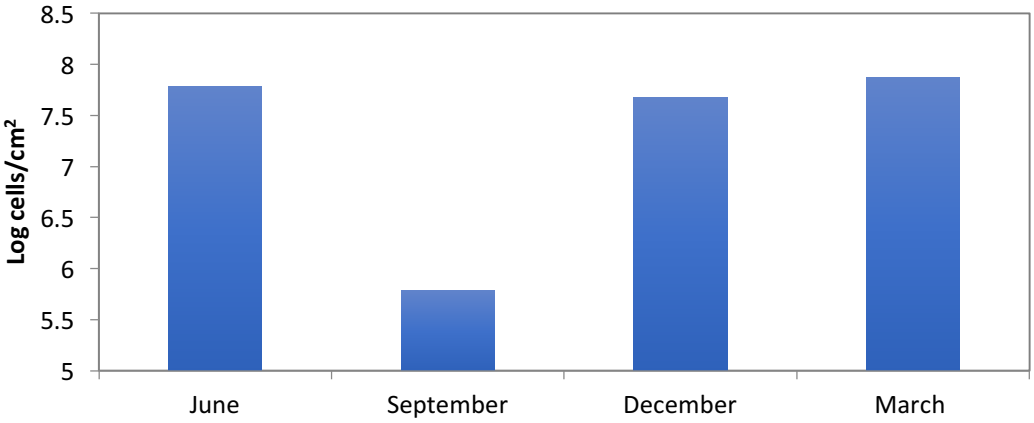

Figure 108: Graph displaying total biomass abundance at point 6 during the months of June 2015, September 2015, December 2015 and March 2016.

Cell abundance was the highest in March (7.9 x 10^7), while it was lowest in September (5.8 x 10^5). At this point, the dry conditions of the summer meant that there was very little current in September, compromising microbial viability.

At this location, the following eukaryotic species were identified: *Euglena mutabilis*, *Cyanidium* sp., *Pinnularia* sp., *Zygnemopsis* sp., *Klebsormidium* sp., *Dunaliella* sp., *Oxytrichia* sp., *Rotaria* sp. and *Naegleria* sp. Their average relative abundance is shown in the following graph:

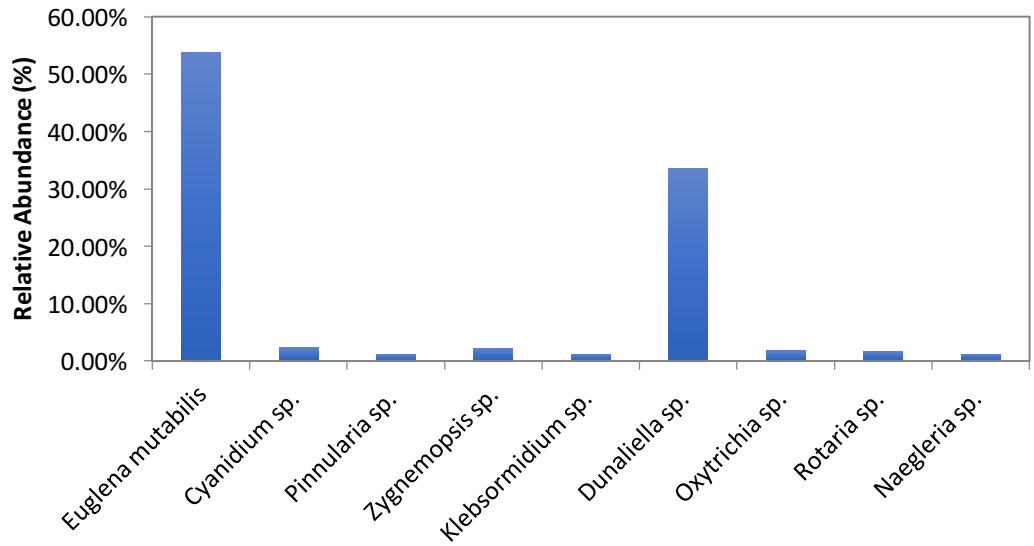

Figure 109: Graph illustrating the average relative abundance of the different species present at point 6.

At this point, the predominant species were *Euglena mutabilis*, in first place, followed by *Dunaliella* sp., in second place. A suite of other species were also present

in very low numbers: *Cyanidium* sp., *Pinnularia* sp., *Zygnemopsis* sp., *Klebsormidium* sp., *Oxytrichia* sp., *Rotaria* sp. and *Naegleria* sp.

- Point 7

At point 7 (located at an effluent arising from North Slagheap drainage filtrations), direct microscopic screening revealed no microbial presence. This is possibly due to the very high current flowing at this stream, which makes it incredibly difficult for biofilms to form, and is reflected in the very low detected oxygen levels in solution.

- Point 8

Sampling at point 8 (located downstream of the confluence between the effluents proceeding from the North Slagheap drainage filtrations and Tunnel 5) revealed the presence of microorganisms at this site.

Estimated biomass abundance at this point is shown in the following graph:

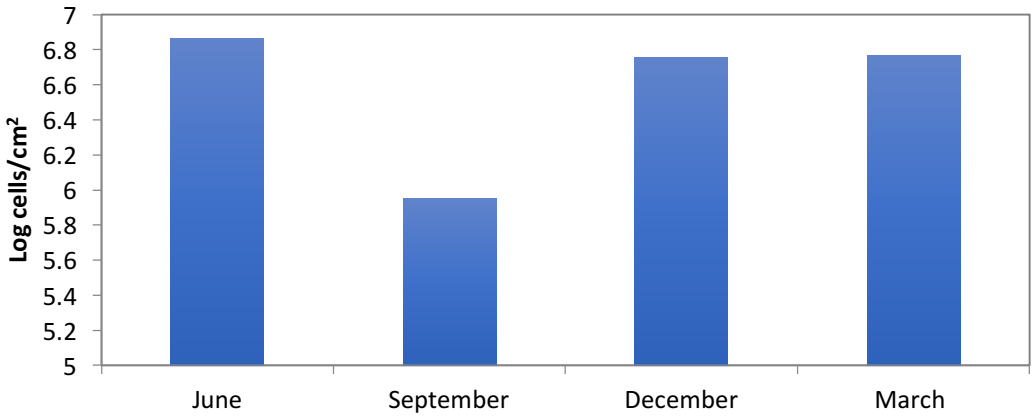

Figure 110: Graph displaying total biomass abundance at point 8 during the months of June 2015, September 2015, December 2015 and March 2016.

Cell abundance was the highest in June (7.2×10^6), while it was lowest in September (5.9×10^5).

The evolution of biomass at this point is similar to the exit of Tunnel 5 (point 6), with the difference that the effect of the summer is mitigated at point 8, due to the drainage effluent component (the minimum value of total biomass observed in September is higher at point 8 than at point 6).

At this point, the following eukaryotic species were identified: *Chlamydomonas* sp., *Euglena mutabilis*, *Cyanidium* sp., *Pinnularia* sp., *Zygnemopsis* sp., *Klebsormidium* sp., *Chlorella* sp., *Dunaliella* sp., *Oxytrichia* sp. and *Naegleria* sp.

The average relative abundance of the various species found at this site is shown in the following graph:

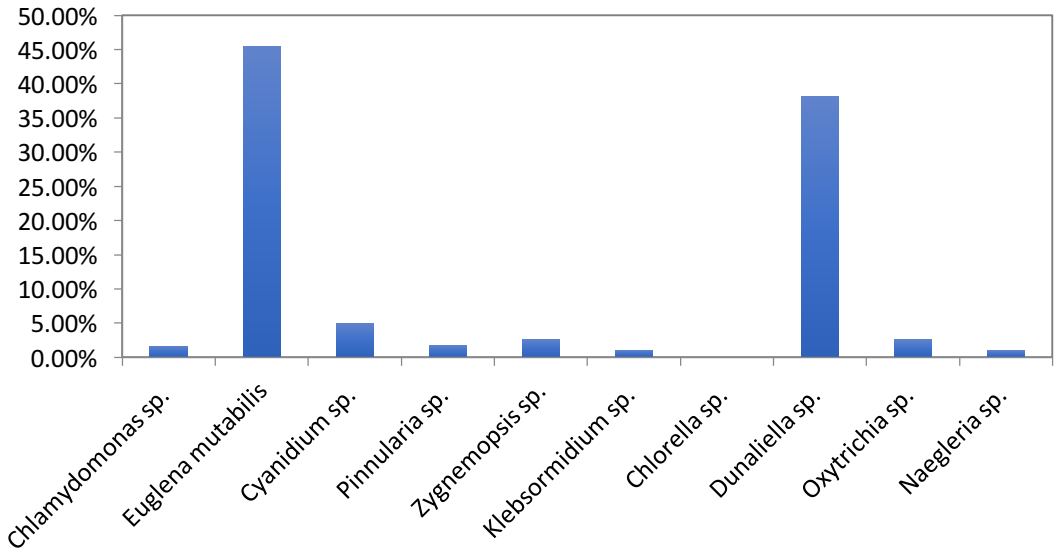

Figure 111: Graph showing the average relative abundance of the different species present at point 8.

At this point, similarly to the exit of tunnel 5, the species present in higher numbers were *Euglena mutabilis* and *Dunaliella* sp. In lower numbers, the following species were found: *Cyanidium* sp., followed by *Zygnemopsis* sp., *Oxytrichia* sp., *Chlamydomonas* sp., *Pinnularia* sp., *Klebsormidium* sp., *Naegleria* sp. and *Chlorella* sp.

Area C: Tunnel 11, North Slagheap drainage and train area

This area is located by an abandoned railway tunnel that was originally used to transport mineral from the Cerro Colorado open pit to a processing plant in Huelva.

This emplacement is similar to Area B, as an acid mine drainage current that travels through the abandoned tunnel traverses this area, bearing elevated concentrations of metals in a very acidic solution.

However, despite being notably extreme, the physicochemical conditions observed in this area are milder than those found at Area B.

- Point 9

Evidence of microbial presence was found at point 9 (located by the old train station, at an effluent coming from Tunnel 11).

Again, biomass abundance was estimated at this point, as shown in the following graph:

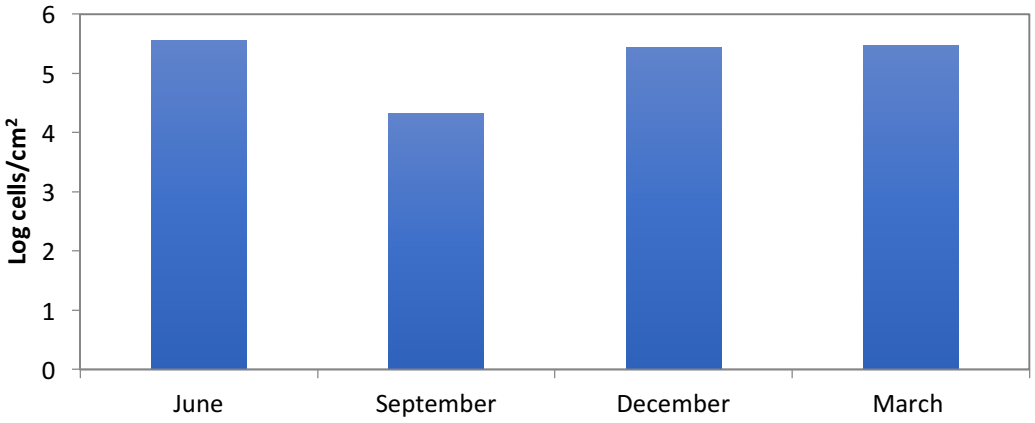

Figure 112: Graph displaying total biomass abundance at point 9 during the months of June 2015, September 2015, December 2015 and March 2016.

Cell abundance was the highest in June (3.6×10^5), while it was lowest in September (2.1×10^4). This pattern is similar to points 6 and 8; the effect of the dry season is evidenced by the drop in biomass that is observed in September.

At this point, the following eukaryotic species were identified: *Chlamydomonas* sp., *Euglena mutabilis*, *Cyanidium* sp., *Pinnularia* sp., *Zygnemopsis* sp., Klebsormidi*um* sp., *Chlorella* sp., *Dunaliella* sp and *Oxytrichia* sp.

Their average relative abundance is shown in the following graph:

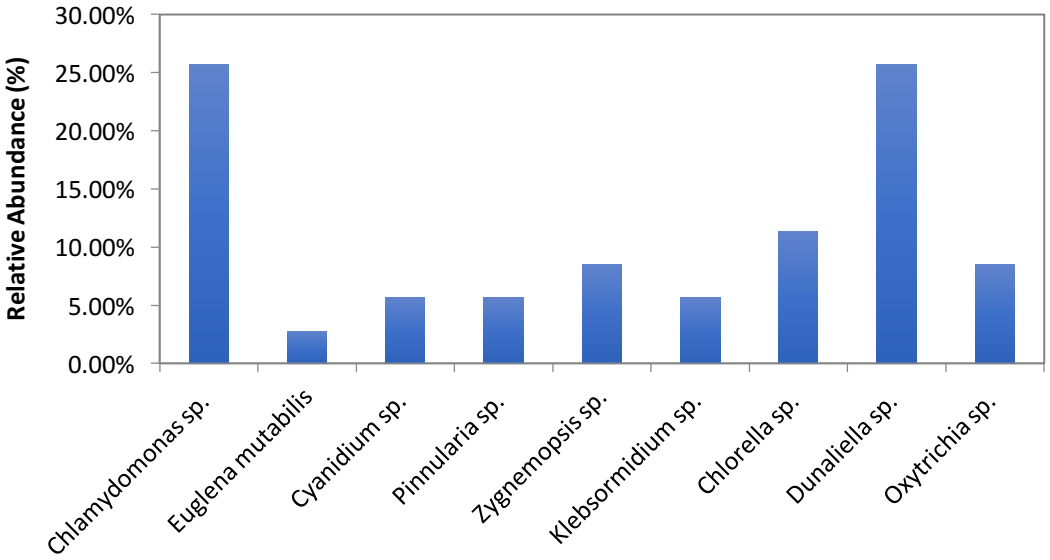

Figure 113: Graph showing the average relative abundance of the different species present at point 9.

At this point, the predominant species were *Chlamydomonas* sp. and *Dunaliella* sp.

The rest of the species were present in lower numbers (*Chlorella* sp. followed by *Zygnemopsis* sp., *Oxytrichia* sp., *Cyanidium* sp., *Pinnularia* sp., *Klebsormidium* sp. and *Euglena mutabilis)*.

- Point 10

As for point 9, evidence of microbial presence was found at this site (located by the effluent coming from Tunnel 11, after a stream with residual waters has merged with it; it is of considerable interest due to the fact that the residual waters are particularly rich in organic compounds, contributing to the diversity of the microbial community).

As usual, biomass abundance was estimated at this point, and is shown in the following graph:

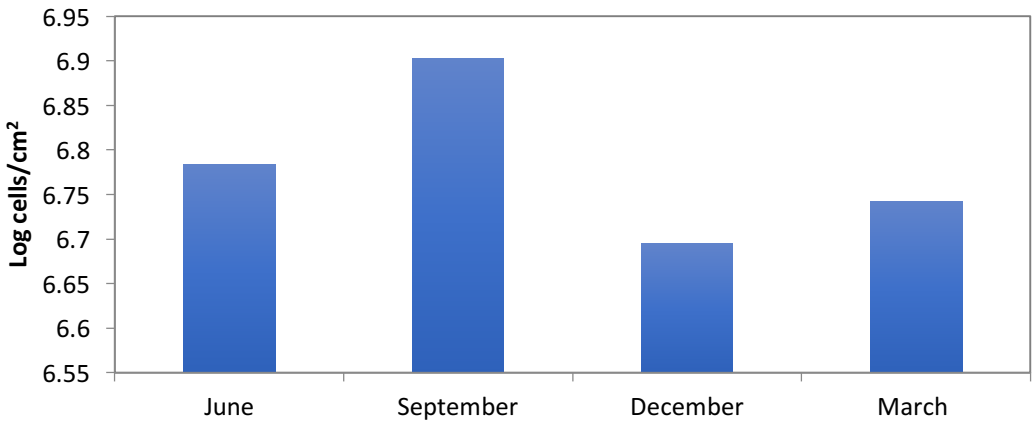

Figure 114: Graph displaying total biomass abundance at point 10 during the months of June 2015, September 2015, December 2015 and March 2016.

Cell abundance was the highest in June (7.9×10^6), while it was lowest in December (4.8×10^6).

The biomass amount observed at this point is higher than that seen at point 9, possibly due to the addition of the residual water stream constituting an input of organic matter.

At this point, the following eukaryotic species were identified: *Chlamydomonas* sp., *Euglena mutabilis*, *Cyanidium* sp., *Pinnularia* sp., *Zygnemopsis* sp., *Klebsormidium* sp., *Chlorella* sp., *Dunaliella* sp., *Cercomonas* sp., *Labirynthula* sp., *Rotaria* sp., *Vahlkampfia* sp. and *Naegleria* sp.

The average relative abundance of the different species is shown in the following graph:

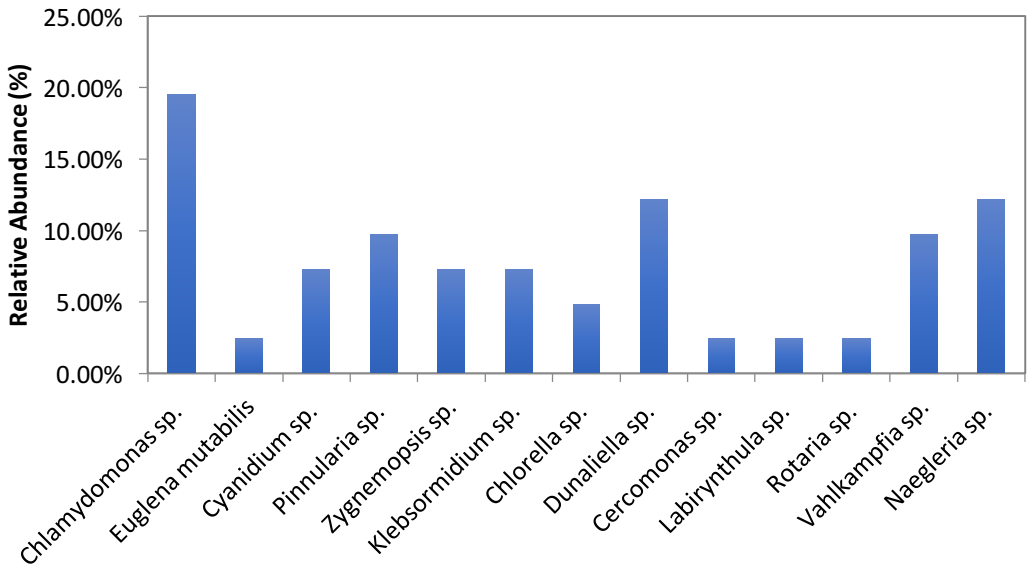

Figure 115: Graph showing the average relative abundance of the different species present at point 10.

At this point, the predominant species was *Chlamydomonas* sp. Secondly, a few species were found in middle numbers; *Dunaliella* sp., *Naegleria* sp., *Pinnularia* sp., *Vahlkampfia* sp., *Cyanidium* sp., *Zygnemopsis* sp., and *Klebsormidium* sp. In low numbers, *Euglena mutabilis*, *Chlorella* sp., *Cercomonas* sp., *Labirynthula* sp. and *Rotaria* sp. were present.

- Point 11

Again, microbial presence was detected at point 11 (located on the effluent from Tunnel 11, downstream of point 9 and after a stream from North Slagheap filtration drainage has merged with the initial effluent).

Microbial abundance was estimated at this point, as shown in the following graph:

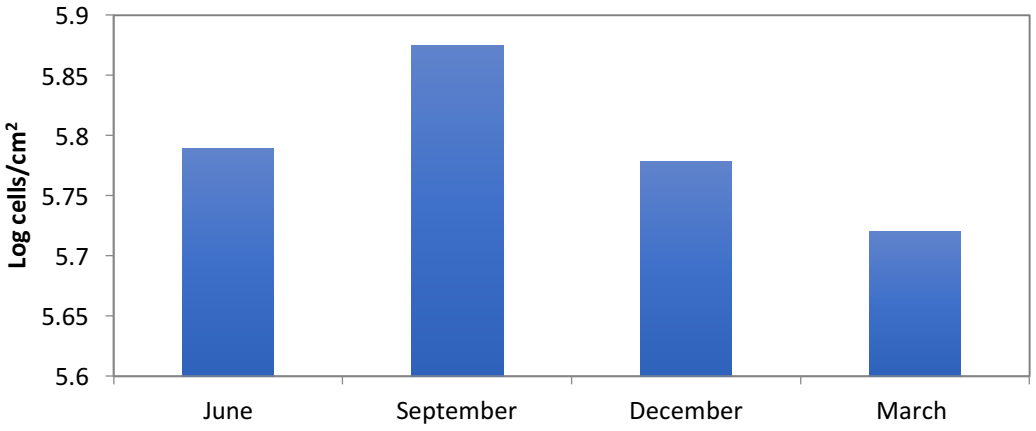

Figure 116: Graph displaying total biomass abundance at point 11 during the months of June 2015, September 2015, December 2015 and March 2016.

Cell abundance was the highest in September (7.5×10^5), while it was lowest in March (5.2×10^5).

The biomass observed at this point is fairly constant throughout the year, reflecting the little fluctuation in current and physicochemical conditions inflicted by the weather.

At this point, the following eukaryotic species were identified: *Chlamydomonas* sp., *Euglena mutabilis*, *Cyanidium* sp., *Pinnularia* sp., *Zygnemopsis* sp., *Klebsormidium* sp., *Chlorella* sp., *Dunaliella* sp., *Oxytrichia* sp. and *Labirynthula* sp.

The average relative abundance of the different species is shown in the following graph:

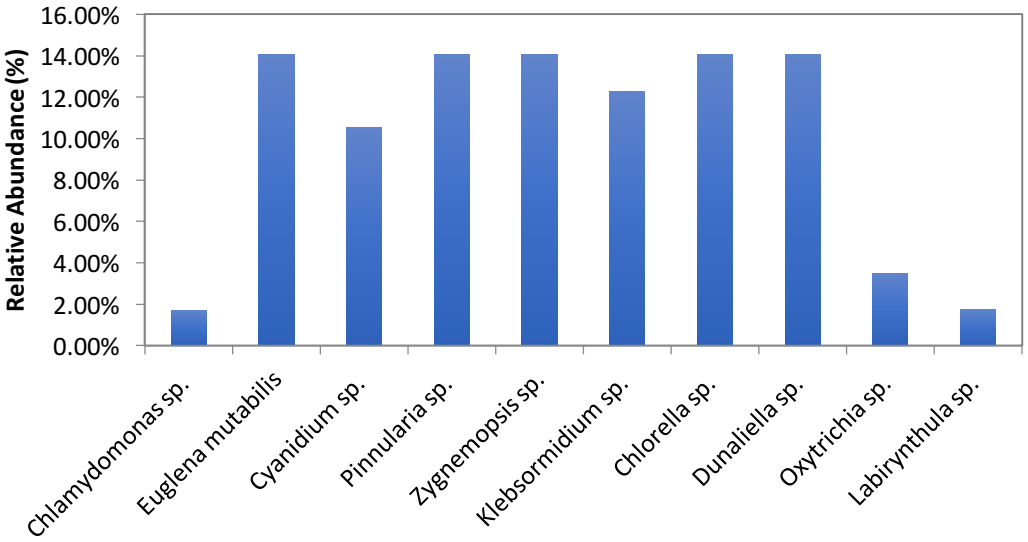

Figure 117: Graph showing the average relative abundance of the different species present at point 11.

At this point, seven species were present in similar high quantities: *Euglena mutabilis*, *Pinnularia* sp., *Zygnemopsis* sp., *Chlorella* sp. and *Du*naliella sp. followed by *Klebsormidium* sp. and *Cyanidium* sp. The remaining three species were present in very low quantities: *Oxytrichia* sp., *Chlamydomonas* sp. and *Labirynthula* sp.

- Point 12

Sampling at point 12 revealed the presence of microorganisms at this site (located on the effluent from Tunnel 11, downstream of points 9, 10 and 11, by the new train station).

As point 12 is located downstream point 11 and relatively close to it (about 300 feet apart, at the other side of a short tunnel), we would expect both sites to be alike from a biological perspective, given as well that both are similar from a physicochemical point of view, as seen in Chapter 4.

As usual, microbial abundance was estimated at this point, as shown in the following graph:

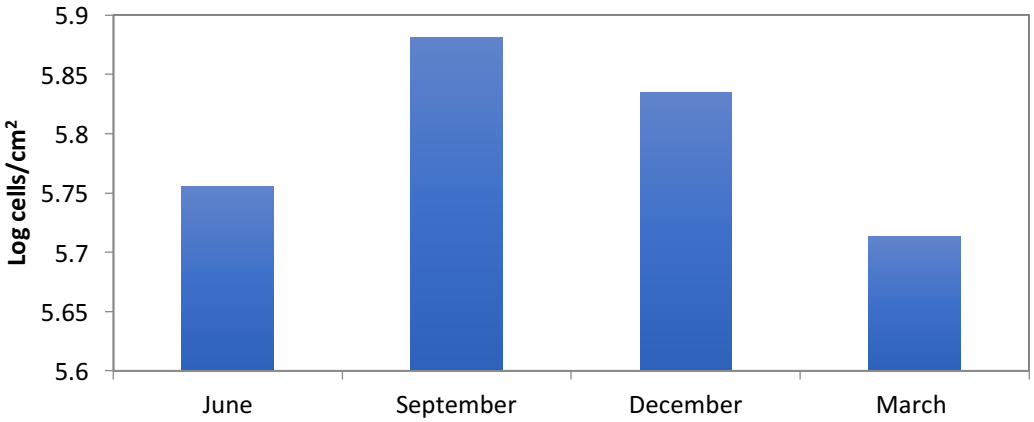

Figure 118: Graph displaying total biomass abundance at point 12 during the months of June 2015, September 2015, December 2015 and March 2016.

Cell abundance was the highest in September (7.6 x 10^5), while it was lowest in December (6.8 x 10^6). The biomass observed at this point is remarkably similar to that at point 11, reflecting the very similar physicochemical conditions at both points, as expected.

At this point, the following eukaryotic species were identified: *Chlamydomonas* sp., *Euglena mutabilis*, *Cyanidium* sp., *Pinnularia* sp., *Zygnemopsis* sp., *Klebsormidium* sp., *Chlorella* sp., *Dunaliella* sp., *Oxytrichia* sp., *Cercomonas* sp., *Labirynthula* sp. and *Rotaria* sp. The average relative abundance of the different species is shown in the following graph:

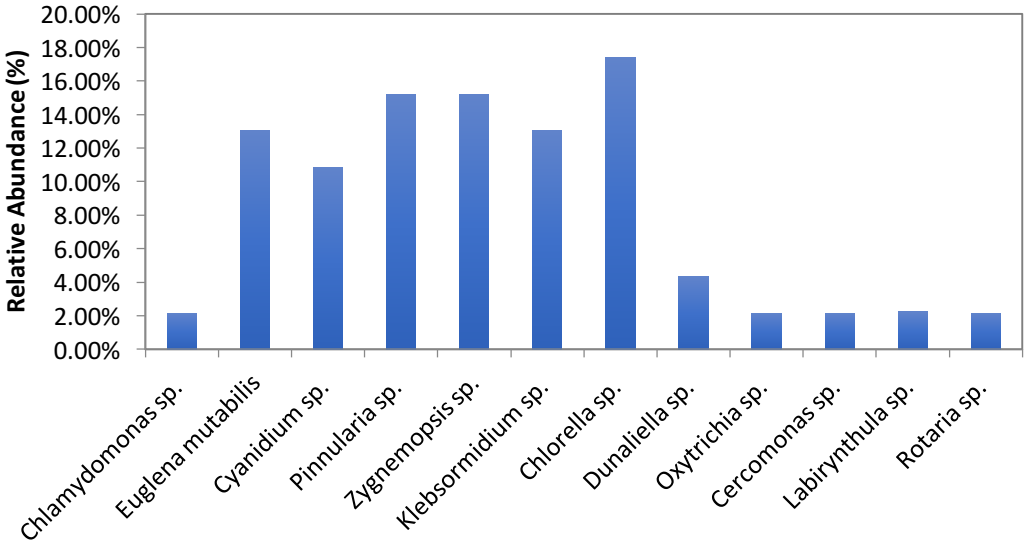

Figure 119: Graph showing the average relative abundance of the different species present at point 12.

At this point, six species were present in similar high quantities: *Euglena mutabilis*, *Cyanidium* sp., *Pinnularia* sp., *Zygnemopsis* sp., *Klebsormidium* sp. and *Chlorella* sp.

The remaining six species were present in low quantities: *Chlamydomonas* sp., *Dunaliella* sp., *Oxytrichia* sp., *Cercomonas* sp., *Labirynthula* sp. and *Rotaria* sp.

Area D: Atalaya Slagheap drainage, Gangosa stream and Tintillo River area

Area D is found by the Atalaya Slagheap, west of the open pit, which is currently flooded.

As the sampling sites in this area correspond to filtration and acid mine drainage streams, we would expect these to exhibit high acidity as well as bearing high levels of leached metals in solution. However, this area was found to exhibit the mildest physicochemical conditions out of all the sampled areas, and is characterised by relatively high pH levels (except for point 14), accompanied with comparatively low Toxicity Index values.

- Point 13

Evidence of microbial presence was found at point 13 (located at an effluent originating from the Atalaya Slagheap filtration drainage, coinciding with the head of the Tintillo River).

Microbial abundance was estimated at this point, as shown in the following graph:

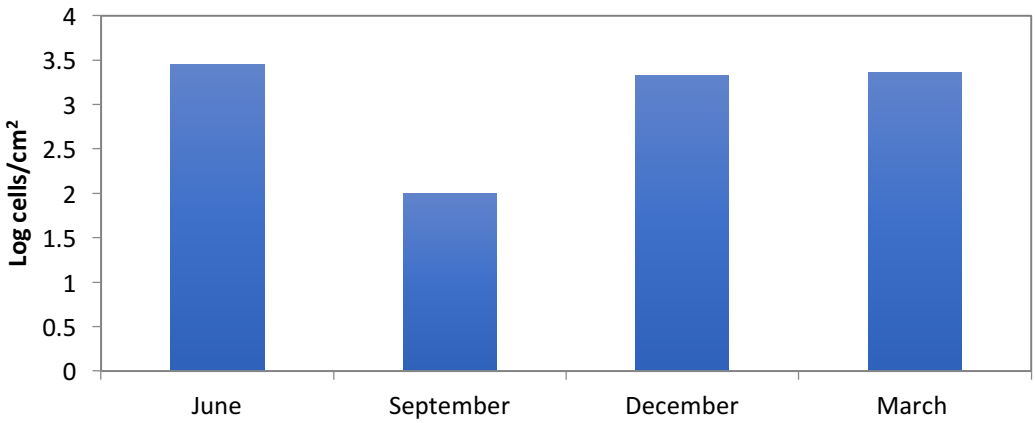

Figure 120: Graph displaying total biomass abundance at point 13 during the months of June 2015, September 2015, December 2015 and March 2016.

Cell abundance was the highest in June (2.8×10^3), while it was lowest in September (1.0×10^2). Therefore, microorganisms were present in very small densities at this point in comparison with the rest of the sampling sites, which is interesting given the fact that physicochemical conditions at this location are relatively mild.

In addition, a strong influence of the physicochemical parameters on the biomass present is observed at this point, given its high exposure to its fluctuations.

At this point, a number of eukaryotic species were identified; their average relative abundance is shown in the following graph:

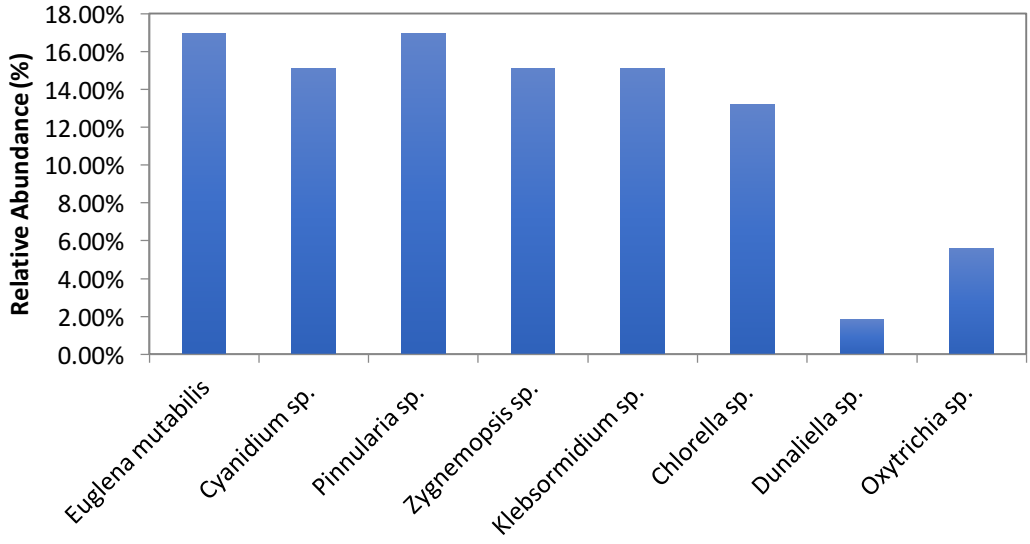

Figure 121: Graph showing the average relative abundance of the different species present at point 13.

At point 13, six species were present in similar high quantities: *Euglena mutabilis*, *Cyanidium* sp., *Pinnularia* sp., *Zygnemopsis* sp., *Klebsormidium* sp. and *Chlorella* sp. The other two species present appeared in low quantities: *Dunaliella* sp. and *Rotaria* sp.

- Point 14

The presence of microorganisms was detected at this point (located at the exit of an old railway tunnel, emerging from the Atalaya open pit).

Microbial abundance was estimated at this sampling site, as shown in the following graph:

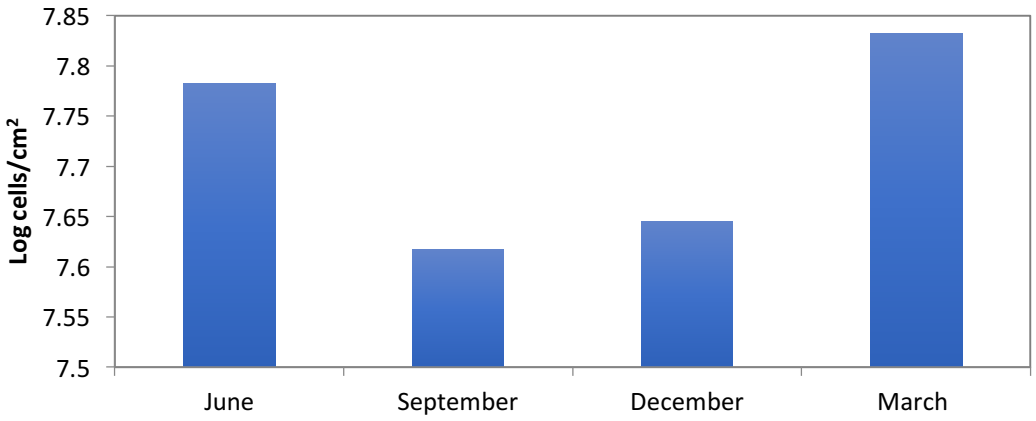

Figure 122: Graph displaying total biomass abundance at point 14 during the months of June 2015, September 2015, December 2015 and March 2016.

Cell abundance was the highest in March (6.8 x 10^7), while it was lowest in September (4.1 x 10^7). This is similar to the pattern observed at point 6; the dryness of the summer translates into lower cell numbers by the end of the warm period.

At this point, the following eukaryotic species were identified: *Euglena mutabilis*, *Cyanidium* sp., *Pinnularia* sp., *Klebsormidium* sp., *Dunaliella* sp., *Oxytrichia* sp., *Cercomonas* sp., *Labirynthula* sp., *Rotaria* sp., *Vahlkampfia* sp. and *Naegleria* sp.

Thei average relative abundance of the various eukaryotic species identified at this site is shown in the following graph:

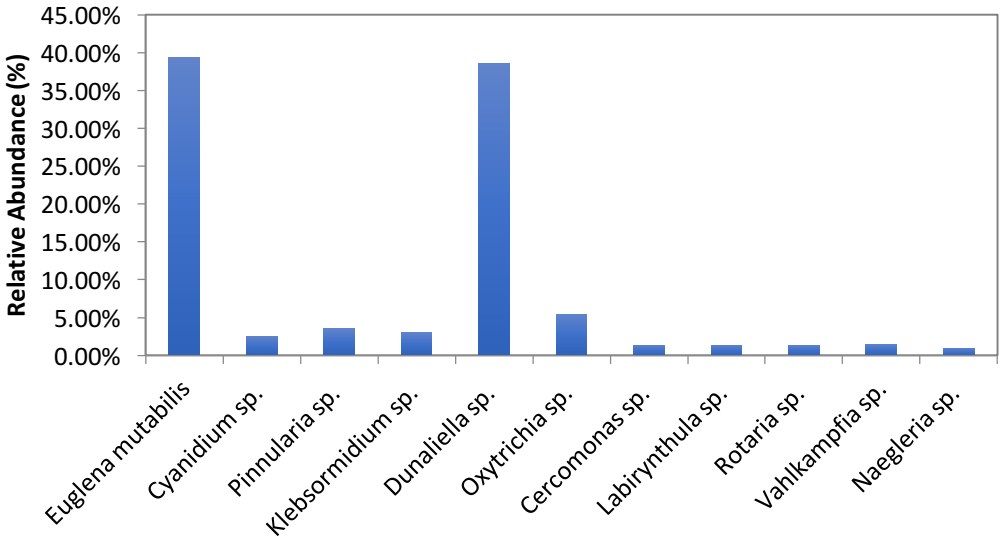

Figure 123: Graph showing the average relative abundance of the different species present at point 14.

At this point, both *Euglena mutabilis* and *Dunaliella* sp. were the dominant species, as was the case at the exit of Tunnel 5 (point 6) and downstream (point 8).

In lower numbers, the following species were found: *Cyanidium* sp., *Pinnularia* sp., *Klebsormidium* sp., *Oxytrichia* sp., *Cercomonas* sp., *Labirynthula* sp., *Vahlkampfia* sp. and *Naegleria* sp.

- Point 15

The presence of microorganisms was again identified at point 15 (located at a stream called La Gangosa, which arises from drainage of the Atalaya Slagheap filtrations).

This point is particularly interesting from a biological point of view, due to the observation that it displays the highest microbial diversity, as revealed by Simpson's coefficient (seen further ahead in this chapter). It is logical that the highest microbial diversity is found in Area D, given that the relatively milder physicochemical conditions found in this area enable a wider microbial range in comparison with the restricted diversity found in other areas, as a result of their tougher and thus more limiting physicochemical conditions.

As usual, microbial abundance was estimated at this point, as shown in the following graph:

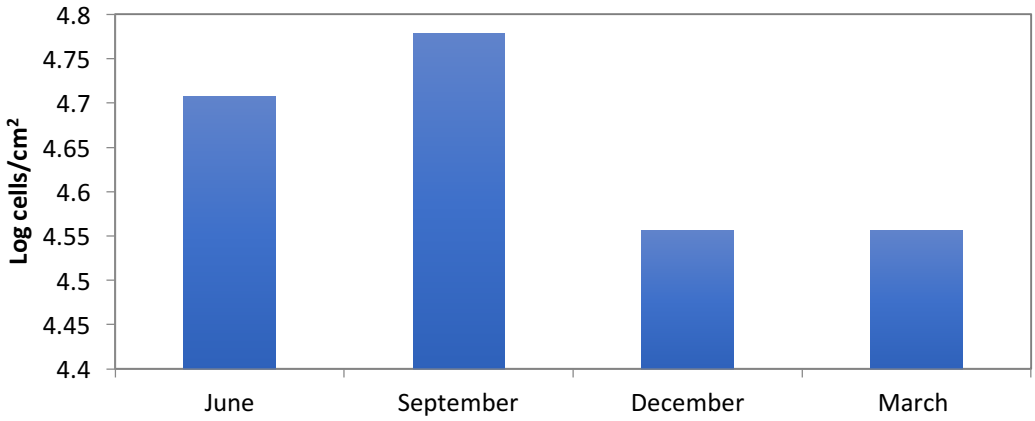

Figure 124: Graph displaying total biomass abundance at point 15 during the months of June 2015, September 2015, December 2015 and March 2016.

Cell abundance was the highest in September (6.0×10^4), while it was lowest in December (3.6×10^4).

At this point, the following eukaryotic species were identified: *Euglena mutabilis*, *Cyanidium* sp., *Pinnularia* sp., *Zygnemopsis* sp., *Klebsormidium* sp., *Chlorella* sp., *Dunaliella* sp., *Oxytrichia* sp., *Cercomonas* sp., *Labirynthula* sp., *Rotaria* sp., *Vahlkampfia* sp. and *Naegleria* sp. The average relative abundance of the different species is illustrated in the following graph:

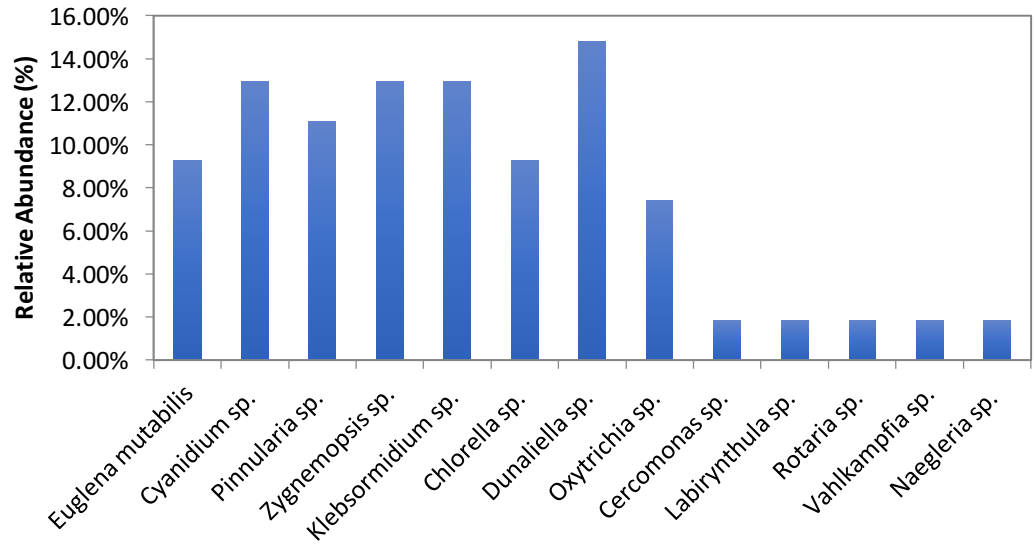

Figure 125: Graph showing the average relative abundance of the different species present at point 15.

At this point, eight species were present in high numbers: *Euglena mutabilis*, *Cyanidium* sp., *Pinnularia* sp., *Zygnemopsis* sp., *Klebsormidium* sp., *Chlorella* sp., *Dunaliella* sp. and *Oxytrichia* sp. In lower numbers, *Cercomonas* sp., *Labirynthula* sp., *Rotaria* sp., *Vahlkampfia* sp. and *Naegleria* sp. were found.

Area E: Tintillo River by the zone of confluence of drainages

- Point 16

Lastly, evidence of microbial presence was detected at point 16 (located downstream of Area D, by the Tintillo River, following the confluence of various drainages originating from filtrations through the Atalaya Slagheap). Microbial abundance was estimated at this point, as shown in the following graph:

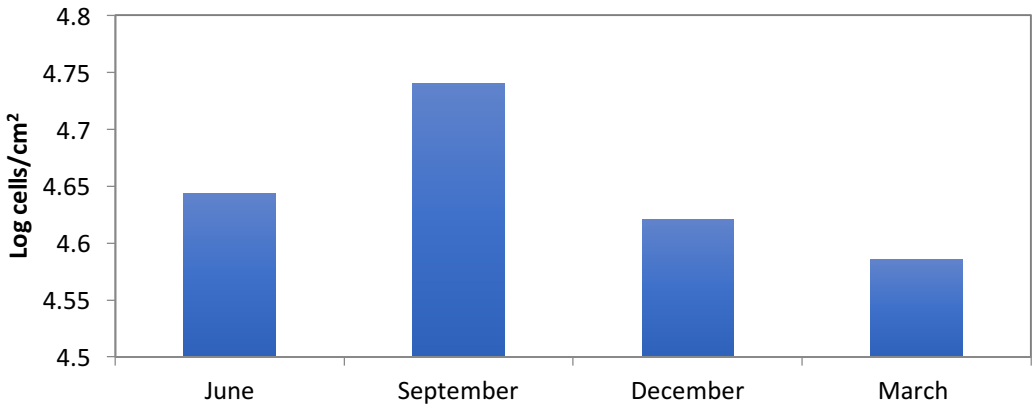

Figure 126: Graph displaying total biomass abundance at point 16 during the months of June 2015, September 2015, December 2015 and March 2016.

Cell abundance was the highest in September (5.5 x 10^4), while it was lowest in December (4.2 x 10^4). This is similar to the pattern observed at points 11 and 12, where dryness is not a crucial factor.

At this site, the following eukaryotic species were identified: *Chlamydomonas* sp., *Euglena mutabilis*, *Cyanidium* sp., *Pinnularia* sp., *Zygnemopsis* sp., *Klebsormidium* sp., *Chlorella* sp., *Dunaliella* sp., *Oxytrichia* sp., *Cercomonas* sp., *Rotaria* sp., *Vah*lkampfia sp. and *Naegleria* sp. The average relative abundance of the different species is illustrated in the following graph:

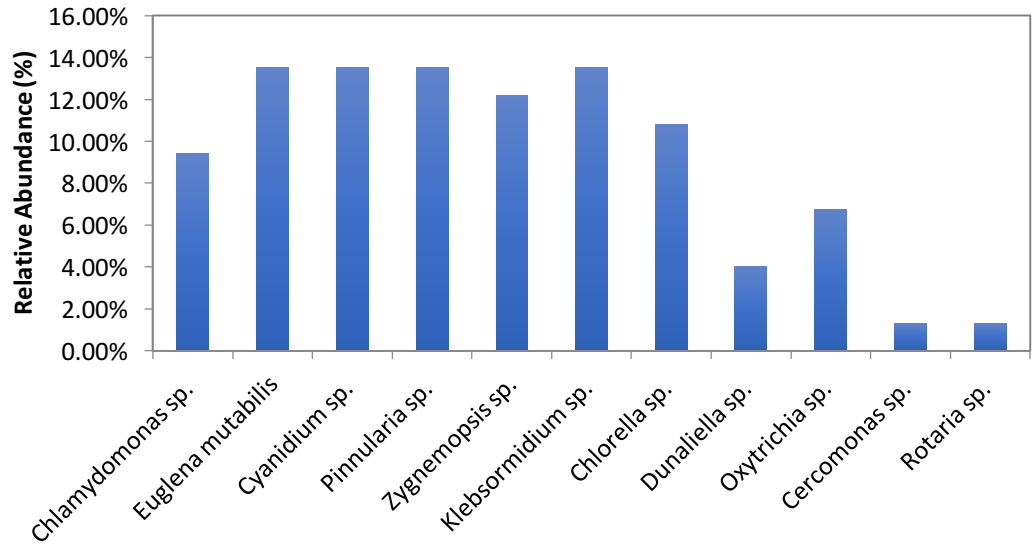

Figure 127: Graph showing the average relative abundance of the different species *present at point 16.*

At this point, seven species were present in high numbers: *Chlamydomonas* sp., *Euglena mutabilis*, *Cyanidium* sp., *Pinnularia* sp., *Zygnemopsis* sp., *Klebsormidium* sp. and *Chlorella* sp. Secondly, in lower numbers, *Dunaliella* sp., *Oxytrichia* sp., *Cercomonas* sp. and *Rot*aria sp. were found.

Diversity

Diversity was assessed by calculating and evaluating Simpson's coefficient, for the average relative abundance of the various species at each point across the year. This is shown in the following graph:

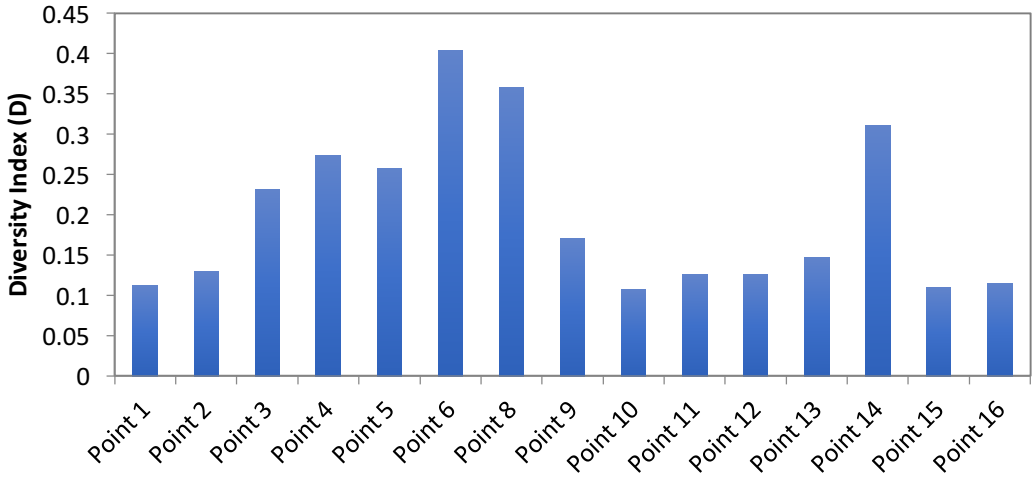

Figure 128: Graph showing Simpson's coefficient for the average microbial diversity at the sampled points where eukaryotic presence was detected.

Simpson's coefficient varied from D = 0.11 (point 15) to D = 0.40 (point 6). Firstly, the lowest diversity was observed at the most acidic points, i.e. the exit of the tunnels. That is, the lowest diversity was observed at point 6 (the exit from Tunnel 5), followed by point 8 (downstream of point 6) and point 14 (the Corta Atalaya tunnel). It is logical that microbial diversity is restricted at these sites, as the extremely harsh physicochemical conditions severely limit the presence of otherwise viable species. On the other hand, the sites with relatively milder physicochemical conditions displayed a wider microbial range and diversity (e.g. points 1, 10 and 16).

Correlation

In order to assess the relationship between the presence of the different microbial species and the physicochemical parameters, a statistical study was undertaken on the gathered data.

The correlation coefficient R is studied, indicating the strength and positive or negative character of a possible linear relationship between two variables of interest, ranging from +1 (a perfect positive linear relationship) to -1 (a perfect

inverse linear relationship, where 0 implies no linear relationship at all. The correlation coefficient R is presented in the following tables, for the different microbial species observed as well as dissolved oxygen, pH, electrical conductivity, Toxicity Index and iron content:

	O_2	pH	EC	TI	Fe
Chlamydomonas sp.	0.72	0.10	0.02	0.24	0.69
Euglena mutabilis	-0.29	-0.73	0.43	-0.42	-0.28
Cyanidium sp.	-0.48	0.65	-0.52	0.02	-0.79
Pinnularia sp.	-0.42	0.75	-0.55	0.03	-0.59
Zygnemopsis sp.	-0.55	0.76	-0.55	0.24	-0.61
Klebsormidium sp.	-0.52	0.79	-0.59	0.10	-0.67
Chlorella sp.	-0.32	0.78	-0.43	0.22	-0.31
Dunaliella sp.	0.38	-0.78	0.64	-0.06	0.51
Oxytrichia sp.	0.30	0.14	-0.11	0.22	0.53
Cercomonas sp.	0.19	0.27	-0.35	0.28	0.36
Labirynthula sp.	-0.04	0.13	0.19	-0.04	0.25
Rotaria sp.	-0.06	0.05	-0.21	-0.02	0.21
Vahlkampfia sp.	0.26	0.17	-0.25	0.03	0.13
Naegleria sp.	0.22	0.07	-0.20	0.04	0.13

Table 9: Table showing the correlation coefficient R between the different identified microbial species and the physicochemical parameters (dissolved oxygen, pH, electrical conductivity, Toxicity Index and total iron content).

The physicochemical factor exhibiting the highest levels of correlation with various microbial species was pH (both the case for positive and negative correlation).

The highest levels of positive correlation found were 0.79, 0.78, 0.76 and 0.75 (observed between *Klebsormidium* sp. with pH, *Chlorella* sp. with pH, *Zygnemopsis* sp. with pH and *Pinnularia* sp. with pH, respectively). In turn, the maximum levels of negative correlation observed were -0.78 and -0.73 (seen between *Dunaliella* sp. with pH and *Euglena mutabilis* with pH). However, not all microbial species display a strong correlation with pH; *Rotaria* sp., *Naegleria* sp., *Chlamydomonas* sp., *Labirynthula* sp., *Oxytrichia* sp. and *Vahlkampfia* sp. show very little dependence on pH (0.05, 0.07, 0.10, 0.13, 0.14 and 0.17 correlation coefficients R, respectively).

Conversely, the variable displaying the lowest levels of correlation with the various microbial species was Toxicity Index.

The minimum values of positive correlation between found were 0.02 (between *Cyanidium* sp. and Toxicity Index), 0.03 (both between *Pinnularia* sp. with Toxicity Index and *Vahlkampfia* sp. with Toxicity Index) and 0.04 (between *Naegleria* sp. with Toxicity Index). In turn, the minimum levels of negative correlation observed

were -0.02, -0.04 and -0.06 (between *Rotaria* sp. with Toxicity Index, *Labirynthula* sp. with Toxicity Index and *Dunaliella* sp. with Toxicity Index).

Finally, dissolved oxygen, electrical conductivity and total iron content displayed intermediate levels of correlation with the various microbial species identified.

The maximum positive correlation observed between dissolved oxygen and microbial species was 0.72 (with *Chlamydomonas* sp.) while the highest negative correlation was -0.55 (with *Zygnemopsis* sp.). Conversely, the smallest correlation values occurred between the subject factor and *Rotaria* sp. and *Labirynthula* sp. (correlation coefficient R values of -0.04 and -0.06, respectively).

Electrical conductivity showed maximum positive correlation values of 0.64 and 0.43 (with *Dunaliella* sp. and *Euglena mutabilis*, respectively) and largest negative correlation values of -0.59 (with *Klebsormidium* sp.), -0.55 (both with *Zygnemopsis* sp. and *Pinnularia* sp.) and -0.52 (with *Cyanidium* sp.). Nonetheless, there is just one value that indicates very little correlation, corresponding to that between electrical conductivity and *Chlamydomonas* sp. (0.02).

Finally, the highest positive correlation values observed between total iron content and microbial species were 0.69, 0.53 and 0.51 (with *Chlamydomonas* sp., *Oxytrichia* sp. and *Dunaliella* sp., respectively). In turn, the maximum negative correlation values observed were -0.79, -0.67 and -0.61 (with *Cyanidium* sp., *Klebsormidium* sp. and *Zygnemopsis* sp.). The minimum level of correlation observed between total iron content and the various microbial species was found to be 0.13, between the subject variable and both *Vahlkampfia* sp. and *Naegleria* sp.

Discussion

As previously seen was the case for physicochemical parameters, the seasonal variations that take place throughout the year are also reflected by the eukaryotic biomass levels. Therefore, these are considerably higher in the summer as opposed to the winter, in which minimum levels are usually recorded. A variety of parameters factor in, such as higher temperatures, higher light intensity and availability as well smaller flow of current, encouraging biofilm proliferation.

In the screening of eukaryotic microorganisms, nine different genera were identified over all sampling sites (except for point 7, where no evidence of microbial presence was found). These are the following: Amoeba, Bacillariophyta, Chlorophyta, Ciliates, Euglenophyta, Flagellates, Rhodophyta, Rotifer and Streptophyta.

A total of 14 different species were identified, as outlined thus:

- Amoeba: *Vahlkampfia* sp. and *Naegleria* sp.
- Bacillariophyta (Diatoms): *Pinnularia* sp.
- Chlorophyta: *Chlamydomonas* sp., *Chlorella* sp. and *Dunaliella* sp.
- Ciliates*: Oxytrichia* sp.
- Euglenophyta: *Euglena mutabilis*

- Flagellates: *Cercomonas* sp. and *Labirynthula* sp.
- Rhodophyta: *Cyanidium* sp.
- Rotifer: *Rotaria* sp.
- Streptophyta (Filamentous algae): *Zygnemopsis* sp. and *Klebsormidium* sp.

The total biomass abundance at each point was estimated by direct microscopic count. Typically, biomass was most abundant in September at the points unaffected by dryness and in June at the points dominated by dryness. Conversely, biomass was typically least abundant in December at the points unaffected by dryness and in September at those affected by it.

The sites that showed the highest fluctuation throughout the year were points 2, 4, 6, 8, 9 and 13. On the other hand, the sites with a more constant biomass throughout the year were points 1, 3, 5, 19, 11, 12, 14 and 15. The biomass ranged from 100 cells/cm^2 at point 13 in September up to 7.9x10^7 cells/cm^2 at point 6 in March.

On the other hand, microbial diversity was studied by analysing Simpson's coefficient, diversity index (D). The average diversity was 0.20, ranging from 0.11 up to 0.40, with the lowest diversity appearing at the sites with the harshest toxicity and pH conditions (points 6, 8 and 14), while the highest diversity was characteristic of sites with less tough physicochemical conditions, such as points 1 and 10. This finding is in agreement with previous studies relating low pH with reduced microbial diversity (Niederlehner and Cairns, 1990).

While a broader range and diversity of microorganisms was present at the points with relatively milder physicochemical conditions, the harshest locations showed little diversity, with *Euglena mutabilis* and *Dunaliella* sp. being the predominant species. This indicates that both of these species are well adapted to tolerate high concentrations of heavy metals as well as very low pH conditions.

The relationship between microbial diversity and the physicochemical parameters was studied by undertaking a statistical analysis of these. Thus, the correlation coefficient R was calculated for every pair of variables, both biotic and abiotic. Regarding the physicochemical parameters, as it should by definition be the case, a strong negative correlation between pH and electrical conductivity was found (R = -0.72). This is because the lower the pH, the higher the ionic content is, partly due to protons and partly due to metals (hence the positive correlation between the content of metals such as iron and electrical conductivity).

On the biotic side, a strong positive correlation was found between *Chlamydomonas* sp. and oxygen (R = 0.72). Regarding acidity toleration, a very strong negative correlation was found between *Euglena mutabilis*, *Dunaliella* sp. and pH (R = -0.73 and R = -0.78, respectively). Conversely, a few species demonstrated a positive correlation with pH; *Klebsormidium* sp. (R = 0.79), *Chlorella* sp. (R = 0.78), *Zygnemopsis* sp. (R = 0.76), *Pinnularia* sp. (R = 0.75) and *Cyanidium* sp. (R = 0.65). With respect to electrical conductivity, apart from *Dunaliella* sp. (R = 0.64), microbial species display either a weak positive (in some cases) or a notably negative correlation (in most cases) with electrical conductivity. This reveals that microbial communities tend to prefer media containing lower ionic contents,

despite tolerating high concentrations of ions to a considerable extent. The relation between the Toxicity Index, iron levels and microbial diversity reveals that the significant correlations between microorganisms and electrical conductivity are due to both pH and metal levels.

Finally, certain species displayed a strong positive correlation with one another. This was particularly evident in the case of *Cyanidium* sp., *Pinnularia* sp., *Zygnemopsis* sp., *Klebsorbidium* sp. and Chlorella sp. Unsurprisingly, given the preference for lower pH, *Euglena mutabilis* and *Dunaliella* sp. displayed a positive correlation.

From this statistical study, we can conclude that the microbial species consistently tolerating the harshest physicochemical conditions is *Dunaliella* sp., as it exhibits a strong preference for and is able to thrive in low pH, high electrical conductivity and elevated total iron content. The tolerance of extreme physicochemical conditions by various species of *Dunaliella*, particularly towards incredibly low pH (*Dunaliella acidophila)* as well as high ionic content of the growth medium (*Dunaliella salina*), has previously been reported in the literature (Pick, 1998).

In second place, *Euglena mutabilis* displays a notable tolerance to extreme physicochemical conditions, withstanding conditions of very low pH and relatively high electrical conductivity, although it displays a negative correlation with iron content.

In conclusion, it is fascinating how both *Dunaliella* and *Euglena mutabilis* are able to thrive within such an extreme physicochemical environment. Thus, the biofilms found in this study are extraordinarily unique.

5.2. Biological Photovoltaic Cells based on *Dunaliella acidophila*

The aim of this study was to inoculate a BPV device with a strain that would tolerate a very high electrical conductivity, due in particular to high acidity. The hypothesis was that, in comparison to BPV cells operating under standard conditions of near-neutral pH, this higher electrical conductivity would decrease the internal resistance of the BPV device, as well as facilitate the cathode reaction (due to the increased availability of protons for the reduction of oxygen), which would result in enhanced BPV performance.

The ultimate goal of this study is to find a set of naturally-occurring acidophilic microorganisms to serve as the biological material in a BPV cell platform. However, the first step consisted in testing a BPV cell using a commercially available acidophilic strain as the biological material, in order to confirm the hypothesis that higher acidity and electrical conductivity of the medium results in enhanced BPV performance.

The microorganism of choice was *Dunaliella acidophila*, as the previous statistical study pointed towards this strain as the most robust microorganism out of all those identified for the desired BPV cell operating conditions.

- Growth profiling of *D. acidophila* as a function of pH

The hypothesis of this study is that a BPV operating under very acid conditions would display an improved performance, in comparison to standard BPV platforms working at near-neutral pH. In order to do so, a photosynthetic acidophile (*Dunaliella acidophila*) was selected, to be used as the biological material with which to inoculate the BPV device.

In the previous statistical study on the microbial diversity of the Rio Tinto ecosystem, *Dunaliella* was found to tolerate extreme levels of pH as well as considerably high electrical conductivity, and is therefore a robust strain for the purpose of this study. Moreover, *Dunaliella acidophila* is commercially available and a standard growth medium is recommended for it.

Dunaliella acidophila is a eukaryotic (green) alga that is able to thrive in very low pH environments, which is why it was selected for this investigation. Prior to undertaking electrochemical studies, the growth of the subject acidophile was profiled, in order to test the pH limits tolerated by the strain as well as to corroborate its optimum growth conditions.

Materials and Methods

Cultures and biofilm growth

Dunaliella acidophila was purchased from Culture Collection of Algae and Protozoa (CCAP), SAMS Research Services Ltd. This strain, of reference CCAP 19/35, was originally isolated from an acidic sulphurous pool in Pisciarelli, Naples (Italy) (Albertano et al. 1981).

The *D. acidophila* culture was grown in AJS medium, which is an acidified 97:3 mixture of JM (Jaworski's Medium) and SE (Soil extract) for freshwater and terrestrial protozoa. The pH was adjusted by addition of sulphuric acid, in order to produce different mediums with a range of pH values.

D. acidophila thrives at a temperature between 18°C and 26°C, so it was cultured at 22°C. The experiments were all performed at this temperature.

D. acidophila was cultured at a light intensity of 43 Wm^{-2}, as higher radiation may be harmful for it.

The growth of culture suspensions cultured in JM at the recommended pH of 1.5 was followed by spectrophotometrical OD_{680} determination. On the other hand, biofilm growth was monitored by inoculating 2 ml of exponential phase culture onto a graphite electrode placed inside a beaker filled with growth medium at a range of pH values, from pH 0.00 up to pH 3.5, leaving it to grow for 20 days, rinsing with fresh medium, scraping the biofilm from the electrode and measuring OD_{680} after resuspension in fresh medium. The same biofilm growth determination method was subsequently employed at a narrower pH range, based on the preliminary results, this time following 10 days of biofilm growth in order to better detect pH sensibility.

Results

Effect of pH on cell growth

Initially, the tolerance of *Dunaliella acidophila* to extremes of pH was assessed over a wide range of pH values, from 0.00 up to 3.50. Subsequently, given the growth range indicated by the first test, a second evaluation of biofilm growth was undertakn over a narrower pH range and shorter period of time, in order to detect responses to pH with a higher sensibility. These results are shown in the following graphs:

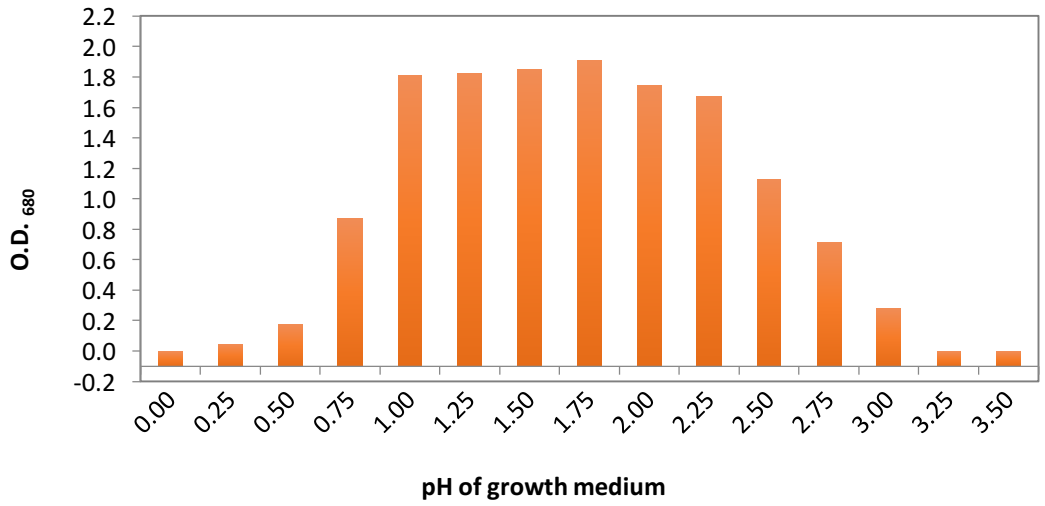

Figure 129: O.D. at 680 nm of biofilms growing in different conditions of pH, from pH 0.25 up to pH 3.5, harvested after 20 days of growth.

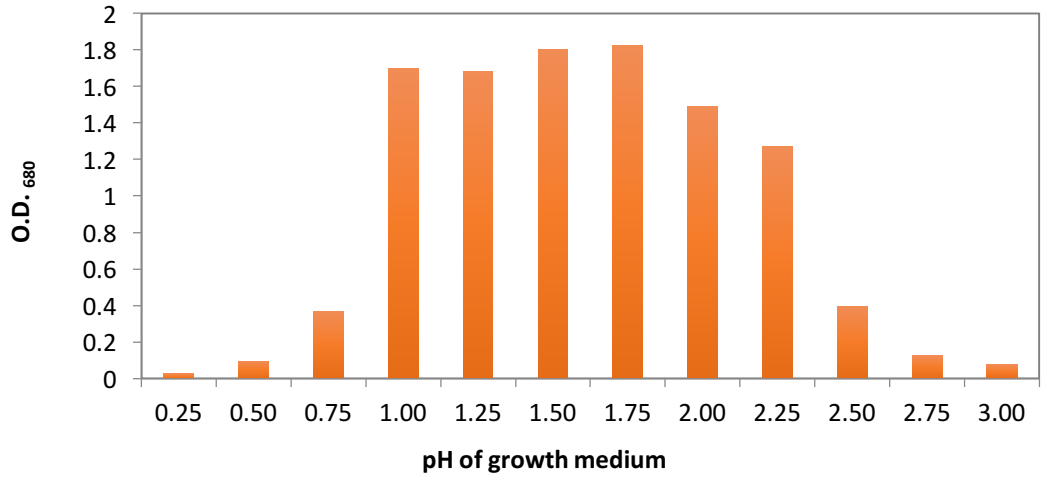

Figure 130: O.D. at 680 nm of biofilms growing in different conditions of pH, from pH 0.75 up to pH 3.0, harvested following 10 days of growth.

Discussion

The results show that *Dunaliella acidophila* does indeed thrive in very acidic conditions, as expected from prior literature (Albertano et al. 1981). In particular, it may be observed that maximum growth is achieved between pH 1.00 and pH 1.75. In terms of the pH limits tolerated by the strain, we may appreciate that, on the one hand, it is able to survive under extremely low pH conditions (levels down to pH 0.25, i.e. 0.28 M H_2SO_4). On the other hand, the highest pH at which growth is observed corresponds to pH 3.00 (0.5 mM H_2SO_4). While the decline in growth is very abrupt for the lower limit of pH, with $O.D._{680}$ dropping sharply from pH 1.00 down to pH 0.00, this decline is considerably smoother in the higher pH limit range, decreasing softly from pH 1.75 up to pH 3.25. This can be explained by the logarithmic relation between pH and concentration of sulphuric acid; the change in concentration is tremendously larger for the lower pH range than for the higher pH range (i.e. the change in concentration of sulphuric acid is 0.45 M between pH 1.00 and pH 0.00, while being just 8.6 mM between pH 1.75 and pH 3.0). Therefore, changes in growth dynamics are considerably milder in the upper pH range.

It is worth noting that *Dunaliella acidophila* might tolerate pH conditions below pH 0.25 and above pH 3.0. However, in such a case, growth would be extremely slow or would need a longer adaptation period (i.e. more than the twenty days of this study would be required in order for biofilm growth to be perceived).

- Use of *D. acidophila* as the anodic photosynthetic material in a Biological Photovoltaic Cell

The aim of this study was to investigate the electricity generation capacity of *Dunaliella acidophila* as the biological material in a BPV. Firstly, the power output of a biofilm of this microorganism attached to the anode electrode of a single-chamber BPV was studied. Subsequently, the exoelectrogenic capacity of this acidophilic alga was compared to that of the neutrophiles *Chlorella vulgaris* and *Synechococcus elongatus*.

All three strains are photoautotrophic, which is advantageous from a BPV maintenance point of view. Regarding cellular structure, both *D. acidophila* and *C. vulgaris* are eukaryotic, while *S. elongatus* is prokaryotic. This implies that the electron transport apparatus are more exposed in the case of the latter species as opposed to the former two species, where the additional compartmentalisation further isolates the electronic chain from the cell exterior and the anode electrode. On the other hand, the electrical conductivity of the growth medium of *D. acidophila* is considerably higher than that of the other two tested species, implying a lower internal resistance of the BPV cell. Moreover, the increased availability of protons for the cathode oxygen reduction reaction is expected to further enhance BPV performance. Hence, while it is clear that we should expect *C. vulgaris* to display the lowest current output, the comparative performance of *D. acidophila* and *C. vulgaris* will be dictated by the relative contribution of electrical conductivity of the electrolyte as well as proton availability versus the degree of exposure of the electron transport apparatus.

Materials and Methods

- Cultures and biofilm growth

The *Dunaliella acidophila* strain was obtained and grown as described in Chapter 2.

Prior to the introduction into the BPV, aliquots of the cultures were centrifuged and resuspended in fresh media, to then be transferred onto the electrode surface.

- Construction of the BPV cells

The fuel cell configuration used was the same as that employed for the tests with *C. vulgaris* and *S. elongatus*, described in chapter 2, in order for results to be directly comparable across strains.

In summary, the device consisted of a single-chamber BPV, with a circular, 4 cm in diameter Toray paper anode electrode, and Platinum catalyst-coated, 4x1 cm rectangular carbon paper cathode. The material for the connections used to contact both electrodes was carbon yarn. Circular Perspex pieces were again used as the scaffold, at the upper and bottom ends, to sandwich an inner Perspex separator and two PDMS gaskets, ensuring a liquid-proof seal. The devices were sterilised prior to each experiment.

- BPV operation and measurement

The same protocol as that employed for the electrochemical tests in Chapter 2 was used in the present experiment:

Firstly, polarization curves were undertaken by varying the external circuit resistance, from 1 MΩ down to 220 Ω, measuring the resulting potential difference for each resistance and calculating the corresponding power output. This allowed to determine the external resistance of choice in order to operate the BPV cell under optimum conditions of maximum power output.

Secondly, once the optimum external resistance had been determined, voltage was continuously recorded with an ADC16 Pico Technology High Resolution Data Logger, via PicoLog software interface.

Results

- Electrochemical tests

  - Polarisation curves

Firstly, polarisation curves were performed by measuring cell voltage as a function of varying external circuit resistance and calculating the corresponding power output.

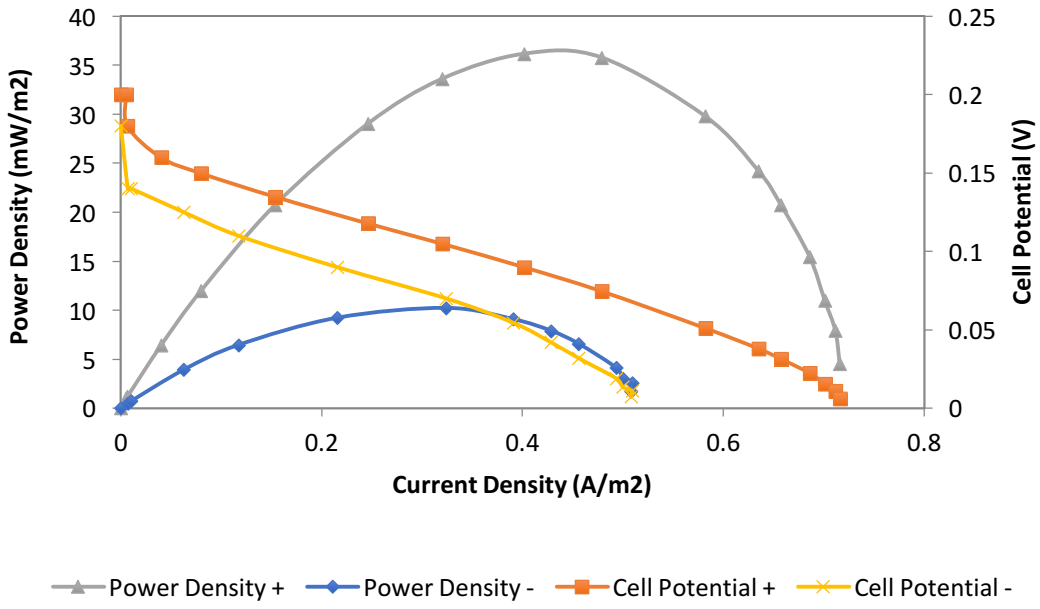

Figure 131: BPV performance of Dunaliella acidophila, showing polarisation curves and power curves for both the inoculated device and negative control device (containing AJS medium only). The external resistance applied at maximum power output was 560 Ω.

- Power output

Secondly, power output was measured continuously under a 12 hour light : 12 hour dark cycle, during twenty days. The BPV cells were fitted with an external resistance for maximum power output, as indicated by the polarisation curves.

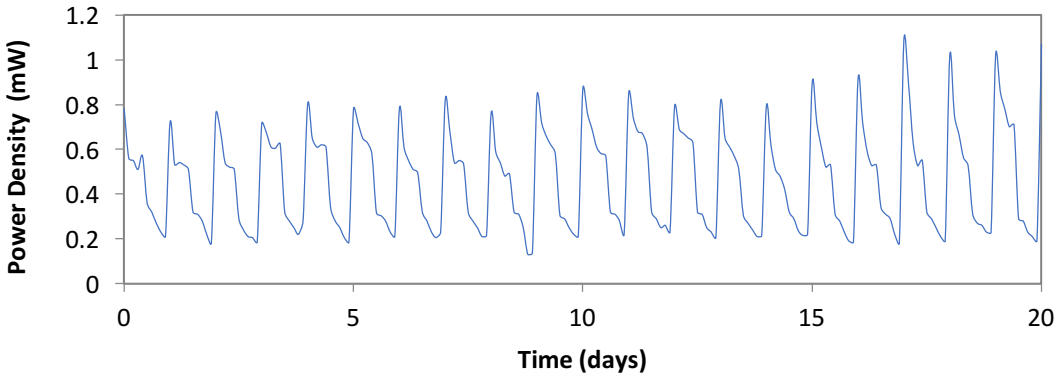

Figure 132: Power output of Dunaliella acidophila BPV under a 12 hour light: 12 hour dark cycle during 20 days, fitted with an external resistance of 560 Ω.

The average power output of *D. acidophila* was compared to that of the two reference species, *C. vulgaris* and *S. elongatus*, as described in Chapter 2.

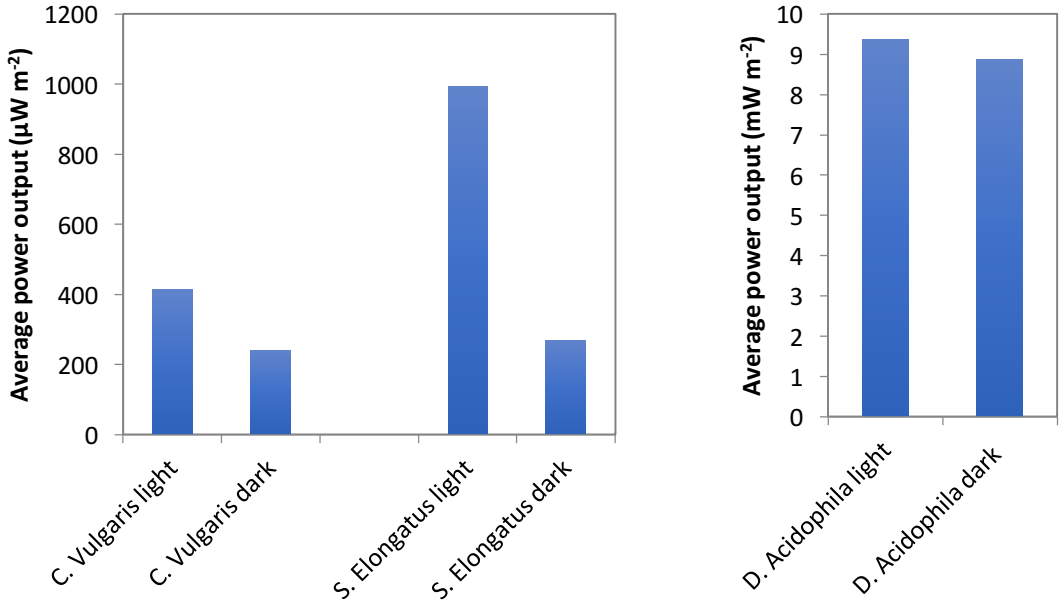

Figure 133: Average power output in the light vs. average power output in the dark exhibited by Chlorella vulgaris and Synechococcus elongatus (left) and Dunaliella acidophila (right).

Discussion

The results show that *Dunaliella acidophila* does indeed display an exoelectrogenic capacity. Moreover, the findings reveal that the subject strain performs considerably better than its neutrophile counterparts on a power output level.

While it seemed simpler to predict the comparative performances of *Chlorella vulgaris* and *Synechococcus elongatus*, based on the different exposure of the electron transport machinery as a result of the prokaryotic or eukaryotic cellular structure, it appeared more difficult to predict which of *Synechococcus elongatus* or *Dunaliella acidophila* would generate the highest power output.

In the case of the two subject neutrophiles, as both of their growth mediums have similar electrical conductivity, it should be expected for the prokaryote to perform better, due to the enhanced exposure of its electron transport chain machinery, in comparison to the more isolated version of it bared by the eukaryote. However, it is more complex to predict whether or not *Dunaliella acidophila* will outperform *Synechococcus elongatus* at the electrical level. This is due to the fact that, on the one hand, *Dunaliella acidophila* is eukaryotic and therefore counts with more inaccessible electron transport chain machinery. Nonetheless, on the other hand, its growth medium is very acidic and is thus higher in electrical conductivity, thereby

facilitating the cathode oxygen reduction reaction. Hence, it is a priori difficult to predict which of the two strains will achieve a better power output.

Looking at the results, we can see that, in practice, the acidophile performs considerably better than *Synechococcus elongatus* (and, correspondingly, better than *Chlorella vulgaris*). From this finding, it can be concluded that electrical conductivity and availability of protons, at least in this case, have a larger impact on power output than that of the difference in exposure of the electron transport chain machinery between eukaryotes and prokaryotes. Indeed, the extremely high electrical conductivity may be appreciated in the behaviour displayed by the negative control; it is so favourable for BPV operation that this biofilm-less cell even outperforms the BPV device inoculated with *Chlorella vulgaris.*

The average power output produced in the light by *Dunaliella acidophila* was 9.4 mW m^{-2}, which is about ten times higher and more than twenty times higher than that displayed by *Synechococcus elongatus* (992 µW m^{-2}) and *Chlorella vulgaris* (417 µW m^{-2}), respectively. In turn, the average power output in the dark was 8.9 mW m^{-2} for *Dunaliella acidophila*, as compared to the one-order-of-magnitude lower values of 272 µW m^{-2} for *Synechococcus elongatus* and 241 µW m^{-2} for *Chlorella vulgaris*. Therefore, while *Synechococcus elongatus* consistently displayed a higher power output in comparison to *Chlorella vulgaris*, their power outputs are comparable in relation to that of *Dunaliella acidophila*, which is an indisputably superior, i.e. one order of magnitude higher.

A large difference is observed between the external loads corresponding to maximum power output for the BPV cells inoculated with the different strains. While for the neutrophiles the magnitude of these is relatively high (18 kΩ and 2.6 kΩ for *Chlorella vulgaris* and *Synechococcus elongatus*, respectively), it is comparatively low for the acidophile (560 Ω for *Dunaliella acidophila*). This is a clear reflection of the disparity in internal resistance between the various biological materials used, quite possibly due to the variation in electrical conductivity of the different growth media to a large extent, showing that higher electrical conductivity does lead to a lower internal resistance of the device and hence to improved performance (for the same device).

All three strains displayed a very sensitive light-dependent exoelectrogenic response, as higher power outputs were exhibited under light conditions vs. dark conditions, with constant temperature.

A direct comparison between the various strains is possible thanks to the use of the same BPV device. This is very important, as device configuration has a large impact on results. Therefore, unfortunately, it is not accurate to quantitatively compare results across various studies employing different BPV devices, but rather do so qualitatively.

The long-term recording of power output revealed that the longevity of BPVs inoculated with *Dunaliella acidophila* was comparable to that of *Synechococcus elongatus* and *Chlorella vulgaris*, i.e. about twenty days. This finding is similar to previous reports on the prolonged power outputs of *S. elongatus* and *C. vulgaris*

(McCormick et al. 2011), although this study seems to be the first to look at the power output of *Dunaliella acidophila*.

The shape of the long-term recording of power output reveals a diurnal pattern consisting of sharp peaks corresponding to the shift from dark to light, followed by a decrease in power that is initially very steep and gradually becomes milder, on occasions rising slightly towards the end of the light period. Conversely, the dark period is characterised by a sharp drop in power (corresponding to the shift form light to dark), followed by a milder decrease in power until the end of the dark period.

The very characteristic shape described by power output resembles that previously reported in the literature for *Synechococcus elongatus* and *Chlorella vulgaris* (McCormick et al. 2011), which exhibit a similar diurnal power output pattern that lasts for at least one month, with the light-dependent performance of *Synechococcus elongatus* improving over time, as is the case of *Dunaliella acidophila*, while *Chlorella vulgaris* initially displays its highest light-dependent power output and it gradually decreases over time.

Although the shape of the diurnal pattern does not appear to be justified in prior literature, the sharp peaks corresponding to the beginning of exposure to light strongly resemble the shape of chronoamperometries, which are characterised by a peak in current upon initial voltage application, followed by a (gradually decelerating) decrease in current as the electrochemically active species are depleted and current becomes increasingly limited by diffusion (true for unstirred/static electrode systems, which is not the case for rotating disk electrodes).

5.3. Implementation of an in-situ Biological Photovoltaic Cell at an acid mine drainage site

The aim of this study was to implement and test a BPV device, in situ, at a chosen AMD site in which physicochemical conditions are as extreme as possible while still hosting living microorganisms.

The purpose of this experiment was to probe the efficiency of extremophile biofilms growing under their natural conditions (as extreme as possible on a physicochemical level, i.e. highly acidic pH and elevated electrical conductivity), for which purpose point 6 was chosen. This site was selected as the implementation location due to it exhibiting the most extreme physicochemical conditions all year round out of the sixteen sampled sites while still bearing living biofilms. Under their natural conditions, outdoors and as the corresponding mixed consortia biofilms, these would be expected to display the best electrical performance thus far in this investigation.

For this study, a fuel cell device adapted to outdoor conditions was built and set up at point 6, where it was operated and electrochemical measurements were undertaken.

Materials and Methods

- Construction of the sediment fuel cell

The aim of this study was to implement an in-situ microbial fuel cell at the site with the naturally-occurring set of acidophiles tolerating the most extreme physicochemical conditions possible. For this purpose, a microbial fuel cell device, adapted for the new outdoor requirements, as built and implemented on the sediment bed of point 6, as illustrated thus:

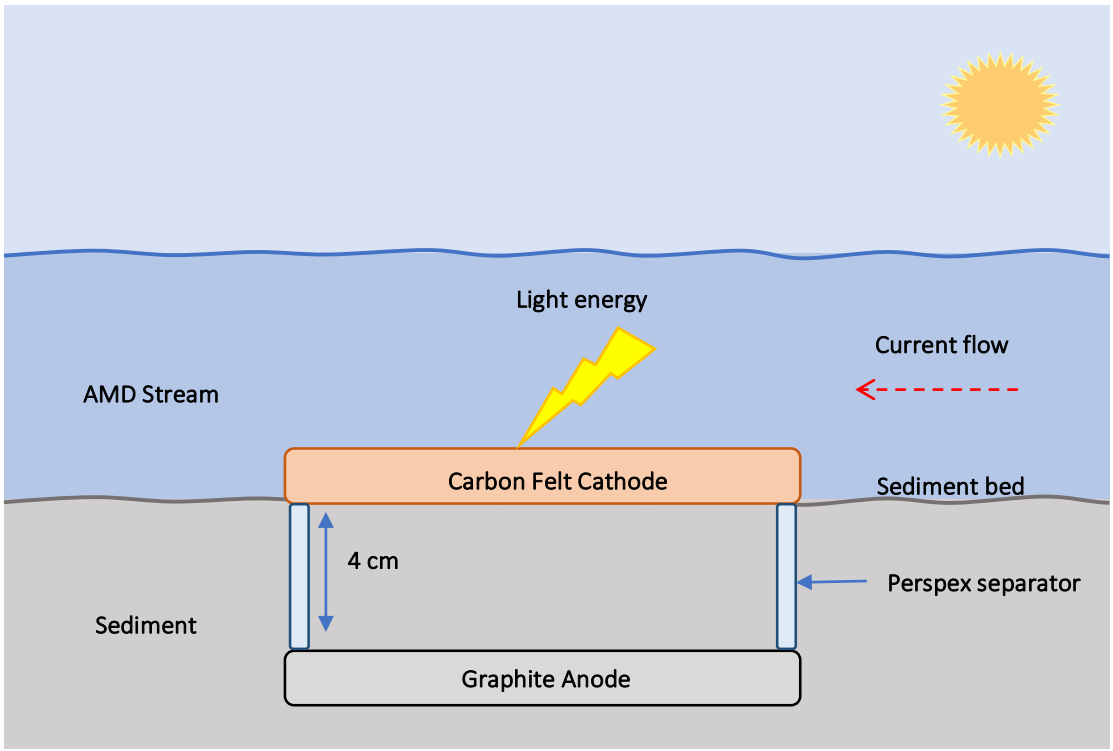

Figure 134: Diagram showing the configuration and set-up of the in-situ sediment fuel cell device at point 6.

A new microbial fuel cell device design was employed for this experiment, as it needed adaptation to the outdoors environment with its new requirements. Therefore, the new fuel cell platform would need to take into account that one of the electrodes would be buried within the underwater sediment, while the other electrode would rest on the sediment bed, within the acid mine drainage stream. Hence, the new design should be robust, guaranteeing a fixed separation between the two electrodes.

The device consisted of a rectangular, 5x10x1 cm graphite electrode, buried horizontally in the sediment, and a rectangular, 5x10x1 cm carbon felt electrode, resting on the sediment floor (immersed in the liquid), directly above the anode electrode. The material used for the connections was Teflon-coated carbon yarn. A distance of 4 cm was maintained between the two electrodes by Perspex separators.

- Biofilm growth

The previously sterilised electrodes were placed on the floor of the AMD stream at point 6 (the graphite electrode buried in the sediment and the graphite felt electrode resting on the sediment floor). Biofilms were allowed to form on the electrodes for ten days prior to the beginning of the electrochemical tests.

- BPV cell operation and electrochemical measurements

First, polarization curves were carried out by changing the external load, from 1 MΩ down to 1 Ω, measuring the corresponding cell voltage and calculating power output, following a period of ten days during which the electrodes had been left in place at point 6 for biofilms to form. This allowed the determination of the optimum resistance (corresponding to maximum power output).

In second place, the BPV cell was connected to the optimum resistance and output voltage was measured daily, for a period of twenty days. Continuous recording of potential difference with a data logger, as used to monitor the performance of the BPV devices at the laboratory, was not possible given the new outdoors location. Hence, potential difference was measured manually with a portable voltmeter on a daily basis.

- Identification of microorganisms

After the test period, the fuel cell was removed from the sediment bed and the electrodes were cleaned (scraped and rinsed using PBS buffer). Samples were then screened for the presence and identity of microorganisms.

Firstly, eukaryotic microorganisms were identified via direct microscopic observation, by looking at distinctive phenotypic features (as described in previous studies of eukaryotic communities in the Tinto River; Amaral et al. 2002, Lopez-Archilla et al. 1999 and Lopez-Archilla et al. 2001).

Secondly, prokaryotic microorganisms were identified by 16S rRNA cloning (into *E. Coli* cells with a pGEMT vector) and subsequent BLAST analysis of the output sequences.

Results

- Electrochemical tests

  - Polarisation curves

In first place, the sediment cell was subjected to a polarisation curve after it had been left for ten days at the test site. The external load was varied from 1 MΩ down to 1 Ω and the corresponding cell voltage values were measured. This allowed determining the resistance at which maximum power output is obtained, which was used for the subsequent long-term power-monitoring test.

The polarisation curve and power curve of the sediment cell is shown as follows:

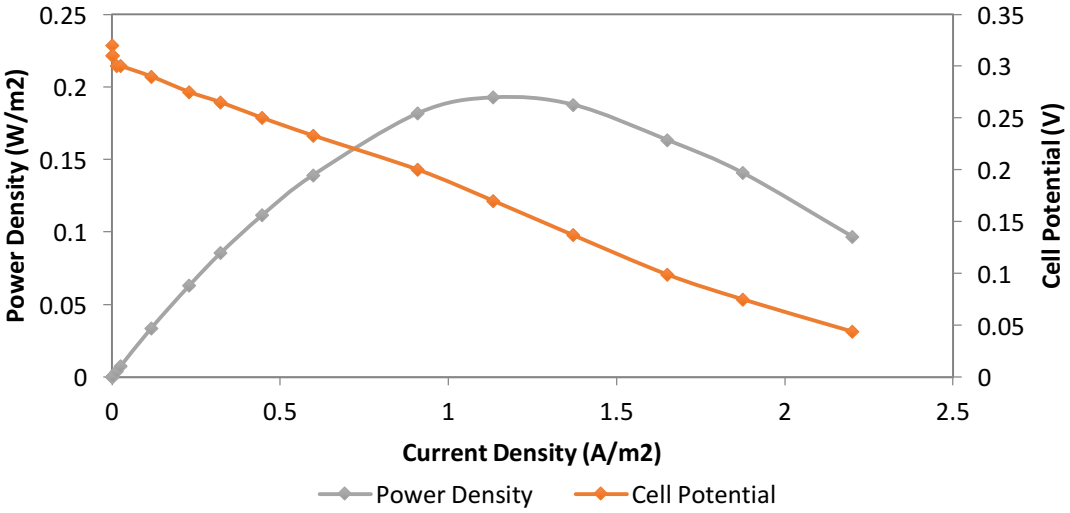

Figure 135: Performance of the sediment cell at point 6, showing the polarisation curve and the power curve corresponding to day 10 after the device was installed at point 6. The external resistance corresponding to maximum power output was 15 Ω.

- Current density and power output

Secondly, cell voltage was measured daily, for a period of twenty days (starting after the initial adaptation period of ten days). For this test, the sediment cell was fitted with a 15 Ω external resistance, as determined from the previous polarisation and power output curves, which was used to calculate current density and power density.

The evolution of current density and power density are shown thus:

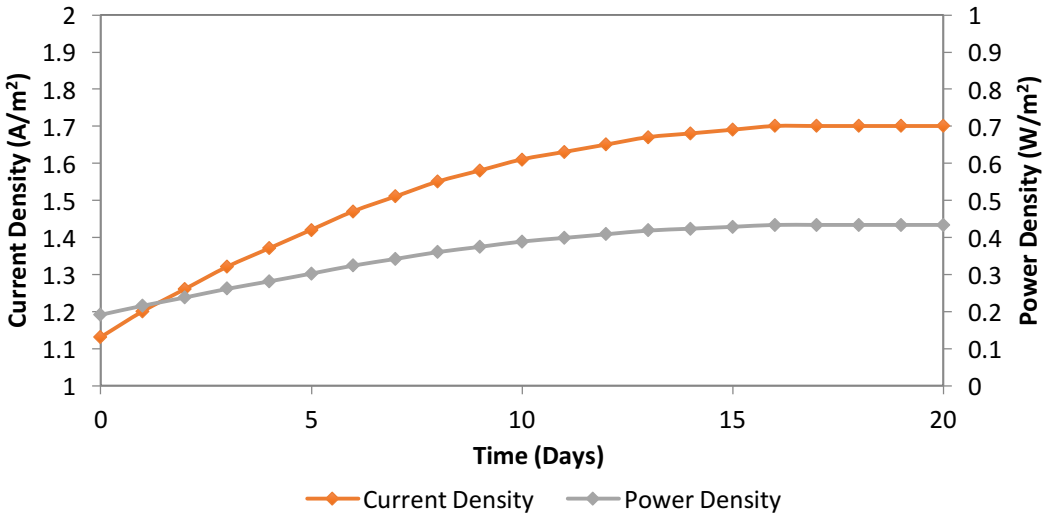

Figure 136: Current density (red) and power density (green) evolution of the sediment cell at point 6 for 20 days, with an external resistance of 15 Ω.

The results confirm the exoelectrogenic capacity of naturally-occurring extremophile consortia. Cell potential is somewhat higher (OCP of 320 mv) than that observed for the pure-culture BPV cell based on *Dunaliella acidophila* (OCP of 205 mV). However, the largest difference lies in current density; in comparison to the intensity of 0.402 mA/m^2 displayed by *Dunaliella acidophila* at peak power in the polarisation curve, the subject mixed consortia equivalently exhibit a current density of 1.13 A/m^2.

Looking at the polarisation curve, the linear relationship between cell voltage and current density reveals that the drop in voltage that accompanies the decrease in external load is dominated by ohmic resistance. This differs from the behaviour of the pure-culture laboratory BPV cells, where cell voltage does not drop linearly for low values of current density.

On the other hand, the long-term monitoring of power output showed that the sediment cell took 16 days to reach maximum current density and power output values, from the beginning of the electrochemical test (i.e. 26 days since implementation). These parameters plateau off and, following day 16, they are seen to remain constant, denoting that the point of biofilm equilibrium and stable power output has been attained.

Measured current density values begin at 1.13 A/m^2 , gradually increasing up to 1.70 A/m^2. Likewise, power output values start at 0.19 W/m^2 and smoothly increase up until a maximum value of 0.43 W/m^2. The maximum current density and power output values recorded, which are higher than those seen at peak power output in the polarisation curve, are superior to those corresponding to the tested pure-culture acidophilic BPV and, in fact, unprecedentedly high in comparison to reported prior work.

- Microbial identification

The microorganisms present on the electrodes of the sediment cell were analysed at the conclusion of the electrochemical tests.

  - Eukaryotic fauna

The following eukaryotic species were found on the surface of the electrodes:

Electrode	**Microorganisms identified**
Anode	*Rotaria* sp. (100.0%)
Cathode	*Euglena mutabilis* (48.5%), *Dunaliella* sp. (43.7%), *Cyanidium* sp. (2.3%), *Pinnularia* sp. (1.6%), *Zygnemopsis* sp. (2.3%) and *Klebsormidium* sp. (1.6%)

Table 10: Table showing the various eukaryotic microorganisms identified on the surface of the anode and cathode electrodes from the sediment fuel cell after conclusion of the electrochemical tests, indicating relative abundance (as a percentage).

- Prokaryotic fauna
  - The following prokaryotic species were found on the surface of the anode electrode:

Affiliation (phylum/class/family/genus)	**A**	**GeneBank Acc.**	**S**
Proteobacteria			
Alphaproteobacteria			
Unc. Alphaproteobacteria			
Uncultured Alphaproteobacteria	1	JF737897	99
Candidatus Paracaedibacteraceae			
Uncultured Alphaproteobacteria	2	AM991220	99
Acetobacteraceae			
Uncultured Acidisphaera	2	JF737912	99
Acidiphilium	9	AP012035	99
Betaproteobacteria			
Ferrovaceae			
Uncultured *Ferrovum*	2	JF737909	99
Gammaproteobacteria			
Unc.Gammaproteobacteria			
Uncultured Gammaproteobacteria	1	KC619550	99
Xanthomonadaceae			
Uncultured *Metallibacterium*	9	JF737879	99
Acidithiobacillaceae			
Unc. *Acidithiobacillus ferrivorans*	2	JF737875	99
Acidithiobacillus ferrooxidans	8	FN391835	99
Actinobacteria			
Actinobacteria			
Acidimicrobiaceae			
Uncultured *Acidithrix*	5	JF737910	99

Table 11: Table showing the various prokaryotic microorganisms identified on the surface of the anode electrode from the sediment fuel cell after conclusion of the electrochemical tests, representing affiliation (phylum, class, family and genus),

abundance of clones, A, as well as information about the closest relative found (BLAST GeneBank Accession number and percentage of similarity, S).

- The following prokaryotic species were found on the surface of the cathode electrode:

Affiliation (phylum/class/family/genus)	**A**	**GeneBank Acc.**	**S**
Proteobacteria			
Gammaproteobacteria			
Acidithiobacillaceae			
Unc. *Acidithiobacillus ferrivorans*	1	JF737925	99
Acidithiobacillus ferrooxidans	14	LN717052	99
Nitrospirae			
Nitrospira			
Nitrospiraceae			
Unc. *Leptospirillum ferroxidans*	16	JF737922	99
Unc. *Leptospirillum ferriphilum*	5	EF446240	99
Actinobacteria			
Actinobacteria			
Acidimicrobiaceae			
Uncultured *Ferrimicrobium*	8	JQ81567	99
Uncultured *Actinobacterium*	1	JQ815670	99
Firmicutes			
Clostridia			
Clostridiales			
Uncultured *Sulfobacillus*	1	DQ464143	99
Bacilli			
Alicyclobacillaceae			
Uncultured Alicyclobacillus	2	HQ730616	99

Table 12: Table showing the various prokaryotic microorganisms identified on the surface of the cathode electrode from the sediment fuel cell after conclusion of the electrochemical tests, representing affiliation (phylum, class, family and genus), abundance of clones, A, and information about the closest relative found (BLAST GeneBank Accession number and percentage of similarity, S).

Discussion

The results obtained from this test reflect not only the exoelectrogenic capacity of naturally occurring extremophile consortia, but also the enormous possibilities behind extremophile fuel cells. While the device configuration is different to that used in the previous tests, due to the need to adapt it to outdoors conditions (and hence a direct quantitative comparison is not possible), it is qualitatively evident that the electrical performance of this cell is clearly superior to the configurations used in the previous tests.

The purpose of this study was to investigate electrical power generation by extremophiles growing under their natural conditions, in particular by a consortium of acidophilic microorganisms thriving in the most extreme physicochemical ecosystem observed among the monitored sampling sites, aiming to obtain the best power output results of this study. As expected, the electrical performance of the in-situ fuel cell unquestionably surpasses that of the BPV cells that were previously tested in the laboratory.

A surprising finding from this study, however, is that the role of the electrodes is reversed with respect to the laboratory devices; the electrode supporting the biofilms exposed to light acts as the cathode. This observation is in part surprising in light of the laboratory tests, in which the electrode supporting the biofilm always performed the role of the anode (i.e. the investigated photosynthetic biofilms displayed exoelectrogenic activity at the anode electrode). However, as the BPV devices tested in the laboratory employed cathodes coated with platinum catalyst, these forced the direction of electrical current such that the electrode supporting the photosynthetic biofilms always acted as the anode. Moreover, in addition to none of the electrodes composing the in-situ fuel cell device bearing an oxygen reduction catalyst, one of its electrodes was buried in the sediment and therefore immersed in an anaerobic atmosphere that favours its role as the anode. Therefore, on the one hand, the BPV devices at the laboratory favoured the role of the biofilm electrode as the anode, while the sediment in-situ fuel cell encouraged the electrode exposed to light to act as the cathode.

It can be observed that, while cell potential is slightly higher for the sediment cell than for the pure-culture BPV cell inoculated with *Dunaliella acidophila* (OCP of 320 mV for the former in comparison to 205 mV for the latter), the largest difference responsible for the disparity in power output between the two modalities lies in current density. This is, in comparison to the intensity of 0.402 mA/m^2 displayed by *Dunaliella acidophila* at peak power output in the polarisation curve, the mixed consortia exhibit a current density of 1.13 A/m^2 at the equivalent point, which is four orders of magnitude higher.

There are several key differences between the pure-culture BPV cell inoculated with *Dunaliella acidophila* and the in-situ sediment fuel cell that could contribute to the remarkable enhancement in performance. Firstly, the in-situ microbial fuel cell is based on a range of microorganisms that are thriving under their natural conditions. Hence, on the one hand, microorganisms are at optimum conditions from a physicochemical point of view, regarding adequacy of and adaptation to growth

medium, temperature and light factors. Moreover, on the other hand, the conditions of the sediment fuel cell are optimum from a biological standpoint; as explained previously, mixed consortia exhibit higher power outputs than pure cultures. In addition, the biological material hosted by this microbial fuel cell is a natural mixed consortium (unlike artificially grown mixed cultures in laboratory microbial fuel cells) and is therefore based on a natural symbiotic equilibrium.

Secondly, as the AMD stream is constantly flowing, the growth medium and electrochemically active species within are constantly being replenished, unlike in the laboratory BPV cell. It is also worth noting that the AMD stream has higher concentrations of (electrochemically active) heavy metals in solution, which could contribute to the registered current. In addition, the anode and cathode electrodes vary between the two cell platforms. On the one hand, while the cathode is doted with a platinum catalyst layer for the oxygen reduction reaction in the case of the Toray paper cathode used in the laboratory BPV, this is not the case in the in-situ cell. As it is larger and needs to tolerate harsher outdoors conditions, the cathode electrode used by the in-situ cell is a graphite felt rectangle, which, whilst lacking the platinum catalyst, does have a significantly larger surface area than its Toray paper counterpart. Moreover, while the cathode in the laboratory BPV cell does not accommodate a biofilm on it, the in-situ fuel cell does allow for a biofilm of naturally occurring microorganisms to form on the cathode electrode, i.e. there may be biocathode activity. On the other hand, while the anode electrode is under similar conditions to the cathode electrode in the laboratory BPV cell, this is not the case in the outdoors cell. In the latter platform, the anode is immersed several cm beneath the sediment floor of the AMD stream, which, while increasing the internal resistance of the fuel cell, does grant a reductive environment around the anode electrode. Finally, the dimensions of the in-situ sediment cell are larger than those of the laboratory BPVs, which could mask electrochemical losses that could be proportionally larger in the smaller platforms.

From the polarisation curve, we can infer that the drop in voltage as the external load diminishes is dominated by ohmic resistance; there is a linear relationship between cell voltage and current output. This is not so much the case for the laboratory BPV cells, in which cell voltage does not drop linearly for low values of current density.

The long-term monitoring of power output reveals that the sediment cell took 16 days from the start of the electrochemical test (i.e. 26 days from implementation) to reach maximum values of current density and associated power output, possibly due to biofilm growth. From day 16 onwards, these values are seen to remain constant, indicating that a point of biofilm equilibrium and stable power output has been reached. Current density starts at 1.13 A/m^2 and gradually rises up to 1.70 A/m^2, while power output begins at 0.19 W/m^2 and increases to reach a maximum value of 0.43 W/m^2. The maximum current density and power output values recorded are unprecedentedly high, revealing an incredible untapped potential for extremophile-based fuel cells.

Regarding the microbial analysis, this showed that microbial diversity varied significantly between the anode and cathode electrode environments. Firstly, the

eukaryotic screening revealed that a number of photosynthetic algae were present on the cathode (most abundantly *Euglena mutabilis* and *Dunaliella*, with smaller proportions of *Cyanidium*, *Pinnularia*, *Zygnemopsis* and *Klebsormidium*). However, these were not present on the anode, at which just *Rotaria* was identified. This is logical, as the cathode was exposed to sunlight and hence the photosynthetic algae did grow on it, while this was not the case of the anode, as it was buried within the sediment of the AMD stream.

Secondly, the prokaryotic screening revealed significant differences between the fauna of the two electrodes as well. For instance, the proteobacteria at the cathode are just gammaproteobacteria, with a significant presence of *Acidithiobacillus ferrooxidans*, while the anode counts with alphaproteobacteria and betaproteobacteria as well, with *Acidiphilium* (of the family Acetobacteraceae) being the most abundant proteobacteria. On the other hand, actinobacteria were present at both electrodes, yet doubly as abundantly at the cathode electrode. Finally, while just these two phyla were identified at the anode electrode, a total of four phyla were identified at the cathode electrode (nitrospirae and firmicutes in addition to the previous two). In fact, the genus found to have the highest abundance at the cathode was *Leptospirillum* (of the phylum nitrospirae), followed by *Acidithiobacillus ferrooxidans*, as previously mentioned.

Based on the prokaryotic analysis, it can be deduced that the main electron donors at the anode are probably organic compounds. In fact, it has been previously reported that *Acidiphilium* sp., the dominant prokaryote at the anode electrode, is able to produce a significant power output as a result of glucose oxidation (Malki et al. 2008). In contrast, the reaction at the cathode could be based on the biocatalysed reduction of oxygen. Indeed, *Acidithobacillus ferrooxidans* has been shown to catalyse oxygen reduction directly (Carbajosa et al. 2010).

In conclusion, the results obtained in this experiment reveal that extremophile-based fuel cells pose a competitive green electricity source that performs significantly better than standard near-neutral pH BPVs. Moreover, it can be seen that extremophiles represent a viable alternative to platinum-based catalysts for the oxygen reduction reaction at the cathode, entailing the possibility of building cheaper fuel cells (not only this type of sediment cell, but also standard BPV cells using the pertinent microorganisms as the biocathode).

Conclusions

This project fulfilled the aim of the thesis, which consisted in developing and operating acid-based BPV cells, with the purpose of enhancing electrical performance with respect to prior work on BPV cell platforms.

In first place, standard BPV cells were studied, based on classic prokaryotic and eukaryotic strains. The devices were built, tested and characterised via electrochemical techniques, confirming that the BPV cells used in this study were comparable to those previously reported in the literature, serving as a starting point of reference for the rest of the study.

Secondly, fluorescence techniques, in combination with a short-term potential difference conditioning steps, were used to study the effect of working electrode potential on the efficiency and kinetics of photosynthesis and associated electron transport of the biofilms in question. The results shed light on the various fates of the absorbed light energy, revealing that higher electrical currents are associated with augmented levels of biofilm stress.

Following the study on the classic neutrophile prokaryotic and eukaryotic strains, the realms of the acidophilic microorganisms that could be used in the acid-based BPV cell sought after in this study were explored. For this purpose, a series of locations throughout the Rio Tinto system were exhaustively monitored during a whole natural year, with the aim of identifying those sites exhibiting the harshest physicochemical conditions while bearing the presence of microorganisms. The study revealed very tough conditions of pH, electrical conductivity and heavy metal content generally throughout the sampling sites, which, with the exception of one point, all exhibited the presence of microorganisms.

Finally, the site with most acidic conditions throughout the year was selected for the implementation of an in-situ sediment fuel cell. Previously, a standard BPV cell was operated under acidic conditions in the laboratory, using a commercially available photosynthetic acidophile. The results confirmed the hypothesis that operation under lower pH enhances electrical performance, principally by reducing the internal resistance of the BPV device. Ultimately, a tailored sediment cell was built, implemented within an acid mine drainage stream and tested. The findings from this study revealed that, contrary to the behaviour of the BPV cells tested in the laboratory, the photosynthetic microorganisms were located at the cathode electrode in the sediment fuel cell. Nonetheless, as expected, the microbial fuel cell based on naturally-occurring acidophiles, operating in situ, exhibited an improved power output in comparison with the tested pure-culture acid-operated BPV, which was in fact unprecedentently high in comparison with reported prior work.

In conclusion, the findings from this study reveal that extremophile-based fuel cells exhibit a considerably improved electrical performance with respect to standard near-neutral pH BPV cells, while posing a viable alternative to expensive platinum-based catalysts. Therefore, this study sheds light on the potential of extremophile-based fuel cells as a robust electricity source that could pave the way towards the development of cheap and competitive green electricity generation.

Future Work

The aim of future research is to build on the work of this thesis on acid-operating MFCs, using it as the starting point to continue developing extremophile-based MFCs.

In particular, the objective is to keep exploring the applications of extremophiles as the biological material in MFC and BPV cell platforms. On the one hand, this will allow the improvement of power output, as extremophiles grant the possibility of implementing physicochemical conditions that have previously not been an option with standard mesophile microorganisms.

On the other hand, exploring the potential of extremophile-based MFCs opens a window of opportunities to employ these microorganisms in parallel to electricity generation, including a suite of chemical processes that may be performed simultaneously to power generation and that are beyond the possibilities of the mesophiles currently used in MFC applications such as domestic wastewater treatment. For instance, the implementation of extremophiles in wastewater treatment could enable the simultaneous power generation and bioremediation of a wider range of effluents, including contaminated waters arising from mining activity (e.g. with metallotolerant acidophiles) or high-temperature liquid effluents such as those from refineries and other industrial treatment plants (e.g. with thermophiles).

Providentially, there is an enormous untapped potential for the implementation of extremophile-based MFCs, inviting to develop a wide variety of applications for use in more extreme environments or physicochemical conditions.

Lastly, another important focus of future research should be to continue investigating the electron transfer mechanisms behind MFC and BPV cell operation, in particular those of extremophile-electrode interactions, for a better understanding of the underlying working principle of these electrochemical platforms. This will allow to more successfully tackle the limitations of microbial and extremophile-based fuel cells, enabling their optimisation and performance enhancement.

In conclusion, future work should keep focusing on the development of low-cost, environmentally friendly renewable energy sources and self-sustainable technologies. Microbial Fuel Cells, and Biological Fuel Cells in particular, represent an extremely attractive technology that can pave the way to a green, sustainable, solar-powered future.

Acknowledgements

I would like to thank Dr. Fisher for the supervision of this thesis and very helpful guidance throughout the research and write-up of this work.

I would also like to thank the staff from the Department of Chemical Engineering and Biotechnology at the University of Cambridge, as well as the staff from Proyecto Riotinto, whose help was fundamental for the development of this work.

In addition, I would like to thank the Department of Chemical Engineering and Biotechnology at the University of Cambridge as well as EMED Mining for the funding of this thesis.

References

1. Al-Zuhair, S. (2007). Production of biodiesel: Possibilities and challenges. *Biofuels, Bioproducts and Biorefining,* 1, pp. 57-66.
2. Albertano, P. et al. (1981). Spermatozopsis acidophila Kalina (Chlorophyta, Volvocales), a little known alga from highly acidic environments. *Nuovo Giornale Botanico Italiano*, 115, pp. 65–76.
3. Aletsee, L. and Jahnke, J. (1992). Growth and productivity of the psychrophilic marine diatoms *Thalassiosira antarctica* Comber and *Nitzschia frigida* Grunow in batch cultures at temperatures below the freezing point of sea water. *Polar Biology,* 11, pp. 643-647.
4. Alexander, N. et al. (2009). *Fundamental Laboratory Approaches for Biochemistry and Biotechnology*. United Sates: Wiley, pp. 408-410.
5. Amaral, L.A. et al. (2002). Eukaryotic diversity in Spain's river of fire. *Nature*, 417, pp. 137.
6. Amieva, M. and Peek, R.M. (2016). Pathobiology of Helicobacter pylori-induced Gastric Cancer. *Gastroenterology,* 150 (1), pp. 64-78.
7. Amils, R. et al. (2004). Extremofilia Astrobiológica: El caso del río Tinto*. Boletín SEA*, 12, pp.19-26.
8. Badura, A. et al. (2011). Wiring photosynthetic enzymes to electrodes*. Energy & Environmental Science*, 4(9), pp. 3263-3274.
9. Barnard, D. et al. (2010). Extremophiles in biofuel synthesis. *Journal of Environmental Technology,* 31, pp. 871-888.
10. Barták, M. et al. (2007). Low-temperature limitation of primary photosynthetic processes in Antarctic lichens Umbilicaria Antarctica and Xanthoria elegans. *Polar Biology,* 31 (1), pp. 47-51.
11. Berk, R. S. and Canfield, J. H. (1964). Bioelectrochemical energy conversion. *Applied Microbiology*, 12, pp. 10-12.
12. Blöchl, E. et al. (1997). Pyrolobus fumarii, gen. and sp. Nov., represents a novel group of archaea, extending the upper temperature limit for life to 113 degrees C. *Extremophiles,* 1 (1), pp. 14-21.
13. Boehnke, M. et al. (1989). Fine-structure genetic mapping of human chromosomes using the polymerase chain reaction on single sperm. *American Journal of Human Genetics,* 45 (1), pp. 21-32.
14. Bombelli, P. et al. (2011a). Quantitative analysis of the factors limiting solar power transduction by Synechocystis sp. PCC 6803 in biological photovoltaic devices. *Energy & Environmental Science*, 4 (11), pp. 4690–4698.
15. Bombelli, P. et al. (2011b). Harnessing solar energy by bio-photovoltaic (BPV) devices. *Communications in Agricultural and Applied Biological Sciences*, 76 (2), pp. 89-91.
16. Bond, D.R. and Lovley, D.R. (2003). Electricity production by Geobacter Sulfurreducens attached to electrodes*. Applied Environmental Microbiology*, 69, pp. 1548-1555.
17. Borowitzka, M.J. and Siva, C.J. (2007). The taxonomy of the genus Dunaliella (Chlorophyta, Dunaliellales) with emphasis on the marine and halophilic species. *Journal of Applied Phycology,* 19, pp. 567-590.
18. Brierley, C.L. and Brierley, J.A. (2013). Progress in bioleaching. Part B. Applications of microbial processes by the minerals industry. *Applied Microbial Biotechnology,* 97, pp. 7543-7552.

19. Burton, F.L. (1996). *Water and Wastewater Industries: Characteristics and Energy Management Opportunities*. Electric Power Research Institute Report. Report CR-106941.
20. Cai, H. et al. (2014). Nonculture Molecular Techniques for Fiagnosis of Bacterial Disease in Animals: A Diagnostic Laboratory Perspective. *Veterinary Pathology,* 51 (2), pp. 341-350.
21. Calkins, J.O. et al. (2013). High photo-electrochemical activity of thylakoid-carbon nanotube composites for photosynthetic energy conversion. *Energy & Environmental Science*, 6, pp. 1891-1900.
22. Carbajosa, S. et al. (2010). Growth of Acidithiobacillus ferrooxidans on a graphite electrode for obtaining a biocathode for direct electrocatalytic reduction of oxygen*. Biosensors and Bioelectronics*, 26, pp. 877-880.
23. Chang, I.S. et al. (2006). Electrochemically Active Bacteria (EAB) and Mediator-Less Microbial Fuel Cell*. Journal of Microbiology and Biotechnology*, 16 (2), pp. 163-177.
24. Chien, A. et al. (1976). Deoxyribonucleic acid polymerase from the extreme thermophile Thermus aquaticus. *Journal of Bacteriology,* 127 (3), pp. 1550-1557.
25. Ciniciato, G.P.M.K. et al. (2016). Investigating the association between photosynthetic efficiency and generation of biophotoelectricity in autotrophic microbial fuel cells. Scientific Reports, 6, Article number 31193.
26. Coker, J.A. (2016). Extremophiles and biotechnology: current uses and prospects. *F1000Research,* 5, F1000 Faculty Rev – 396.
27. DasSarma, P. et al. (2009). Halophiles, Industrial Applications. In: *Encyclopedia of Industrial Biotechnology*. Hoboken, NJ, USA: John Wiley & Sons.
28. De Caprarii et al. (2014). Exoelectrogenic Activity of a Green Microalgae, Chlorella vulgaris, in a Bio-Photovoltaic Cells (BPVs). Chemical Engineering Transactions, 34, pp. 523-528.
29. De Luca, P. et al. (1981). Acidophilic algae from the fumaroles of Mount Lawu (Java) locus classius of Cyanidium caldarium Geitler. *Giornale Botanico Italiano,* 115, pp. 1-9.
30. Delaney, G.M. et al. (1984). Electron-transfer coupling in microbial fuel cells. 2. Performance of fuel cells containing selected microorganism-mediator-substrate combinations. *Journal of Chemical Technology and Biotechnology*, 34 (1), pp. 13-27.
31. Doherty, S.J. et al. (2009). Lessons learned from IPCC AR4: Scientific Developments Needed To Understand, Predict, And Respond To Climate Change. *Bulletin of the American Meteorological Society*, 90 (4), pp. 497.
32. DTI. (2005). Regional Electricity Consumption Statistics, UK.
33. Dworkin, M. and Falkow, S. (2006). *The Prokaryotes: a handbook on the biology of bacteria.* New York: Springer-Verlag.
34. Edwards, H.G. et al. (2007). The Rio Tinto Mars analogue site: an extremophilic Raman spectroscopic study*. Spectrochimica Acta Part A,* 68 (4), pp. 1133-1137.
35. Erable, B. et al. (2009). Marine Aerobic Biofilm as Biocathode Catalyst. *Bioelectrochemistry,* 78 (1), pp. 51-56.
36. Fantazzini, D. et al. (2011). Global oil risks in the early 21st century*. Energy Policy*, 39 (12), pp. 7865–7873
37. Feris, K.P. et al. (2004). Seasonal dynamics of shallow-hyporheic-zone microbial community structure along a heavy metal contamination gradient. *Applied Environmental Microbiology*, 70, pp. 23-31.

38. Fernandez-Remolar, D. et al. (2003). Geological record of an acidic environment driven by iron hydrochemistry: The Tinto River system. *Journal of* Geophysical Research, 108, pp. 5080-5095.
39. Fiala, G. et al. (1986). Pyrococcus furiosus sp. nov. represents a novel genus of marine heterotrophic archaebacteria growing optimally at 100 °C. *Archives of Microbiology*, 145, pp. 56-61.
40. Franks, A.E. and Nevin, K.P. (2010). Microbial Fuel Cells, a Current Review. *Energies*, 3(5), pp. 899–919.
41. Frey, E. And Mackenzie Lamb, I. (1939). A new species of Umbilicaria from the Antarctic. *Transactions of the British Mycological Society,* 22 (3-4), pp. 270-273.
42. Garcia, M.T. et al. (1987). Taxonomic study and amended description of *Vibrio costicola*. *International Journal of Systematic Bacteriology*, 37, pp. 251-256.
43. Garibyan, A. (2013). Polymerase Chain Reaction. *Journal of Investigative Dermatology,* 133, pp. 1-4.
44. Ghasemi, M. et al. (2012). Effect of pre-treatment and biofouling of proton exchange membrane on microbial fuel cell performance. *International Journal of Hydrogen Energy,* 38, pp. 5480-5484.
45. Gil, G. et al. (2003). Operational parameters affecting the performance of a mediator-less microbial fuel cell. *Biosensors and Bioelectronics*, 18 (4), pp. 327-334.
46. Gontia-Mishra, I. Et al. (2017). Diversity of halophilic bacteria and actinobacteria from India and their biotechnological appications. *Indian Journal of Geological and Marine Sciences*, 46 (8), pp. 1575-1587.
47. Gorby, Y.A. et al. (2005). Electrically conductive bacterial nanowires produced by Shewanella oneidensis strain MR-1 and other microorganisms. *PNAS,* 103, pp. 11358-11363.
48. Gross, E.L. et al. (1978). An FMN-Photosystem I Photovoltaic Cell, *Photochemistry and Photobiology*, 28 (2), pp.249-256.
49. Gude, V.G. et al. (2013). Beneficial bioelectrochemical systems for energy, water and biomass production. *Journal of Microbial and Biochemical Technology,* 6, pp. 2.
50. Gude, V.G. (2015). Energy and water autarky of wastewater treatment and power generation systems. *Renewable and Sustainable Energy Reviews*, 45, pp. 52-68.
51. Gupta, G.N. et al. (2014). Extremophiles: An Overvie of Microorganism from Extreme Environment. *International Journal of Agriculture, Environment and Biotechnology*, 7 (2).
52. Guzman, J.J. (2010). *Benthic Microbial Fuel Cells: Long-Term Power Sources for Wireless Marine Sensor Networks*. Proceedings, SPIE 7666, Sensors, and Command, Control, Communications, and Intelligence (C3I), Technologies for Homeland Security and Homeland Defense IX, 76662M.
53. Hagelberg, E. et al. (1994). DNA from ancient mammoth bones. *Nature,* 370 (6488), pp. 333-334.
54. Håkanson, L. (1980). An Ecological Risk Index for Aquatic Pollution Control: A Sedimentological Approach. *Water Research*, 14, pp. 975–1001.
55. Hards, S. and Higgins, J.P. (2004). *Bioremediation of Acid Rock Drainage Using Sulfate Reducing Bacteria*. Ontario: Jacques Whit Environment Limited.
56. Hook, M. et al. (2013). Depletion of fossil fuels and anthropogenic climate change—A review. *Energy Policy,* 52, pp. 797-809.

57. Horiike, T. et al. (2009). *Phylogenetic construction of 17 bacterial phyla by new method and carefully selected orthologs.* Gene, 429 (1-2), pp. 59-64.
58. Huber, R. et al. (1998). The complete genome of the hyperthermophilic bacterium *Aquifex aeolicus. Nature,* 392, pp. 353-358.
59. Hug, H. et al. (2014). Biophotovoltaics: Natural pigments in dye-sensitized solar cells. *Applied Energy,* 115, pp. 216-225.
60. Jodlowska, S. and Sliwinska, S. (2014). Effects of light intensity and temperature on the photosynthetic irradiance response curves and chlorophyll fluorescence in three picocyanobacterial strains of *Synechococcus. Photosynthetica*, 52 (2), pp. 223-232.
61. Jothinathan, D. and Wilson, R. T. (2017). Comparative analysis of power production of pure, coculture, and mixed culture in a microbial fuel cell. *Energy Sources, Part A: Recovery, Utilization, and Environmnetal Effect,* 39 (5), pp. 520-527.
62. Kanal, H. et al. (1995). Natronococcus amylolyticus sp. nov., a haloalkaliphilic archaeon. *International Journal of Systematic Bacteriology,* 45 (4), pp. 762-766.
63. Kashefi, K. et al. (2002). Use of Fe(III) as an electron acceptor to recover previously uncultured hyperthermophiles: isolation and characterization of Geothermobacterium ferrireducens gen. nov., sp. nov. *Applied Environmental Microbiology,* 68 (4), pp. 1735-1742.
64. Kashefi, K. and Lovley, D.R. (2003). Extending the upper temperature limit for life. *Science,* 301, pp. 934.
65. Kayano, H. et al. (1981). Photochemical energy conversion system using immobilized chloroplasts. *Biotechnology and Bioengineering*, 23 (10), pp. 2283–2291.
66. Khandan, N. et al. (2014). *Options for energy recovery from urban wastewaters.* In: 9th Conference on Sustainable Development of Energy, Water and Environmental Systems.
67. Kim, B.H. et al. (1999). Direct electrode reaction of Fe(III) reducing bacterium, Shewanella putrefaciens*. Journal of Microbiology and Biotechnology,* 9, pp. 127-131.
68. Kim, S.J. et al. (2012). Genome Sequence of a Novel Member of the Genus Psychrobacter Isolated from Antarctic Soil. *Journal of Bacteriology,* 194 (9), pp. 2403.
69. Kwok, S. Et al. (1987). Identification of HIV sequences by using in vitro enzymatic amplification and oligomer cleavage detection. *Journal of Virology*, 61 (5), pp. 1690-1694.
70. Lamed, R. and Zeikus, J.G. (1980). Glucose fermentation pathway of Thermoanaerobium brockii. *Journal of Bacteriology,* 141, pp. 1251-1257.
71. Leong, C.S. et al. (2009). Some Key Issues In the Processing and Fabrication of Higher Efficiencies Silicon Solar Cells. *3rd WSEAS International Conference on Energy Planning*, pp. 304-307.
72. Levin, D.B. et al. (2006). Hydrogen production by Clostridium thermocellum 27405 from cellulosic biomass substrates. *International Journal of Hydrogen Energy,* 31, pp. 1496-1503.
73. Li, X. et al. (2015). Light-Induced Extracellular Electron Transport by the Marine Raphidophyte *Chattonella marina. Environmental Scence and Technoogy*, *49* (3), pp. 1392–1399.

74. Logan, B.E. (2004). Extracting hydrogen and electricity from renewable resources. *Environmental Science and Technology,* 38, pp. 160-167.
75. Logan, B. et al. (2006). Microbial Fuel cells: Methodology and Technology. *Environmental Science and Technology,* 40 (17), pp. 5181-5192.
76. Logan, B. E. (2008). Microbial fuels for the future. *Nature*, 454, pp. 943-944.
77. López-Archilla, A.I. et al. (1999). A comparative ecological study of two acidic rivers in SW Spain. *Microbial Ecology*, 38, pp. 146-156.
78. López-Archilla, A.I. et al. (2001). Microbial community composition and ecology of an acidic aquatic environment: the Tinto river, Spain. *Microbial Ecology*, 41, pp. 20-35.
79. Lewis, N.S. and Nocera, D.G. (2006). Powering the planet: Chemical challenges in solar energy utilization*. PNAS,* 103 (43), pp. 15729-15735.
80. Lieu, H. et al. (2005). Electrochemically assisted microbial production of hydrogen from acetate. *Environmental Science and Technology,* 39, pp. 4317-4320.
81. Lieu, B. et al. (2006). The synergistic effect of two photosynthetic pigments in dye-sensitized mesoporous TiO_2 solar cells*. Dyes and Pigments,* 76 (2), pp. 327–331.
82. Littlechild, JA. (2015). Archaeal Enzymes and Applications in Industrial Biocatalysts. *Archaea*, 2015, 147671.
83. Logan, B.E. (2009). Exoelectrogenic bacteria that power microbial fuel cells*. Nature Reviews Microbiology*, 7(5), pp. 375-385.
84. Loveland-Curtze, J. Et al. (2009). Novel Ultramicrobacterial Isolates from a Deep Greenland Ice Core Represent a Proposed New Species, Chryseobacterium greenandense sp. nov. *Extremophiles*, 14, pp. 61-69.
85. Luimstra, V.M. et al. (2014). A cost-effective microbial fuel cell to detect and select for photosynthetic electrogenic activity in algae and cyanobacteria. *Journal of Applied Phycology*, 26 (1), pp. 15-23.
86. Lundberg, K.S. et al. (1991). High-fidelity amplification using a thermostable DNA polymerase isolated from Pyrococcus furiosus. *Gene*, 108 (1), pp.1-6.
87. Madigan, M.T. and Martino, J.M. (2006). *Brock Biology of Microorganisms (11th edition).* New Jersey: Pearson Prentice Hall, pp. 136.
88. Malki, M. et al. (2008). Preferential use of an anode as an electron acceptor by an acidophilic bacterium in the presence of oxygen*. Applied Environmental Microbiology,* 74, pp. 4472-4476.
89. Marjanovic, D. et al. (2006). Optimisation of forensic genetics procedures used in disputed paternity testing: adjustment of the PCR reaction volume. *Bosnian Journal of Basic Medical Sciences,* 6 (2), pp.76-81.
90. Martens, N. and Hall, E.A.H. (1994). Diaminodurene as a mediator of a photocurrent using intact cells of cyanobacteria. *Photochemistry and Photobiology*, 59 (1), pp. 91-98.
91. Martins, M.B. and Carvalho, I. (2007). Diketopiperazines: Biological activity and synthesis. *Tetrahedron*, 63 (40), pp. 9923-9932.
92. Maruyama, A. et al. (2000). Phylogenetic analysis of psychrophilic bacteria isolated from the Japan Trench, including a description of the deep-sea species Psychrobacter pacificensis sp. Nov. *International Journal of Systematic and Evolutionary Microbiology,* 50 (2), pp. 835-46.
93. Mattews, J.A. (2008). Carbon-negative biofuels*. Energy Policy*, 36(3), pp. 940–945.

94. McCormick, A.J. et al. (2011). Photosynthetic biofilms in pure culture harness solar energy in a mediatorless bio-photovoltaic cell (BPV) system. *Energy and Environmental Science*, 4, pp. 4699-4709.
95. McMinn, A. and Hegseth, E.N. (2003). Early spring pack ice algae from the Arctic and Antarctic: how different are they?. *Antarctic Biology in a Global Context*. Leiden: Backhuis Publishers, pp. 182-6.
96. Mellado, D. et al. (2006). Geologia y estructura de la Mina de Rio Tinto (Faja Piritica Iberica, España). *Geogaceta*, 40, pp. 231-234.
97. Mongodin, E.F. (2005). The genome of Salinibacter ruber: Convergence and gene Exchange among hyperhalophilic bacteria and archaea. *Proceedings of the National Academy of Sciences,* 102 (50), pp. 18147-18152.
98. Mosleh Arany, A. et al. (2018). The effects of carbon dioxide concentrations on some morphological and physiological characteristics of ligustrum vulgare. *Plant Physiology*, 8(84), pp. 2549-2554.
99. Mullakhanbhai, M.F. and Larsen, H. (1975). *Halobacterium volcanii* spec. nov., a Dead Sea halobacterium with a moderate salt requirement. *Archives of Microbiology,* 104, pp. 207-214.
100. Mullis, K.B. et al. (1987). *Process for amplifying, detecting, and/or cloning nucleic acid sequences*. U.S. Patent 4, 683, 195.
101. Myers, C.R. and Myers, J.M. (1992). Localization of cytochromes to the outer membrane of anaerobically grown Shewanella putrefaciens MR-1. *Journal of Bacteriology*, 174, pp. 3429–3438.
102. Natarajan, J. et al. (2014). Biochemical characterization of the tandem HAMP domain from Natronomonas pharaonis as an intraprotein signal transducer. *FEBS Journal,* 281, pp. 3218-3227.
103. Neufeld, J. et al. (2013). A Low Temperature Limit for Life on Earth. *PLoS ONE,* 8 (6): e66207.
104. Niederlehner, B.R. and Cairns, J. (1990). Effects of increasing acidity on aquatic protozoan communities. *Water, Air & Soil Pollution,* 52, pp.183-196.
105. Ochiai, H. et al. (1983). Properties of semiconductor electrodes coated with living films of cyanobacteria. *Applied Biochemistry and Biotechnology*, 8 (4), pp. 289-303.
106. Ollivier, B. et al. (1994). Anaerobic bacteria from hypersaline environments. *Microbiological Reviews,* 58 (1), pp. 27-38.
107. Panikov, N.S. et al. (2006). Microbial activity in soils frozen to below -39°C. *Soil Biology and Biochemistry,* 38, pp. 785-794.
108. Pankowski, A. and McMinn, A. (2009). Iron availability regulates growth, photosynthesis and production of ferredoxin and flavodoxin in Antarctic sea ice diatoms. *Aquatic Biology*, 4, pp. 273–288.
109. Pant, D. et al. (2010). A review of the substrates used in microbial fuel cells (MFCs) for sustainable energy production. *Bioresource Technology,* 101 (6), pp. 1533-1543.
110. Patten, C.L. et al. (2009). *Molecular Biotechnology: Principles and Applications of Recombinant DNA.* Washington, D.C: ASM Press.
111. Pettipher, G.L. et al. (1997). Methods for the detection and enumeration of *Alicyclobacillus acidoterrestris* and investigation of growth and production of taint in fruit juice and fruit juice-containing drinks. *Letters in Applied Microbiology*, 24 (3), pp. 185-189.
112. Pick, U. (1998). Dunaliella acidophila a most extreme acidophilic alga.

Enigmatic microorganisms and life in extreme environments. Dordrecht: Kluwer Academic Publishers, pp. 467-472.
113. Pinhassi R. I. et al. (2015). Photosynthetic membranes of *Synechocystis* or plants convert sunlight to photocurrent through different pathways due to different architectures. *PLoS ONE*, 10 (4): e0122616.
114. Pisciotta, J.M. et al. (2010). Light-dependent electrogenic activity of cyanobacteria. *PLoS ONE*, 5 (5): e10821.
115. Potter, M.C. (1911). Electrical effects accompanying the decomposition of organic compounds. *Royal Society*, 84, pp. 260–276.
116. Pulz, O. and Gross, W. (2004). Valuable products from biotechnology of microalgae. *Applied Microbiology and Biotechnology,* 65, pp. 635-648.
117. Quill, E. (2008). Blood-Matching Goes Genetic. *Science Magazine,* 14 March 2008, pp. 1478-1479.
118. Rabaey, K. et al. (2005). Microbial phenazine production enhances electron transfer in biofuel cells. *Environmental Science and Technology*, 39, pp. 3401-3408.
119. Reguera, G. et al. (2005). Extracellular electron transfer via microbial nanowires. *Nature,* 435, pp. 1098-1101.
120. Rickard, T.A. (1928). The Mining of the Romans in Spain. *The Journal of Roman Studies*, 18, pp.129–143.
121. Rozendal, R.A. et al. (2006). Principle and perspectives of hydrogen production through biocatalyzed electrolysis. *International Journal of Hydrogen Energy,* 31, pp. 1632-1640.
122. Ryu, W.H. et al. (2010). Direct Extraction of Photosynthetic Electrons from Single Algal Cells by Nanoprobing System. *Nano Letters*, 10 (4), pp. 1137-1143.
123. Saiki, R. et al. (1985). Enzymatic amplification of beta-globin genomic sequences and restriction site analysis for diagnosis of sickle cell anaemia. *Science*, 230 (4732), pp. 1350-1354.
124. Sawa, M. et al. (2017). Electricity generation from digitally printed cyanobacteria. *Nature communications*, 8, Article number: 1327.
125. Schippers, A. et al. (2014). Biomining: metal recovery from ores with microorganisms. *Advanced Biochemical Engineering and Biotechnology*, 141, pp. 1-47.
126. Schultze, M. et al. (2009). Localization of cytochrome b_6f complexes implies an incomplete respiratory chain in cytoplasmic membranes of the cyanobacterium *Synechocystis* sp. PCC 6803. *Biochimica et Biophysica Acta (BBA) – Bioenergetics*, 1787 (12), pp. 1479–1485.
127. Seckbach, J. et al. (2013). *Polyextremophiles – life under multiple forms of stress.* Dordrecht: Springer.
128. Segerer, A. et al. (1986). Acidianus infernus gen. nov., sp. Nov., and Acidianus brierleyi Comb. Nov.: Facultatively Aerobic, Extremely Acidophilic Thermophilic Sulfur-Metabolizing Archaebacteria. *International Journal of Systematic Bacteriology,* 36 (4), pp. 559-564.
129. Shantaram, A. et al. (2005). Wireless Sensors Powered By Microbial Fuel Cells. *Environmental Scicence and Technology,* 39, pp.5037-5042.
130. Sharma, Y. And Li, B. (2010). The variation of power generation with organic substrates in single-chamber microbial fuel cells (SCMFCs). *Bioresource Technology,* 101, pp. 1844-1850.
131. Shoener, B.D. et al. (2014). Energy positive domestic wastewater treatment:

the roles of anaerobic and phototrophic technologies. *Environmental Science: Processes and Impact,* 16 (6), pp. 1204-1222.
132. Simpson, E.H. (1949). Calculation of diversity coefficients in ecology*. Nature,* 163, pp. 688.
133. Snoeijs, P. and Snoeijs, F. (1993). A simple sampling device for taking quantitative microalgal samples from stone surfaces. *Archiv für Hydrobiologie*, 129**,** pp. 121-126.
134. Stuart, E.S. et al. (2001). Antigen presentation using novel particulate organelles from halophilic archaea.*Journal of Biotechnology*, 88 (2), pp. 119-128.
135. Stuart, E.S. et al. (2004). Cassette-based presentation of SIV epitopes with recombinant gas vesicles from halophilic archaea. *Journal of Biotechnology,* 114 (3), pp. 225-237.
136. Suarez, D.L. et al. (2003). The effect of various disinfectants on detection of avian influenza virus by real time RT-PCR. *Avian Diseases,* 47 (3), pp. 1091-1095.
137. Sun, M. et al. (2008). An MEC-MFC-coupled system for biohydrogen production from acetate. *Environmental Science and Rechnology,* 42 (21), pp. 8095-8100.
138. Sun, J. et al. (2013). Redox mediator enhanced simultaneous decolorization of azo dye and bioelectricity generation in air-cathode microbial fuel cell*. Bioresource Technology*, 142, pp. 407-414.
139. Takai, K. et al. (2008). Cell proliferation at 122°C and isotopically heavy CH4 production by a hyperthermophilic methanogen under high-pressure cultivation. *Proceedings of the National Academy of Sciences,* 105 (31), pp. 10949-10954.
140. Tanaka, K. et al. (1988). Effects of light on the electrical output of bioelectrochemical fuel-cells containing Anabaena variabilis M-2: Mechanism of the post-illumination burst*. Journal of Chemical Technology and Biotechnology*, 42 (3), pp. 235-240.
141. Tang, C.W. and Albrecht, A.C. (1975). Chlorophyll-a photovoltaic cells*. Nature,* 254, pp. 507–509.
142. Tender, L. et al. (2002). Harnessing microbially generated power on the seafloor. *Nature Biotechnology*, 20, pp. 821-825.
143. Tender, L. et al. (2008). The first demonstration of a microbial fuel cell as a viable power supply: Powering a meteorological buoy. *Journal of Power Source*, 179, pp. 571-575.
144. Thirugnanasambandam, M. et al. (2010). A review of solar thermal technologies. *Renewable and Sustainable Energy Reviews*, 14, pp. 312–322.
145. Thorne, R. et al. (2011). Porous ceramic anode materials for photo-microbial fuel cells. *Journal of Materials Chemistry*, 21 (44), pp. 18055-18060.
146. Tindall, K.R. and Kunkel, T.A. (1988). Fidelity of DNA synthesis by the Thermus aquaticus DNA polymerase. *Biochemistry*, 27 (16), p. 6008-6013.
147. Torimura, M. et al. (2001). Electrochemical investigation of cyanobacteria *Synechococcus* sp. PCC7942-catalyzed photoreduction of exogenous quinones and photoelectrochemical oxidation of water*. Journal of Electroanalytical Chemistry*, 496 (1-2), pp. 21-28.
148. Vera, M. et al. (2013). Progress in bioleaching: fundamentals and mechanisms of bacterial metal sulfide oxidation—part A. *Applied Microbiology and Biotechnology*, 97 (17), pp. 7529-7541.
149. Wang, Y. et al. (2011). A review of polymer electrolyte membrane fuel cells:

technology applications and needs on fundamental research. *Applied Energy*, 88, pp. 981-1007.
150. Xie, H.X. et al. (2010). Mediator toxicity and dual effect of glucose on the lifespan for current generation by Cyanobacterium *Synechocystis* PCC 6714 based photoelectrochemical cells. *Journal of Chemical Technology and Biotechnology*, 86 (1), pp. 109-114.
151. Yagishita, T. et al. (1993). Effects of light, CO2 and inhibitors on the current output of biofuel cells containing the photosynthetic organism *Synechococcus* sp. *Journal of Chemical Technology and Biotechnology*, 56 (4), pp. 393-399.
152. Yagishita, T. et al. (1997). Behavior of glucose degradation in *Synechocystis* sp. M-203 in bioelectrochemical fuel cells. *Biochemistry and Bioenergetics*, 43 (1), pp. 177-180.
153. Yao, D.C.I. et al. (2012). Photosystem II component lifetimes in the cyanobacterium *Synechocystis* sp. strain PCC 6803: Small Cab-like proteins stabilize biosynthesis intermediates and affect early steps in chlorophyll synthesis. *Journal of Biological Chemistry,* 287, pp. 682–692.
154. Yehezkeli, O. et al. (2012). Integrated Photosystem II-based photo-bioelectrochemical cells*. Nature Communications*, 3, pp. 742.
155. Yuan, H. et al. (2016). Oxygen reduction reaction catalysts used in microbial fuel cells for energy-efficient wastewater treatment: a review*. Materials Horizons*, 3, pp. 382-401.
156. Zaldivar, J. Et al. (2001). Fuel ethanol production from lignocellulose: A challenge for metabolic engineering and process integration. *Applied Microbiology and Biotechnology,* 56, pp. 17-34.
157. Zhang, Y. and Angelidaki, I. (2012). Innovative self-powered submersible microbial electrolysis cell (SMEC) for biohydrogen production from anaerobic reactors. *Water Resources,* 46 (8), pp. 2727-2736.

Appendix: Analysis of heavy metals at sampling sites 1-16

- Point 1

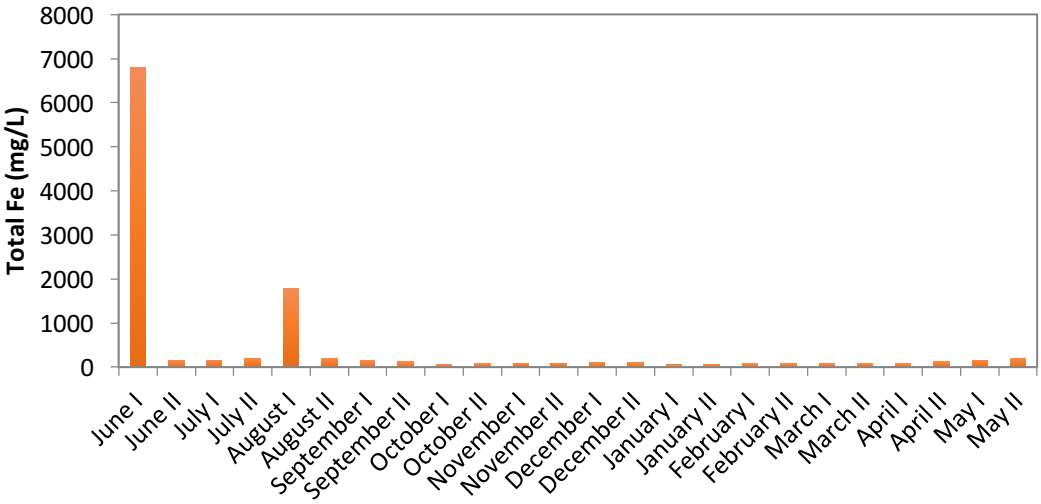

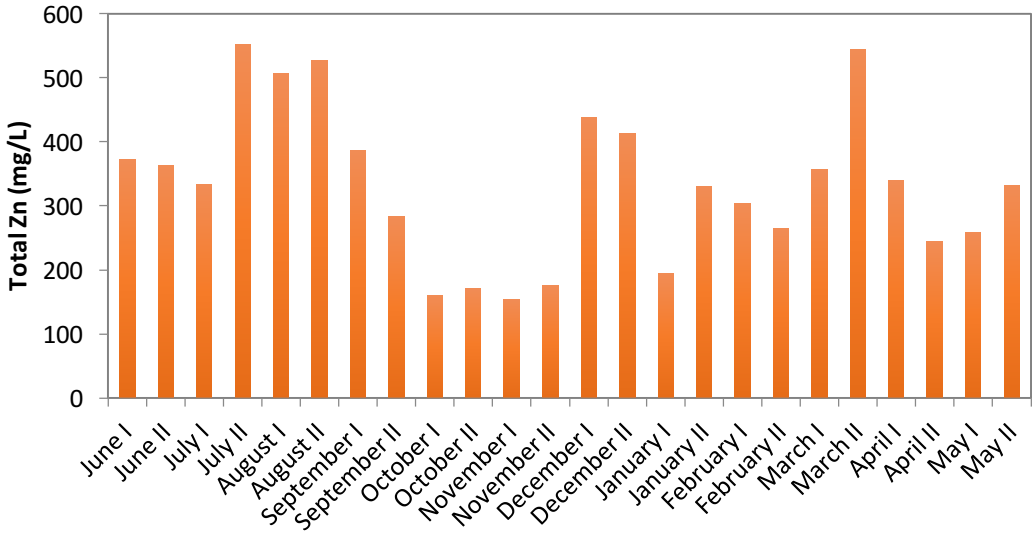

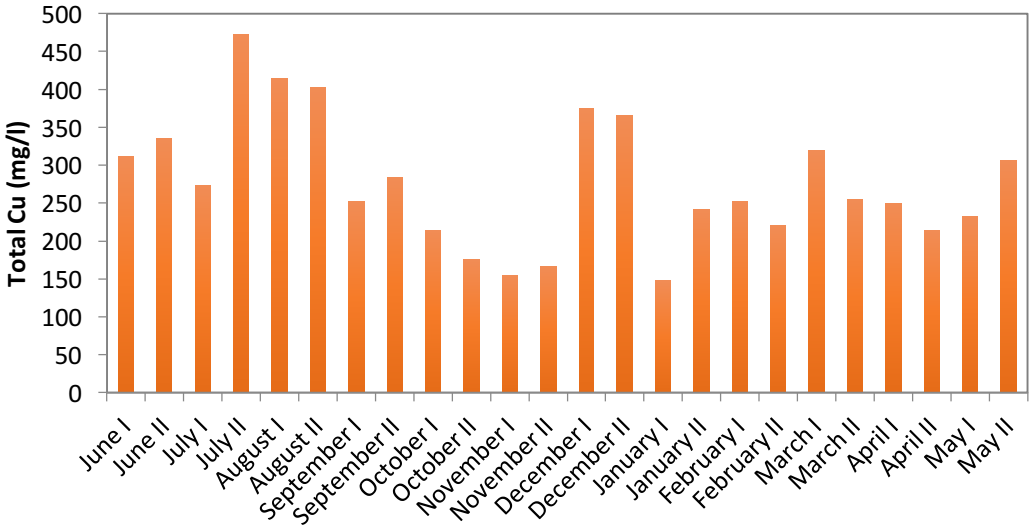

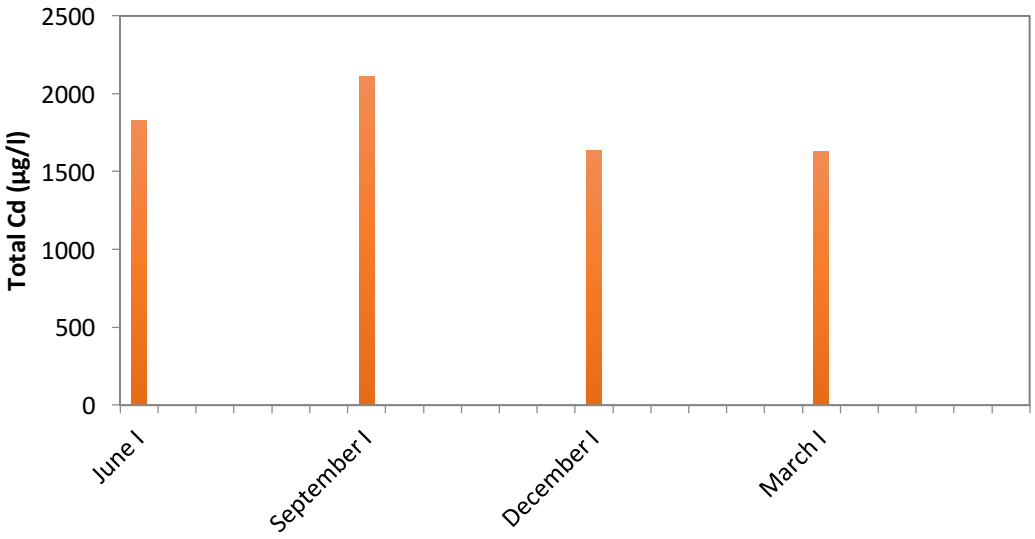
Total Cd (µg/l)
2500
2000
1500
1000
500
0
June I
September I
December I
March I

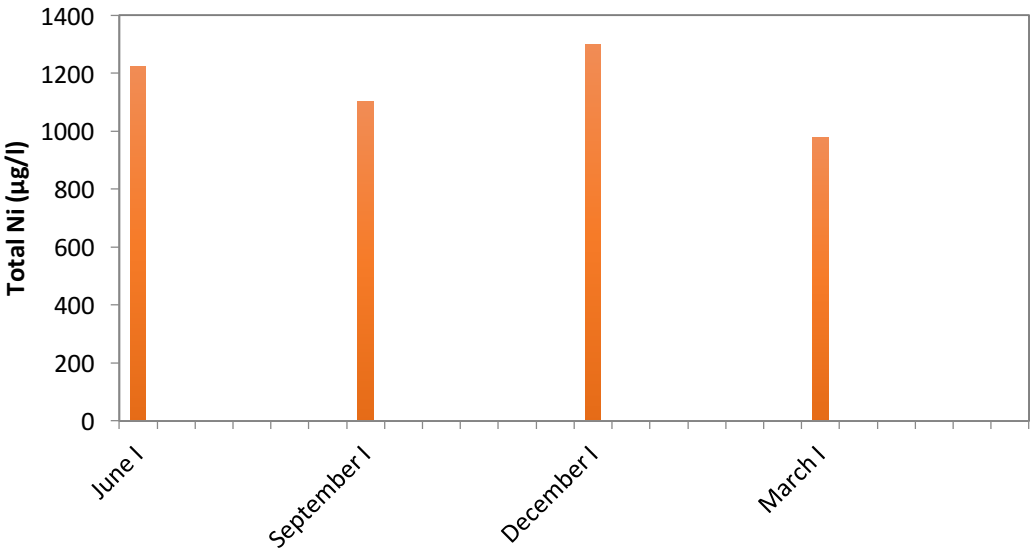
Total Ni (µg/l)
1400
1200
1000
800
600
400
200
0
June I
September I
December I
March I

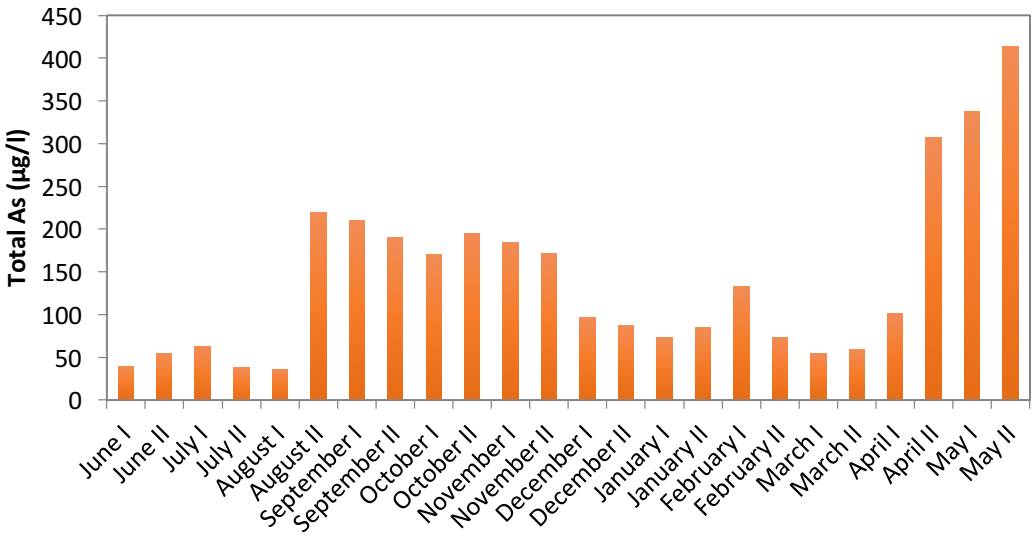
Total As (µg/l)
450
400
350
300
250
200
150
100
50
0
June I
June II
July I
July II
August I
August II
September I
September II
October I
October II
November I
November II
December I
December II
January I
January II
February I
February II
March I
March II
April I
April II
May I
May II

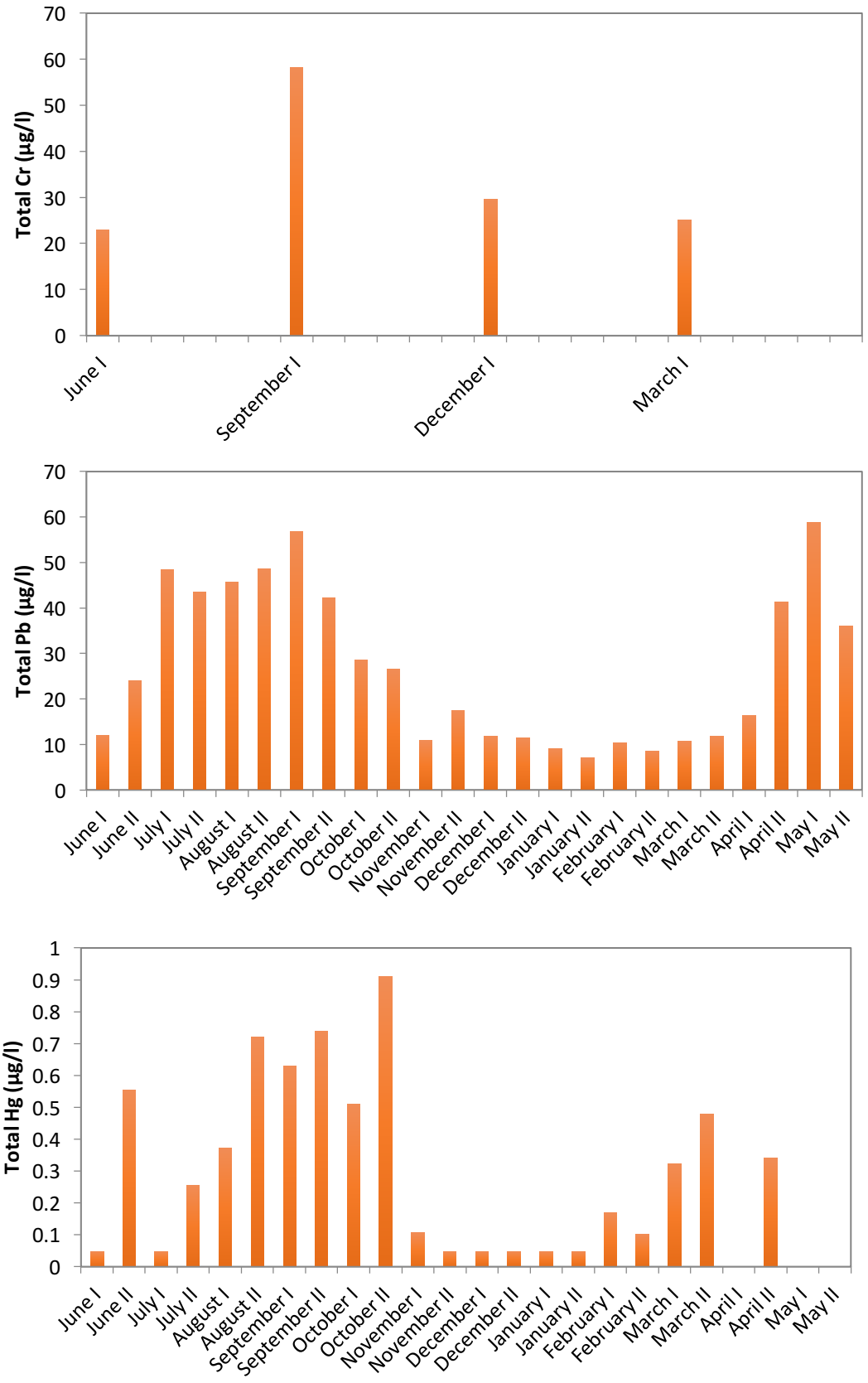

Figure A1: Graphs showing the bimonthly evolution of total Iron, Copper, Zinc, Arsenic, Lead and Mercury and the quarter-yearly evolution of Cadmium, Nickel and Chromium in solution at point 1, from June 2015 until May 2016.

- Point 2

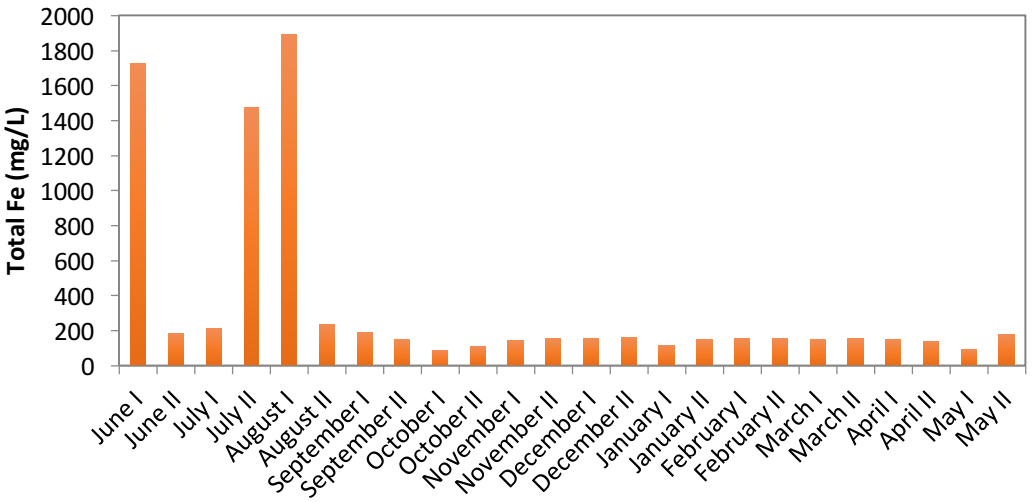
Total Fe (mg/L)
2000
1800
1600
1400
1200
1000
800
600
400
200
0
June I
June II
July I
July II
August I
August II
September I
September II
October I
October II
November I
November II
December I
December II
January I
January II
February I
February II
March I
March II
April I
April II
May I
May II

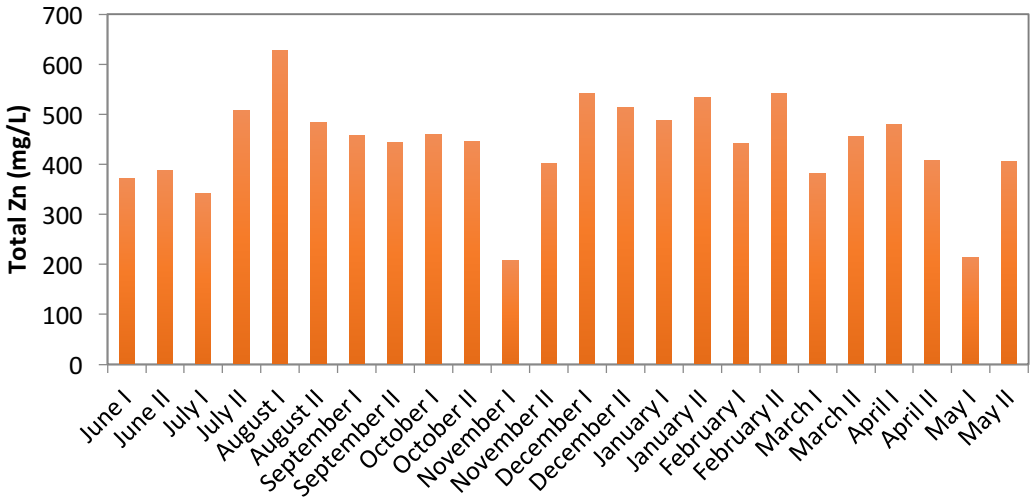
Total Zn (mg/L)
700
600
500
400
300
200
100
0
June I
June II
July I
July II
August I
August II
September I
September II
October I
October II
November I
November II
December I
December II
January I
January II
February I
February II
March I
March II
April I
April II
May I
May II

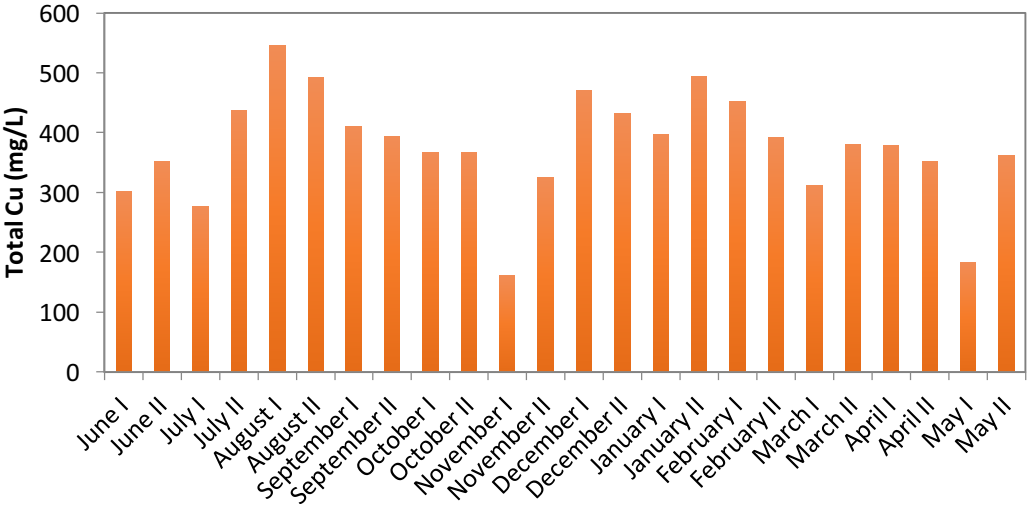
Total Cu (mg/L)
600
500
400
300
200
100
0
June I
June II
July I
July II
August I
August II
September I
September II
October I
October II
November I
November II
December I
December II
January I
January II
February I
February II
March I
March II
April I
April II
May I
May II

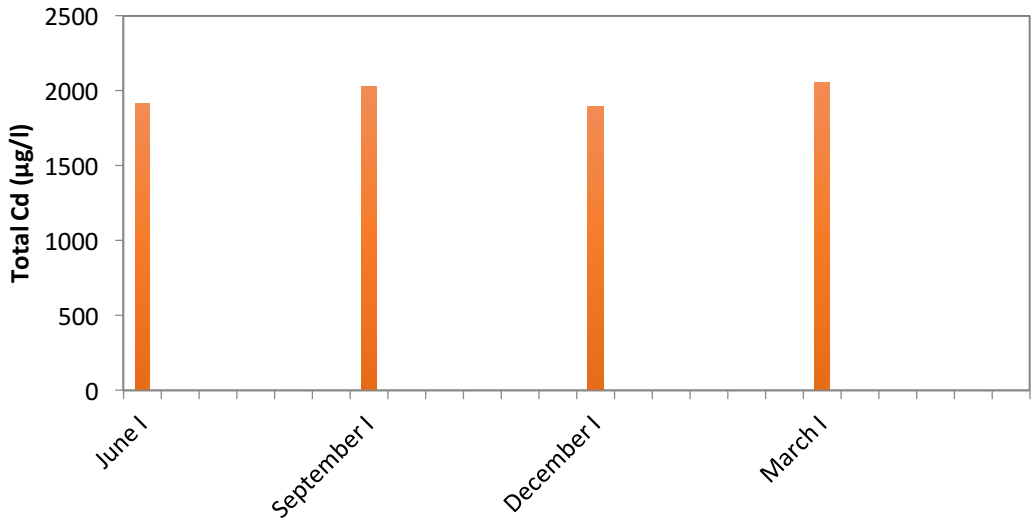
Total Cd (µg/l)
2500
2000
1500
1000
500
0
June I
September I
December I
March I

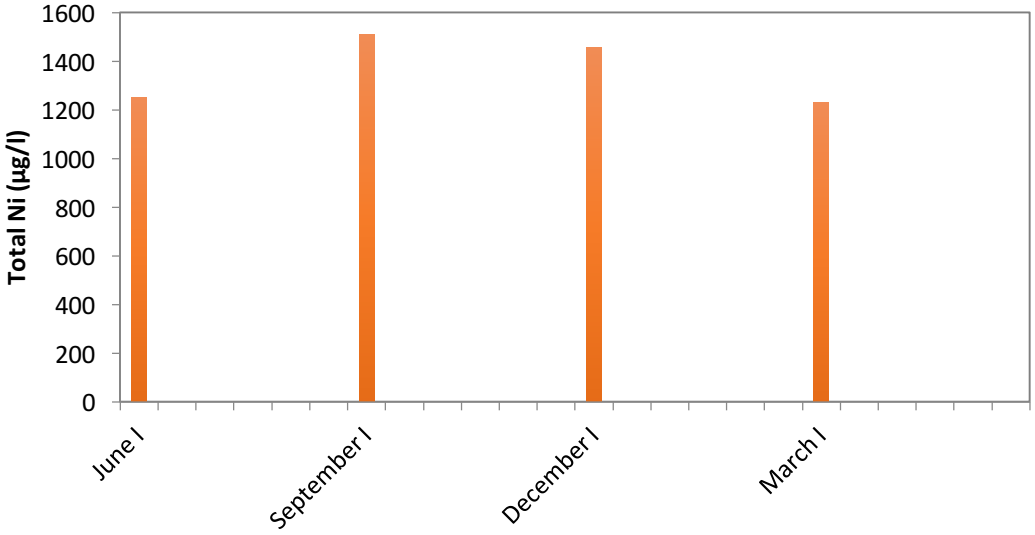
Total Ni (µg/l)
1600
1400
1200
1000
800
600
400
200
0
June I
September I
December I
March I

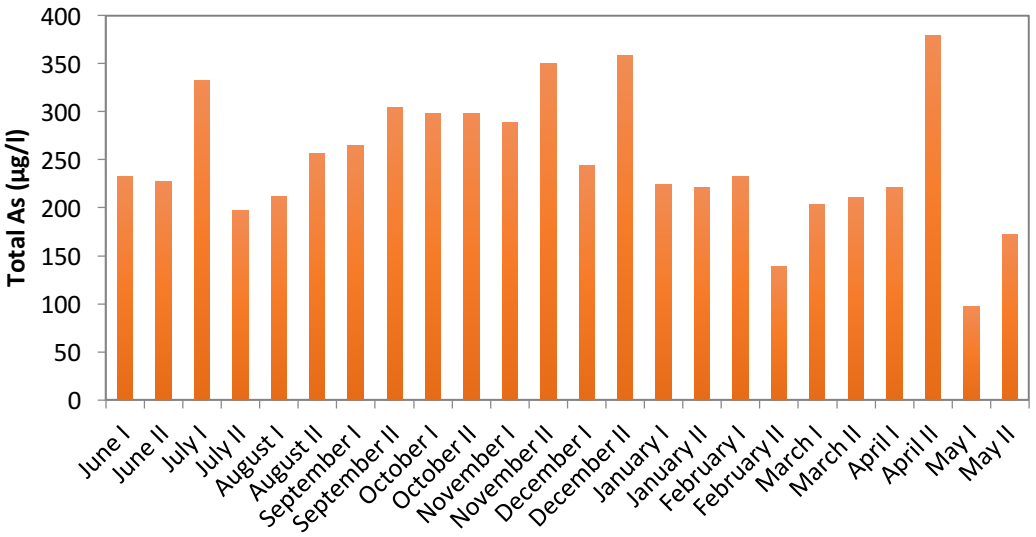
Total As (µg/l)
400
350
300
250
200
150
100
50
0
June I
June II
July I
July II
August I
August II
September I
September II
October I
October II
November I
November II
December I
December II
January I
January II
February I
February II
March I
March II
April I
April II
May I
May II

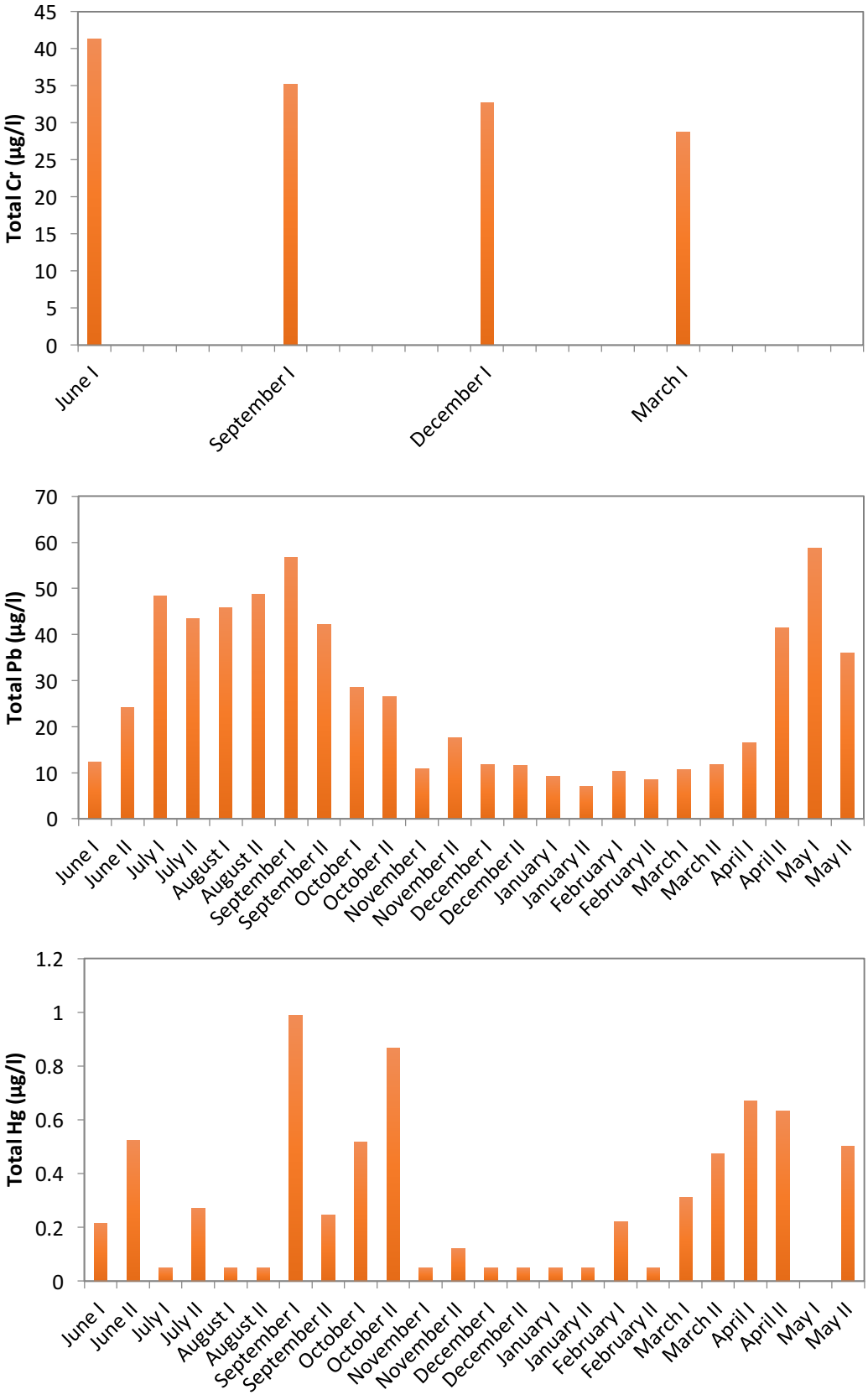

Figure A2: Graphs showing the bimonthly evolution of total Iron, Copper, Zinc, Arsenic, Lead and Mercury and the quarter-yearly evolution of Cadmium, Nickel and Chromium in solution at point 2, from June 2015 until May 2016

- Point 3

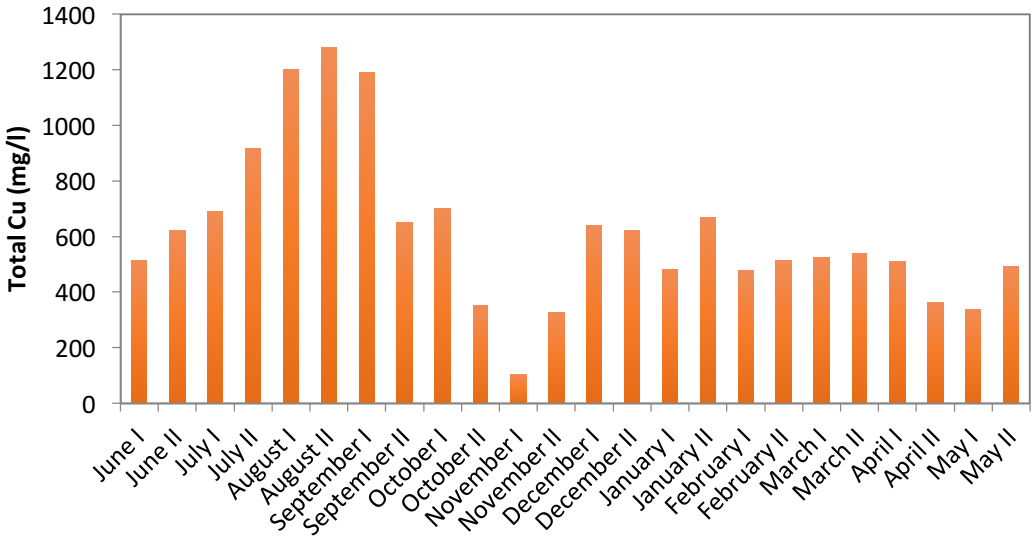
Total Cu (mg/l)
1400
1200
1000
800
600
400
200
0
June I
June II
July I
July II
August I
August II
September I
September II
October I
October II
November I
November II
December I
December II
January I
January II
February I
February II
March I
March II
April I
April II
May I
May II

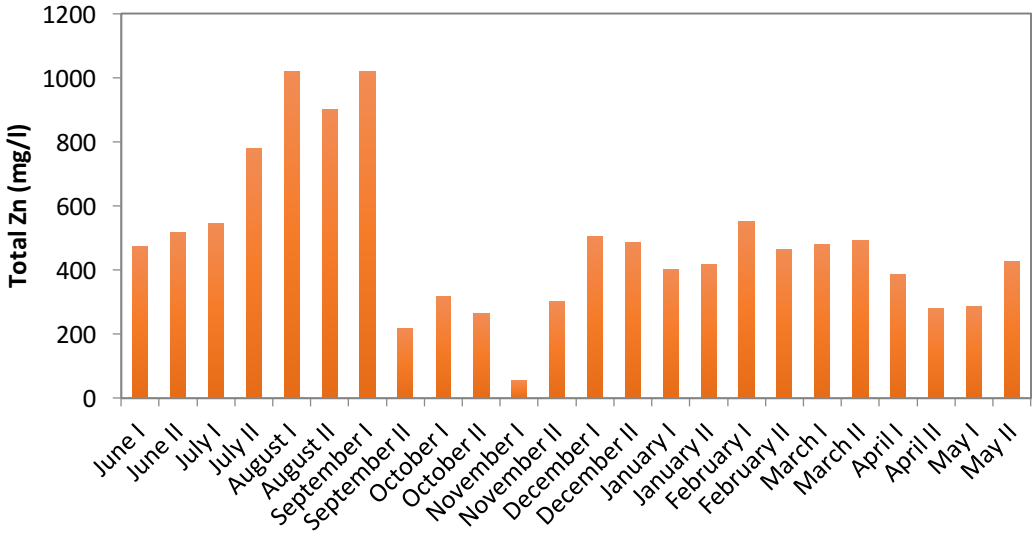
Total Zn (mg/l)
1200
1000
800
600
400
200
0
June I
June II
July I
July II
August I
August II
September I
September II
October I
October II
November I
November II
December I
December II
January I
January II
February I
February II
March I
March II
April I
April II
May I
May II

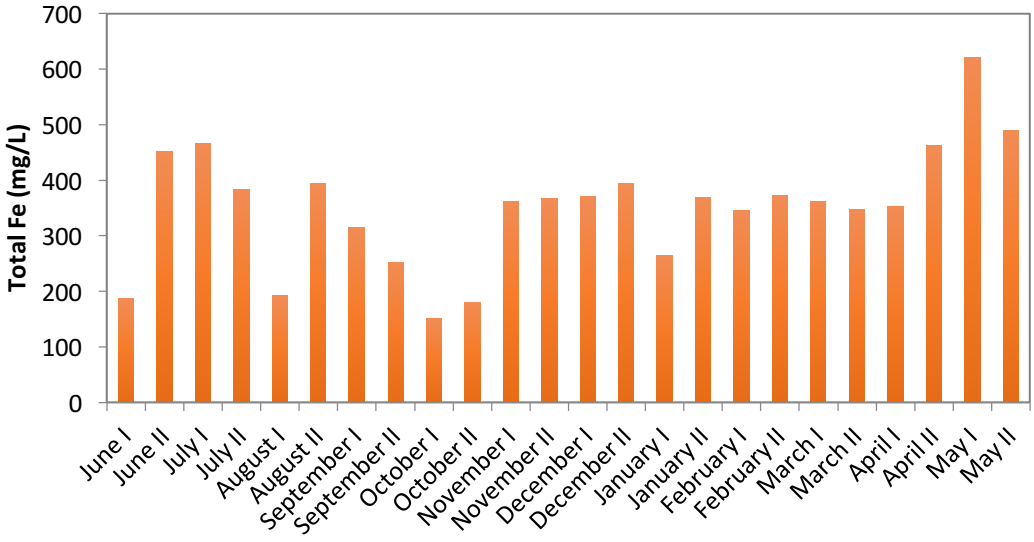
Total Fe (mg/L)
700
600
500
400
300
200
100
0
June I
June II
July I
July II
August I
August II
September I
September II
October I
October II
November I
November II
December I
December II
January I
January II
February I
February II
March I
March II
April I
April II
May I
May II

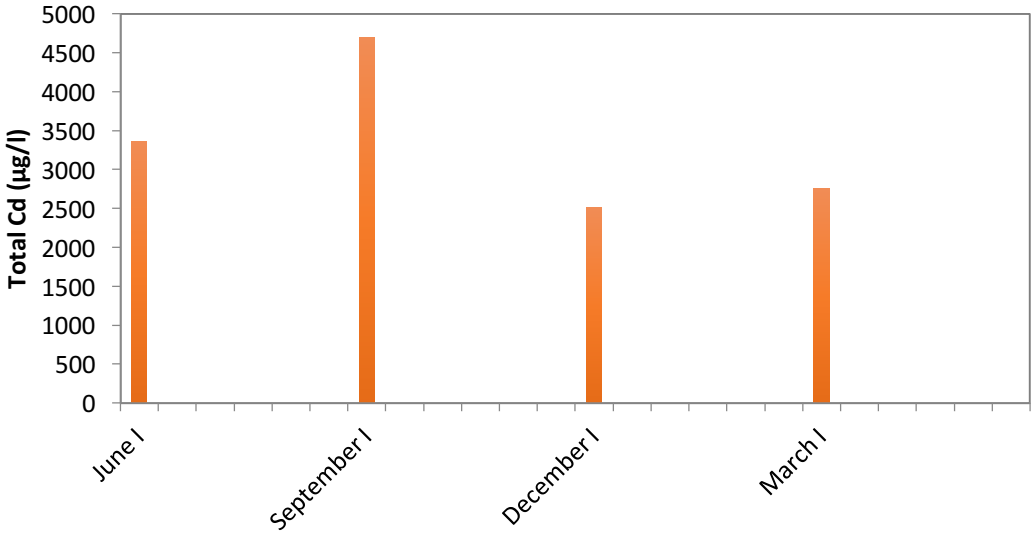
Total Cd (µg/l)
5000
4500
4000
3500
3000
2500
2000
1500
1000
500
0
June I
September I
December I
March I

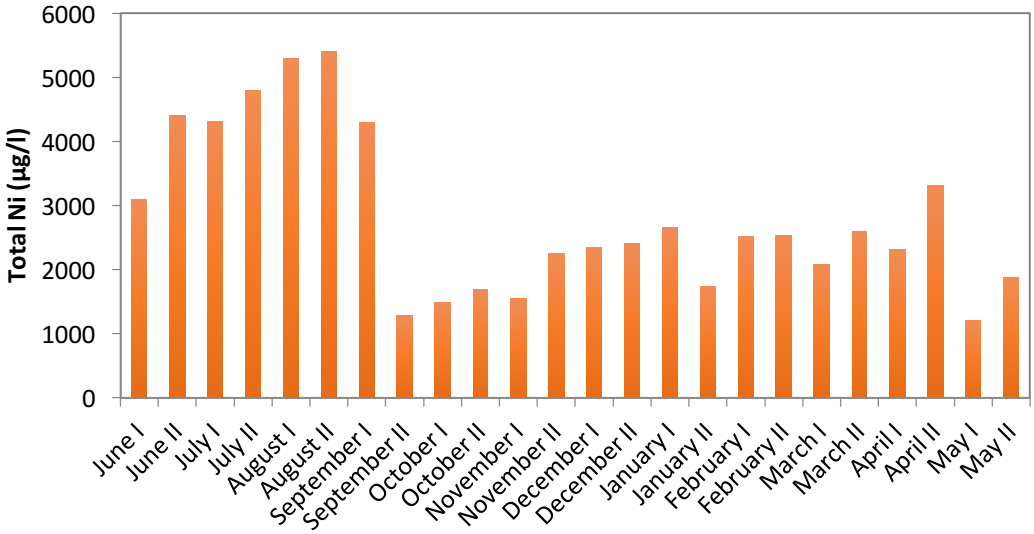
Total Ni (µg/l)
6000
5000
4000
3000
2000
1000
0
June I
June II
July I
July II
August I
August II
September I
September II
October I
October II
November I
November II
December I
December II
January I
January II
February I
February II
March I
March II
April I
April II
May I
May II

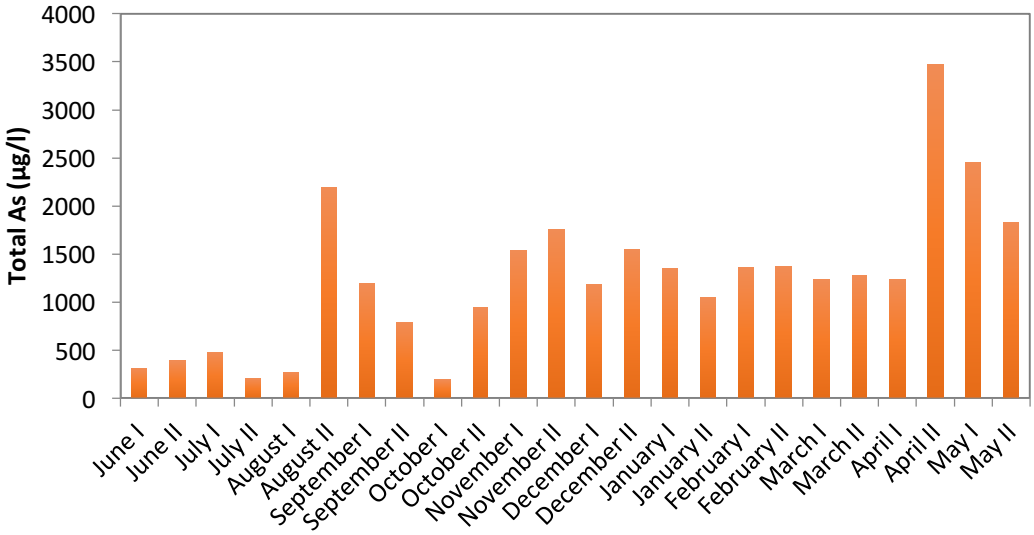
Total As (µg/l)
4000
3500
3000
2500
2000
1500
1000
500
0
June I
June II
July I
July II
August I
August II
September I
September II
October I
October II
November I
November II
December I
December II
January I
January II
February I
February II
March I
March II
April I
April II
May I
May II

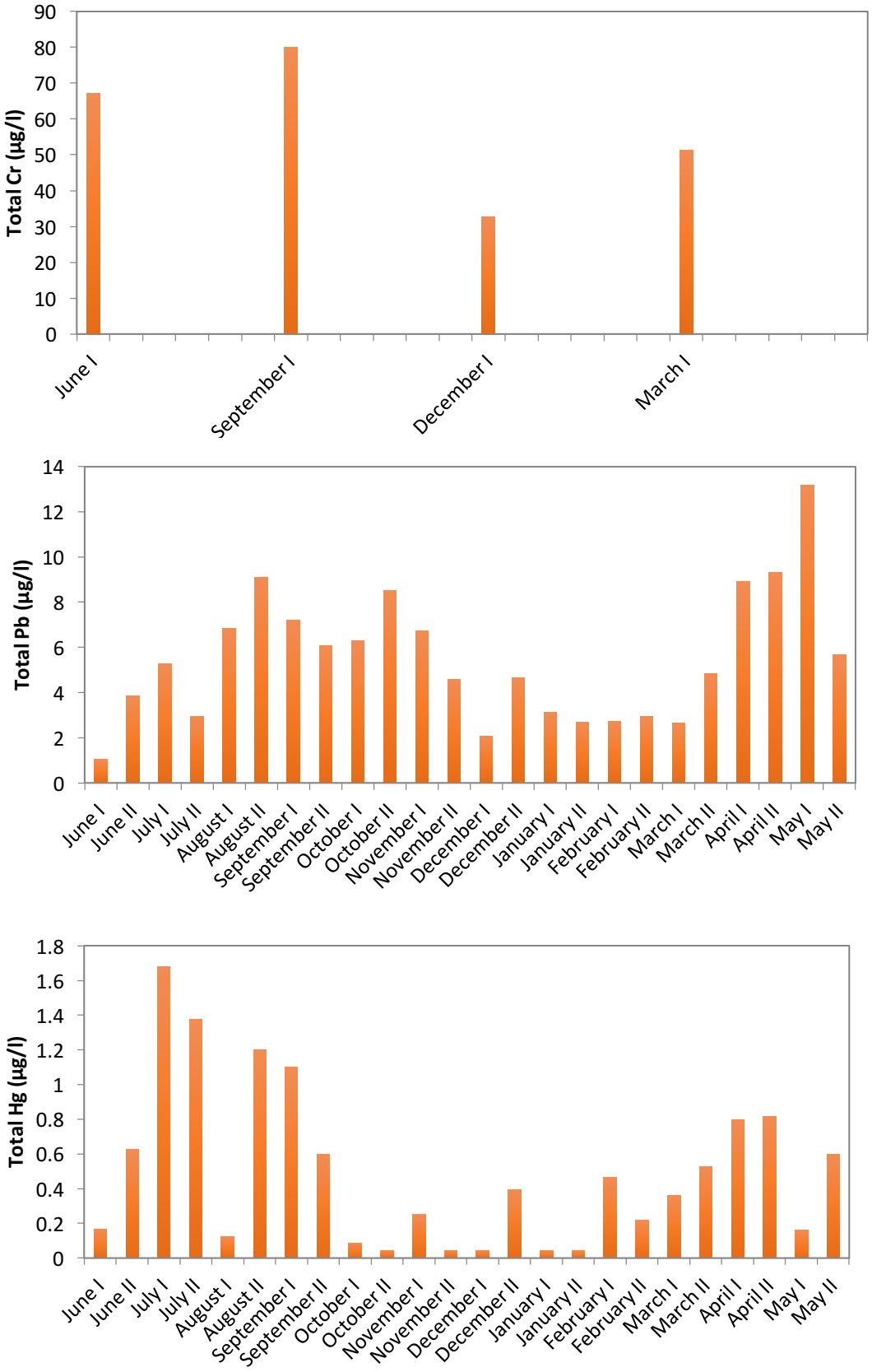

Figure A3: Graphs showing the bimonthly evolution of total Iron, Copper, Zinc, Arsenic, Lead and Mercury and the quarter-yearly evolution of Cadmium, Nickel and Chromium in solution at point 3, from June 2015 until May 2016.

- Point 4

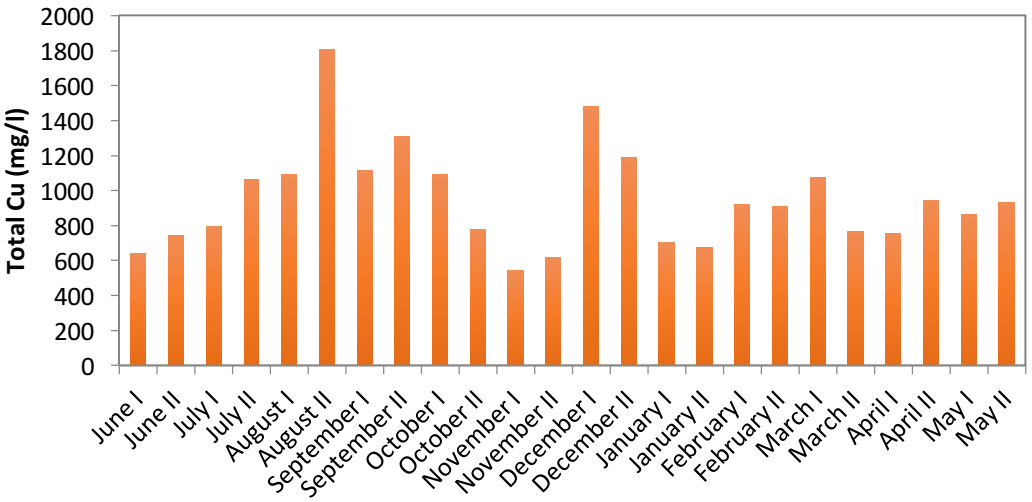
Total Cu (mg/l)
2000
1800
1600
1400
1200
1000
800
600
400
200
0
June I
June II
July I
July II
August I
August II
September I
September II
October I
October II
November I
November II
December I
December II
January I
January II
February I
February II
March I
March II
April I
April II
May I
May II

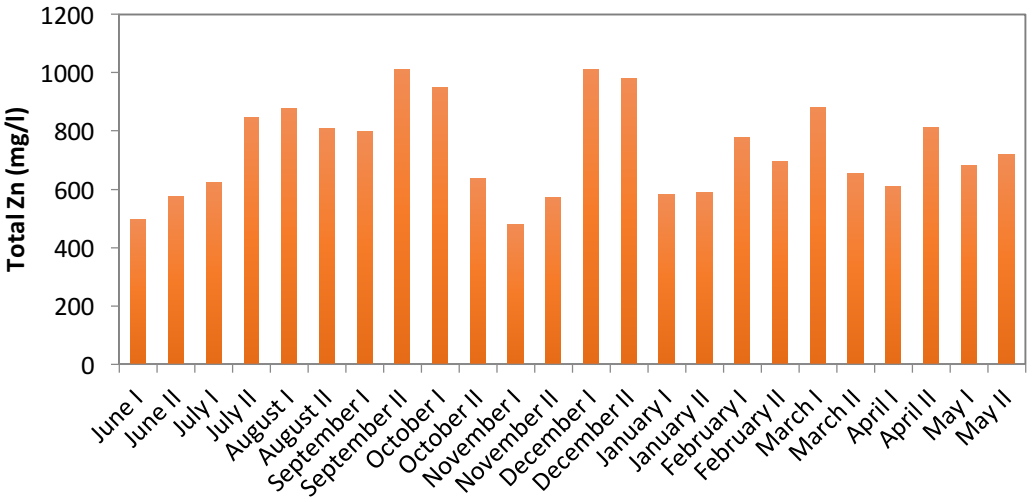
Total Zn (mg/l)
1200
1000
800
600
400
200
0
June I
June II
July I
July II
August I
August II
September I
September II
October I
October II
November I
November II
December I
December II
January I
January II
February I
February II
March I
March II
April I
April II
May I
May II

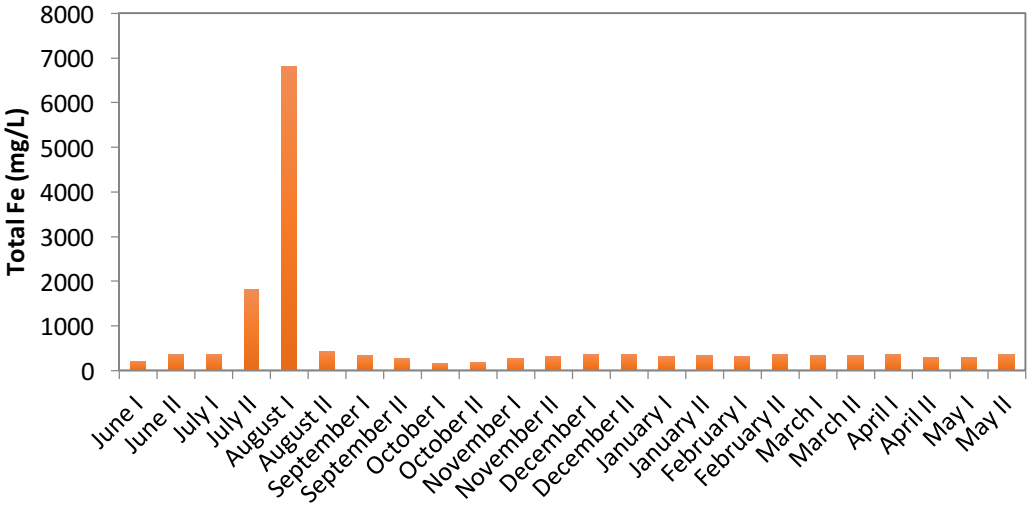
Total Fe (mg/L)
8000
7000
6000
5000
4000
3000
2000
1000
0
June I
June II
July I
July II
August I
August II
September I
September II
October I
October II
November I
November II
December I
December II
January I
January II
February I
February II
March I
March II
April I
April II
May I
May II

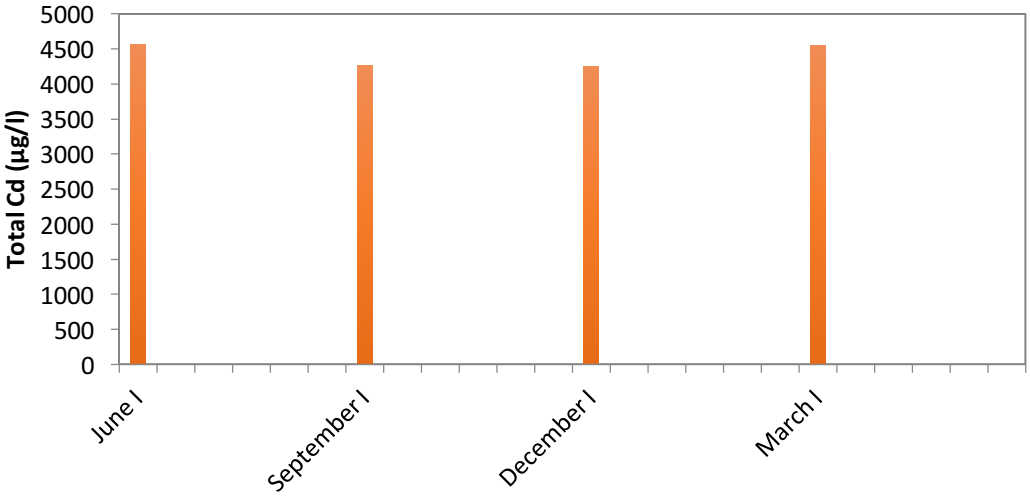
Total Cd (µg/l)
5000
4500
4000
3500
3000
2500
2000
1500
1000
500
0
June I
September I
December I
March I

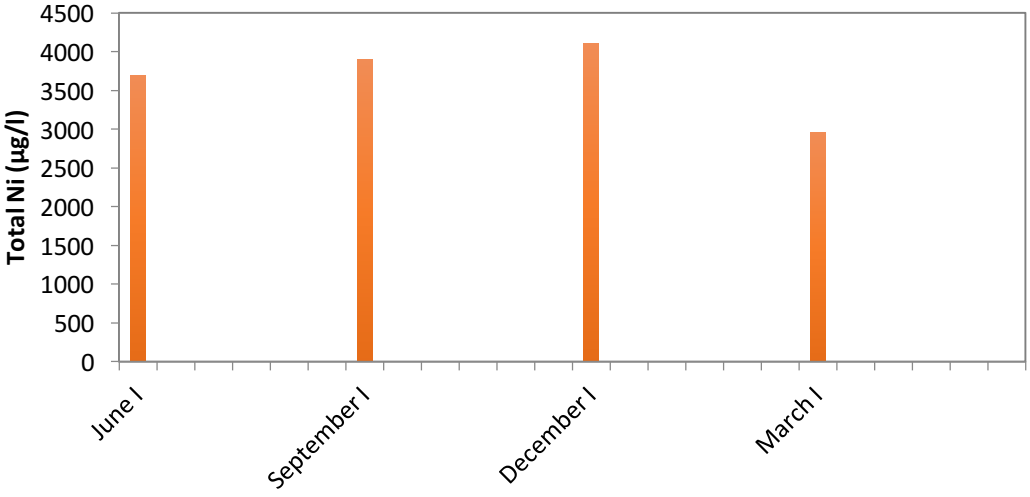
Total Ni (µg/l)
4500
4000
3500
3000
2500
2000
1500
1000
500
0
June I
September I
December I
March I

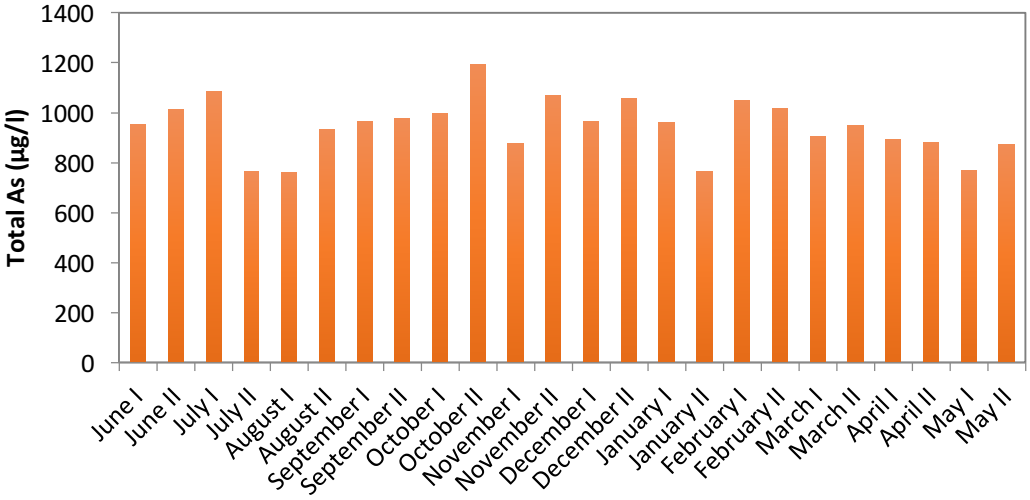
Total As (µg/l)
1400
1200
1000
800
600
400
200
0
June I
June II
July I
July II
August I
August II
September I
September II
October I
October II
November I
November II
December I
December II
January I
January II
February I
February II
March I
March II
April I
April II
May I
May II

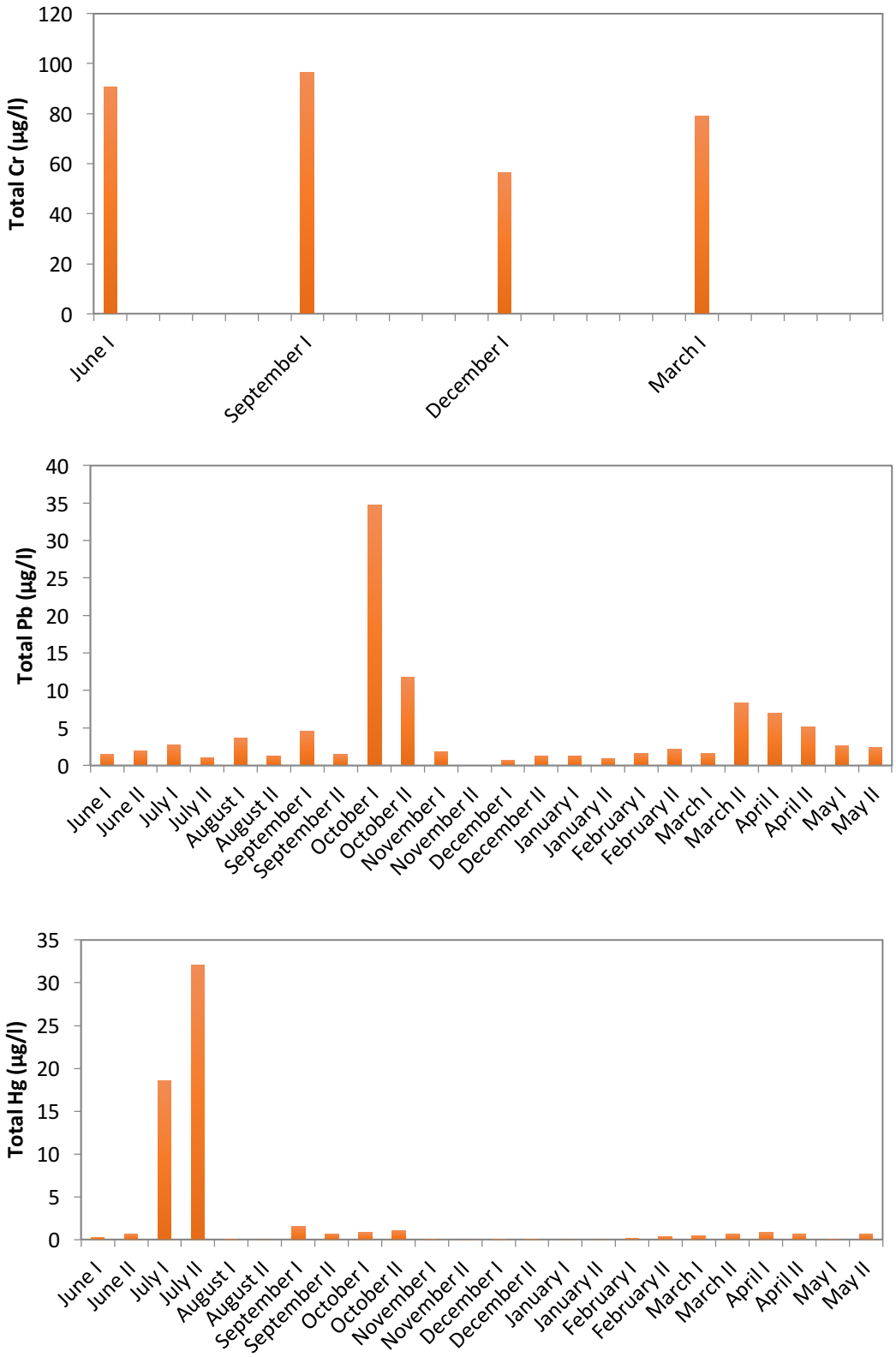

Figure A4: Graphs showing the bimonthly evolution of total Copper, Zinc, Iron, Arsenic, Lead and Mercury and the quarter-yearly evolution of Cadmium, Nickel and Chromium in solution at point 4, from June 2015 until May 2016.

- Point 5

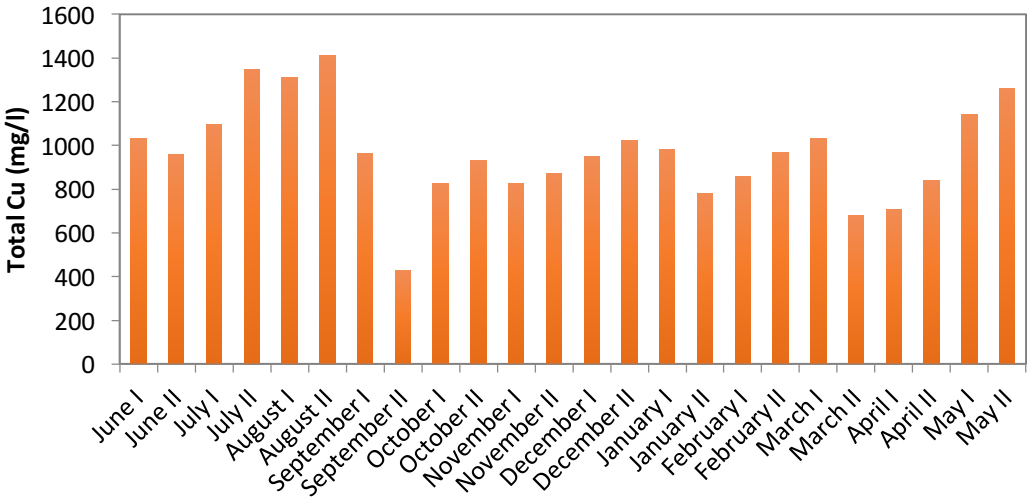
Total Cu (mg/l)
1600
1400
1200
1000
800
600
400
200
0
June I
June II
July I
July II
August I
August II
September I
September II
October I
October II
November I
November II
December I
December II
January I
January II
February I
February II
March I
March II
April I
April II
May I
May II

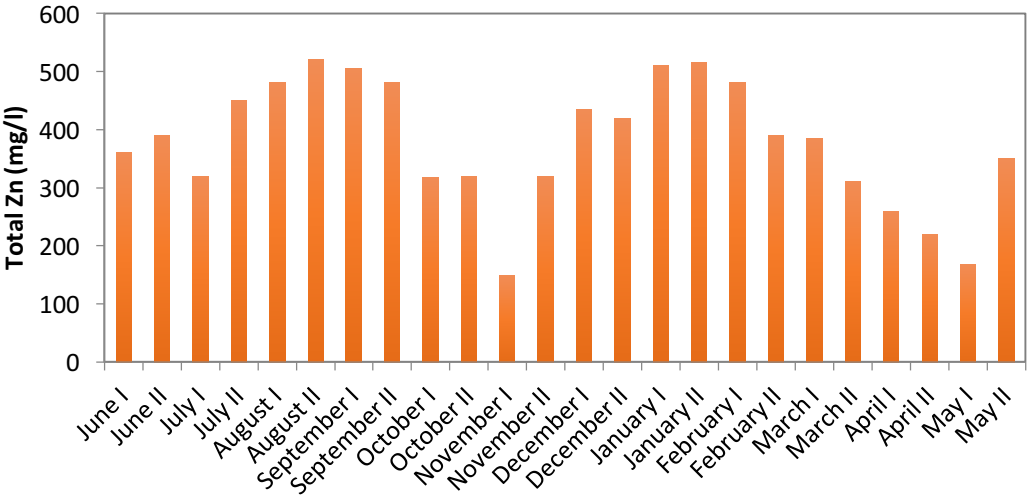
Total Zn (mg/l)
600
500
400
300
200
100
0
June I
June II
July I
July II
August I
August II
September I
September II
October I
October II
November I
November II
December I
December II
January I
January II
February I
February II
March I
March II
April I
April II
May I
May II

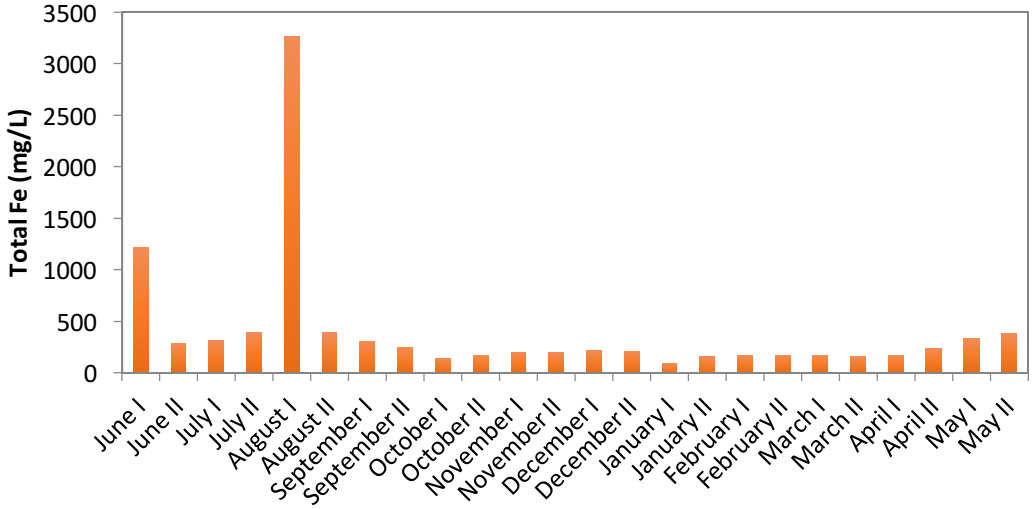
Total Fe (mg/L)
3500
3000
2500
2000
1500
1000
500
0
June I
June II
July I
July II
August I
August II
September I
September II
October I
October II
November I
November II
December I
December II
January I
January II
February I
February II
March I
March II
April I
April II
May I
May II

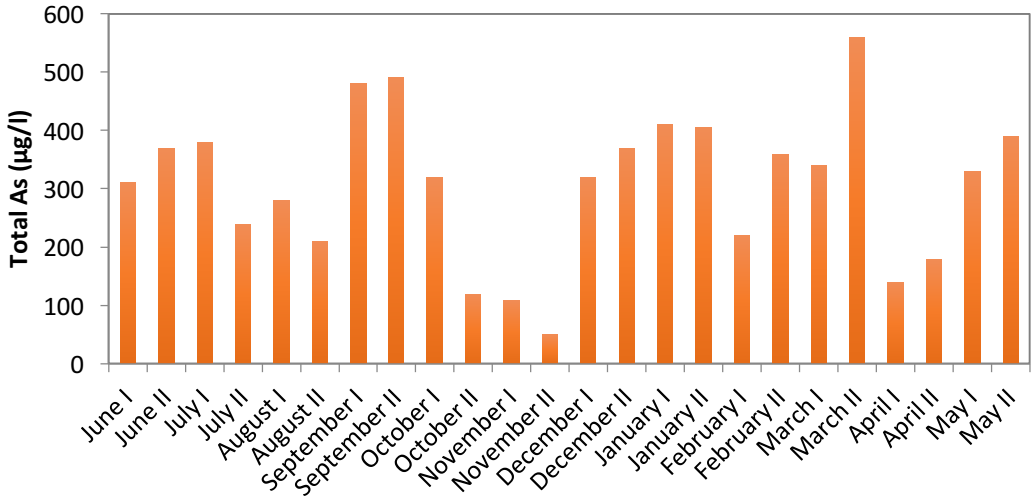

Figure A5: Graphs showing the bimonthly evolution of total Iron, Copper, Zinc and Arsenic at point 5, from June 2015 until May 2016.

- Point 6

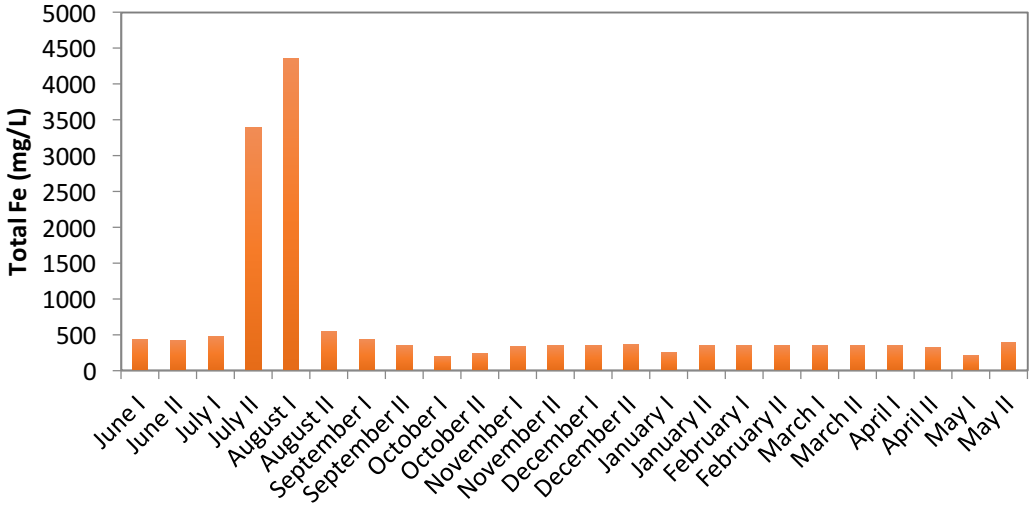

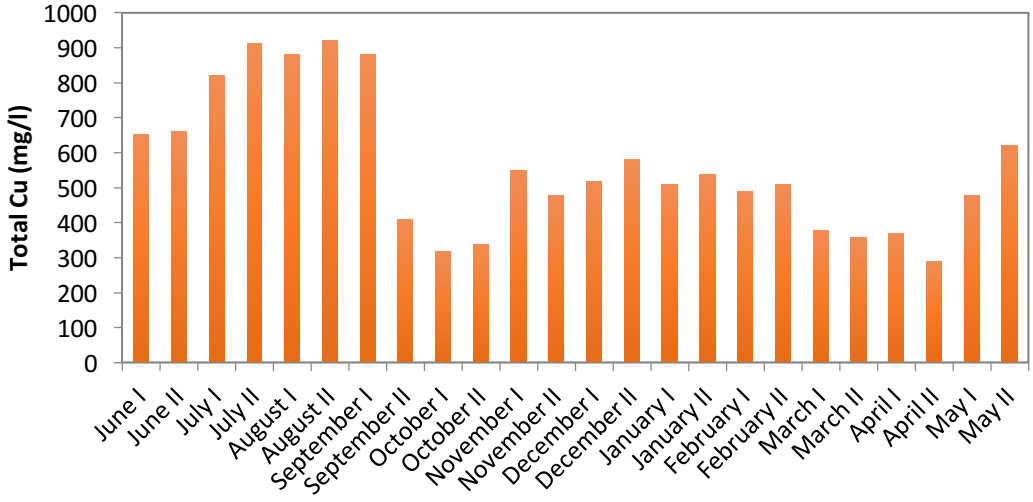

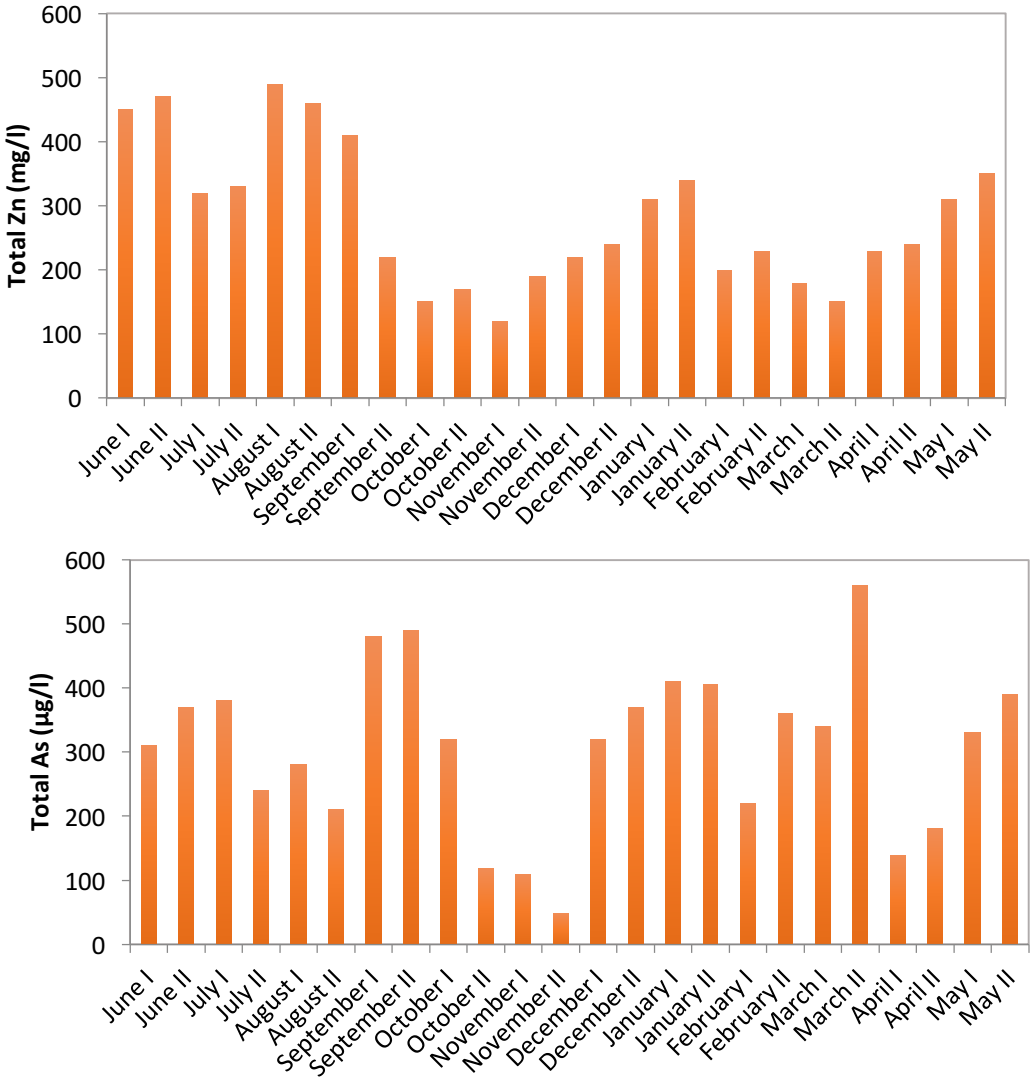

Figure A6: Graphs showing the bimonthly evolution of total Iron, Copper, Zinc and Arsenic at point 6, from June 2015 until May 2016.

- Point 7

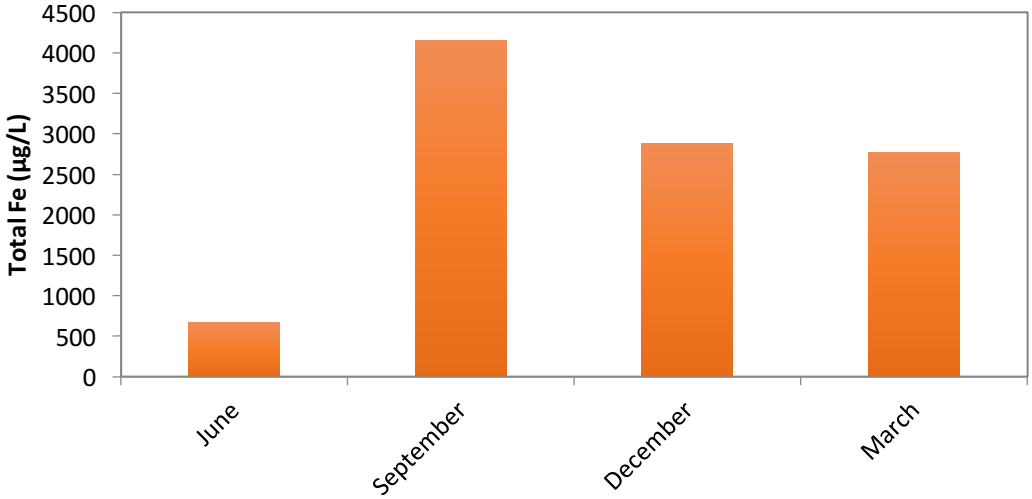

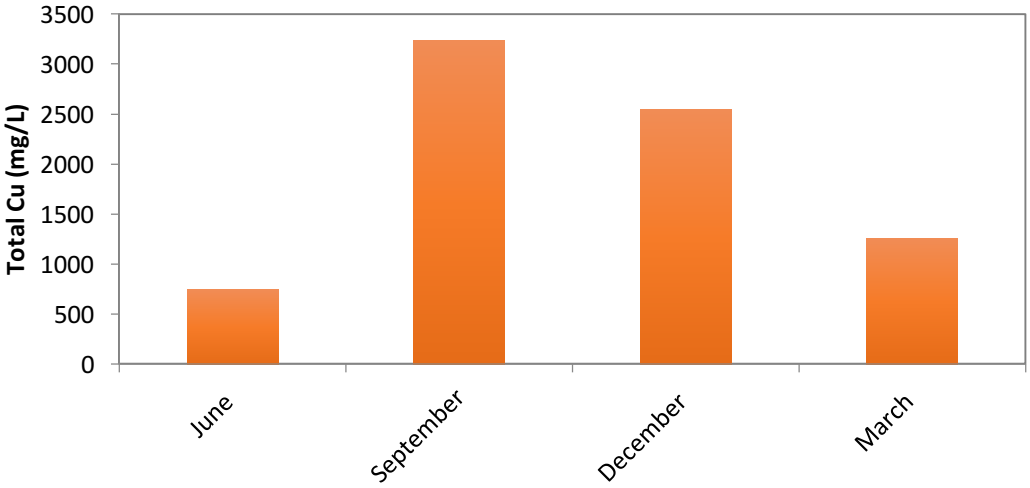
Total Cu (mg/L)
3500
3000
2500
2000
1500
1000
500
0
June
September
December
March

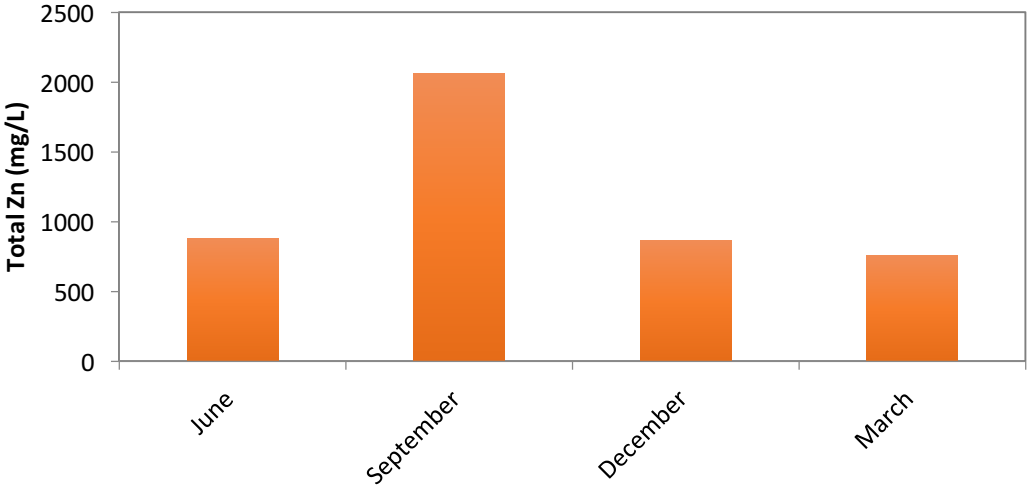
Total Zn (mg/L)
2500
2000
1500
1000
500
0
June
September
December
March

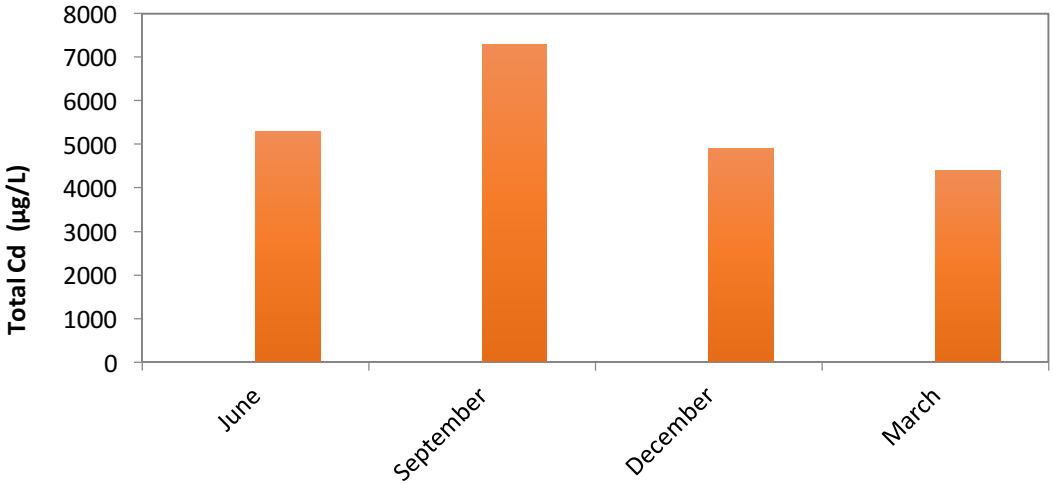
Total Cd (µg/L)
8000
7000
6000
5000
4000
3000
2000
1000
0
June
September
December
March

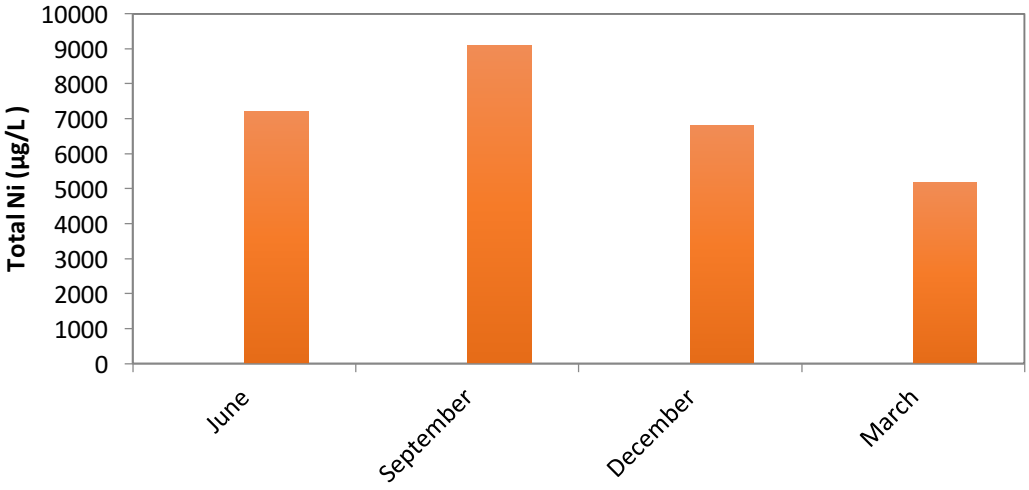
Total Ni (µg/L)
10000
9000
8000
7000
6000
5000
4000
3000
2000
1000
0
June
September
December
March

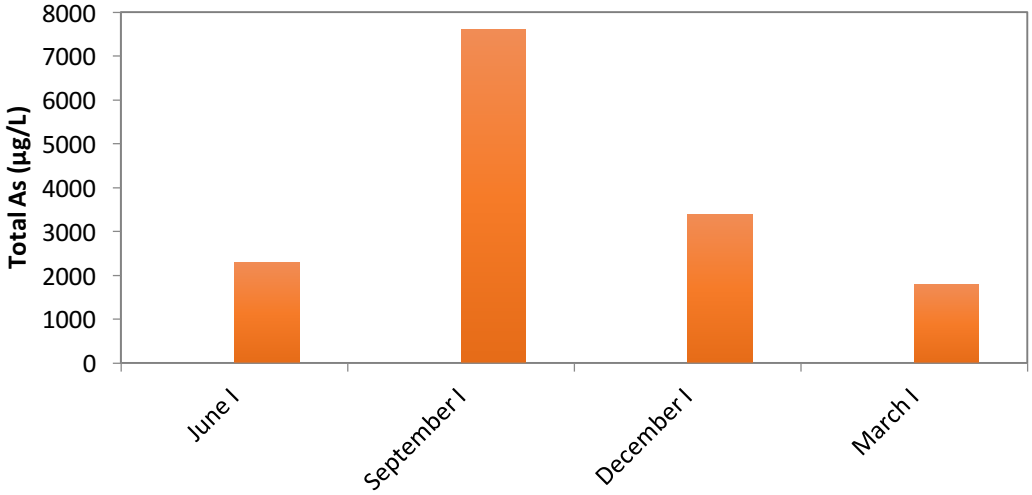
Total As (µg/L)
8000
7000
6000
5000
4000
3000
2000
1000
0
June I
September I
December I
March I

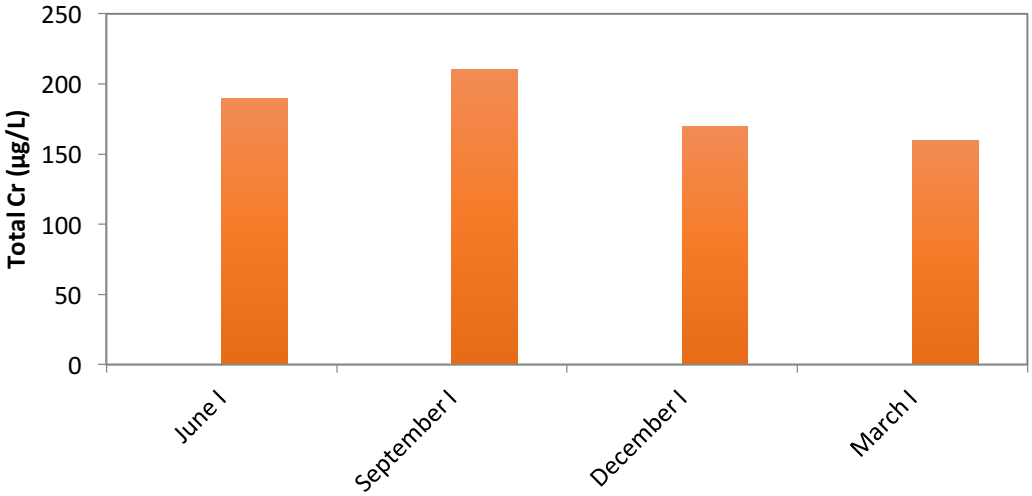
Total Cr (µg/L)
250
200
150
100
50
0
June I
September I
December I
March I

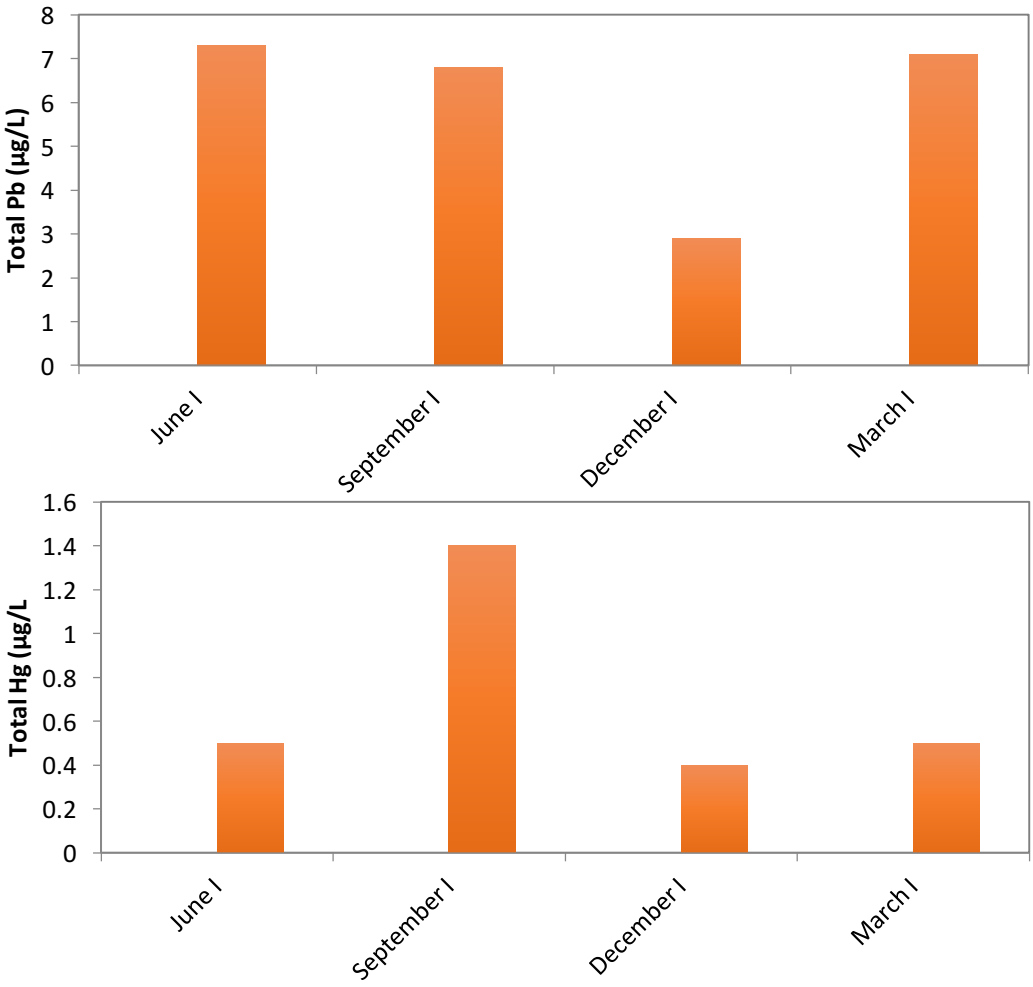

Figure A7: Graphs showing the trimestral evolution of total Iron, Copper, Zinc, Cadmium, Nickel, Arsenic, Chromium, Lead and Mercury in solution at point 7, showing June 2015, September 2015, December 2015 and March 2016.

- Point 8

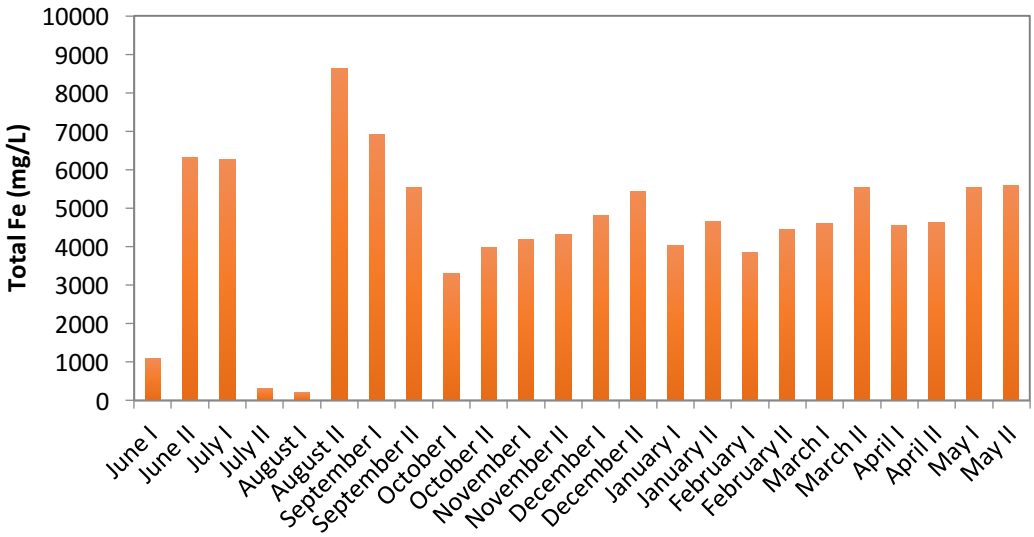

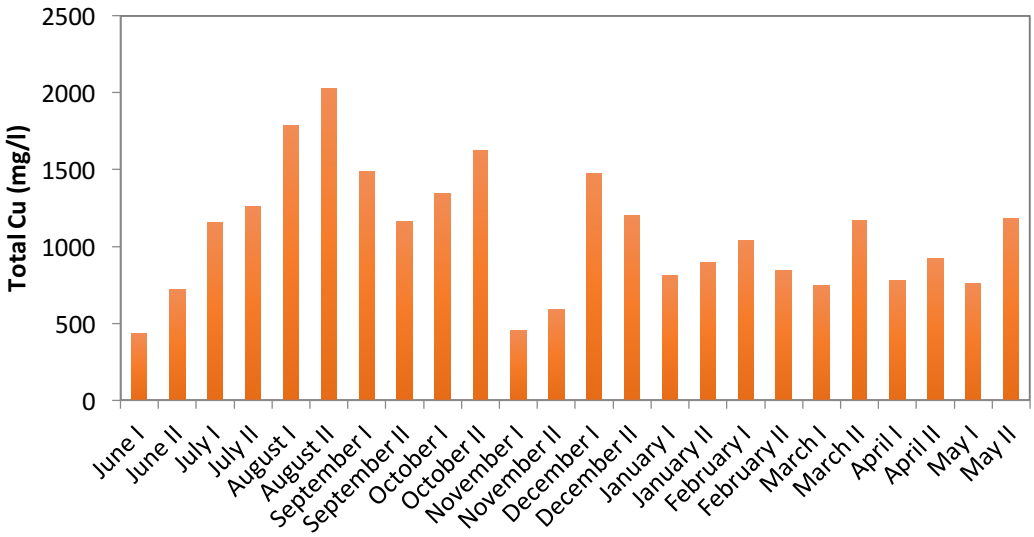
Total Cu (mg/l)
2500
2000
1500
1000
500
0
June I
June II
July I
July II
August I
August II
September I
September II
October I
October II
November I
November II
December I
December II
January I
January II
February I
February II
March I
March II
April I
April II
May I
May II

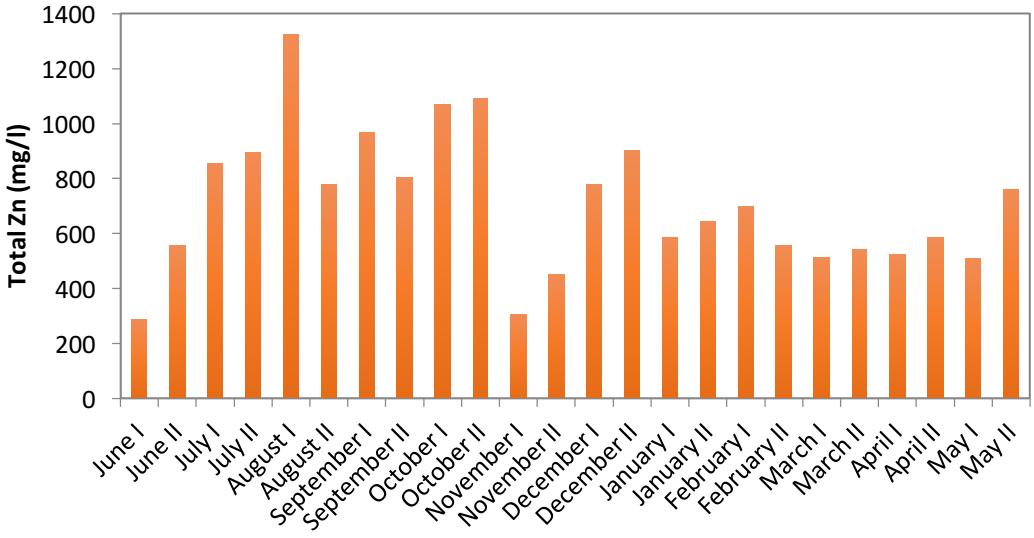
Total Zn (mg/l)
1400
1200
1000
800
600
400
200
0
June I
June II
July I
July II
August I
August II
September I
September II
October I
October II
November I
November II
December I
December II
January I
January II
February I
February II
March I
March II
April I
April II
May I
May II

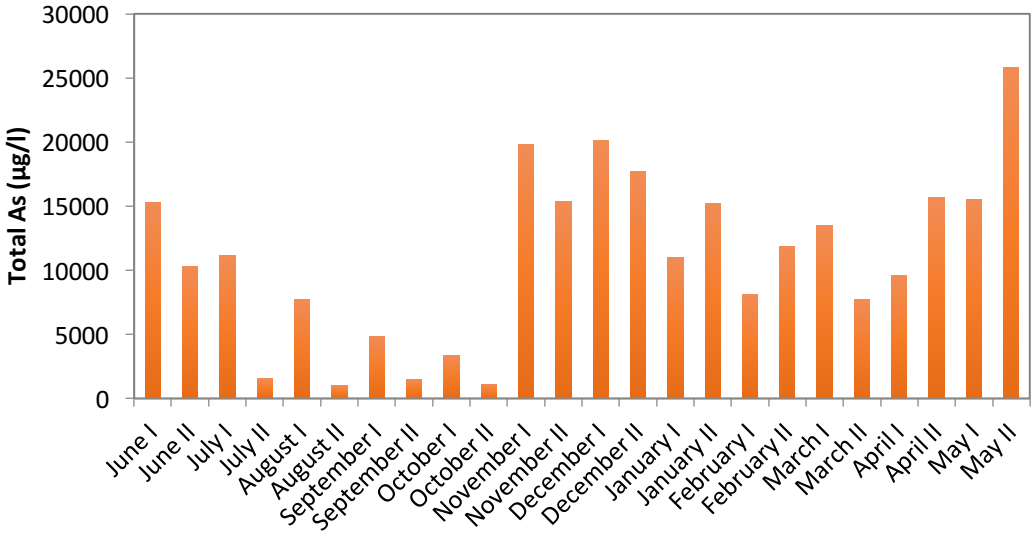
Total As (µg/l)
30000
25000
20000
15000
10000
5000
0
June I
June II
July I
July II
August I
August II
September I
September II
October I
October II
November I
November II
December I
December II
January I
January II
February I
February II
March I
March II
April I
April II
May I
May II

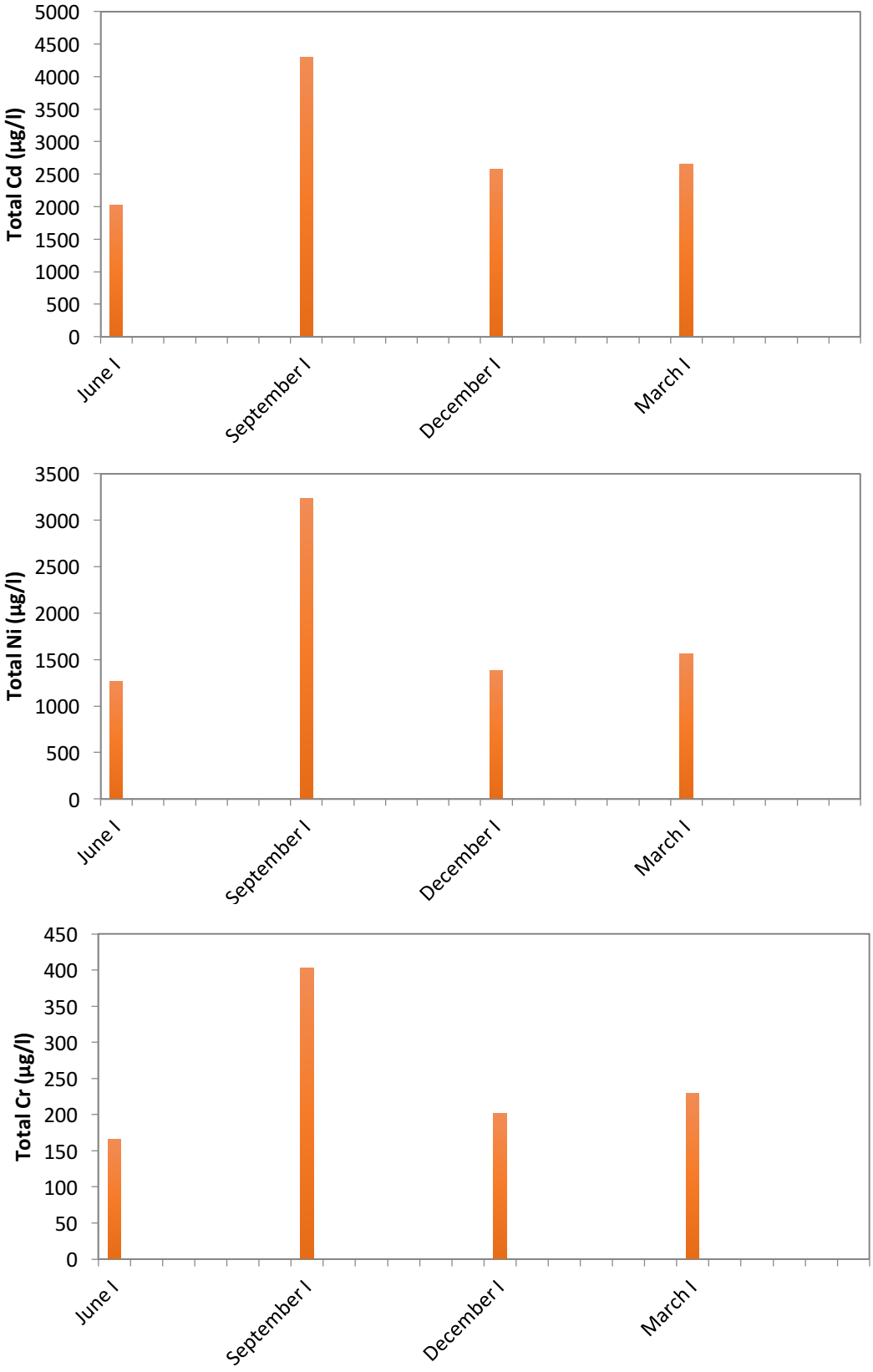

Figure A8: Graphs showing the bimonthly evolution of total Iron, Copper, Zinc and Arsenic and the quarter-yearly evolution of Cadmium, Nickel and Chromium in solution at point 8, from June 2015 until May 2016.

- Point 9

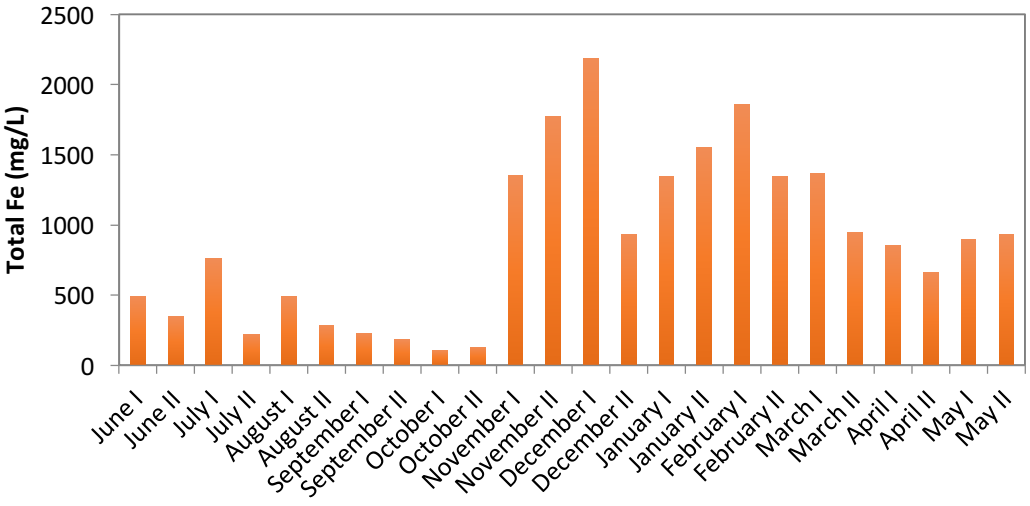
Total Fe (mg/L)
2500
2000
1500
1000
500
0
June I
June II
July I
July II
August I
August II
September I
September II
October I
October II
November I
November II
December I
December II
January I
January II
February I
February II
March I
March II
April I
April II
May I
May II

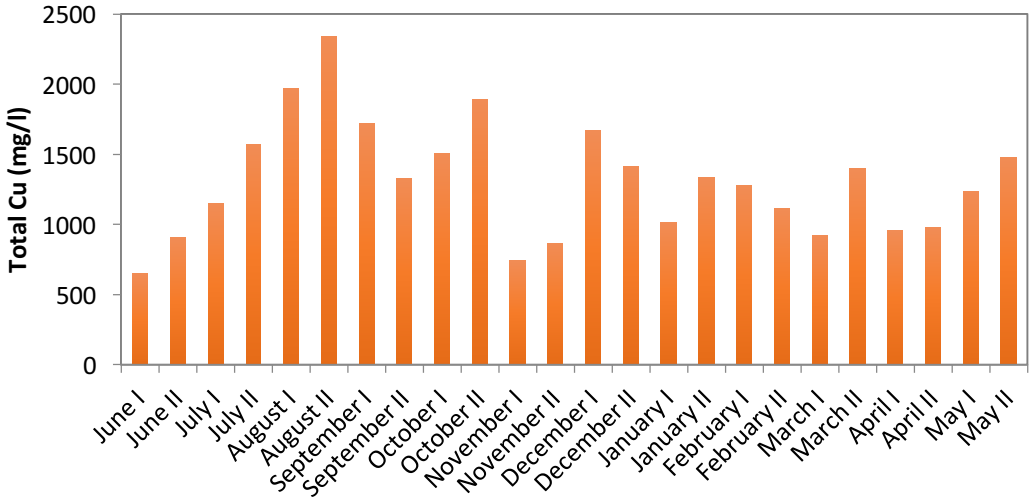
Total Cu (mg/l)
2500
2000
1500
1000
500
0
June I
June II
July I
July II
August I
August II
September I
September II
October I
October II
November I
November II
December I
December II
January I
January II
February I
February II
March I
March II
April I
April II
May I
May II

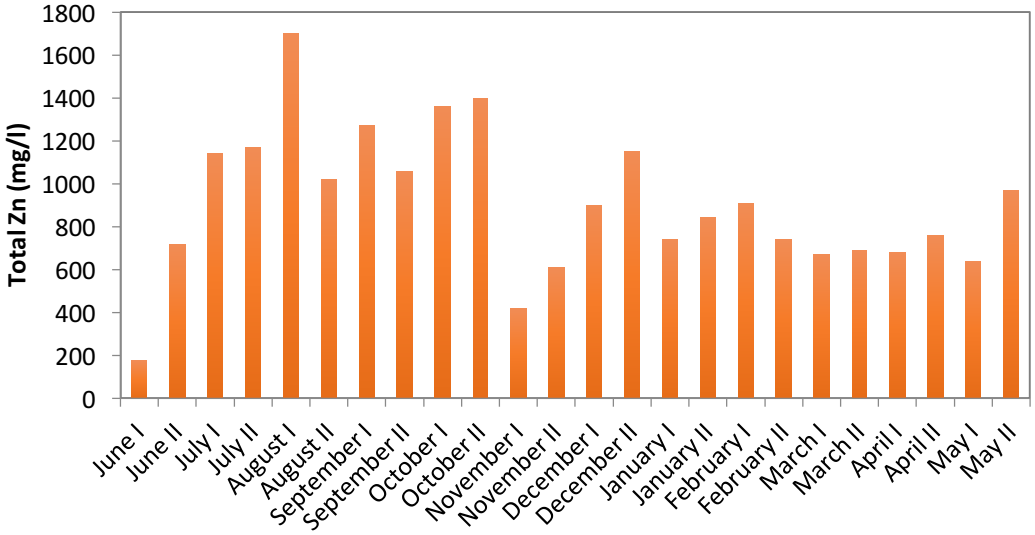
Total Zn (mg/l)
1800
1600
1400
1200
1000
800
600
400
200
0
June I
June II
July I
July II
August I
August II
September I
September II
October I
October II
November I
November II
December I
December II
January I
January II
February I
February II
March I
March II
April I
April II
May I
May II

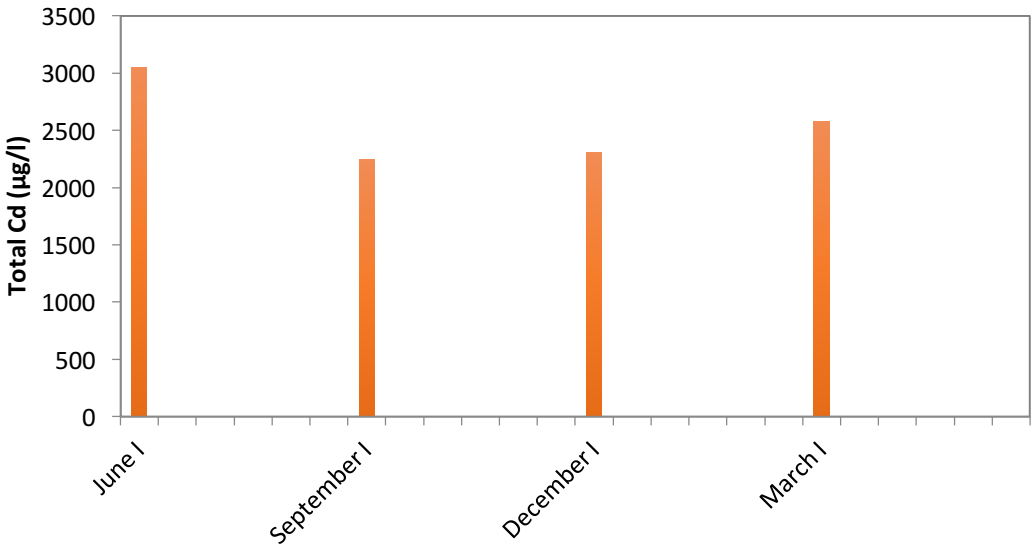
Total Cd (µg/l)
3500
3000
2500
2000
1500
1000
500
0
June I
September I
December I
March I

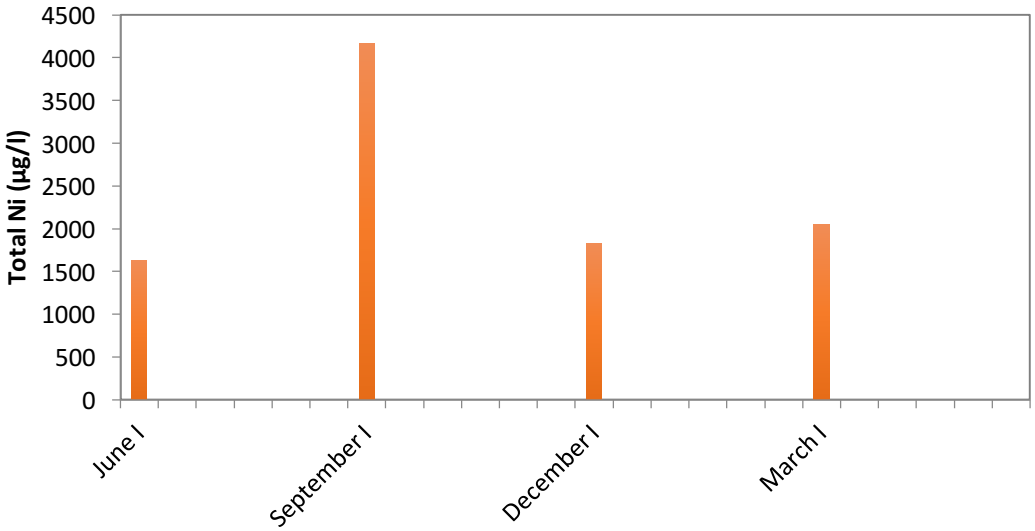
Total Ni (µg/l)
4500
4000
3500
3000
2500
2000
1500
1000
500
0
June I
September I
December I
March I

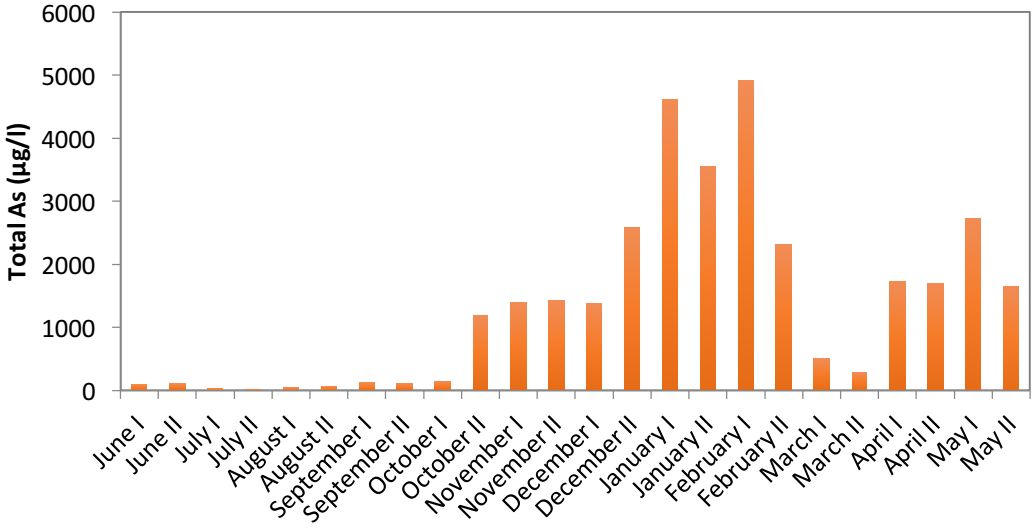
Total As (µg/l)
6000
5000
4000
3000
2000
1000
0
June I
June II
July I
July II
August I
August II
September I
September II
October I
October II
November I
November II
December I
December II
January I
January II
February I
February II
March I
March II
April I
April II
May I
May II

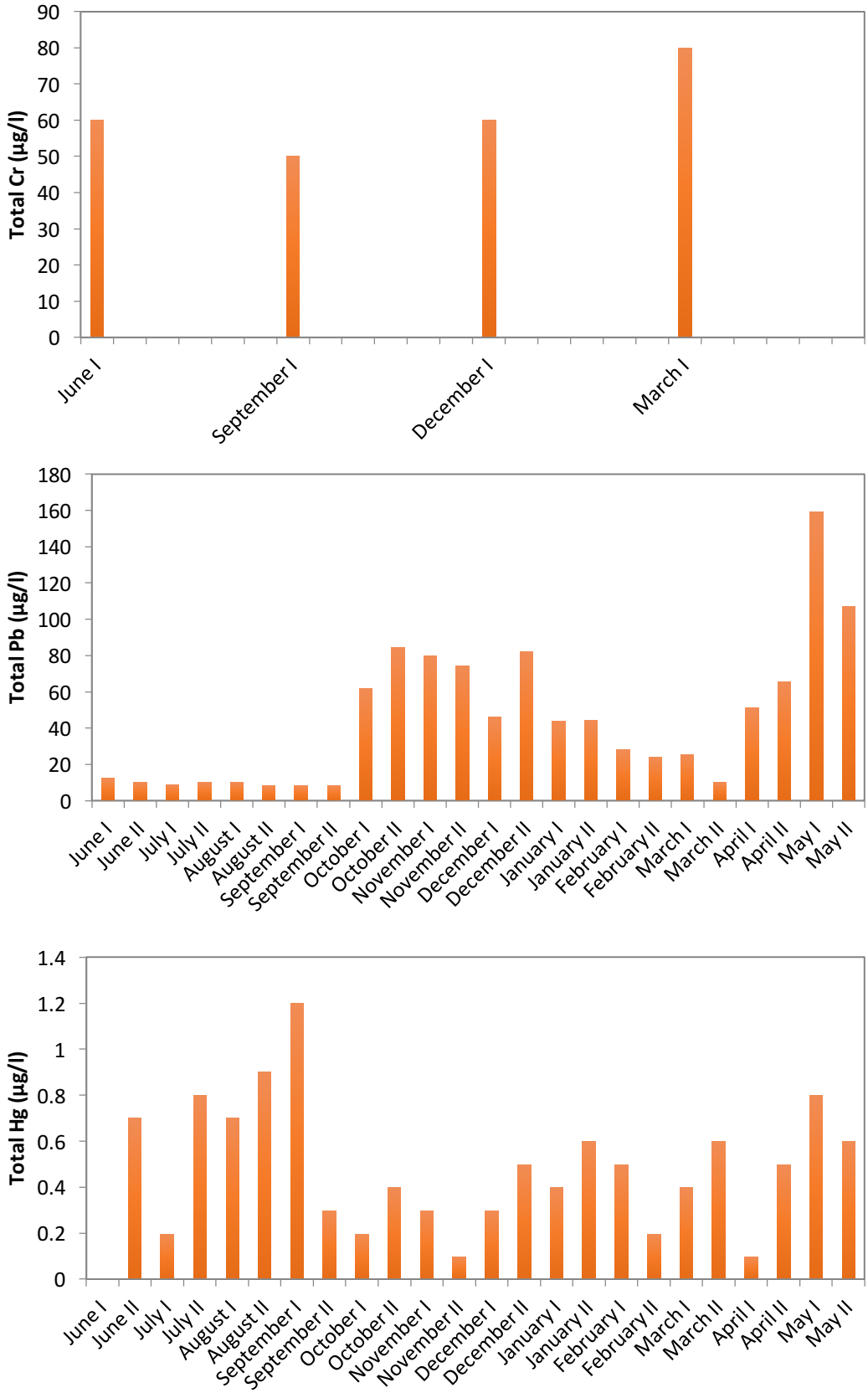

Figure A9: Graphs showing the bimonthly evolution of total Iron, Copper, Zinc, Arsenic, Lead and Mercury and the quarter-yearly evolution of Cadmium, Nickel and Chromium in solution at point 9, from June 2015 until May 2016.

- Point 10

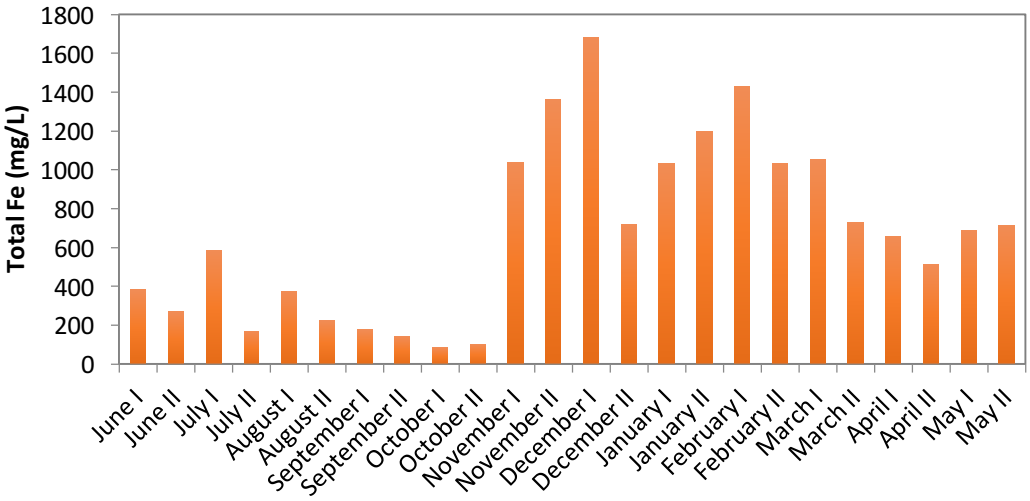
Total Fe (mg/L)
1800
1600
1400
1200
1000
800
600
400
200
0
June I
June II
July I
July II
August I
August II
September I
September II
October I
October II
November I
November II
December I
December II
January I
January II
February I
February II
March I
March II
April I
April II
May I
May II

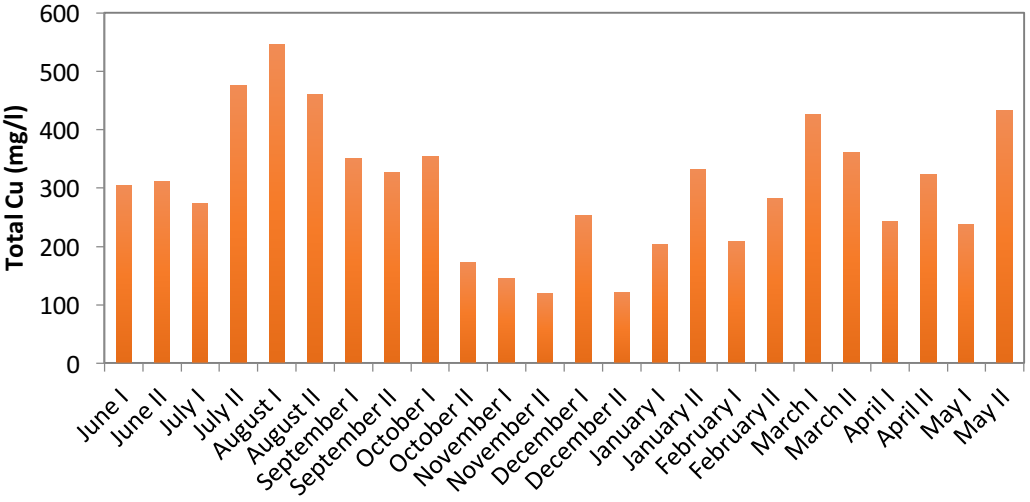
Total Cu (mg/l)
600
500
400
300
200
100
0
June I
June II
July I
July II
August I
August II
September I
September II
October I
October II
November I
November II
December I
December II
January I
January II
February I
February II
March I
March II
April I
April II
May I
May II

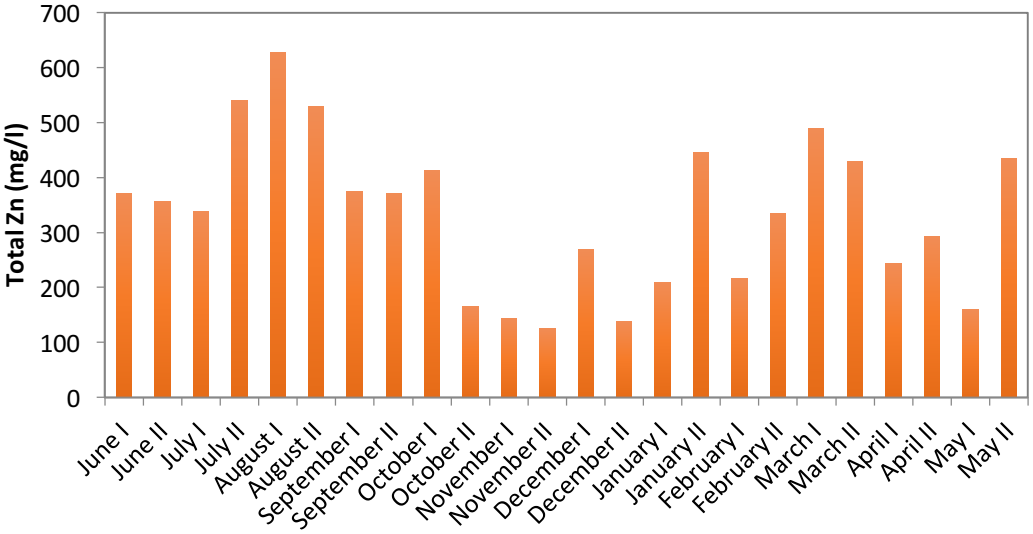
Total Zn (mg/l)
700
600
500
400
300
200
100
0
June I
June II
July I
July II
August I
August II
September I
September II
October I
October II
November I
November II
December I
December II
January I
January II
February I
February II
March I
March II
April I
April II
May I
May II

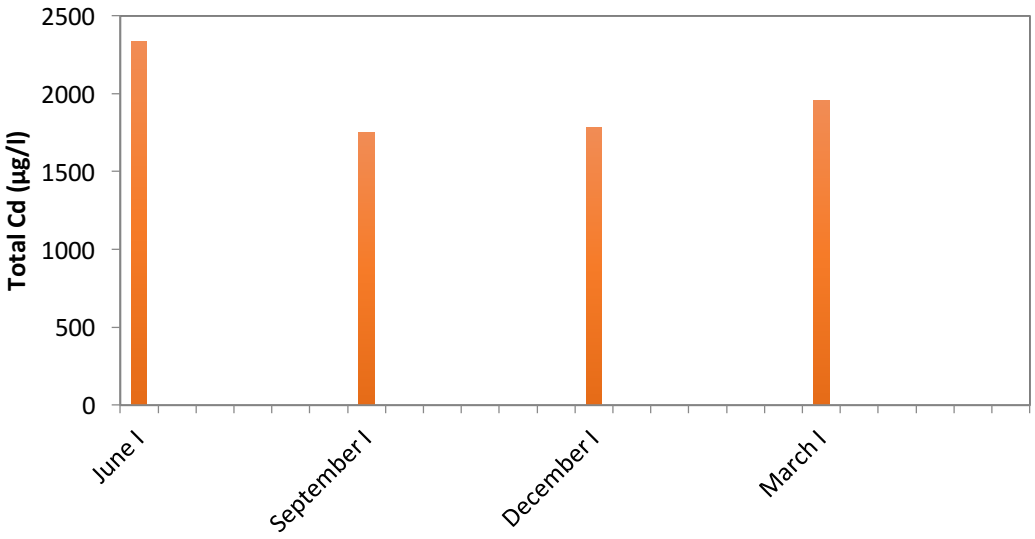
Total Cd (µg/l)
2500
2000
1500
1000
500
0
June I
September I
December I
March I

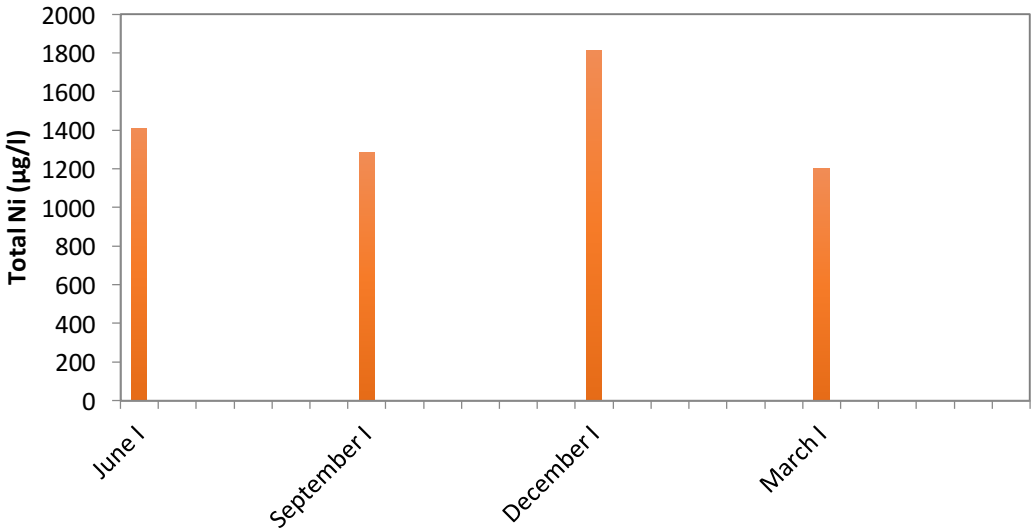
Total Ni (µg/l)
2000
1800
1600
1400
1200
1000
800
600
400
200
0
June I
September I
December I
March I

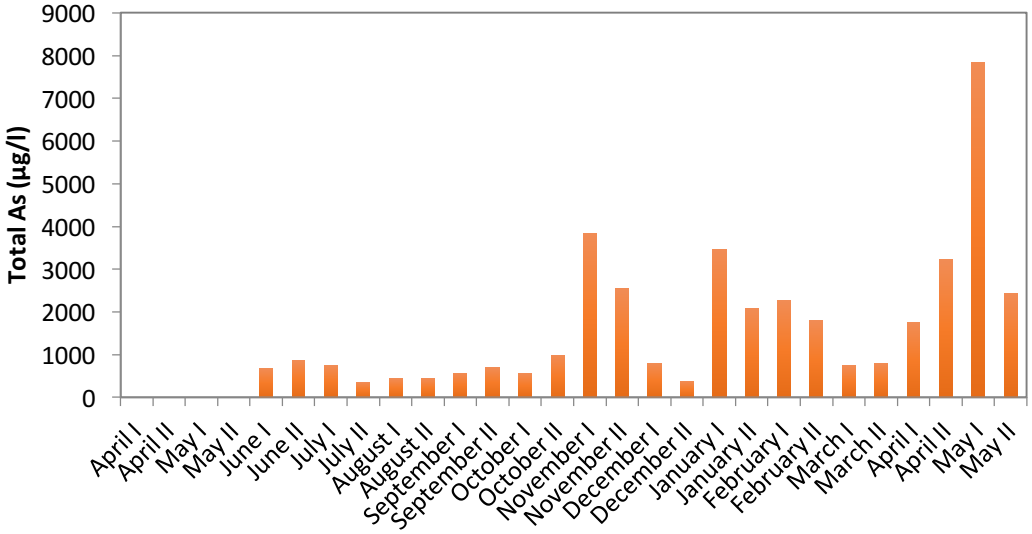
Total As (µg/l)
9000
8000
7000
6000
5000
4000
3000
2000
1000
0
April I
April II
May I
May II
June I
June II
July I
July II
August I
August II
September I
September II
October I
October II
November I
November II
December I
December II
January I
January II
February I
February II
March I
March II
April I
April II
May I
May II

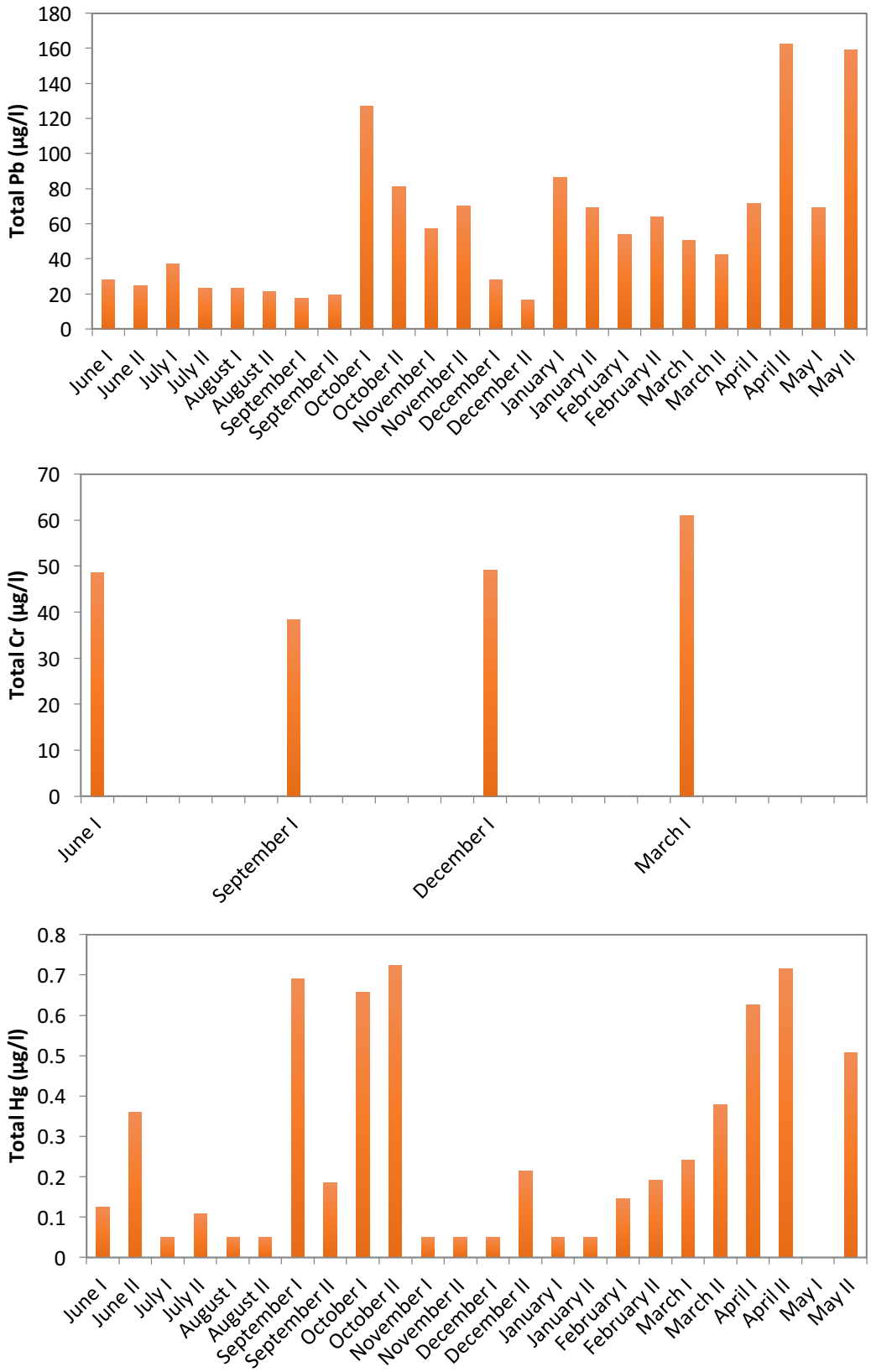

Figure A10: Graphs showing the bimonthly evolution of total Iron, Copper, Zinc, Arsenic, Lead and Mercury and the quarter-yearly evolution of Cadmium, Nickel and Chromium in solution at point 10, from June 2015 until May 2016.

- Point 11

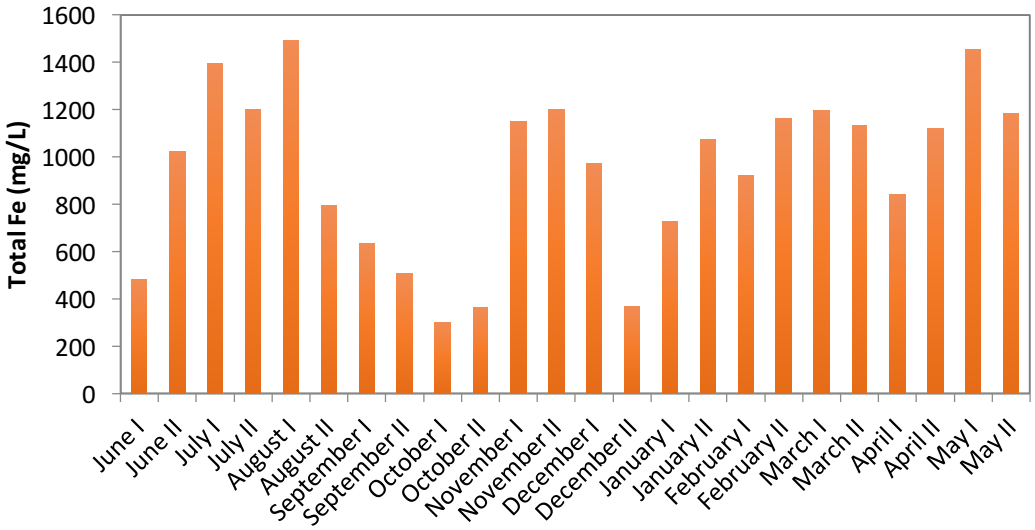
Total Fe (mg/L)
1600
1400
1200
1000
800
600
400
200
0
June I
June II
July I
July II
August I
August II
September I
September II
October I
October II
November I
November II
December I
December II
January I
January II
February I
February II
March I
March II
April I
April II
May I
May II

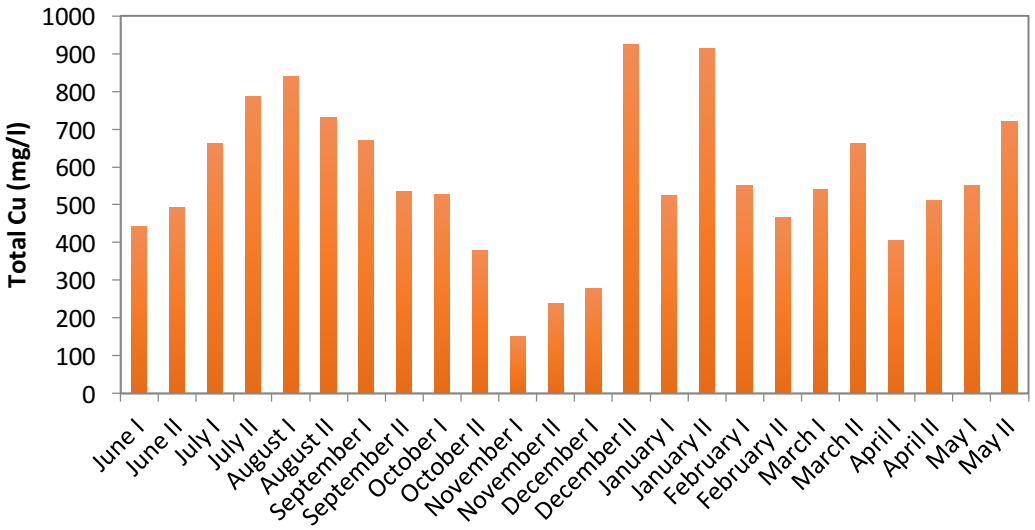
Total Cu (mg/l)
1000
900
800
700
600
500
400
300
200
100
0
June I
June II
July I
July II
August I
August II
September I
September II
October I
October II
November I
November II
December I
December II
January I
January II
February I
February II
March I
March II
April I
April II
May I
May II

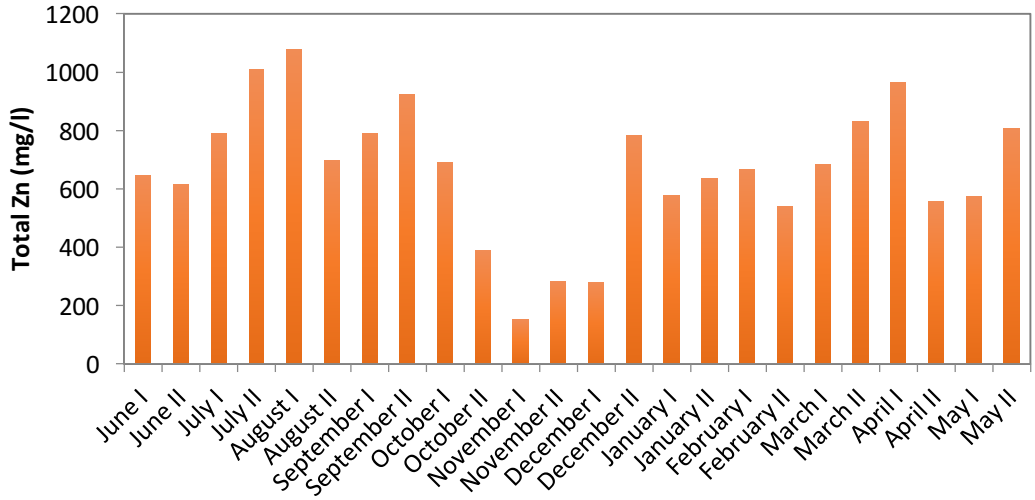
Total Zn (mg/l)
1200
1000
800
600
400
200
0
June I
June II
July I
July II
August I
August II
September I
September II
October I
October II
November I
November II
December I
December II
January I
January II
February I
February II
March I
March II
April I
April II
May I
May II

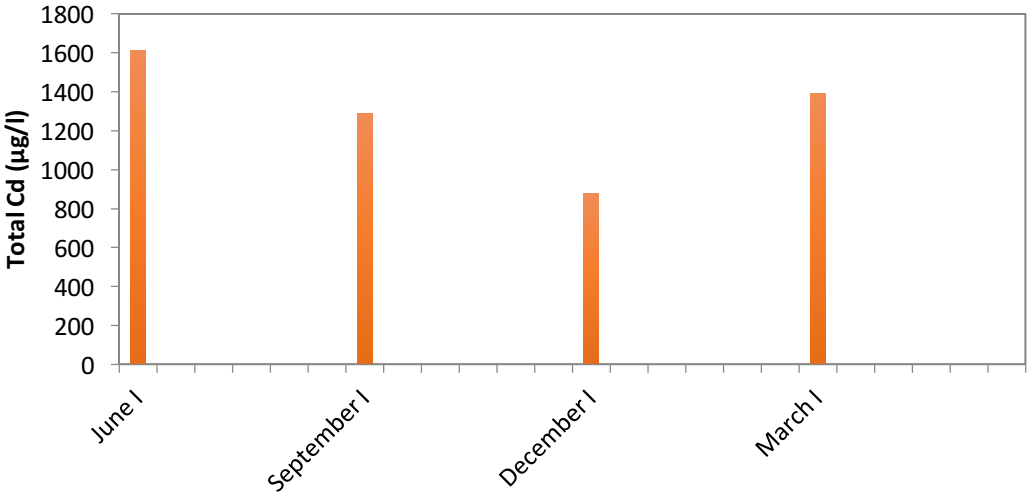
Total Cd (µg/l)
1800
1600
1400
1200
1000
800
600
400
200
0
June I
September I
December I
March I

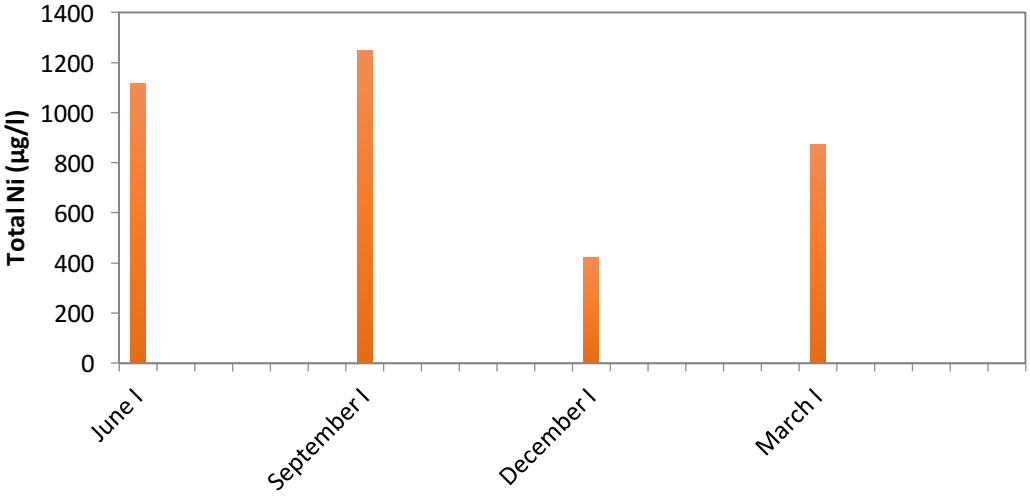
Total Ni (µg/l)
1400
1200
1000
800
600
400
200
0
June I
September I
December I
March I

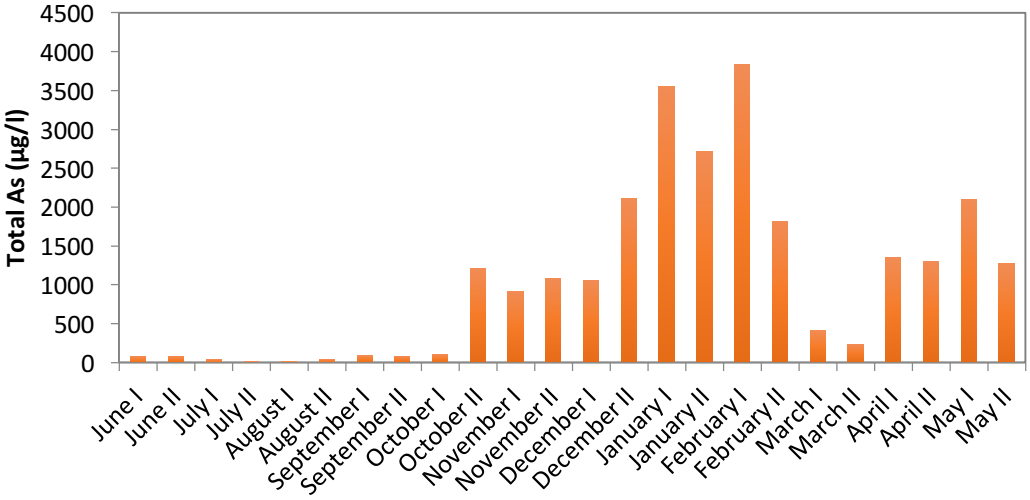
Total As (µg/l)
4500
4000
3500
3000
2500
2000
1500
1000
500
0
June I
June II
July I
July II
August I
August II
September I
September II
October I
October II
November I
November II
December I
December II
January I
January II
February I
February II
March I
March II
April I
April II
May I
May II

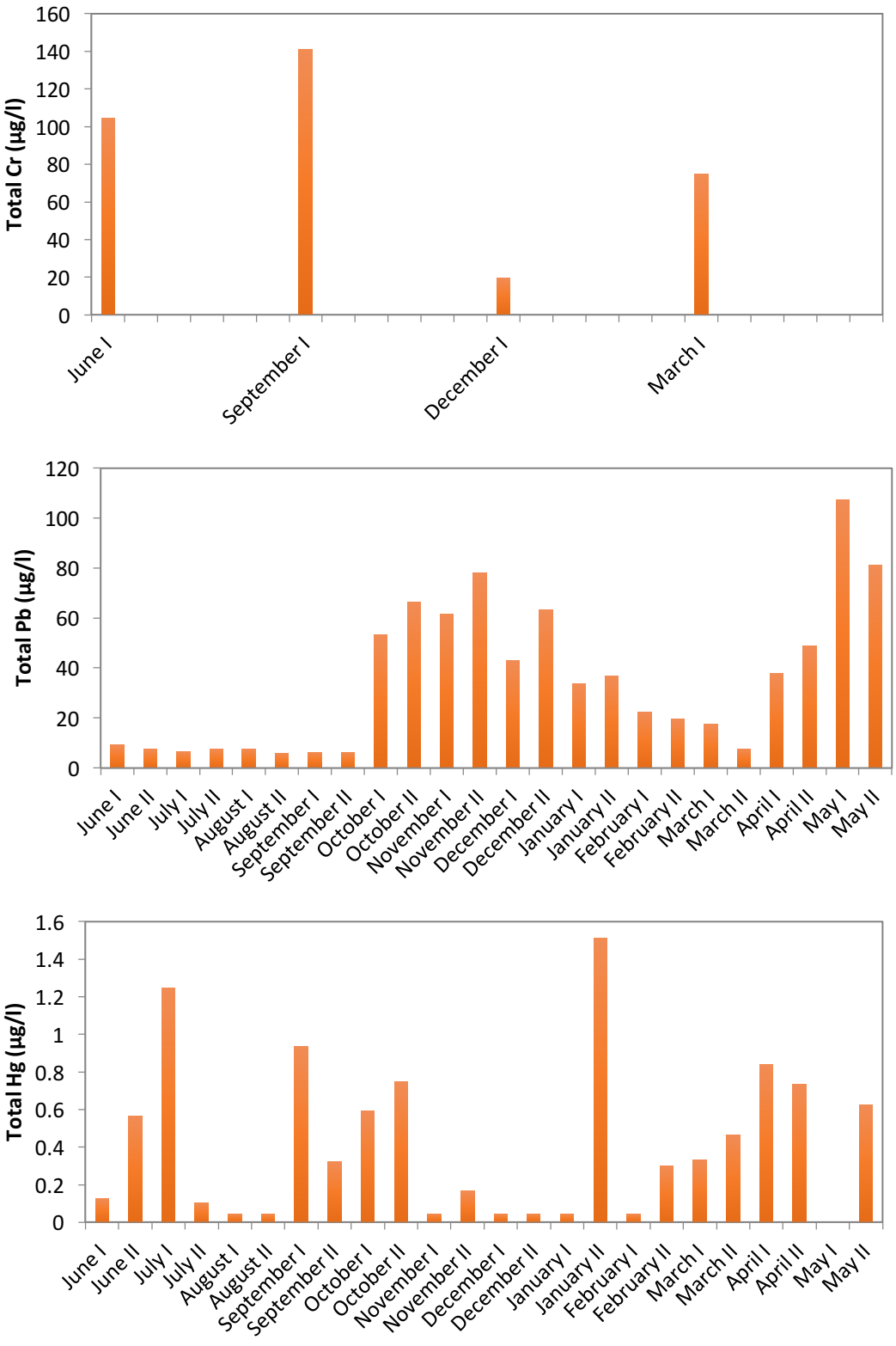

Figure A11: Graphs showing the bimonthly evolution of total Iron, Copper, Zinc, Arsenic, Lead and Mercury and the quarter-yearly evolution of Cadmium, Nickel and Chromium in solution at point 11, from June 2015 until May 2016.

- Point 12

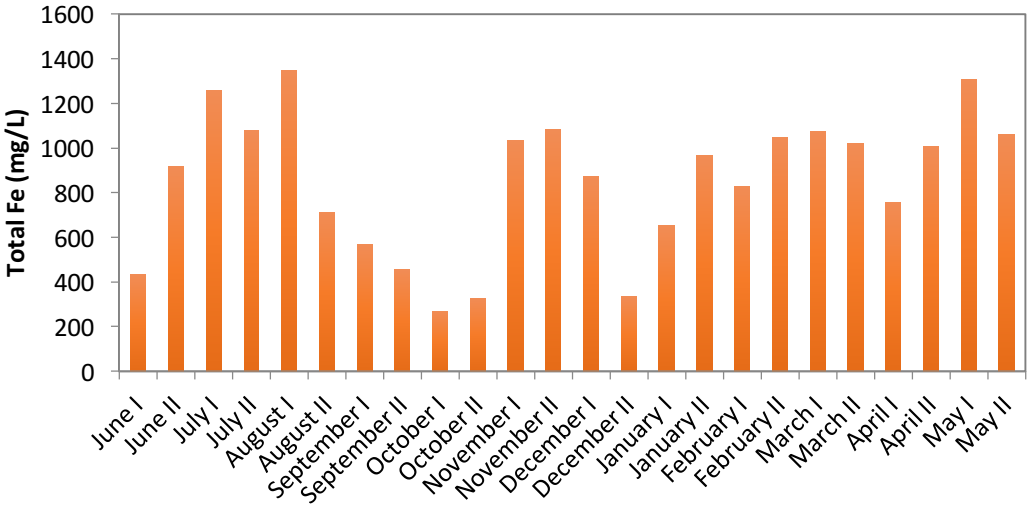
Total Fe (mg/L)
1600
1400
1200
1000
800
600
400
200
0
June I
June II
July I
July II
August I
August II
September I
September II
October I
October II
November I
November II
December I
December II
January I
January II
February I
February II
March I
March II
April I
April II
May I
May II

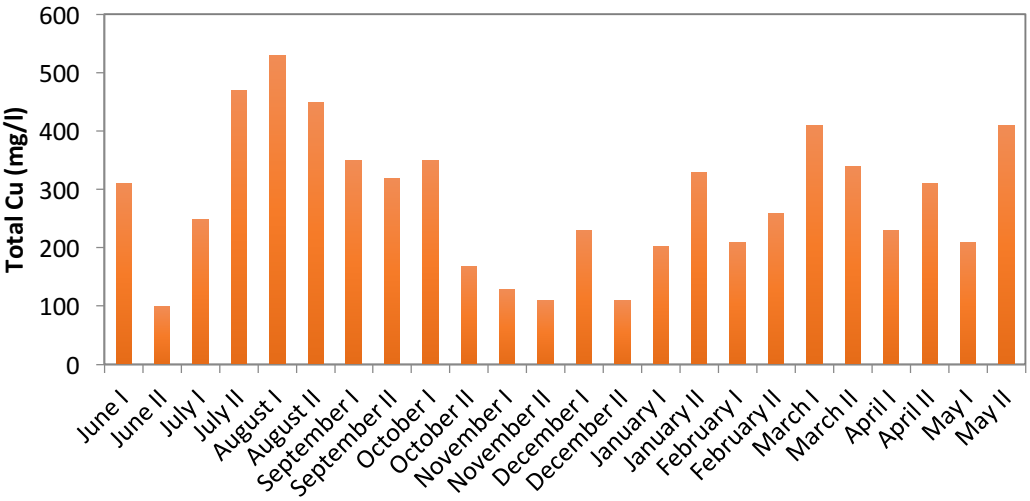
Total Cu (mg/l)
600
500
400
300
200
100
0
June I
June II
July I
July II
August I
August II
September I
September II
October I
October II
November I
November II
December I
December II
January I
January II
February I
February II
March I
March II
April I
April II
May I
May II

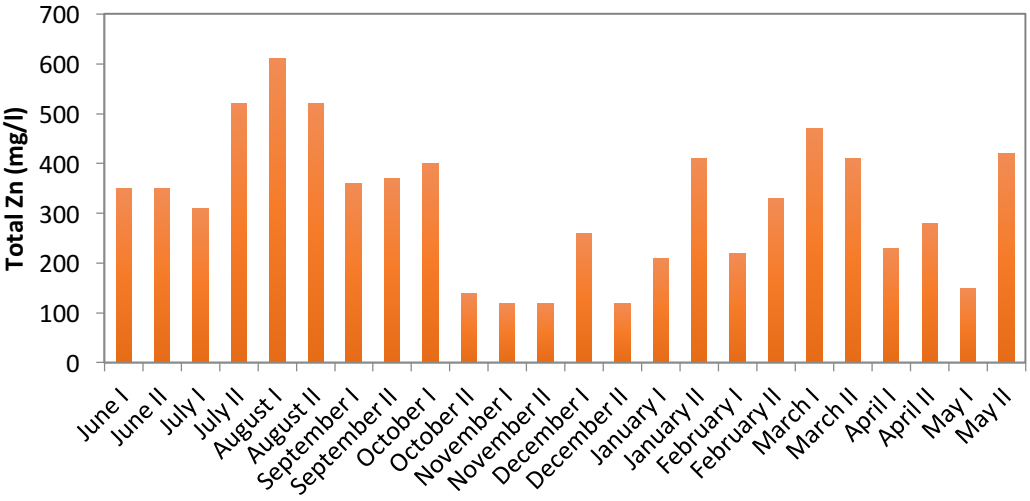
Total Zn (mg/l)
700
600
500
400
300
200
100
0
June I
June II
July I
July II
August I
August II
September I
September II
October I
October II
November I
November II
December I
December II
January I
January II
February I
February II
March I
March II
April I
April II
May I
May II

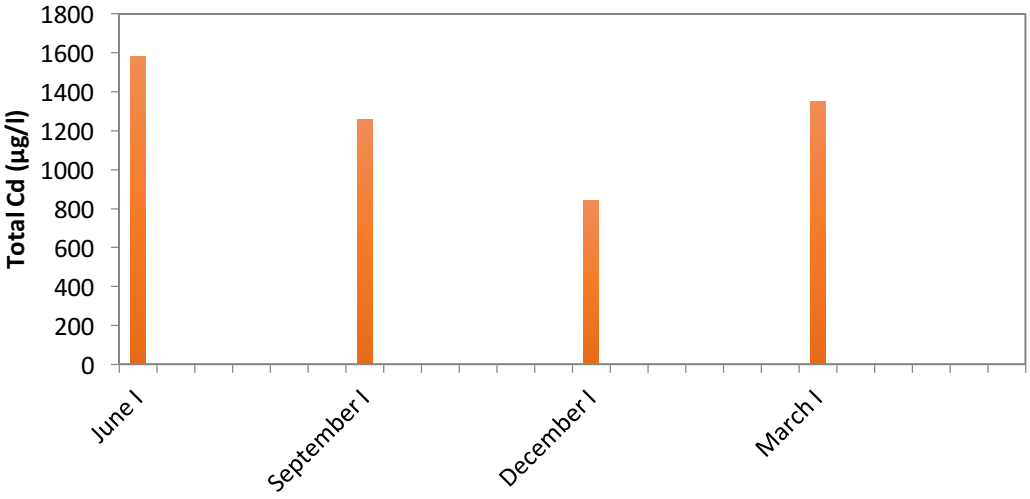
Total Cd (µg/l)
1800
1600
1400
1200
1000
800
600
400
200
0
June I
September I
December I
March I

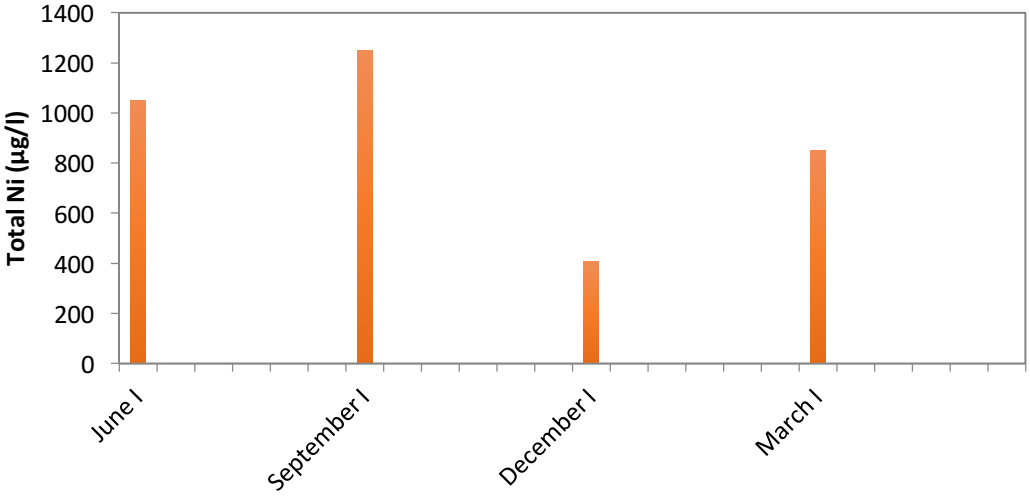
Total Ni (µg/l)
1400
1200
1000
800
600
400
200
0
June I
September I
December I
March I

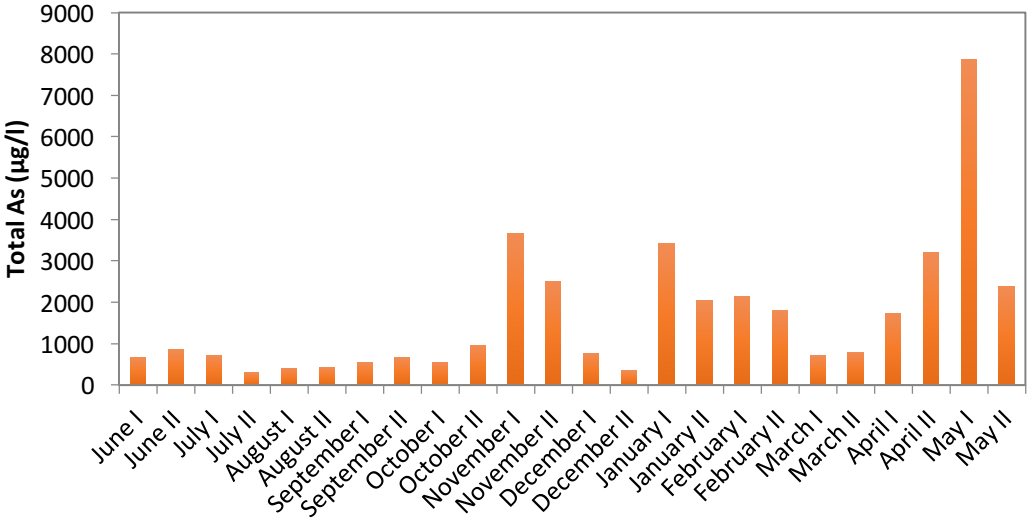
Total As (µg/l)
9000
8000
7000
6000
5000
4000
3000
2000
1000
0
June I
June II
July I
July II
August I
August II
September I
September II
October I
October II
November I
November II
December I
December II
January I
January II
February I
February II
March I
March II
April I
April II
May I
May II

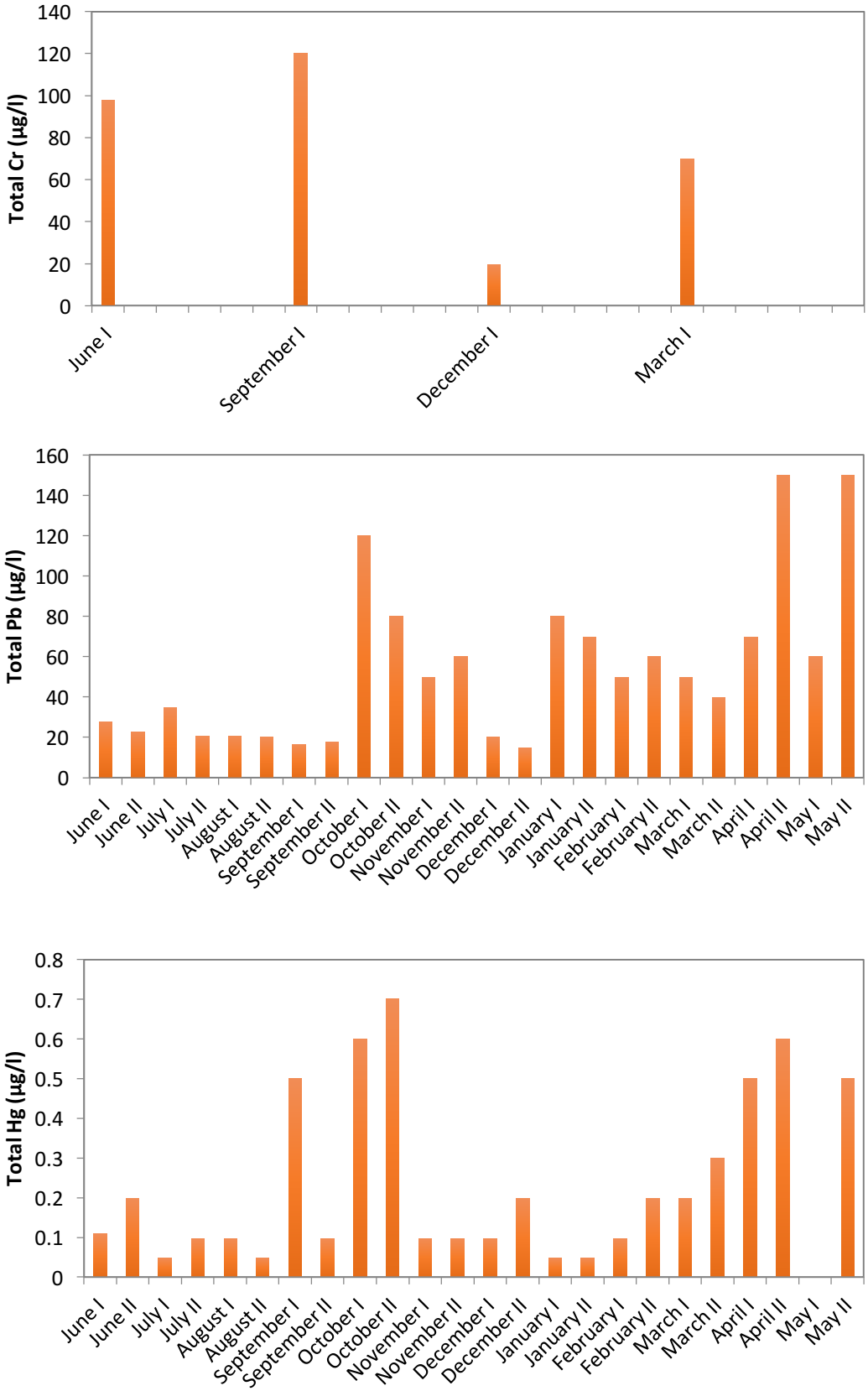

Figure A12: Graphs showing the bimonthly evolution of total Iron, Copper, Zinc, Arsenic, Lead and Mercury and the quarter-yearly evolution of Cadmium, Nickel and Chromium in solution at point 12, from June 2015 until May 2016.

- Point 13

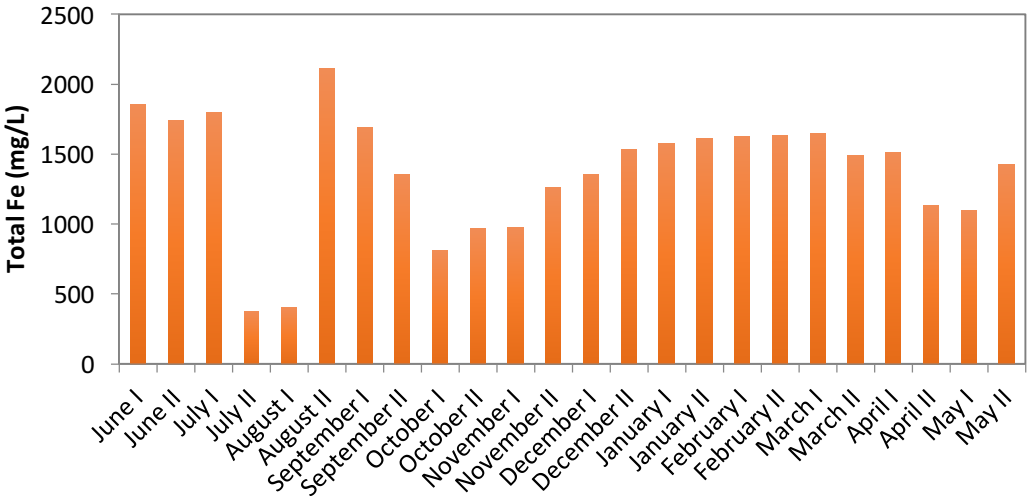
Total Fe (mg/L)
2500
2000
1500
1000
500
0
June I
June II
July I
July II
August I
August II
September I
September II
October I
October II
November I
November II
December I
December II
January I
January II
February I
February II
March I
March II
April I
April II
May I
May II

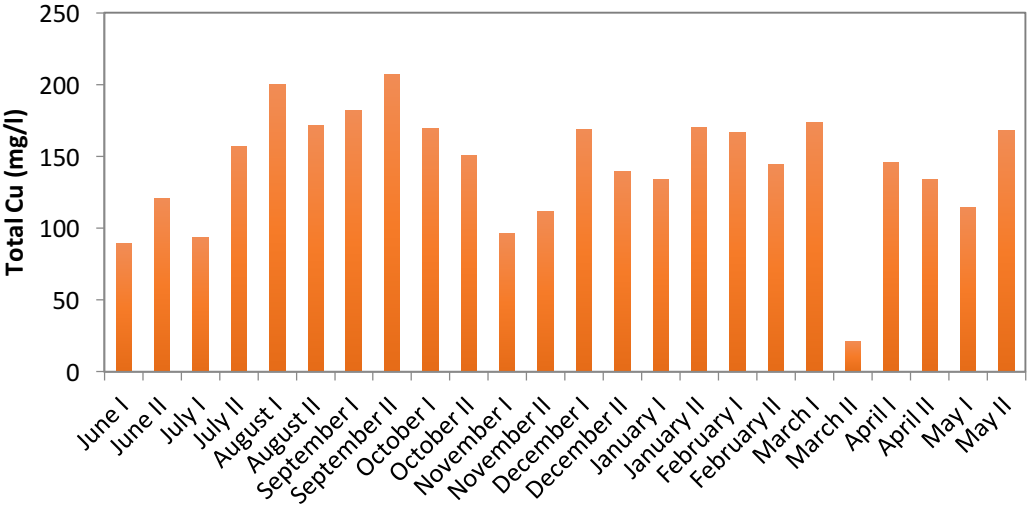
Total Cu (mg/l)
250
200
150
100
50
0
June I
June II
July I
July II
August I
August II
September I
September II
October I
October II
November I
November II
December I
December II
January I
January II
February I
February II
March I
March II
April I
April II
May I
May II

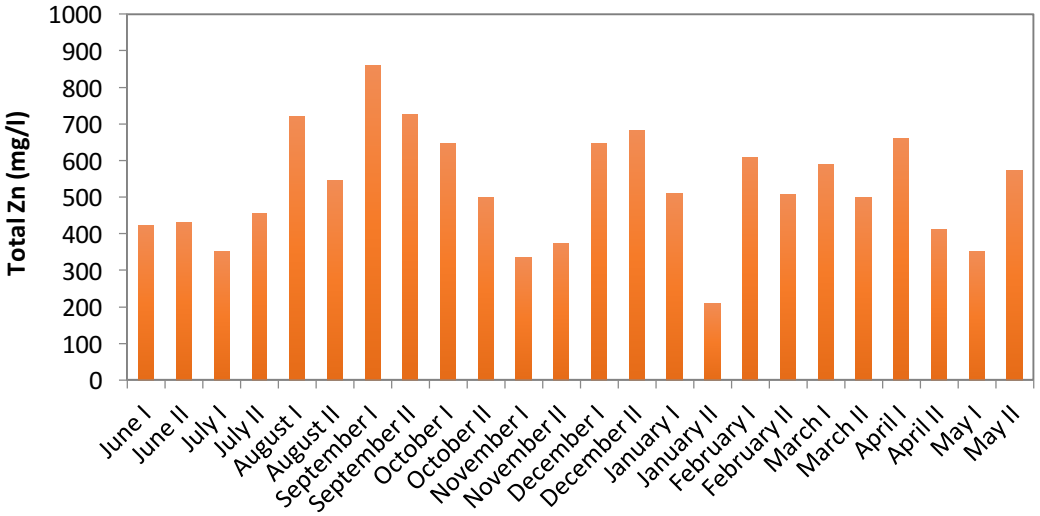
Total Zn (mg/l)
1000
900
800
700
600
500
400
300
200
100
0
June I
June II
July I
July II
August I
August II
September I
September II
October I
October II
November I
November II
December I
December II
January I
January II
February I
February II
March I
March II
April I
April II
May I
May II

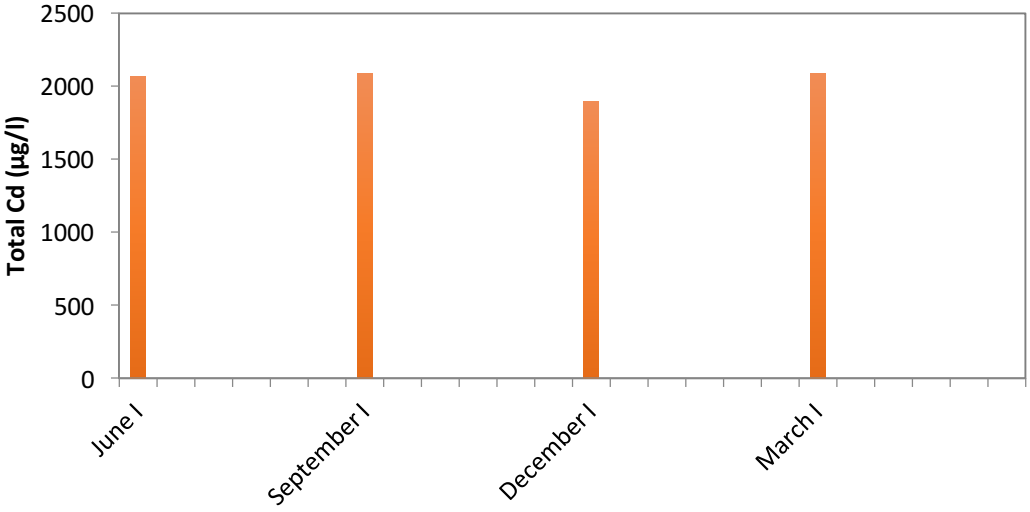
Total Cd (µg/l)
2500
2000
1500
1000
500
0
June I
September I
December I
March I

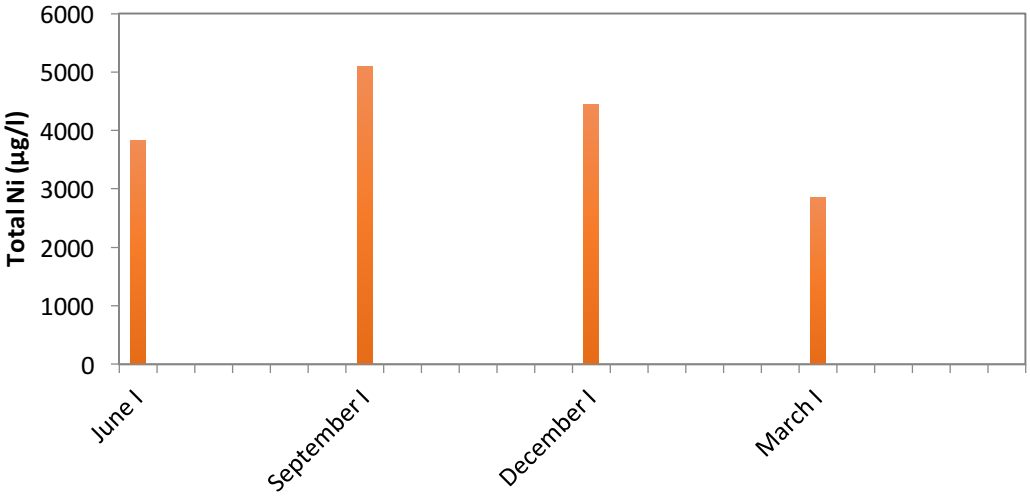
Total Ni (µg/l)
6000
5000
4000
3000
2000
1000
0
June I
September I
December I
March I

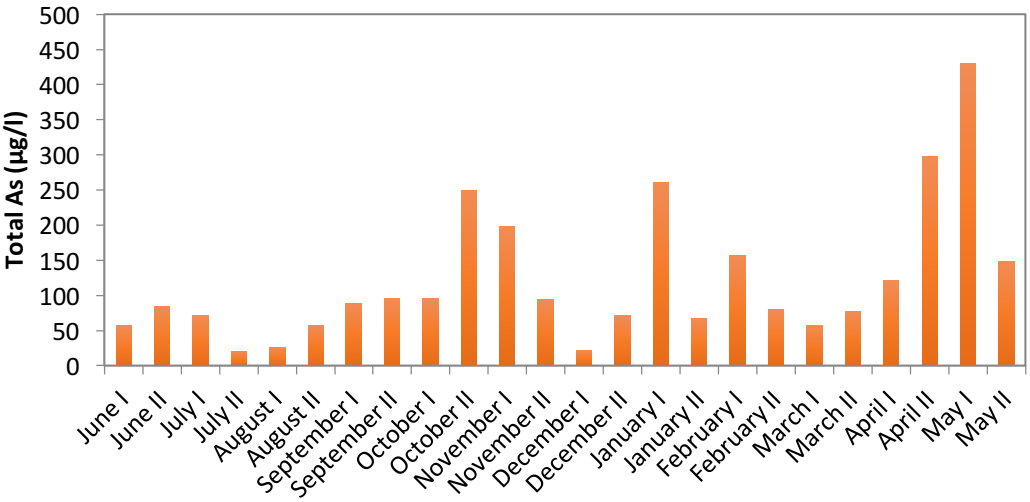
Total As (µg/l)
500
450
400
350
300
250
200
150
100
50
0
June I
June II
July I
July II
August I
August II
September I
September II
October I
October II
November I
November II
December I
December II
January I
January II
February I
February II
March I
March II
April I
April II
May I
May II

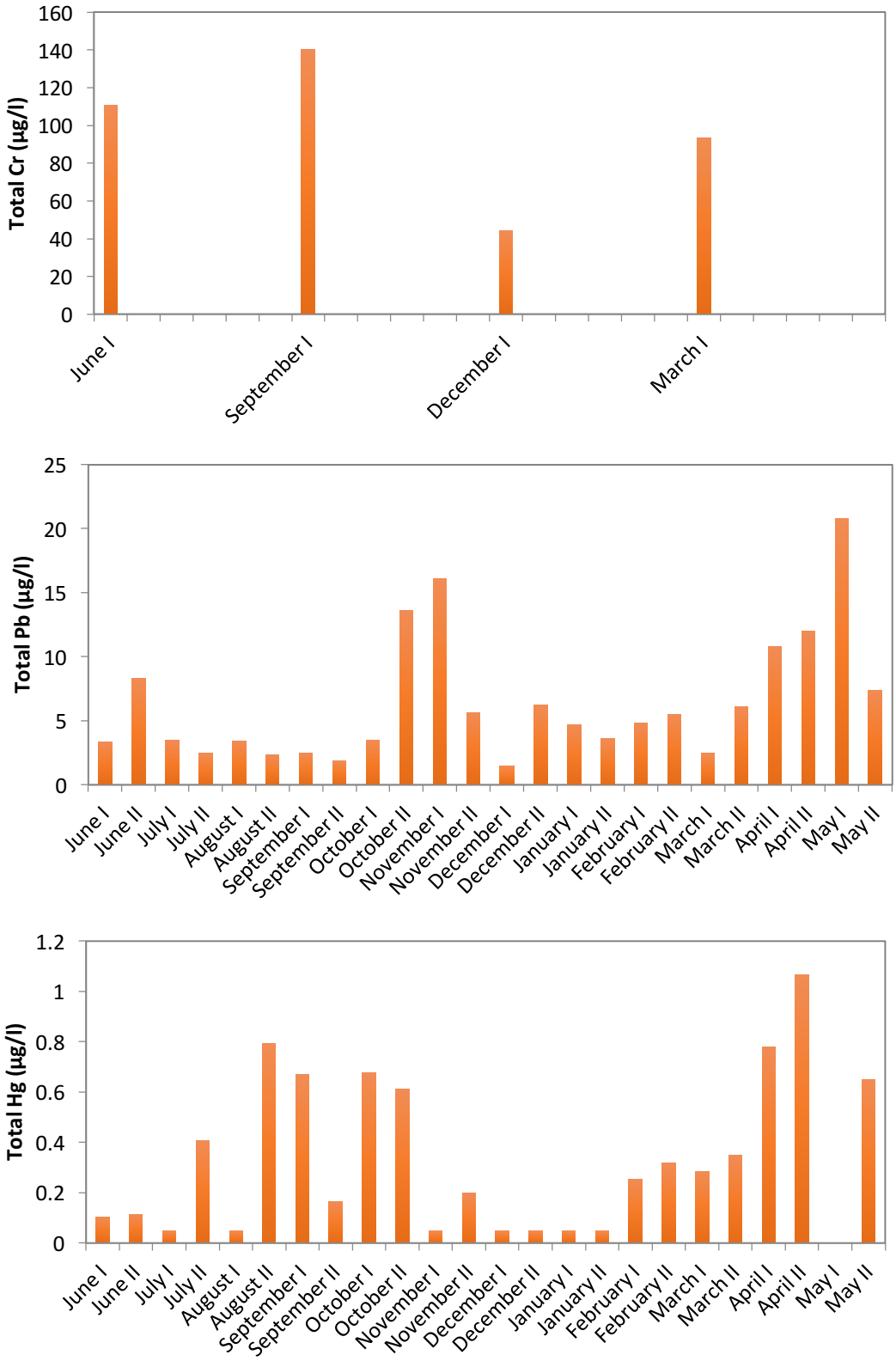

Figure A13: Graphs showing the bimonthly evolution of total Iron, Copper, Zinc, Arsenic, Lead and Mercury and the quarter-yearly evolution of Cadmium, Nickel and Chromium in solution at point 13, from June 2015 until May 2016.

- Point 14

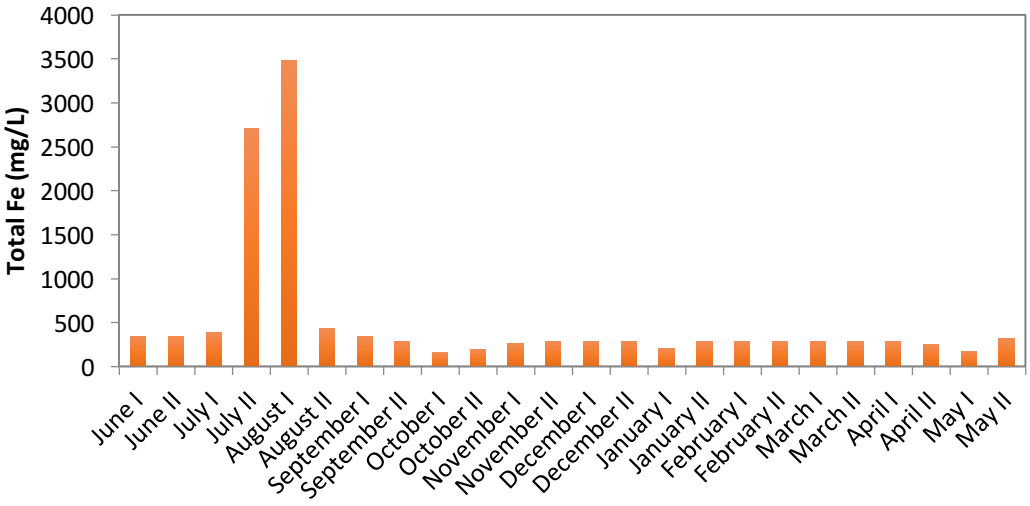
Total Fe (mg/L)
4000
3500
3000
2500
2000
1500
1000
500
0
June I
June II
July I
July II
August I
August II
September I
September II
October I
October II
November I
November II
December I
December II
January I
January II
February I
February II
March I
March II
April I
April II
May I
May II

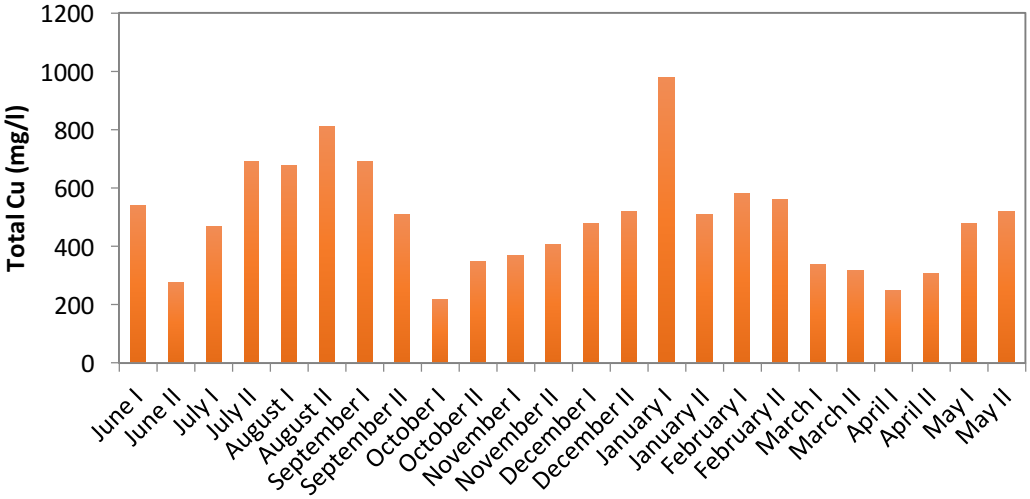
Total Cu (mg/l)
1200
1000
800
600
400
200
0
June I
June II
July I
July II
August I
August II
September I
September II
October I
October II
November I
November II
December I
December II
January I
January II
February I
February II
March I
March II
April I
April II
May I
May II

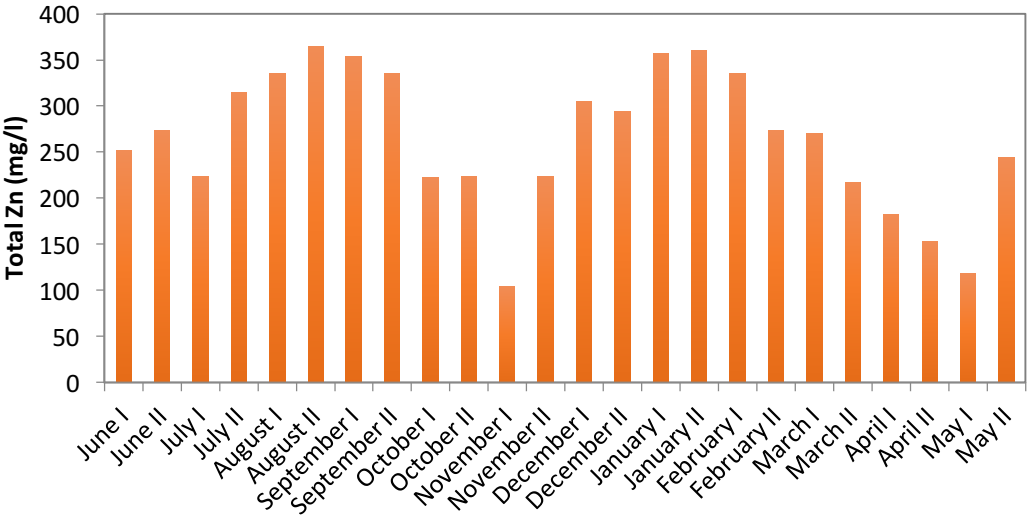
Total Zn (mg/l)
400
350
300
250
200
150
100
50
0
June I
June II
July I
July II
August I
August II
September I
September II
October I
October II
November I
November II
December I
December II
January I
January II
February I
February II
March I
March II
April I
April II
May I
May II

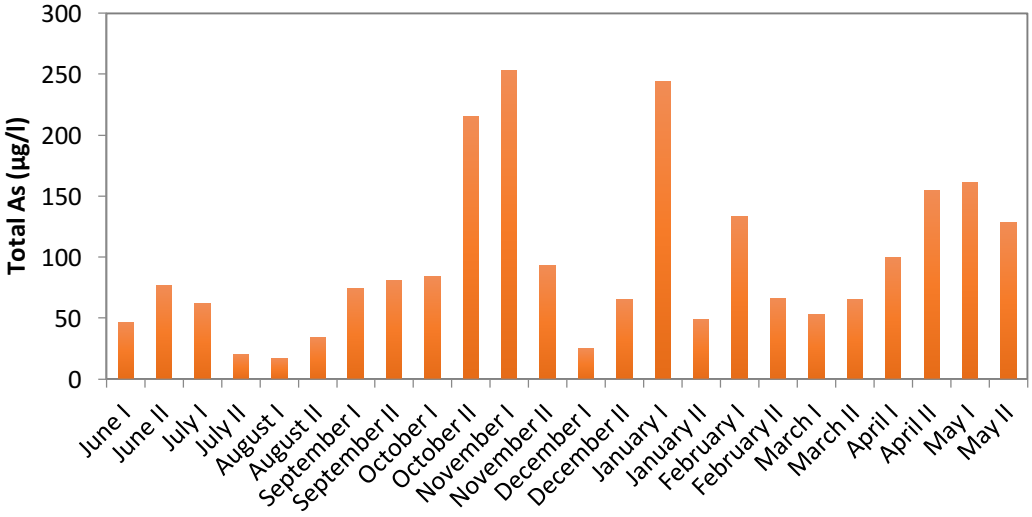

Figure A14: Graphs showing the bimonthly evolution of total Iron, Copper, Zinc and Arsenic in solution at point 14, from June 2015 until May 2016.

- Point 15

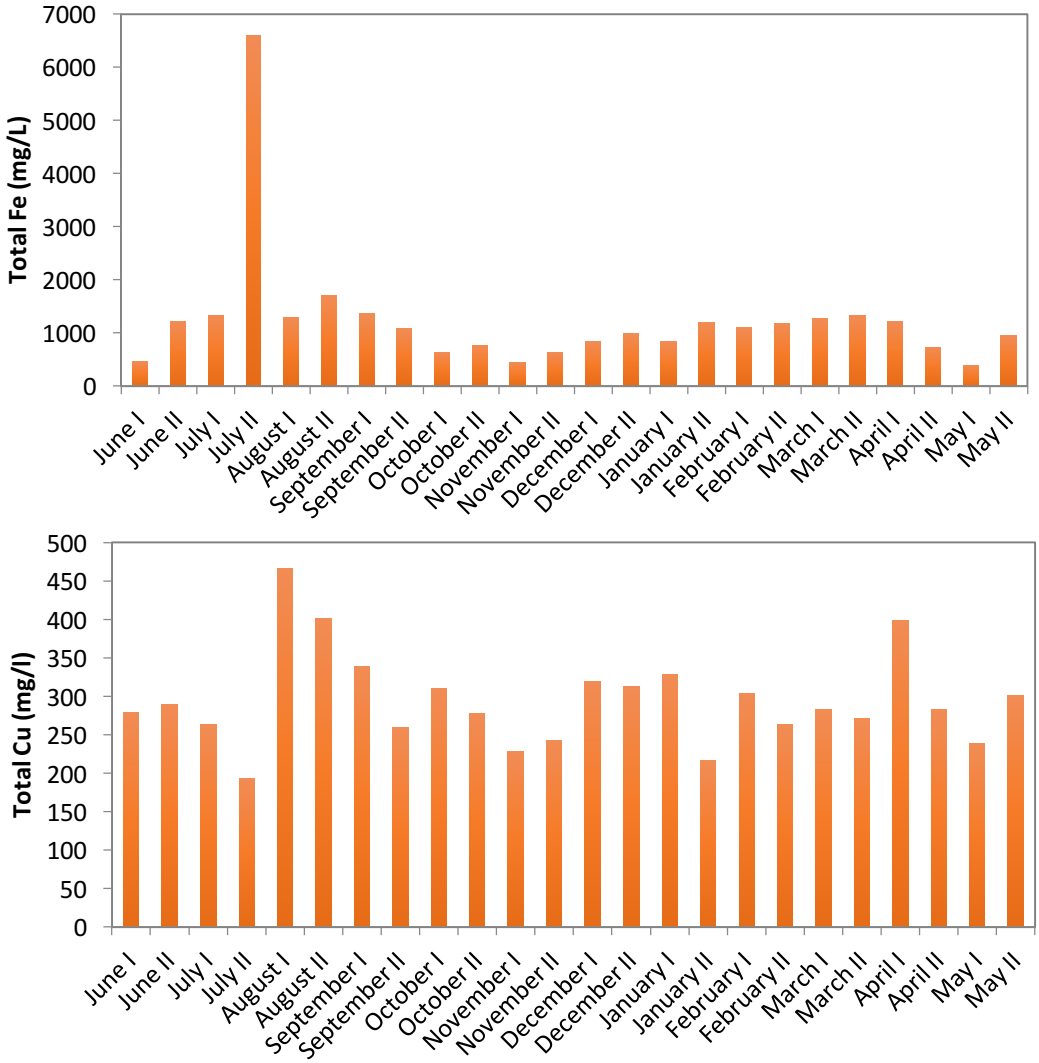

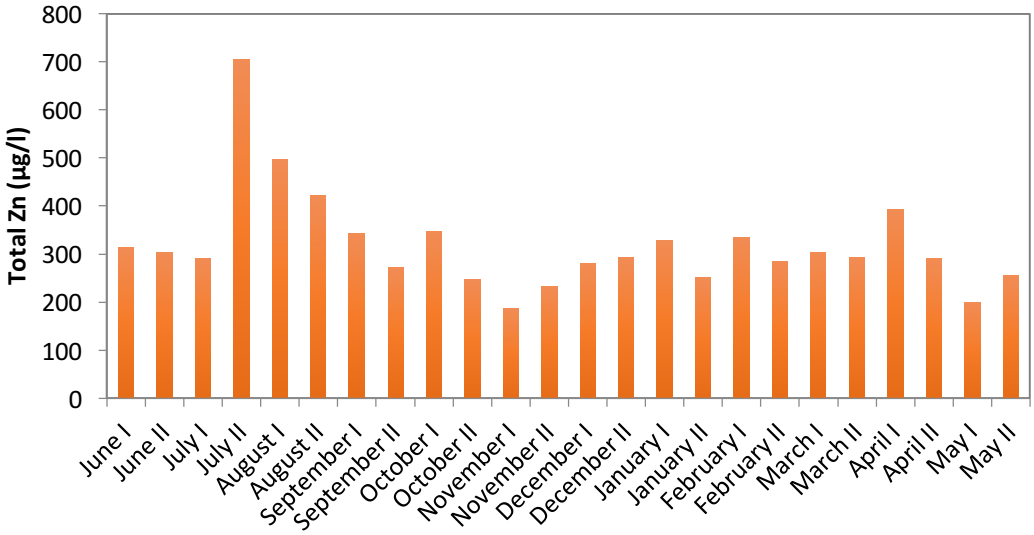
Total Zn (µg/l)
800
700
600
500
400
300
200
100
0
June I
June II
July I
July II
August I
August II
September I
September II
October I
October II
November I
November II
December I
December II
January I
January II
February I
February II
March I
March II
April I
April II
May I
May II

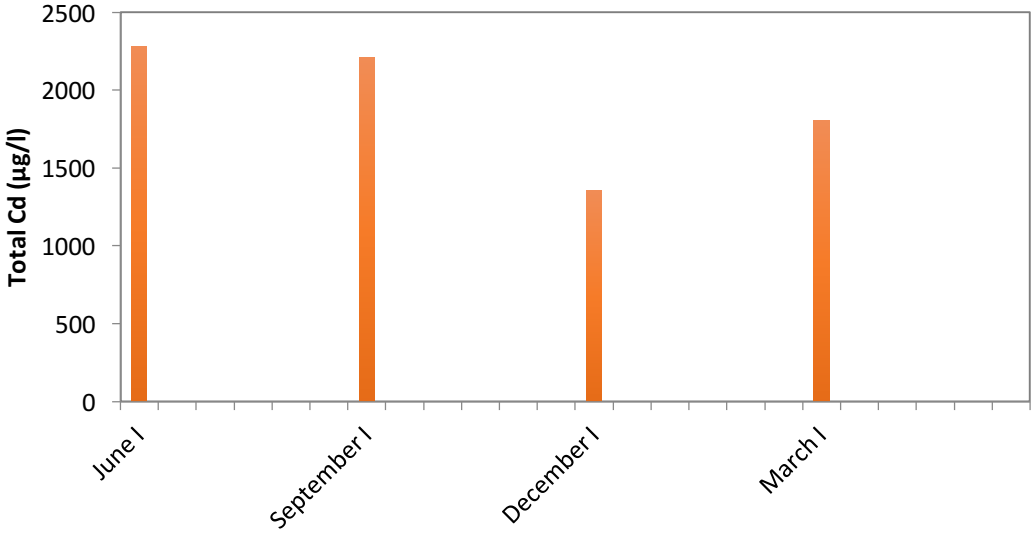
Total Cd (µg/l)
2500
2000
1500
1000
500
0
June I
September I
December I
March I

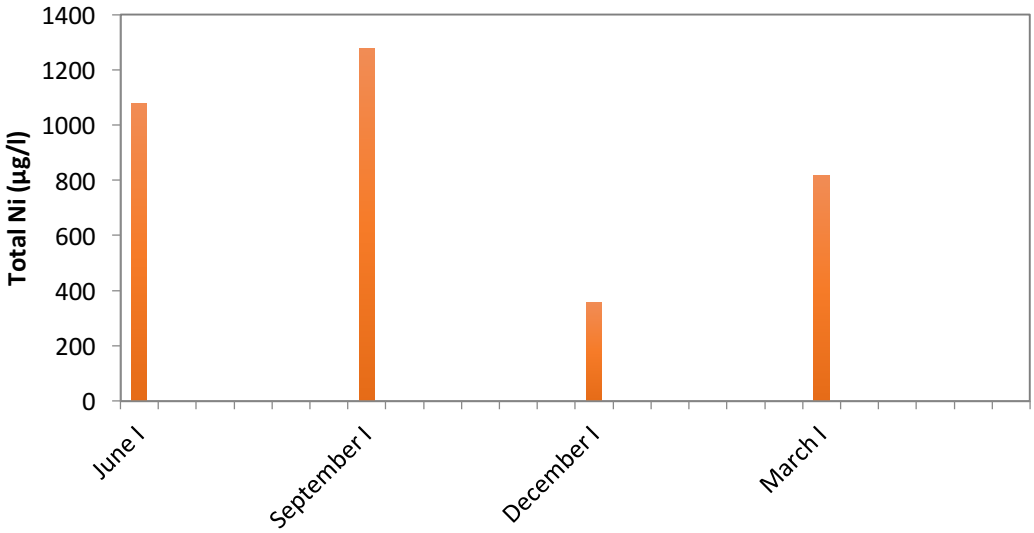
Total Ni (µg/l)
1400
1200
1000
800
600
400
200
0
June I
September I
December I
March I

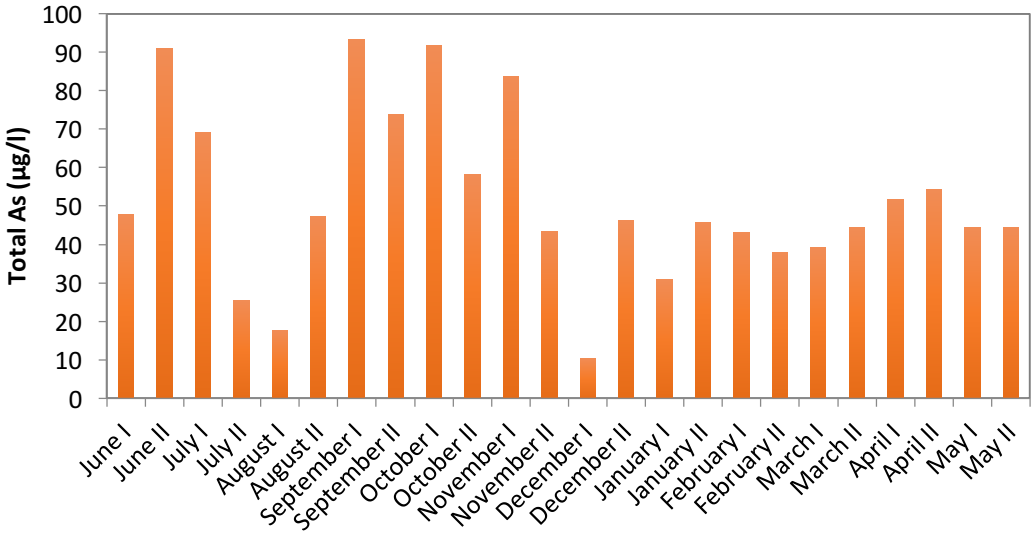
Total As (µg/l)
100
90
80
70
60
50
40
30
20
10
0
June I
June II
July I
July II
August I
August II
September I
September II
October I
October II
November I
November II
December I
December II
January I
January II
February I
February II
March I
March II
April I
April II
May I
May II

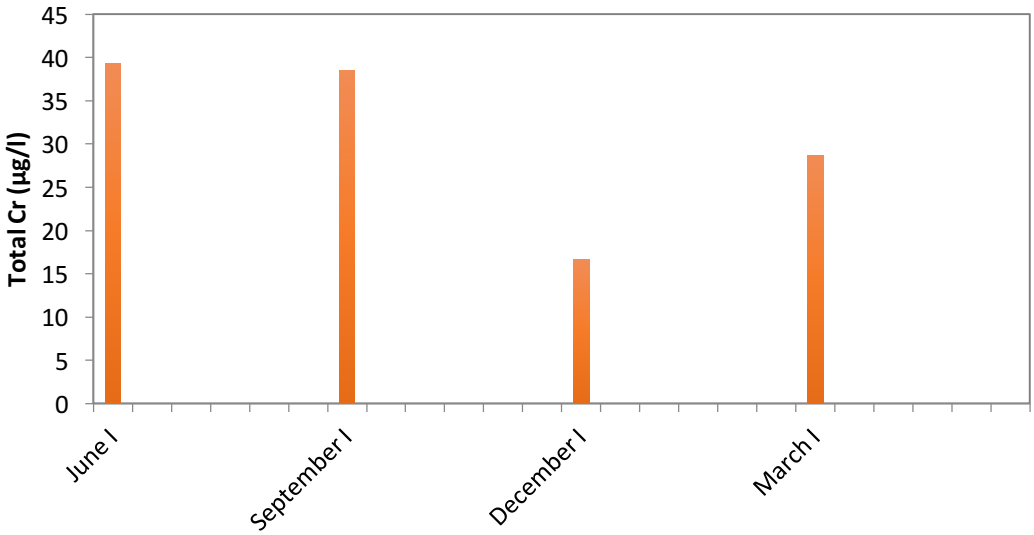
Total Cr (µg/l)
45
40
35
30
25
20
15
10
5
0
June I
September I
December I
March I

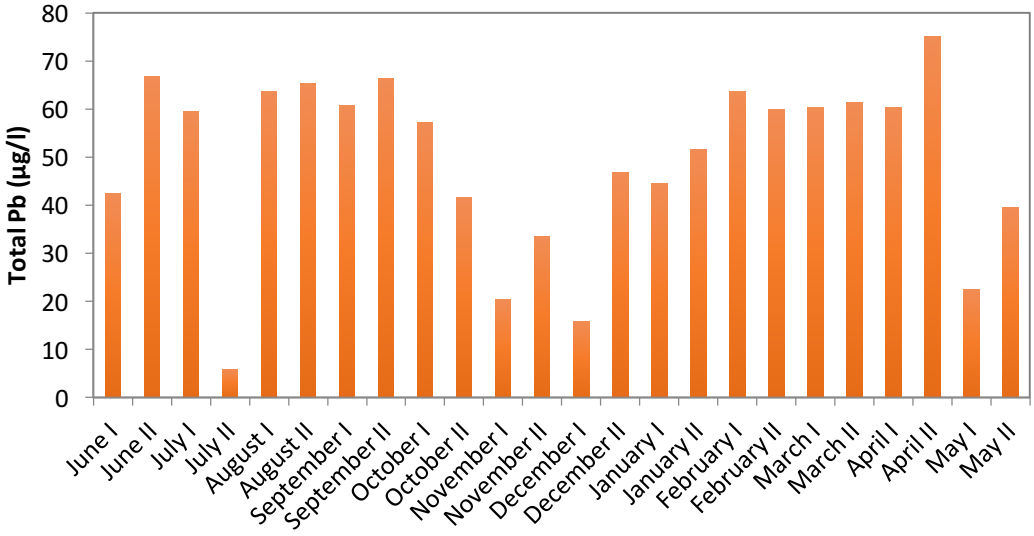
Total Pb (µg/l)
80
70
60
50
40
30
20
10
0
June I
June II
July I
July II
August I
August II
September I
September II
October I
October II
November I
November II
December I
December II
January I
January II
February I
February II
March I
March II
April I
April II
May I
May II

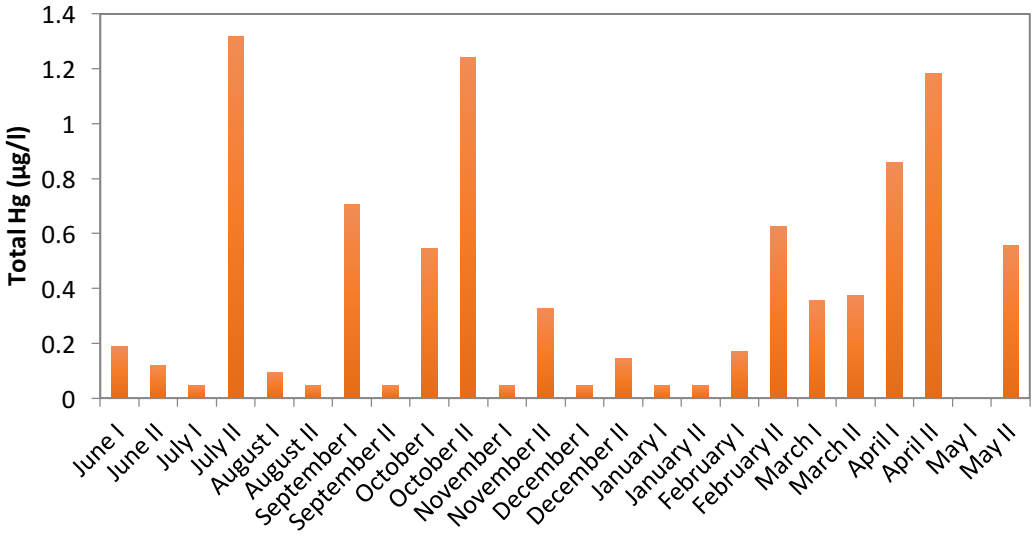

Figure A15: Graphs showing the bimonthly evolution of total Iron, Copper, Zinc, Arsenic, Lead and Mercury and the quarter-yearly evolution of Cadmium, Nickel and Chromium in solution at point 15, from June 2015 until May 2016

- Point 16

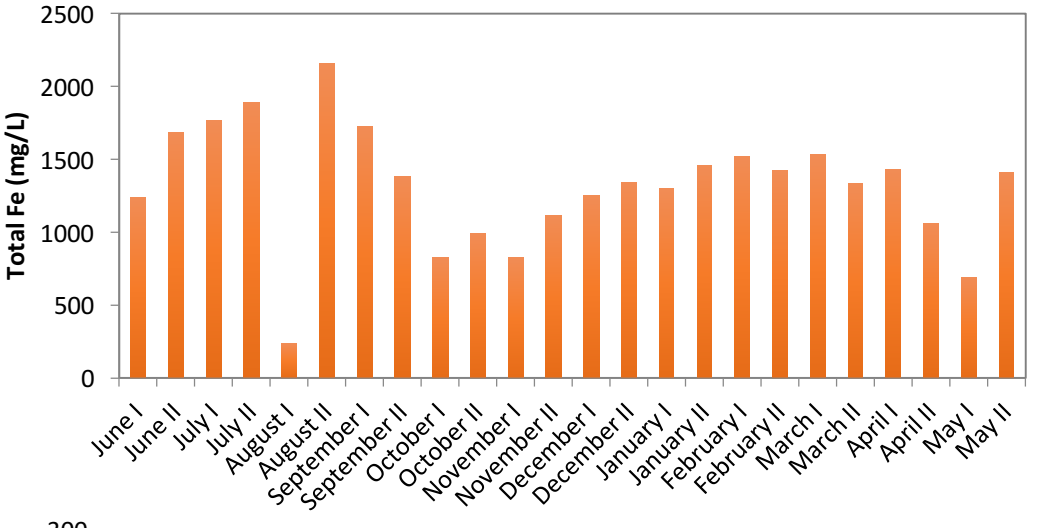

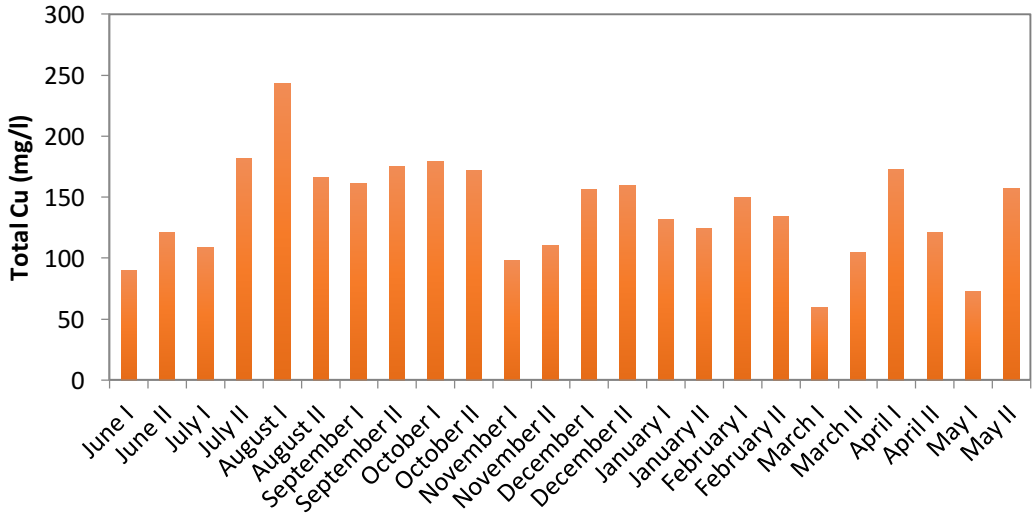

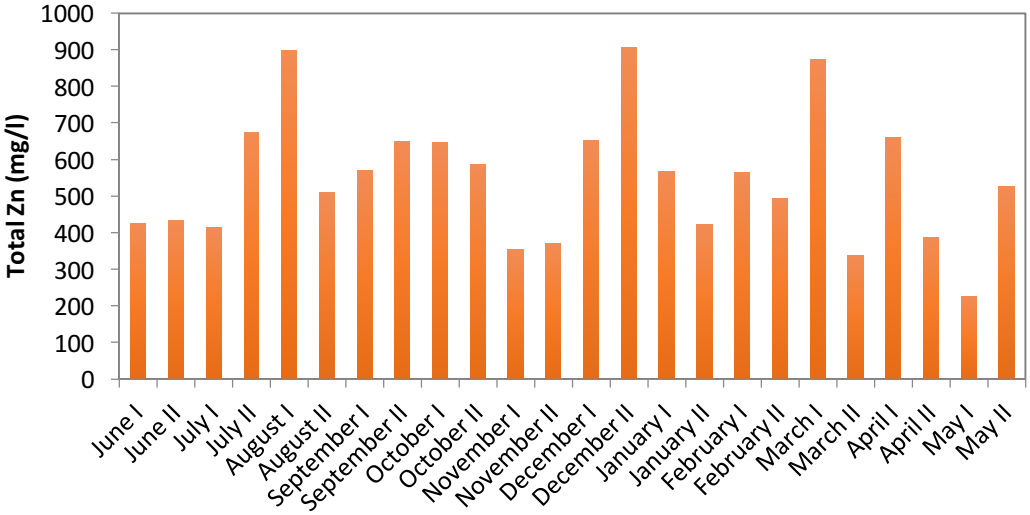
Total Zn (mg/l)
1000
900
800
700
600
500
400
300
200
100
0
June I
June II
July I
July II
August I
August II
September I
September II
October I
October II
November I
November II
December I
December II
January I
January II
February I
February II
March I
March II
April I
April II
May I
May II

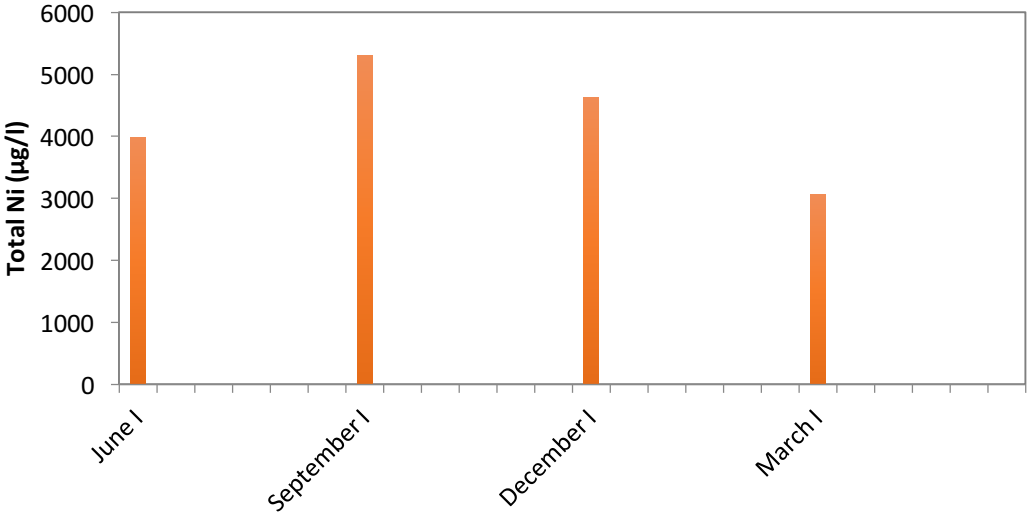
Total Ni (µg/l)
6000
5000
4000
3000
2000
1000
0
June I
September I
December I
March I

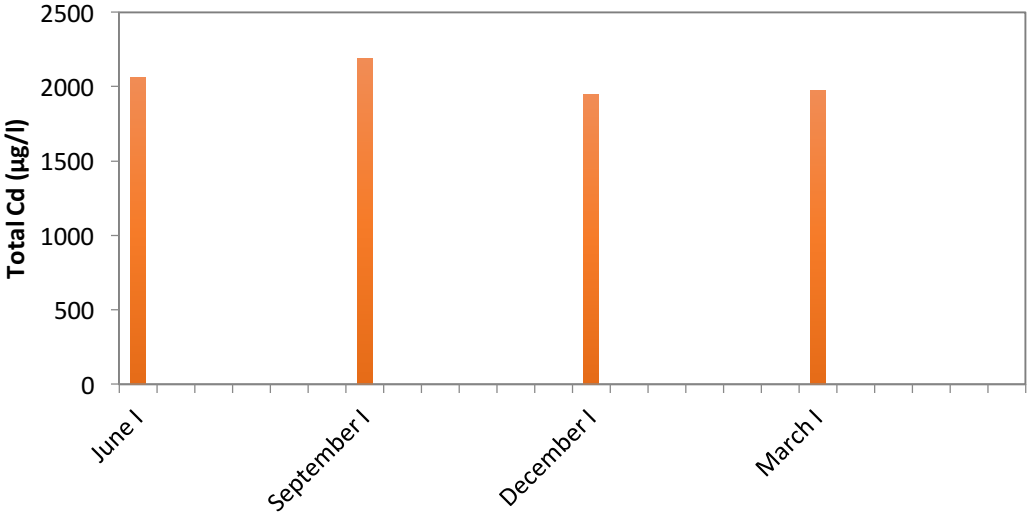
Total Cd (µg/l)
2500
2000
1500
1000
500
0
June I
September I
December I
March I

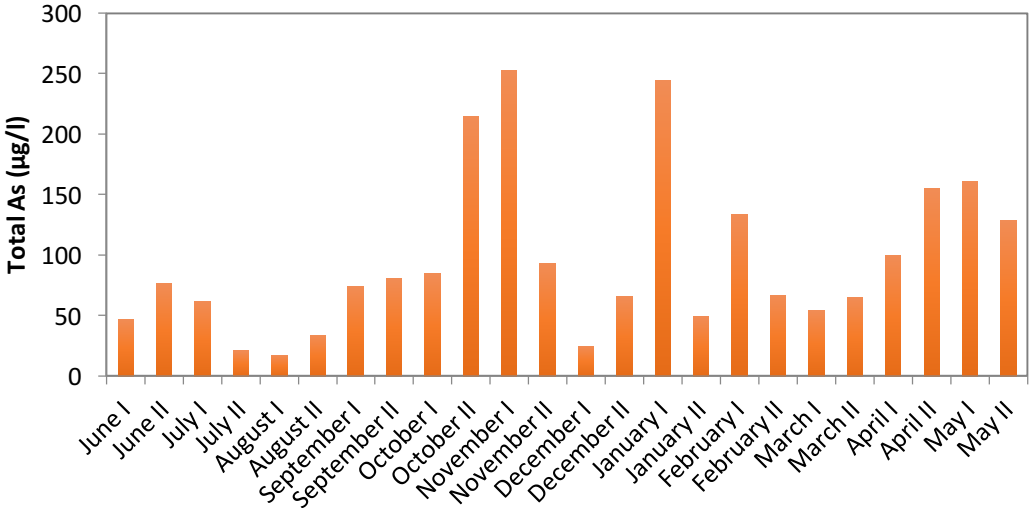
Total As (µg/l)
300
250
200
150
100
50
0
June I
June II
July I
July II
August I
August II
September I
September II
October I
October II
November I
November II
December I
December II
January I
January II
February I
February II
March I
March II
April I
April II
May I
May II

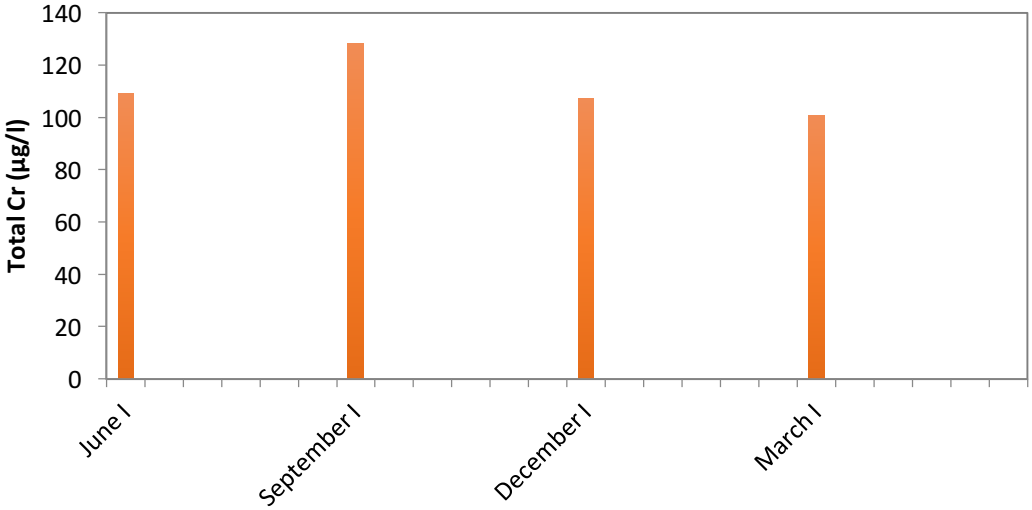
Total Cr (µg/l)
140
120
100
80
60
40
20
0
June I
September I
December I
March I

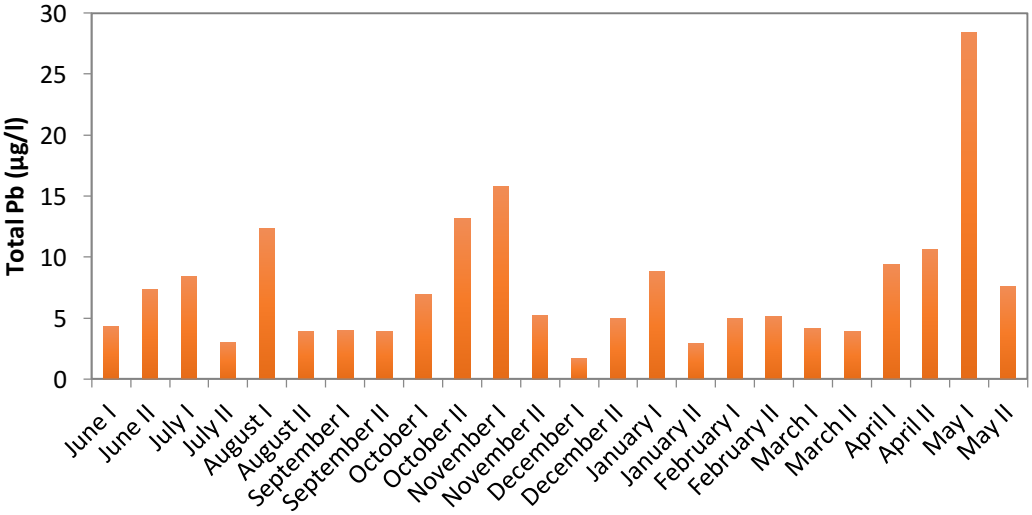
Total Pb (µg/l)
30
25
20
15
10
5
0
June I
June II
July I
July II
August I
August II
September I
September II
October I
October II
November I
November II
December I
December II
January I
January II
February I
February II
March I
March II
April I
April II
May I
May II

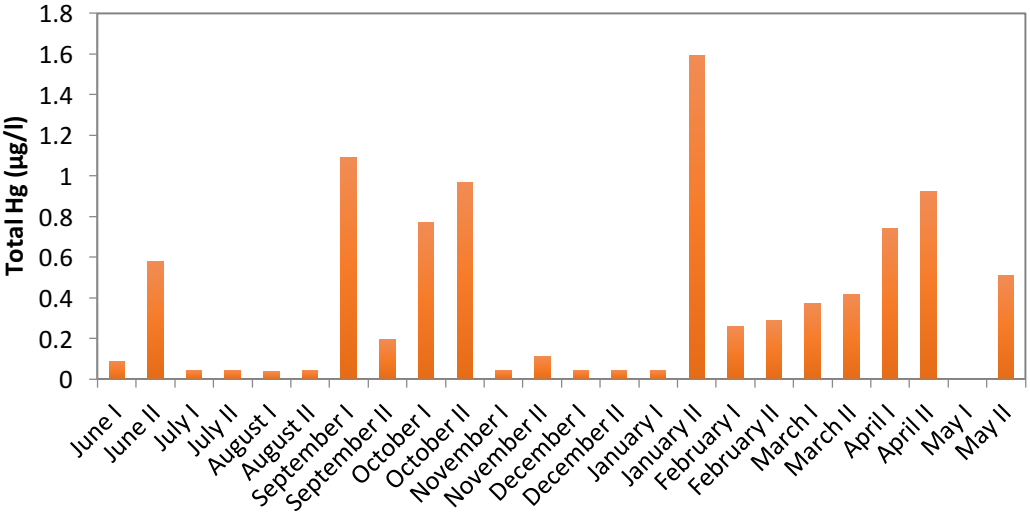

Figure 16: Graphs showing the bimonthly evolution of total Iron, Copper, Zinc, Arsenic, Lead and Mercury and the quarter-yearly evolution of Cadmium, Nickel and Chromium in solution at point 16, from June 2015 until May 2016.